The Hunt for Frozen Organic Molecules in Space

A Laboratory Approach

Proefschrift

ter verkrijging van
de graad van doctor aan de Universiteit Leiden,
op gezag van rector magnificus prof.dr.ir. H. Bijl,
volgens besluit van het college voor promoties
te verdedigen op 9 mei 2023
klokke 16:15 uur
door

Marina Gomes Rachid

geboren te Rio Claro - SP, Brazilië
in 1989

Promotores:

Prof. dr. H.V.J. Linnartz
Prof. dr. E.F. van Dishoeck

Promotiecommissie:

Prof. dr. I.A.G. Snellen	
Prof. dr. S. Viti	
Prof. dr. W.A. Brown	(University of Sussex)
Dr. P.A. Gerakines	(NASA Goddard Space Flight Center)
Prof. dr. T.K. Henning	(Max Planck Institute for Astronomy)
Dr. B. Maté	(Instituto de Estructura de la Materia)

ISBN: 978-94-6419-785-3

Cover art:
A treasure map for COMs by Marina G. Rachid
Coffee, watercolor, milk, and ink on paper. Digital finalization: Marina G. Rachid feat. Katie Slavicinska. *Attention: Contains lactose.*

Contents

Contents

1

Introduction

The first interstellar molecule was detected in 1937 (Swings and Rosenfeld, 1937). This molecule, the methylidyne radical (CH), was identified through its characteristic absorption of visible light. In the following years, other diatomic molecules were also identified, and to date, over 280 molecules have been detected in the interstellar medium (ISM), circumstellar environments, and extragalactic sources (see McGuire 2022). These molecules were identified by their characteristic absorption or emission of light, which compose a spectral signature of every species. The identification of these signatures has become possible due to extensive laboratory measurements investigating the interactions between light and matter, the basis of spectroscopy. Comparing astronomical observations with the spectra of molecules recorded under simulated interstellar conditions allows for identifying molecular species in space and at the same time to obtain information about the physical conditions in their surroundings. The energy level distribution of a molecule and its absorption and emission line profiles are dependent on the temperature, density, radiation field, and kinematics of the medium. Thus, the detection and analysis of molecular features also provide a gauge of interstellar conditions. This thesis focuses on the laboratory spectroscopy of molecules in the ISM, in particular, molecules embedded in the interstellar and circumstellar frozen material, the interstellar ice.

The ISM contains simple molecules such as CH, CO, and H_2, but also larger and more complex organic molecules (COMs[1]) such as glycolaldehyde, the simplest sugar molecule (Hollis et al., 2000). Molecules that are highly unstable in terrestrial environments, such as the cyanopolyynes[2], are also identified in interstellar environments. Carbon-based molecules in which the atoms are connected to form cage-like structures, such as the buckminsterfullerene (C_{60}), also figure in the molecular inventory list. Furthermore, it is estimated that 10 - 20% of all the carbon in the ISM is locked in large carbon-based compounds, the polycyclic aromatic hydrocarbons (PAH, Tielens 2008). These molecules, which on Earth are associated with the combustion of materials such as coal, oil, and wood, are found across a diversity of environments in the ISM.

Probing the chemical composition of our Solar System, taught us that the chem-

[1] Molecule containing a C-H bond and at least 6 atoms
[2] Organic molecules with the chemical formula HC_nN

istry in space could be even more fascinating. Space missions aimed at exploring moons, planets, and comets, revealed that organic molecules are ubiquitous. The Rosetta Orbiter Spectrometer for Ion and Neutral Analysis (ROSINA) onboard the Rosetta spacecraft has probed *in-situ* the composition of the comet 67P/Churyumov-Gerasimenko. These measurements allowed the detection of organic molecules even more complex than the ones found in the ISM, such as the amino acid glycine and benzoic acid, and a range of sulfur-containing molecules, such as sulfur allotropes and salts (Altwegg et al., 2016, 2022; Hänni et al., 2022). In addition, the comparison of the organic molecular inventory in the comet 67P and young stars indicates that the cometary material preserves molecules formed at the early stages of star formation (Drozdovskaya et al., 2019). Thus, the composition of comets reveals the ingredients that were merged to form planets and other solid bodies in our Solar System.

The presence of organic compounds outside Earth does not necessarily imply that larger biological molecules, such as proteins and nucleic acids, exist in extraterrestrial environments. Thus far, laboratory and theoretical works simulating space environments have demonstrated that small organic species are important starting points to form these biological molecules, which are needed for life as we know to flourish (e.g., Meinert et al. 2016; Ligterink et al. 2018; Oba et al. 2019). Observing and studying the molecular diversity in space helps us to understand where and how these molecules are formed, and how they are spread in the cosmos. In the end, molecules can teach us about the origins of the Milky Way, our Solar System, and even ourselves.

1.1 Molecules in the stellar life cycle

The surreal beauty of astronomical pictures can give us the impression that the space between the stars, the ISM, is steady and quiet. This view of a calm place is challenged by the harsh conditions found in the ISM, where different environments experience extremes of temperature, ranging from 3 K to 10^5 K. Stars produce ionizing radiation and stellar winds during their life. Massive stars ($m > 8$ $M_\odot$) at the end of their lives explode as supernovae, heating their surroundings to very high temperatures ($T > 10^4$ K) and producing highly energetic particles (i.e., cosmic rays). These high-mass stars will potentially form a neutron star or black hole, which likely contains an accretion disk, that produces highly energetic radiation and particles. Under these hostile conditions and the generally low pressures found in the ISM (which limit collisions of atoms and molecules), it can be surprising that molecules form and any sort of complex chemistry can flourish.

Molecular clouds are the key to this apparent puzzle. Molecular clouds are large and dense extensions of gas and dust formed by the gravitational collapse of the diffuse ISM material, as shown schematically in Figure 1.1 (indicated by the numbers I and II). The outer parts of a molecular cloud are composed of atomic gas and, in general, simple molecules (Snow and McCall, 2006). In these environments, the lifetime of molecules is relatively short, as ionizing radiation from stars and other sources can dissociate them. Deeper into the cloud, the radiation field is attenuated, as the cloud material shields itself, preventing photons and some particles to reach the cloud's densest parts (Draine, 2010). In such environments, larger molecules can form and survive for long periods.

In the denser parts of a molecular cloud ($\geq 10^4$ cm^{-3}) the gas is mostly molecular, and H_2 and CO are the most abundant species. In these regions, gas-phase formation of a few larger species is possible but these reaction routes generally do not account for the observed abundance of simple species, like water (H_2O), as well as COMs. The reasons for this are associated with the prevalence of two body processes in these environments, low collision rates, and the short time scale of the interaction in the gas phase. Under these conditions, the formation and observed abundances of COMs can only be accounted for by considering chemical reactions occurring on the surface of interstellar dust. Interstellar dust grains are agglomerates of silicates, carbonaceous material, and other minor elements (Draine, 2003) and represent on average 1% of the molecular cloud mass. At the cold temperatures found in the cloud's inner parts ($\sim$ 10 K), molecules and atoms accrete to the surface of these dust grains and form layers of frozen material, the so-called interstellar ice. At these surfaces, atoms can diffuse and react with other atomic or molecular species (Tielens and Hagen, 1982; Linnartz et al., 2015). Thus, these icy dust grains provide a place where interstellar chemistry can occur. Additionally, these grains act as a third body, where the energy released from chemical reactions can be dissipated, stabilizing the reaction products. Further chemical reactions may be triggered by UV photons, energetically charged particles, or the increase in the ice temperature. The research field that experimentally investigates these processes is known as solid-state astrochemistry

With the onset of star formation, the interstellar ice layers will pass through a sequence of physical and chemical transformations. As material falls onto the central forming star, its surroundings are heated (shown in III of Figure 1.1). This eventually causes the interstellar ice layers to sublimate. Once in the gas phase, these molecules can be probed through their rotational transitions at radio or submillimeter frequencies (typically below 2 THz). Indeed, a diversity of molecules, including a remarkably large

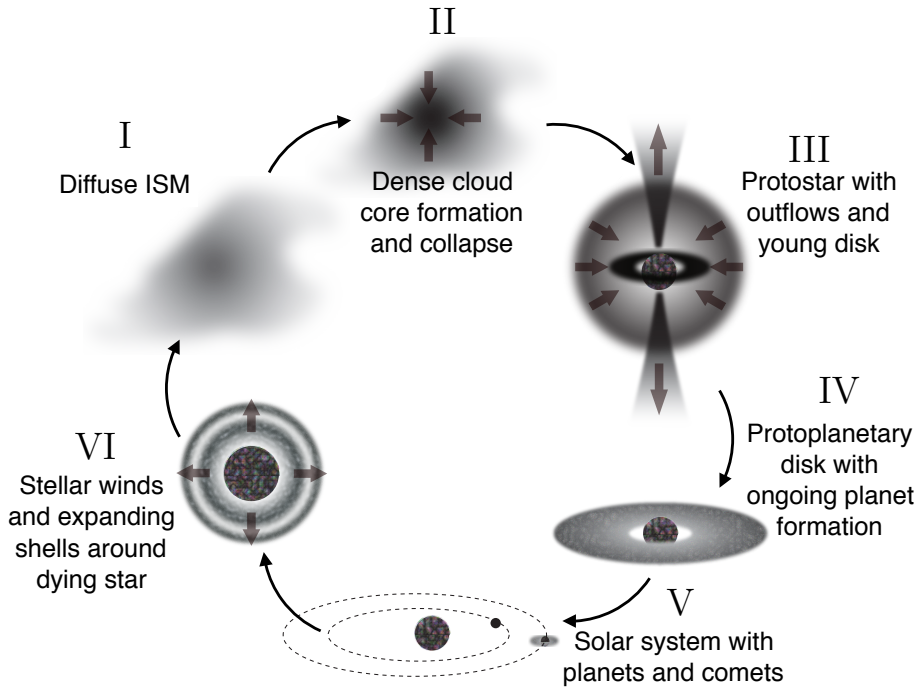

Figure 1.1: Schematic representation of the stellar life cycle. Star formation begins with the diffuse ISM (indicated in I), due to internal and external effects the diffuse ISM can start to collapse forming molecular clouds, and the densest regions of the molecular clouds start to form dense cores (II). The dense cores will collapse and form a protostar (III). As material falls onto the central protostar, a disk is formed, its surrounding is heated, and the protostar produces outflows of gas. After the star is formed a protoplanetary disk remains (IV) and forms planets and comets within $1 - 10$ Myrs (V). At the end of the life of the star (VI) it produces winds or explodes as a supernova bringing the elements produced in the stellar interior by nuclear fusion back to the diffuse ISM where the cycle of the star formation can repeat (based on Öberg, 2016).

number of organic species have been observed in the warm (T $\sim$ 100 K) and dense ($\geq 10^6$ cm^{-3}) gas surrounding high- and low-mass protostars by surveys performed with the Aratama Large Millimeter/submillimeter Array (ALMA, e.g., Jørgensen et al. 2020; van Gelder et al. 2020; Yang et al. 2021). Systematic studies of the warm gas around protostars indicate that the organic molecular inventory of these objects is set at the early stages of cloud evolution (Nazari et al., 2022). At these (pre-stellar) stages, the gas is almost completely frozen onto the dust grains (Caselli et al., 2022). Thus, interstellar ice is considered the main source of organic molecules in the interstellar

medium.

Part of the interstellar grains surrounding the newly formed stellar object will be incorporated into a rotating disk of gas and solid material, the protoplanetary disc (shown in IV of Figure 1.1). There, the interstellar grains will coagulate and form larger solid agglomerates, which will eventually form rocky bodies such as comets, moons, and planets. If the icy material coating the dust grains survives the collapse and the accretion process, the frozen molecular inventory can be incorporated into these bodies of the planetary system (V of Figure 1.1). The extent at which the frozen molecules created in the parent cloud are transferred onto the larger bodies is still uncertain. However, comparisons of the composition of the comet 67P, measured *in-situ* by the Rosetta mission, and solar-type young stars hint at the idea that cometary material is inherited from pre-stellar and protostellar stages (Drozdovskaya et al., 2019).

The stellar life cycle ends after many evolutionary stages. At its final stage (indicated by VI in Figure 1.1), the star produces winds that blow the circumstellar gas into the ISM. The most massive stars explode as supernovae, expelling the circumstellar gas and the heavier elements (e.g. C, N, O, S, Fe, Ni) that were produced through nuclear fusion (Carroll and Ostlie, 2017). All these processes enrich the gas from which a new generation of stars will be formed.

1.2 Interstellar ice

The existence of interstellar dust and its physical properties (e.g., composition, size, extinction) is debated since the 30's. The idea that H_2O and other molecules could stick to interstellar solid particles, coating them with a layer of frozen material, came later (van de Hulst, 1946). The first observational evidence for the existence of solid interstellar material came with the observation of silicate features around the 70's (Knacke et al., 1969; Woolf and Ney, 1969). In the years to come, absorption features of silicates, such as the 9.7 μm (Si-O stretching) and 18 μm (O-Si-O bending) bands, have been observed in absorption and emission toward several objects (e.g., Min et al. 2007; Draine 2003). The unambiguous detection of icy molecules happened in 1973 when the 3.1 μm absorption feature of H_2O ice was convincingly identified toward the Orion BN/KL region (Gillett and Forrest, 1973). In the decades that followed, other broad interstellar absorption bands were observed toward different infrared (IR) sources, which allowed for the identification of other solid-state species, such as CO and CO_2, and the absorption of molecular functional groups whose carriers could not

be fully identified, such as -CH_3 and -C=O (e.g., Soifer et al. 1979; Hagen et al. 1980; Lacy et al. 1984; d'Hendecourt and Jourdain de Muizon 1989; Grim et al. 1991; Lacy et al. 1991).

From 1995 onward, infrared observations using the Very Large Telescope (VLT), the Infrared Space Observatory (ISO), and the *Spitzer* Space Telescope, allowed for observing ice features at much higher resolution and sensitivity, and in the case of ISO and Spitzer, unhindered by the Earth's atmosphere. Several observing programs performed with these and other infrared facilities allowed for tracing the median molecular inventory of ices in different environments, as shown schematically in Figure 1.2 (which also includes abundances obtained by new JWST observations). Figure 1.2 shows that the composition of interstellar ice is dominated by water (H_2O). Carbon dioxide (CO_2) and carbon monoxide (CO) are also abundant, with abundances ranging from a few percent up to $\sim 50\%$ of the H_2O budget. The large variation observed for these molecules is due to the high variation in local conditions, such as dust temperature and radiation field (Boogert et al. 2015 and references therein). Also, methanol (CH_3OH) has been identified at abundances of a few percent up to $\sim 30\%$ with respect to solid H_2O. Ammonia (NH_3) and methane (CH_4) are detected as minor components, with relative abundances of $\leq 10\%$ with respect to solid H_2O. Less abundant species that were also identified are ^{13}CO, $^{13}CO_2$, OCN^-, and OCS. In addition to these molecules, H_2CO, HCOOH, and SO_2 are likely identified but stronger observational evidence is needed for definite assignments.

The James Webb Space Telescope (JWST), launched on the 25th of December of 2021, is capable of performing observations in the 0.6 - 28 μm range with high resolution and sensitivity. These observations will extend our understanding of inter- and circumstellar ices and their link to observed gas phase molecular abundances. At the moment of writing, the first ice observations with the JWST across the mid-infrared range have been made public (Yang et al., 2022; McClure et al., 2023). Figure 1.3 shows the 2.5 - 20 μm spectra of ices at dense parts (visual extinction, A_v, higher than 50) of the Chamaeleon I low-mass star-forming region. These observations show the densest quiescent cloud regions in which interstellar ice has been detected. The absorption bands of frozen molecules identified in these JWST observations are marked in different colors. Many known interstellar species are identified at these lines of sight, and some of them, such as CH_4, $^{13}CO_2$, and ^{13}CO, are detected toward regions illuminated by a background star for the first time. Section 1.2.3 describes in more detail how JWST will further our understanding of the interstellar ice composition.

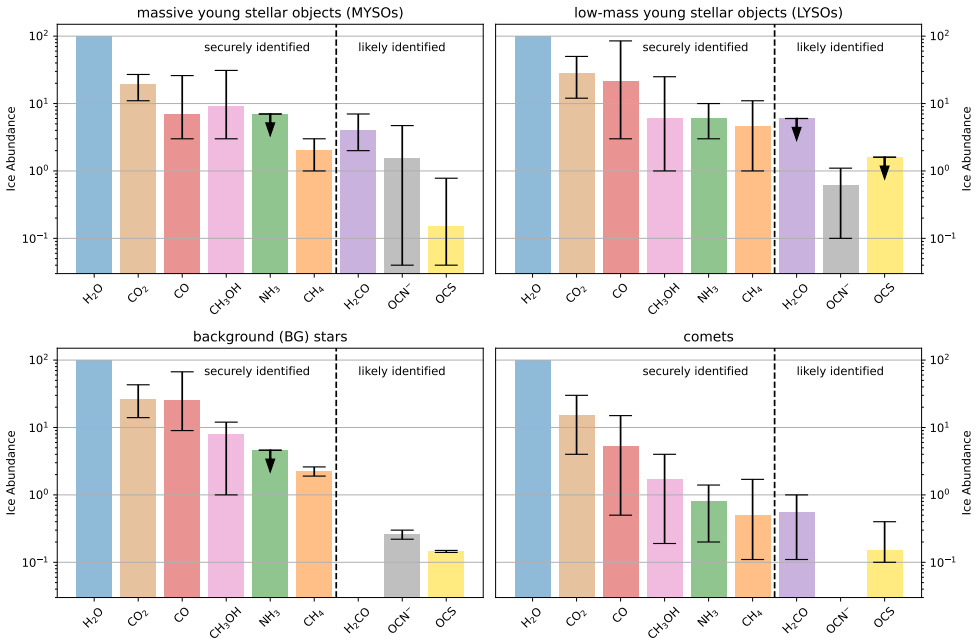

Figure 1.2: Relative abundance with respect to water (H_2O) for the nine most abundant icy molecules detected (or likely detected) towards massive young stellar objects (MYSOs; top left), low-mass young stellar objects (LYSOs; top right), background stars (BG, bottom left) and comets (bottom right). The black bars indicate the minimum and maximum detected values and the arrows indicate upper limits. The relative abundance values for MYSOs are from Boogert et al. 2015 for CO_2, CO, CH_3OH, NH_3, CH_4, and H_2CO, and from Boogert et al. 2022 for OCN^- and OCS. For LYSOs, all values are sourced from the compilation in Boogert et al. 2022. As for BG stars, the values for CO_2, CO, and CH_3OH are from Boogert et al. 2015, while the values for NH_3, CH_4, OCN^-, and OCS are obtained from McClure et al. 2023. For comets, the values for CO_2, NH_3, and H_2CO are from Mumma and Charnley (2011), the values for CH_3OH, CH_4, and CO, are taken from DiSanti and Mumma 2008 and for OCS from Saki et al. 2020.

1.2.1 The formation and evolution of interstellar ices

The identification of interstellar ice molecules has been largely based on accurate laboratory data, as available today from several databases, including LIDA, the Leiden Ice Database for Astrochemistry (Rocha et al., 2022). Spectroscopy works focusing on characterizing molecules under interstellar conditions are essential to determine the composition and morphology of interstellar ice as well as outline its evolutionary history. In the following, the current model for the formation and chemical evolution

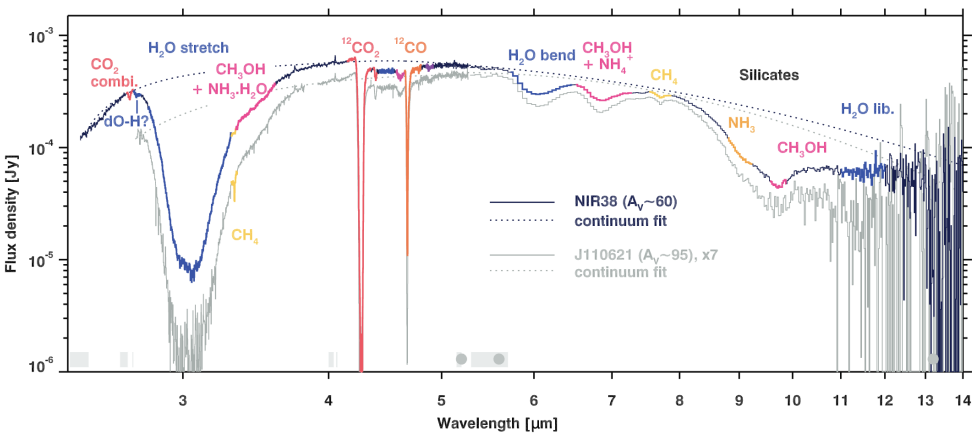

Figure 1.3: Mid-infrared spectrum of ices at dense ($A_v \geq 50$) regions of the Chamaeleon I region taken with JWST (from McClure et al. accepted). Marked in a different color are the different infrared molecular features identified in these ices. These lines of sight probe the interstellar frozen material in quiescent cloud regions, outside of the infalling envelope of a young stellar object (YSO).

of interstellar ice is shortly presented.

Figure 1.4 shows a schematic picture of different phases of ice formation and processing during the molecular cloud life stages. The formation of H_2O ice (indicated in I) starts in translucent clouds, which are regions of relatively low density ($A_v \sim 2$) in the cloud edges or early in the cloud evolution (van Dishoeck and Black, 1986; Whittet et al., 2001; Boogert et al., 2015). Under these conditions, the external ionizing and dissociating radiation are partially shielded, and the formation of icy molecules proceeds faster than their photodesorption, favoring interstellar ice growth. As a consequence, the condensation of hydrogen and oxygen atoms on the dust surfaces results in the formation of solid H_2O (Tielens and Hagen, 1982; Miyauchi et al., 2008; Ioppolo et al., 2008). At the same stage, the accretion of other atomic species is expected to lead to the formation of NH_3 and CH_4 via hydrogenation of nitrogen and carbon, respectively (Fedoseev et al., 2015; Qasim et al., 2020). In addition, the reaction of adsorbed CO molecules with OH leads to the formation of CO_2 (Ioppolo et al., 2011). In this phase, H_2O is the most abundant species, followed by CO_2. The ice formed at this phase is commonly referred to as 'polar ice' due to the high abundance of H_2O.

Deeper into the cloud or at later stages of the cloud evolution, the density increases, and gas-phase reactions lead to higher amounts of CO. Due to the low temperatures ($T \leq 20$ K), part of the CO accretes onto the dust grains. Thus, the formed frozen

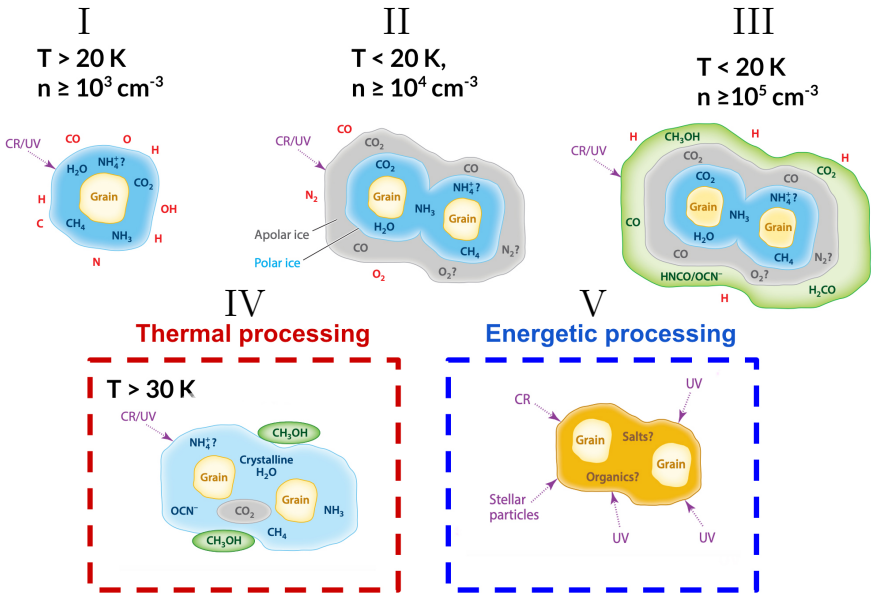

Figure 1.4: Schematic view of the evolution of interstellar ice and its different phases (adapted from Boogert et al., 2015). In phase I, H_2O is the most abundant species formed onto the dust grains, thus, this phase is known as polar ice. In this stage, NH_3, CH_4, and CO_2 are also formed. In phase II, CO is adsorbed, forming a layer of CO with less abundant volatiles, such as N_2 and O_2. The ice at this stage is known as apolar ice. Phase III is called the "catastrophic CO freeze-out" and is marked by increasing CO accretion. The hydrogenated CO leads to the formation of CH_3OH and H_2CO. With the onset of star formation, temperature increase causes desorption of more volatile species and segregation, as shown in IV. Phase V shows the energetic processing of the interstellar ice by UV and cosmic rays, causing chemical and morphological changes. These energetic agents can also process the ice material formed at early stages, inducing morphological changes in the ice and the formation of new molecules (Öberg, 2016).

material is rich in CO and is known as "apolar ice" (shown in II). At even later stages of the molecular cloud evolution, the gas density further increases ($n \geq 10^5$ cm^{-3}), the temperature drops, and consequently the accretion of CO and other volatile species is enhanced. This is phase is shown in III and is known as the 'catastrophic CO freeze-out'. The composition of the interstellar ice formed under such conditions is marked by abundant CO ice (Pontoppidan, 2006), CO_2 and the presence of more complex molecules, particularly the ones originating from the hydrogenation of CO, such as CH_3OH and H_2CO (Pontoppidan et al., 2004; Cuppen et al., 2009). In addition, laboratory work has shown that a variety of other COMs are formed in the hydrogenation network of CO, such as glycolaldehyde, methoxymethanol (H_3COCH_2OH),

and glyoxal (HC(O)CHO, see for example Linnartz et al. 2015; He et al. 2022b).

The onset of star formation leads to further transformations of the composition and morphology of the interstellar icy material (shown in IV). When the temperature increases above 20 K, the more volatile species sublimate. Thus, CO and other possibly present species, such as N_2 and O_2, desorb. In addition, recent laboratory investigation of solid CO indicates that changes in the ice structure below 20 K can induce migration of species buried within the ice, triggering chemical reactions (He et al., 2021, 2022a). Thus, the morphological transformation of CO ice at the early stages of star formation would significantly impact the chemical composition of the interstellar solid material. In this line, a laboratory investigation of structural changes in thick CO ice layers is studied in Chapter 5.

When the interstellar ice temperature rises from 30 K to 80 K, the sublimation of other species takes place. During this process, CO_2 molecules gain mobility and tend to agglomerate, forming domains of pure solid CO_2 within the ice (see IV in Figure 1.4). This process, known as segregation, can be probed by the infrared absorption profile of the CO_2 bending mode, at 15.2 μm (Ehrenfreund et al., 1998). Observing interstellar ice toward lines of sight probing warmer ices, one finds that the 15.2 μm band has a profile that is similar to the band in pure CO_2 (Pontoppidan et al., 2008). However, in lines of sight passing through regions where the ice temperature is below 20 K, the profile of the 15.2 μm is similar to those observed in mixtures with H_2O, CO, and CH_3OH, indicating that CO_2 is closely mixed with these molecules (Ehrenfreund et al., 1998; Pontoppidan et al., 2008). In addition to segregation, the increase in ice temperature can cause the crystallization of water ($T \geq 80$ K) and the formation of more complex organic species through thermal reactions (Theulé et al., 2013).

The energetic processing of interstellar ice (shown in V) by ultraviolet radiation and energetic particles causes several chemical and morphological changes in the ice material. Over the years, a vast amount of experimental works simulated the energetic processing of interstellar ices analogs, showing that these can induce the formation and destruction of frozen species (Munoz Caro et al., 2002; Gerakines et al., 1995; Rothard et al., 2017), photodesorption (Öberg et al., 2007; Bertin et al., 2016; Muñoz Caro et al., 2016) and sputtering (by particles; Dartois et al., 2019) of icy molecules, and morphological changes in the ice structure, as compaction and amorphization (Raut et al., 2007; Dartois et al., 2015). Besides the similarities between the IR profile of interstellar ice and the irradiated laboratory ice analogs, the extent to which energetic processes shape the composition and morphology of the interstellar solid material remains undetermined (Boogert et al., 2015).

1.2.2 COMs in interstellar ices

The high complexity of interstellar molecules detected in the gas phase (Herbst and van Dishoeck, 2009; Belloche et al., 2013; Jørgensen et al., 2016) contrasts with the ice inventory shown in Figure 1.2. In fact, most of the COMs detected in the gas are expected to form in the ice phase (Garrod et al., 2022) and transfer to the gas through different mechanisms, such as thermal-induced sublimation, photodesorption, sputtering, and reactive desorption (Minissale et al., 2022, and references therein). The difficulty in unambiguously detecting frozen COMs has several reasons, among which: i) the low abundances of COMs in ice, which is estimated as a few percent; ii) the overlap of the absorption features of molecules with similar structural characteristics; and iii) the sensitivity and resolution of past interstellar ice surveys, that did not allow to detect and resolve weak COM features, that usually correspond to absorption of a few percent of the continuum level.

Although not conclusive, weak absorption features in the mid-infrared spectrum of protostars have been tentatively associated with COMs, as shown in Figure 1.5. Observations of high-mass YSOs with ISO and low-mass YSO with Spitzer show absorption features at 7.41 and 7.24 μm, which have been tentatively assigned to organic species, such as HCOOH, CH_3CHO, and CH_3CH_2OH (Schutte et al., 1999; Boogert et al., 2011). Some of these tentative defections have been revisited in other works (Öberg et al., 2011; Terwisscha van Scheltinga et al., 2018) but no final assignment was possible. A better agreement with the position and width of these molecule's features in relevant astronomical ices is needed, something that has not been possible due to the blend of features and, in the case of observations performed with Spitzer, low spectral resolving power (R $\sim$ 100). In addition, a decisive assignment of these features would require the detection of other absorption bands assigned to their carriers.

1.2.3 Looking to the future: interstellar ices in the JWST era

JWST is equipped with four instruments, the Near-Infrared Camera (NIRCam), the Near-Infrared Spectrograph (NIRSpec), the Mid-Infrared Instrument (MIRI), and the Fine Guidance Sensor/Near InfraRed Imager and Slitless Spectrograph (FGS/NIRISS), that together cover the range from 0.6 - 28 μm. Combined observations using the NirSpec and MIRI instruments will allow for scanning the ice absorption signatures throughout the whole mid-infrared range. In particular, observations with the MIRI Medium Resolution Spectrometer (MIRI/MRS) allow for the detection of ice features in the 5.3 - 28 μm range with resolving power $\lambda/\Delta\lambda \sim 3000$. This includes the fin-

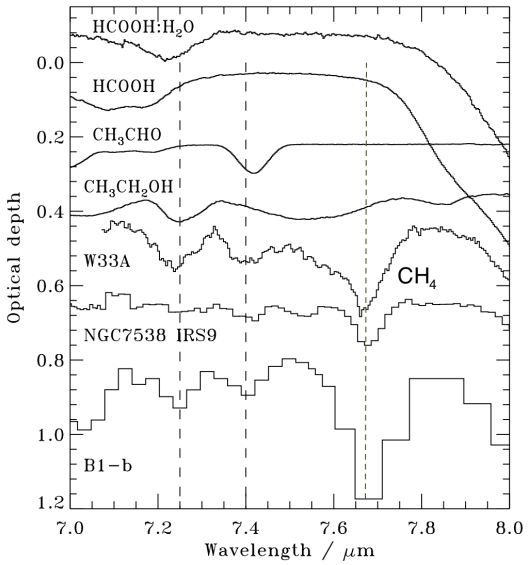

Figure 1.5: Comparison between the ISO spectra of the high-mass YSOs W33 A and NGC 7538 IRS 9, the Spitzer spectrum of the low-mass YSO B1-b and laboratory ice spectra of HCOOH, CH_3CHO, and CH_3CH_2COH (from Öberg et al., 2011). The 7.24, 7.41, and 7.67 μm features are marked with a vertical dashed line.

gerprint region between $\sim$ 6.5 - 20 μm, which is the most suitable spectral window to identify characteristic absorption features of many molecules, including COMs.

Recent observations of interstellar ice with the JWST are already bringing new insights into the composition of the interstellar solid material. Currently, observations of interstellar ice performed within two JWST observation programs have been made public. These are the Early Release Program 'Ice Age' (ID 1309, McClure et al., 2017; McClure et al., 2023) and the General Observer program 'Blazing the trail of COMs from ice to gas' (ID 2151, Yang et al., 2021), here 'Corinos I' (Yang et al., 2022). As previously mentioned, the results of the Ice Age program allowed for a view of ices in dense regions of a molecular cloud ($A_v \geq 50$). Observations with the low-resolution mode of MIRI indicate the presence of COM features, that are tentatively assigned to acetone (CH_3COCH_3), ethanol, and acetaldehyde (CH_3CHO). McClure et al. suggested that these lines of sight should be observed with the MIRI MRS to confirm the identifications.

The observation from the Corinos I revealed a richness of details in the MIRI-MRS spectrum of ices toward a low-mass young stellar object. In the observed spectrum, the 7.41 and 7.24 μm features associated with COMs and absorption features

at 5.83 and 6.7 μm, associated with H_2CO, are seen at much higher resolution. This result is a glimpse into the potential of MIRI-MRS to resolve weak spectral signatures of COMs. In 2023 and the following years, observations of ice at different stages of star formation are envisioned within the Ice Age, the MIRI GTO program JOYS, and other JWST observation programs. This will shed light on the formation history of ices and help to understand when and how organic molecules are formed in the stellar life cycle.

1.3 Laboratory astrophysics: spectroscopy

Laboratory astrophysics consists of experimental and theoretical studies as well as computational modeling of the chemistry in extraterrestrial environments. In other words, this research domain focuses on the chemistry between the stars, dealing with the chemical reactions and spectroscopy of atoms and molecules in simulated astronomical conditions. By performing investigations under fully controlled conditions, the properties and chemical evolution of matter in space can be understood. In this thesis, the focus is on the experimental spectroscopy of molecules in the solid state, with special attention on COMs. The recorded spectra of frozen molecules allow for interpreting interstellar ice observations, linking the interstellar solid and gas-phase molecular inventory, and providing input to astrochemical models. The following sections outline general aspects of vibrational spectroscopy, the tool to identify ices in space, and the laboratory work aimed at supporting astronomical observations, especially the ones performed with JWST.

1.3.1 Vibrational spectroscopy

The interaction of molecules and electromagnetic radiation is ruled by the quantization of energy, the ground principle of quantum mechanics. According to these rules, the energy carried by electromagnetic radiation can be transferred to or from molecules only in very specific amounts, which correspond to the difference between two molecular energy levels. Molecular spectroscopy is the study of the absorption and emission of light based on the involved molecular energy levels.

The absorption of light in different domains of the electromagnetic spectrum induces different transitions within a molecule. The absorption of light in the ultraviolet and visible wavelengths excites electrons to different levels of energy. Light in the infrared domain induces molecular vibrations, and radiation in the microwave and at radio wavelengths induces molecular rotations and transitions of the hyperfine struc-

ture of matter. In the following, some characteristics of vibrational spectroscopy and their importance to interstellar ice observations are presented.

The absorption of infrared light at resonant wavelengths can induce molecular vibrations. To absorb or emit radiation, the molecular vibration must give origin to a non-zero dipole moment derivate, $d\mu/dR \neq 0$ with R the distance between atoms, and the frequency of the radiation and the vibrating dipole has to be the same. This brings us to one important point: isolated homonuclear diatomic molecules (e.g., H_2, O_2, N_2) do not have dipole-allowed transitions. Because the electronegativity of the vibrating atoms is the same, $d\mu/dR$ is zero. However, laboratory experiments have shown that when O_2 is immersed in certain environments (i.e., ice matrices), the absorption of infrared light can be induced (Ehrenfreund et al., 1992; Müller et al., 2018), which leads to an important point about vibrational spectroscopy: *molecular vibrations and thus the infrared absorption profile of a molecule are influenced by its surroundings.*

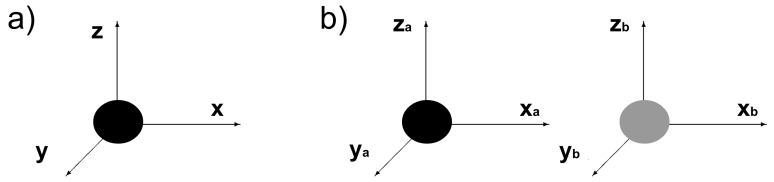

Figure 1.6: Degrees of freedom of a single particle (a), and a two-particle system (b).

Diatomic molecules are simple systems to study molecular motions, as their vibration can just occur in the axis of the molecular bond. The vibrational motions of polyatomic molecules are more complex. The atomic motions within a molecule can be understood and modeled in terms of a limited number of fundamental motions, the so-called normal modes of vibrations. This is schematically visualized in Figure 1.6. The movement of a single particle in space can be fully decomposed into motions along three orthogonal directions, here x, y, and z. Thus, this particle has three degrees of freedom. Consider now a system composed of two particles (e.g., two nuclei of a diatomic molecule). This system has six degrees of freedom. Any motion of the particle can be decomposed into motions along these six coordinates. Three of these degrees of freedom are translation motions of the molecule as a whole (when both particles move in the same direction), two are rotations about the center of mass, and one is the undefined rotation about the molecular axis (which is only defined for non-linear molecules). All the movements of a molecule can be decomposed in terms of these individual motions. This has the consequence that the number of vibrations

of a non-linear molecule with n atoms is given by N = $3n$ - 6, while the number of vibrations for a linear molecule is given by N = $3n$ - 5 (as a rotation around the molecular axis does not lead to any change). As previously mentioned, not all the possible vibrational motions of a molecule will result in the absorption of IR light, just the ones with a non-zero change in the dipole moment. In addition, some vibrational motions have the same energy, the so-called degenerate modes. Thus, the number of observable vibrational bands can slightly differ from the predicted.

In general, specific transitions between vibrational levels of a molecule occur within certain infrared domains and compose the molecular fingerprint. The transition of a combination of fundamental vibrational modes and overtones (transitions from the ground state of a molecule to the second or higher excited states) typically occurs in the near-infrared, around the 1 - 3 μm region. Stretching vibrations of chemical bonds absorb light between 3 - 6 μm. Bending motions and librations occur in the 6 - 30 μm region. Torsional and lattice modes occur in the far-infrared 30 - 300 μm. Since the vibrational spectrum of a molecule is determined by the combined motion of its atoms, the absorption profile of molecules with similar substructures shows commonalities. A group of atoms connected in a specific way causing the molecule to undergo specific chemical reactions is called a functional group. Examples of functional groups are the carbonyl, where the carbon and oxygen are linked by a double bond (C=O), the hydroxyl (O-H), and the primary amine (-NH_2). The vibrational motions of functional groups within molecules give rise to vibrations at similar wavelengths. In solids and liquids, the various chemical environments of a molecule and the intermolecular interactions result in broad absorption bands. This brings another important characteristic of vibrational spectroscopy: *while this is a powerful technique to obtain information about the molecular structure, distinguishing molecules with similar structure in solid and liquid mixtures is challenging.* Figure 1.7 shows examples of the absorption profiles of the following pure ices at 15 K: H_2O, CH_3OH, HCOOH (formic acid), H_2CO, CH_3COCH_3 (acetone), and CH_3NH_2 (methylamine). The yellow-shaded areas show typical frequency regions where a few vibrations occur, namely the O-H, N-H, and C-H stretching and the C=O stretching. In addition, the fingerprint region is indicated with a shaded gray area. In this region, bending modes and other absorption of vibrations that are unique to each molecular structure occur. Figure 1.7 evidences the overlap in the absorption features of molecules containing similar structures. Examples of such overlap are the -OH stretching vibration of CH_3OH and H_2O, the C=O stretching of HCOOH, H_2CO, and CH_3COCH_3, and the C-H stretching of all the organic molecules displayed in the figure.

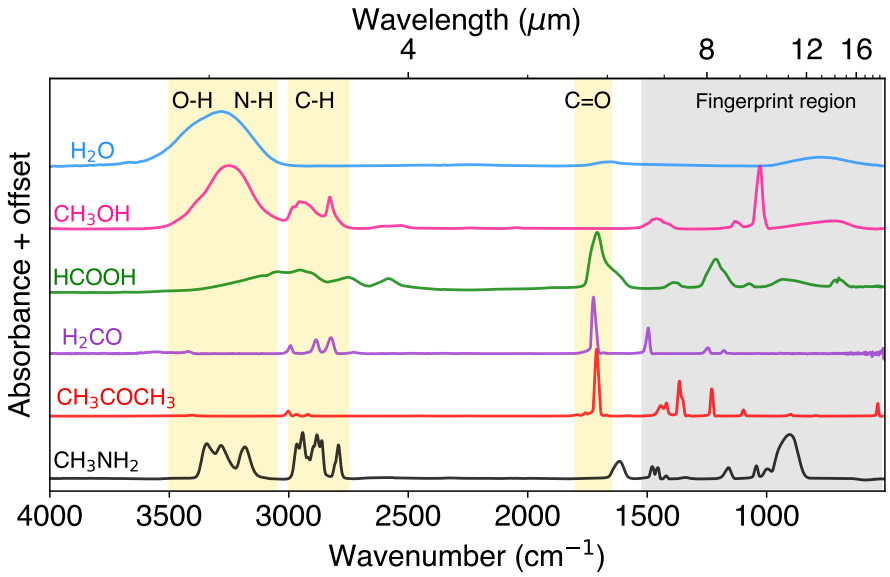

Figure 1.7: Normalized mid-infrared spectra of H_2O, CH_3OH, formic acid (HCOOH), H_2CO, acetone (CH_3COCH_3), and methylamine (CH_3NH_2). The shaded yellow areas indicate the typical frequency regions where a few stretching vibrations occur. The fingerprint region, indicated by the gray shaded area, is where the bending modes and other unique vibration modes absorb. This regions is the most useful to detect organic molecules in interstellar ice observations.

1.3.2 Spectroscopy of interstellar ice analogs

The absorption profile of a molecule is sensitive to the ice temperature, interaction with neighbor species (e.g., hydrogen bonding, dipole-dipole interactions), and ice morphology. The intermolecular interactions alter the electronic density within a molecule, consequently changing the frequency at which a molecular fragment vibrates. Also, the co-existence of different arrangements of a species within the ice structure causes absorption of light at slightly different wavelengths, which produces a broadening of absorption bands. In addition, molecular vibrations originating from molecules with similar structures overlap. In interstellar ice, this results in an absorption profile that is not trivial to disentangle. Laboratory measurements of frozen molecules under interstellar conditions are aimed at characterizing these effects, providing suitable spectroscopic data to compare to astronomical observation. To disentangle the overlap of infrared bands, algorithms that use laboratory spectra to decompose the interstel-

lar ice profile have been developed (Rocha et al., 2021). Still, the carriers of several observed interstellar ice features remain unassigned.

In addition to the ice environment effects, the absorption profile of frozen molecules changes with the shape and size distribution of interstellar grains in space. This is usually observed for major ice components, such as H_2O, CO_2, and CO (Baratta et al., 2000; Pontoppidan et al., 2003; Dartois et al., 2022). Furthermore, the features of the dust material also contribute to the absorption profile in the mid-infrared (Krügel and Siebenmorgen, 1994; Henning, 2010). Thus, in a more complete analysis, the interstellar ice profile in the infrared is only fully accounted for when the absorption and scattering of dust and icy material of specific geometry and size distributions are considered (Preibisch et al., 1993; Min et al., 2007; Dartois et al., 2022).

With the discovery of interstellar ice, back in the 70's, laboratory spectroscopic work at simulated astronomical conditions became essential. At the beginning of the 80's, the Laboratory for Astrophysics at the Leiden Observatory was pioneering in acquiring the spectra of solid samples in interstellar conditions (Hagen et al., 1980, 1981; Greenberg et al., 1983; d'Hendecourt and Allamandola, 1986) aiming at supporting infrared observations. Over the years, the spectroscopic research of ice analogs grew worldwide, especially stimulated by ISO (e.g., Gerakines et al. 1995; Ehrenfreund et al. 1997) allowing all the discoveries outlined in the previous sections. Nowadays, several laboratories perform extensive spectroscopic works aimed at interpreting astronomical data, and more recently supporting the observations obtained with the JWST (see for example Maté et al. 2017; Urso et al. 2017; Luna et al. 2018; Hudson and Gerakines 2018; Terwisscha van Scheltinga et al. 2018; Scirè et al. 2019; Palumbo et al. 2019; Hudson et al. 2021; Terwisscha van Scheltinga et al. 2021; Salter et al. 2021; Müller et al. 2022; Gerakines et al. 2022). Chapters 2, 3, and 4 (Rachid et al., 2020; Rachid et al., 2021; Rachid et al., 2022) of this thesis add to these efforts. In these works, the spectra of three frozen COMs (CH_3COCH_3, CH_3NH_2, and CH_3CN) under a range of interstellar relevant conditions (e.g., temperature, ice composition) are measured. The acquired laboratory data also allow for determining absorption cross-sections that can be used to constrain the abundance of these species in interstellar ice.

To simulate the effects that change the infrared profile of a molecule in the ISM, it is necessary to measure the spectra of samples in realistic astronomical conditions. The ISM regions where interstellar ices exist have gas densities of around 10^3 - 10^6 cm^{-3}, which is orders of magnitude below the conditions found in the Earth's atmosphere ($\sim 10^{19}$ cm^{-3}). Also, the temperatures in which interstellar ice can exist (T $\sim$ 10 - 150 K) require the use of experiments at cryogenic conditions. The experimental setups

used to record infrared spectra of frozen molecules at such conditions are described in detail in Chapter 2.

1.4 Calculation of the molecular vibrational profile

The laboratory methods and investigation described previously deal with the spectroscopy of molecules that are stable under terrestrial conditions. These molecules are easily purchased from chemical suppliers and introduced into experimental setups to perform spectroscopy measurements. In space, however, the different physical conditions allow for the existence of exotic molecules, that are unstable under terrestrial conditions. To study these species, several laboratory methods have been developed (Zack and Maier, 2014), as the *in-situ* generation of unstable species under inert conditions (Gudipati, 2004; Tsuge et al., 2018). Another approach is the use of computational molecular spectroscopy. These are a series of computational methods aimed at modeling the energy levels of a molecule using quantum mechanics (Barone et al., 2021). Shortly, the energy levels of atoms and molecules obey the Schrödinger equation:

$$H\Psi = E\Psi, \tag{1.1}$$

where Ψ is the wavefunction describing the molecule, H is the Hamiltonian operator, which describes the energy of the system, and E is the molecular energy level. Several methods have been developed to numerically solve this equation for molecular systems. One of the most popular methods to predict the electronic structure of large molecules is the density functional theory (DFT, Hohenberg and Kohn, 1964; Levy, 1979; Barone et al., 2015; Candian and Mackie, 2017). This method is based on describing a given system in terms of its electronic density (ρ(r)) as a function of space coordinates only, which simplifies the treatment of large molecules. In Chapter 7 (Candian et al., 2019), the vibrational spectra and insights on the stability of carbon cage molecules (i.e, fullerenes) are presented. The fullerenes C_{60} and C_{70} have been identified for the first time through their vibrational bands in the spectra of the protoplanetary nebula Tc 1 (Cami et al., 2010). Following this detection, fullerenes have been identified toward several objects at late stages of stellar evolution, in the ISM, and YSOs (Sellgren et al., 2010; Castellanos et al., 2014; Berné et al., 2017, and references therein). These discoveries raised speculations if other carbon-cage molecules are present in these environments. Since performing laboratory measurements with these species is challenging and still limited to a few species (Leidlmair et al., 2012; Maier

and Campbell, 2017), computational methods are essential to explore their properties and spectroscopy.

1.5 Thesis outline

This thesis seeks to investigate the spectroscopy of organic molecules in interstellar environments, focusing on the composition of interstellar ice. The ultimate goal is to shed light on the evolution of the chemical inventory throughout stellar evolution. With this purpose, Chapters 3, 4, and 5 present the mid-infrared spectroscopic characterization of three COMs (acetone, methylamine, and methyl cyanide) in different ice mixtures and give insights into their presence in interstellar ice. These molecules were identified in the gas phase in the ISM but their formation routes are expected to happen in interstellar ice. Furthermore, laboratory studies have shown that chemical reactions involving these molecules can give origin to more complex species in interstellar environments (e.g., Ioppolo et al. 2021; Bulak et al. 2021). The spectroscopic studies performed here help to address the questions: i) Can COMs be detected in JWST observations of interstellar ices?, and ii) What information about the ice composition can be derived from the IR spectral profile of these frozen molecules? Chapter 6 provides a systematic study of morphological changes taking place in CO ices using laser interference. Since CO is expected to be one of the main components of interstellar ice, its properties at different conditions will influence the chemistry and spectral profile of molecules mixed with it. Lastly, Chapter 7 is a computational study to predict the stability and the vibrational spectra of fullerenes containing 44 and 70 carbon atoms. More details about these works are summarized below:

- **Chapter 3** presents mid-infrared spectra of frozen CH_3COCH_3 in the pure form and mixed with H_2O, CO_2, CO, and CH_3OH. The spectra are acquired under high-vacuum (P $\sim 10^{-7}$ mbar) conditions and at cryogenic temperatures (T $\sim$ 15 - 160 K). The characterization of peak position and the full width of half maximum (FWHM) of bands that have the highest potential to be detected in upcoming JWST observation of interstellar ice is performed.
- **Chapter 4** uses the same experimental setup and methodology of Chapter 2 to characterize the mid-infrared spectra of frozen CH_3NH_2 in the pure form and mixed with H_2O, CH_4, and NH_3. In addition, this chapter presents upgrades performed to the previously used HV system. The new setup, IRASIS (InfRared Absorption Setup for Ice Spectroscopy) achieves achieve ultra-high-vacuum pressures and allows for measuring the refractive index of ices using

a laser interference technique. The refractive index measurements allowed for measuring ice thicknesses, which are combined with the infrared spectroscopy measurements to provide infrared band strengths of frozen methylamine. In this work, upper limits for the methylamine abundance in interstellar ice toward protostars are derived by comparing the laboratory spectra with observations. The observational data are archival data from Spitzer, Keck, VLT, and IRTF.

- **Chapter 5** presents mid-infrared spectra of frozen CH_3CN in the pure form and mixed with H_2O, CO_2, CO, CH_4, and NH_3, acquired with the IRASIS setup. The refractive index and band strengths of methyl cyanide at 15 K are also presented. The acquired spectroscopy measurements are compared to archival data from Spitzer and ISO, allowing for determining upper limits for CH_3CN in interstellar ice.
- **Chapter 6** uses interference techniques from ultraviolet to visible wavelengths (250 - 750 nm) to investigate morphological transitions in pure CO ice. In this work, μm-thick CO ices are grown under high vacuum conditions (P $\sim 10^{-8}$ mbar) at a temperature ranging from 7.5 - 18 K. After its growth, the ice is opaque and scatters incident light. After a certain time, morphological changes in the ice structure lead to a transparent ice. The aspects that influence the transition of opaque CO ice to transparent ice under various growing conditions, (i.e., deposition rate, temperature, and ice thickness) are analyzed. Insights into the ice structural changes taking place are also discussed.
- **Chapter 7** presents a computational study that uses DFT to investigate the infrared profile of neutral and singly ionized fullerene cages containing 44 up to 70 carbon atoms. The stability of these molecules is analyzed using the standard enthalpy of formation per CC bond, the HOMO–LUMO gap, and the energy required to eliminate a C_2 units. The obtained mid-infrared spectra of the cages were compared to the Spitzer spectra of fullerene-rich planetary nebulae.

1.6 Summary of main conclusions

The major conclusions of this thesis are summarized as follows:

I) Laboratory measurements of the infrared profile of organic molecules under astronomical relevant conditions are essential to interpret interstellar ice observations. Comparing observations with the laboratory spectra acquired under varying conditions allows for obtaining information about the interstellar ice conditions, such as temperature and the degree of mixing of icy molecules. Chapters 3, 4, and 5 present spectro-

scopic work to allow future searches of acetone, methylamine, and methyl cyanide in interstellar ice observations with JWST. From the spectral analysis of these molecules, the following conclusions are drawn:

- The features that show the most potential to identify acetone are a combination of the 5.85, 7.34, and 8.14 μm features.
- Methylamine absorption bands will be challenging to identify in interstellar ices due to significant overlap with H_2O and NH_3 features. With this caveat, the most promising features to identify this species in ice observations are the 3.45 μm and the 8.62 μm features. Using the 3.45 μm feature, the upper limits for methylamine abundance toward YSOs are estimated to be around $\leq$ 4 % with respect to solid H_2O.
- The features that show the most potential to identify methyl cyanide in interstellar ices are a combination of the 4.44 and the 9.60 μm features. Using these features, the methyl cyanide abundance toward YSOs is estimated as a few up to $\leq$ 4.1 % with respect to solid H_2O.

II) Structural transitions after the deposition of μm-thick CO ice can alter its scattering properties. Freshly deposited CO ice scatters visible light. After a certain time period, spontaneous morphology transitions lead to a transparent ice. The time scale for these transitions is dependent on the deposition temperature and thickness of the ice sample. The time scale for these transitions to happen ($\leq$ 1 year) is negligible compared to astronomical time scales but should be accounted for in laboratory experiments.

III) Neutral and singly charged fullerene cages consisting of 44 up to 70 carbon atoms have IR-active modes between 6 – 9 μm and can contribute to the emission profile observed toward the fullerene-rich planetary nebula. However, their vibrational spectra cannot simultaneously account for the 10 - 13 μm emission '*plateau*' observed in the same objects. The calculations show that the smaller fullerene cages show features in the 13 - 15 μm that resemble the emission features observed in LMC56 and SMC16.

References

Altwegg, K., Balsiger, H., Bar-Nun, A., et al., 2016, Science Advances, 2, e1600285
Altwegg, K., Combi, M., Fuselier, S. A., et al., 2022, MNRAS, 516, 3900
Baratta, G., Palumbo, M., and Strazzulla, G, 2000, A&A, 357, 1045

1.6. REFERENCES

Barone, V., Alessandrini, S., Biczysko, M., et al., 2021, Nature Reviews Methods Primers, 1, 1

Barone, V., Biczysko, M., and Puzzarini, C., 2015, Accounts of Chemical Research, 48, 1413

Belloche, A., Müller, H. S., Menten, K. M., et al., 2013, A&A, 559, A47

Berné, O, Cox, N., Mulas, G., et al., 2017, A&A, 605, L1

Bertin, M., Romanzin, C., Doronin, M., et al., 2016, ApJL, 817, L12

Boogert, A. C. A., Brewer, K., Brittain, A., et al., 2022, arXiv e-prints, arXiv:2210.12639

Boogert, A. C. A, Gerakines, P. A., and Whittet, D. C., 2015, ARA&A, 53, 541

Boogert, A. C. A., Huard, T. L., Cook, A. M., et al., 2011, ApJ, 729, 92

Bulak, M, Paardekooper, D., Fedoseev, G, et al., 2021, A&A, 647, A82

Cami, J., Bernard-Salas, J., Peeters, E., et al., 2010, Science, 329, 1180

Candian, A., Gomes Rachid, M., MacIsaac, H., et al., 2019, MNRAS, 485, 1137

Candian, A. and Mackie, C. J., 2017, International Journal of Quantum Chemistry, 117, 146

Carroll, B. W. and Ostlie, D. A. (2017). *An introduction to modern astrophysics*. Cambridge University Press.

Caselli, P., Pineda, J. E., Sipilä, O., et al., 2022, ApJ, 929, 13

Castellanos, P., Berné, O., Sheffer, Y., et al., 2014, ApJ, 794, 83

Cuppen, H. M., van Dishoeck, E. F., Herbst, E., et al., 2009, A&A, 508, 275

Dartois, E, Augé, B, Boduch, P, et al., 2015, A&A, 576, A125

Dartois, E, Chabot, M, Barkach, T. I., et al., 2019, A&A, 627, A55

Dartois, E., Noble, J. A., Ysard, N., et al., 2022, A&A, 666, A153

d'Hendecourt, L. and Allamandola, L., 1986, A&AS, 64, 453

d'Hendecourt, L. and Jourdain de Muizon, M, 1989, A&A, 223, L5

DiSanti, M. A. and Mumma, M. J., 2008, Space Science Reviews, 138, 127

van Dishoeck, E. F. and Black, J. H., 1986, ApJS, 62, 109

Draine, B. T., 2003, ARA&A, 41, 241

Draine, B. T. (2010). *Physics of the interstellar and intergalactic medium*. Vol. 19. Princeton University Press.

Drozdovskaya, M. N., van Dishoeck, E. F., Rubin, M., et al., 2019, MNRAS, 490, 50

Ehrenfreund, P., Boogert, A. C. A., Gerakines, P. A., et al., 1997, A&A, 328, 649

Ehrenfreund, P, Breukers, R, d'Hendecourt, L, et al., 1992, A&A, 260, 431

Ehrenfreund, P, Dartois, E, Demyk, K, et al., 1998, A&A, 339, L17

Fedoseev, G., Ioppolo, S., Zhao, D., et al., 2015, MNRAS, 446, 439

Garrod, R. T., Jin, M., Matis, K. A., et al., 2022, ApJS, 259, 1

van Gelder, M., Tabone, B., van Dishoeck, E., et al., 2020, A&A, 639, A87

Gerakines, P. A., Schutte, W. A., Greenberg, J. M., et al., 1995, A&A, 296, 810

Gerakines, P. A., Yarnall, Y. Y., and Hudson, R. L., 2022, MNRAS, 509, 3515

Gillett, F. C. and Forrest, W. J., 1973, ApJ, 179, 483

Greenberg, J. M., van de Bult, C., and Allamandola, L. J., 1983, The J. Phys. Chem., 87, 4243

Grim, R., Baas, F, Greenberg, J., et al., 1991, A&A, 243, 473

Gudipati, M. S., 2004, The J. Phys. Chem. A, 108, 4412

Hagen, W, Allamandola, L., and Greenberg, J., 1980, A&A, 86, L3

Hagen, W, Tielens, A., and Greenberg, J., 1981, Chem. Phys., 56, 367

Hänni, N., Altwegg, K., Combi, M., et al., 2022, Nat. communications, 13, 3639

He, J., Góbi, S., Ragupathy, G., et al., 2022, ApJL, 931, L1

He, J., Simons, M., Fedoseev, G., et al., 2022, A&A, 659, A65

He, J., Toriello, F. E., Emtiaz, S. M., et al., 2021, ApJL, 915, L23

Henning, T., 2010, ARA&A, 48, 0

Herbst, E. and van Dishoeck, E. F., 2009, ARA&A, 47, 427

Hohenberg, P. and Kohn, W., 1964, Phys. Rev., 136, 864

Hollis, J. M., Lovas, F. J., and Jewell, P. R., 2000, ApJ, 540, L107

Hudson, R. L. and Gerakines, P. A., 2018, ApJ, 867, 138

Hudson, R. L., Gerakines, P. A., Yarnall, Y. Y., et al., 2021, Icarus, 354, 114033

van de Hulst, H. C. (1946). "88. The Solid Particles of Interstellar Space". *A Source Book in A&A, 1900–1975*. Harvard University Press, 605.

Ioppolo, S., Cuppen, H. M., Romanzin, C., et al., 2008, ApJ, 686, 1474
Ioppolo, S., Fedoseev, G., Chuang, K. J., et al., 2021, Nat. Astronomy, 5, 197
Ioppolo, S., van Boheemen, Y., Cuppen, H. M., et al., 2011, MNRAS, 413, 2281
Jørgensen, J. K., Belloche, A., and Garrod, R. T., 2020, ARA&A, 58, 727
Jørgensen, J., Wiel, M. Van der, Coutens, A, et al., 2016, A&A, 595, A117
Knacke, R. F., Gaustad, J. E., Gillett, F. C., et al., 1969, ApJL, 155, L189
Krügel, E and Siebenmorgen, R, 1994, A&A, 288, 929
Lacy, J., Baas, F, Allamandola, L., et al., 1984, ApJ, 276, 533
Lacy, J., Carr, J., Evans, N. J., et al., 1991, ApJ, 376, 556
Leidlmair, C., Wang, Y., Bartl, P., et al., 2012, Phys. Rev. Letters, 108, 076101
Levy, M., 1979, Proceedings of the National Academy of Science, 76, 6062
Ligterink, N., Terwisscha van Scheltinga, J, Taquet, V, et al., 2018, MNRAS, 480, 3628
Linnartz, H., Ioppolo, S., and Fedoseev, G., 2015, Int. Rev. Phys. Chem., 34, 205
Luna, R., Molpeceres, G., Ortigoso, J., et al., 2018, A&A, 617, A116
Maier, J. P. and Campbell, E. K., 2017, Angewandte Chemie International Edition, 56, 4920
Maté, B., Molpeceres, G., Timón, V., et al., 2017, MNRAS, 470, 4222
McClure, M. K., Rocha, W. R. M., Pontoppidan, K. M., et al., 2023, Nat. Astronomy,
McClure, M., Bailey, J., Beck, T., et al. (Nov. 2017). *IceAge: Chemical Evolution of Ices during Star Formation*. JWST Proposal ID 1309. Cycle 0 Early Release Science.
McGuire, B. A., 2022, ApJS, 259, 30
Meinert, C., Myrgorodska, I., De Marcellus, P., et al., 2016, Science, 352, 208
Min, M, Waters, L., Koter, A. de, et al., 2007, A&A, 462, 667
Minissale, M., Aikawa, Y., Bergin, E., et al., 2022, ACS Earth and Space Chemistry, 6, 597
Miyauchi, N., Hidaka, H., Chigai, T., et al., 2008, Chem. Phys. Lett., 456, 27
Muñoz Caro, G. M., Chen, Y. J., Aparicio, S., et al., 2016, A&A, 589, A19
Müller, B., Giuliano, B. M., Vasyunin, A., et al., 2022, A&A, 668, A46
Müller, B, Giuliano, B., Bizzocchi, L, et al., 2018, A&A, 620, A46
Mumma, M. J. and Charnley, S. B., 2011, ARA&A, 49, 471
Munoz Caro, G., Meierhenrich, U. J., Schutte, W. A., et al., 2002, Nat., 416, 403
Nazari, P., Meijerhof, J. D., van Gelder, M. L., et al., 2022, A&A, 668, A109
Oba, Y., Takano, Y., Naraoka, H., et al., 2019, Nat. communications, 10, 1
Öberg, K. I., 2016, Chem. Rev., 116, 9631
Öberg, K. I., Boogert, A. C. A., Pontoppidan, K. M., et al., 2011, ApJ, 740, 109
Öberg, K. I., Fuchs, G. W., Awad, Z., et al., 2007, ApJ, 662, L23
Palumbo, M. E., Baratta, G. A., Fedoseev, G., et al., 2019, Proceedings of the International Astronomical Union, 15, 77
Pontoppidan, K. M., Boogert, A. C., Fraser, H. J., et al., 2008, ApJ, 678, 1005
Pontoppidan, K., 2006, A&A, 453, L47
Pontoppidan, K., Fraser, H., Dartois, E, et al., 2003, A&A, 408, 981
Pontoppidan, K., van Dishoeck, E., and Dartois, E, 2004, A&A, 426, 925
Preibisch, T., Ossenkopf, V, Yorke, H., et al., 1993, A&A, 279, 577
Qasim, D., Fedoseev, G., Chuang, K. J., et al., 2020, Nat. Astronomy, 4, 781
Rachid, M. G., Brunken, N., de Boe, D., et al., 2021, A&A, 653, A116
Rachid, M. G., Rocha, W., and Linnartz, H., 2022, A&A, 665, A89
Rachid, M. G., Terwisscha van Scheltinga, J., Koletzki, D., et al., 2020, A&A, 639, A4
Raut, U, Teolis, B., Loeffler, M., et al., 2007, J. Chem. Phys., 126, 244511
Rocha, W. R. M., Rachid, M. G., Olsthoorn, B., et al., 2022, A&A, 668, A63
Rocha, W. R., Perotti, G., Kristensen, L. E., et al., 2021, A&A, 654, A158
Rothard, H., Domaracka, A., Boduch, P., et al., 2017, Journal of Physics B: Atomic, Molecular and Optical Physics, 50, 062001
Saki, M., Gibb, E. L., Bonev, B. P., et al., 2020, Astronomical Journal, 160, 184
Salter, T. L., Stubbing, J. W., Brigham, L., et al., 2021, Frontiers in Astronomy and Space Sciences, 8, 28
Schrödinger, E., 1926, Phys. Rev., 28, 1049
Schutte, W., Boogert, A., Tielens, A., et al., 1999, A&A, 343, 966

1.6. REFERENCES

Scirè, C, Urso, R., Fulvio, D, et al., 2019, Spectrochimica Acta Part A: Molecular and Biomolecular Spectroscopy, 219, 288

Sellgren, K., Werner, M. W., Ingalls, J. G., et al., 2010, ApJL, 722, L54

Snow, T. P. and McCall, B. J., 2006, ARA&A, 44, 367

Soifer, B., Puetter, R., Russell, R., et al., 1979, ApJ, 232, L53

Swings, P. and Rosenfeld, L., 1937, ApJ, 86, 483

Terwisscha van Scheltinga, J, Ligterink, N., Boogert, A., et al., 2018, A&A, 611, A35

Terwisscha van Scheltinga, J., Marcandalli, G., McClure, M. K., et al., 2021, A&A, 651, A95

Theulé, P, Duvernay, F, Danger, G., et al., 2013, Advances in Space Research, 52, 1567

Tielens, A. G. G. M. and Hagen, W., 1982, A&A, 114, 245

Tielens, A. G. G. M., 2008, ARA&A, 46, 289

Tsuge, M., Tseng, C.-Y., and Lee, Y.-P., 2018, PCCP, 20, 5344

Urso, R. G., Scirè, C., Baratta, G. A., et al., 2017, PCCP, 19, 21759

Whittet, D., Gerakines, P., Hough, J., et al., 2001, ApJ, 547, 872

Woolf, N. J. and Ney, E. P., 1969, ApJL, 155, L181

Yang, Y.-L., Bergner, J., Cleeves, I., et al. (Mar. 2021). *Blazing the trail of COMs from ice to gas.* JWST Proposal. Cycle 1, ID. #2151.

Yang, Y.-L., Green, J. D., Pontoppidan, K. M., et al., 2022, ApJL, 941, L13

Yang, Y.-L., Sakai, N., Zhang, Y., et al., 2021, ApJ, 910, 20

Zack, L. N. and Maier, J. P., 2014, Chemical Society Reviews, 43, 4602

2

Experimental setup and methodology

This chapter presents an overview of the experimental setups used in this thesis and summarizes the used approaches. In the following Sections, an overview of the HV (High vacuum) setup and its upgrade, the IRASIS (InfraRed Absorption Setup for Ice Spectroscopy) setup, as well as the OASIS (Optical Absorption Setup for Ice Spectroscopy) setup is given.

2.1 The HV setup

The HV setup has been used for more than two decades in the LfA, with smaller modifications or experimental upgrades, but performing along the same measuring principle. This setup consists of a stainless steel high vacuum chamber (base pressure $\sim 2 \times 10^{-7}$ mbar) placed in the cavity of a Varian 670 Fourier transform infrared (FTIR) spectrometer. The chamber is pumped by a turbomolecular pump (Oerlikon Leybold TurboVac 361) that is backed by a Edwards E2M8 double-stage rotary vane pump (8 m^3 hr^{-1}). The pressure is measured with an Agilent FRG-720 full-range gauge. In the center of the chamber, there is a ZnSe substrate that is thermally connected to a closed cycle helium cryocooler (Air Products Displex DE-202). The ZnSe can be cooled to temperatures as low as 15 K. The substrate temperature is measured by a silicon diode (DT-670 from Lake Shore Cryotronics) connected to a LakeShore 330 temperature controller. The gaseous sample (pure or mixed) used to grow the ice is stored in a 2L glass bulb attached to the dosing line of the HV setup.

Before the sample deposition, an IR spectrum of the bare substrate is acquired, this is called the "background spectrum". The background spectrum has the purpose of measuring the contribution of the instrument and environment to the spectral signal. These contributions are subtracted from all the sample spectra acquired in the sequence in an automatic procedure performed by the spectrometer. To avoid absorption by atmospheric H_2O and CO_2, present in the optical path of the infrared beam, the system is purged with dry air by a Balston 75-62 FT-IR Purge Gas Generator. The gaseous sample is then admitted into the chamber through a needle valve. The ice is grown by background deposition, which means that the molecules collide with the substrate impacting from random directions. During and after the ice deposition, an FTIR spectrometer (Varian 670) records the spectra in the 5000 – 400 cm^{-1}

(2 – 25 μm) range at resolution from 4 up to 0.1 cm^{-1} (typical values are 0.5 cm^{-1} - 1 cm^{-1}). After the sample deposition, the ice is heated at an adjustable rate (typically 25 K hr^{-1}) until its complete sublimation. During the ice heating, the infrared spectrum of the sample is recorded, which allows for monitoring the change of the infrared profile of the different ice components with temperature. The spectra are acquired by averaging about 128 - 256 scans. The time that it takes to acquire a full spectrum depends on the resolution and the number of scans. Since a spectrum is recorded during the heating of the sample, the scans are acquired at slightly different temperatures. This imposes a temperature resolution for the final spectra that corresponds to a maximum of 3.5 K. In the HV setup, ices are typically grown to a thickness of a few thousand monolayers (column densities of the order 10^{18} molecules cm^{-2}). These thick ices are necessary to ensure that at the relatively high background pressure, the deposition of background contaminants (mainly H_2O and N_2) is negligible.

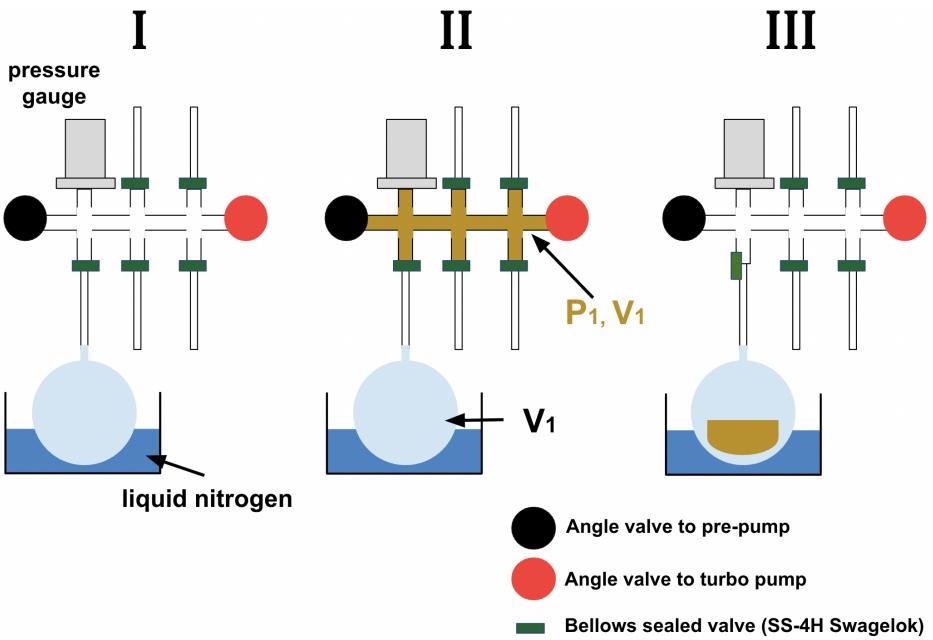

Figure 2.1: Procedure to prepare gaseous mixtures in the mixing system. In I: the bulb and the mixing line used to prepare the mixtures are evacuated to a base pressure of 10^{-4} mbar. The valve to the bulb is closed and the bulb is immersed in a liquid nitrogen container. II: the mixing system is filled with a pressure P_1 of a gas or vapor component. In III: the valve to the bulb is opened and the gas/vapor in the mixing line freezes in the bulb.

The gaseous samples used to grow mixed ices are prepared in a separate mixing

system (base pressure $\sim 10^{-4}$ mbar). The pressure in the mixing system is measured using two mass-independent pressure gauges that cover the 0 - 1000 mbar range. All the gaseous samples are prepared in a 2 liter bulb containing a total pressure of 20 mbar. The partial pressure of each component is proportional to their fraction in the mixture. For example, a gas mixture of H_2O:CO_2(2:1) consists of a mixture of $20 \times \frac{2}{3} \sim 13.3$ mbar of H_2O and $20 \times \frac{2}{3} \sim 6.7$ mbar of CO_2. The mixtures are prepared by the sequential freezing of the individual components to the bulb, which is kept immersed in a liquid N_2 container. The procedure for adding individual components to the gaseous mixture is schematically illustrated in Figure 2.1 and described in the following. Initially, the bulb and mixing line are evacuated and the valve to the bulb is closed (shown in I). The mixing line is filled with the desired amount of gas or vapor component (II). The valve connecting the bulb to the mixing line is opened and the content of the mixing line expands to the bulb. If the freeze-out temperature of the gas or vapor component is above the temperature of the liquid nitrogen (~ 77 K), this component will completely freeze out in the glass bulb, as shown in III. The valve to the bulb is closed, the mixing line is evacuated and the addition of a new component is performed. The partial pressure of the component added to the bulb can be calculated considering the relation $P_1V_1 = P_2V_2$, where P_1 and V_1 are the pressure of the gas when it occupies the volume V_1 (mixing line), V_2 is the volume of the bulb (2 L), and P_2 is the partial pressure of the component in the bulb. In case the freeze-out temperature of the gas component is below 77 K, the gas will expand and occupy the volume of the mixing line and the bulb. In this case, the final volume of the gas will be $V_1 + V_2$ instead of V_2. Gases that freeze out below 77 K are typically added as the last component to the gaseous mixture. Following this methodology, the error estimated for the ratios of a certain component in the gaseous mixtures is estimated as 10%. Additional details about the HV setup can be found in Chapter 2 of the Ph.D. thesis of Terwisscha van Scheltinga 2021.

2.2 IRASIS

In 2020, the HV setup was upgraded to an ultra-high vacuum system, IRASIS, which allows for recording the infrared spectrum of an ice sample and measuring its thickness. In addition, it also allows for measuring the refractive index of ices. Figure 2.2 shows a schematic picture of IRASIS main chamber and its components. The IRASIS setup consists of a stainless steel chamber that reaches a base pressure of $\leq 10^{-9}$ mbar. This lower base pressure decreases the accretion of background gases, which makes

this system more suited to grow thinner ices when compared to the HV setup. The center of the vacuum chamber houses a germanium (Ge) window that is connected to a closed-cycle helium cryocooler (DE-202 - Advanced Research Systems) and can reach temperatures as low as 15 K. The cryocooler head is mounted onto a two-stage differentially pumped rotary platform which allows for 360° rotation of the substrate inside the chamber. A Ge substrate was chosen because this material transmits most of the incident infrared light in most of the mid-infrared region and reflects the visible light at 632.8 nm. This allows for recording the infrared spectra of samples in transmission mode and measuring the refractive index using the laser interference technique described in the following sections. The temperature of the ice sample is measured by a silicon diode (DT-670-CU) connected to a Lakeshore 335 temperature controller. The pressure in the chamber is measured with a Pfeiffer PKR 360 C full-range gauge and is also monitored by a Quadrupole Mass Spectrometer (QMS), that was recently added to the system.

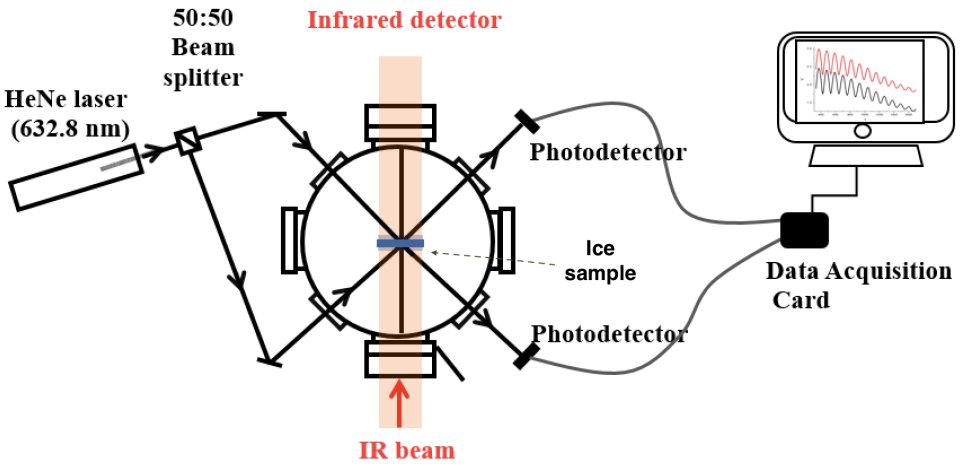

Figure 2.2: Schematic diagram of the IRASIS setup showing a simplified version of the infrared beam path and the laser beams that are used to measure the ice thickness on both sides of the Ge substrate (adapted from Rachid et al., 2021).

IRASIS is coupled to a gas dosing system, which is shown in Figure 2.3 I and schematically depicted in Figure 2.3 II. This dosing system contains three compartments where gases can be stored and independently admitted into the vacuum chamber through adjustable leak valves. Thus, the ice components are mixed during the ice

deposition, without requiring the preparation of a gaseous mixtures. This procedure has advantages for controlling the ratios between the different species in the sample, which results in more accurate measurements of apparent band strengths of molecules in ice mixtures (Yarnall and Hudson, 2022). The works presented in Chapters 3, 4, and 5 were done before the implementation and test of this dosing system. Thus, the gaseous samples used to grow the ices were prepared in a glass bulb, following the methodology described in the previous Section. The experimental procedure to calibrate the deposition of individual gases and vapors using the separate dosing lines will be introduced in future works (Slavicinska et al., *in prep.*). The gaseous sample (pure or mixed) contained in a glass bulb is attached to one of the dosing lines of IRASIS and admitted into the chamber through a leak valve. The ice is grown by background deposition on both sides of the Ge substrate. Using a FTIR spectrometer (Varian 670), the mid-infrared spectrum of the sample (2.5 - 20 μm / 4000 - 500 cm^{-1}) is measured after the ice deposition and during the heating. Since the base pressure on IRASIS is more than two orders of magnitude lower than in the HV setup, ices can be made thinner and the contamination from the deposition of background contaminants is negligible.

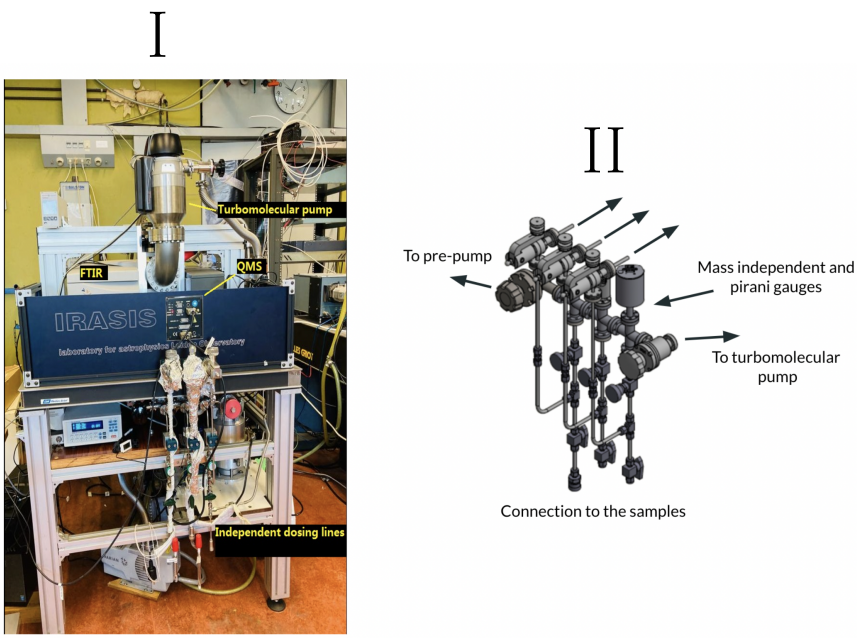

Figure 2.3: Panel I shows the IRASIS setup and panel II shows a schematic picture showing the deposition line.

The number of absorbing molecules in the sample, given by the column density (N, in molecules per cm^{-2}), is related to the area of an absorption feature (i.e., the integrated absorbance of an absorption feature) through a modified version of the Lambert-Beer law:

$$N = \frac{2.3}{A} \int_{\nu} \mathrm{Abs}_{\nu} \, \mathrm{d}\nu, \tag{2.1}$$

where A is the band strength given in cm $molecule^{-1}$, and the integral of the absorbance is performed over the whole wavenumber region of the absorption feature. The factor 2.3 in the Equation is derived from the conversion of optical depth (τ) to absorbance. The optical depth is related to the transmittance of light by the natural logarithm (τ = -ln(T)), while the absorbance is measured by the spectrometer on the logarithm base 10 scale (Abs = -log(T)).

2.2.1 Thickness and refractive index

In addition to the FTIR spectrometer, IRASIS has a laser system that allows for measuring the ice thickness and refractive index of the ice samples during deposition. For these measurements, a technique based on the interference of light is employed. In this technique, a laser beam hits a growing ice, and the reflected light is recorded and analyzed. When the laser light strikes the ice surface, part of it is reflected in the vacuum-ice interface and part is refracted into the ice. The light rays that are refracted into the ice are eventually reflected by the ice-substrate interface (for reflective substrates). These light rays refract back to the vacuum and interfere with the light rays that are reflected by the ice surface, as illustrated in Figure 2.4. The intensity of the resulting signal depends on the phase difference of the interfering light beams. As the ice grows, the optical path inside the ice increases and the phase difference between the light beams alternate between fully in phase (constructive interference) and out of phase (destructive interference). The result is an oscillating constructive and destructive interference pattern, as shown in Figure 2.4.

The ice thickness (d) can be derived from the interference pattern recorded during its deposition following the relation:

$$d = \frac{m\lambda}{2\sqrt{n^2 - \sin^2\theta}}, \tag{2.2}$$

where λ is the laser wavelength (here 632.8 nm), θ is the incident angle, m is the

number of interference fringes, and n is the ice refractive index.

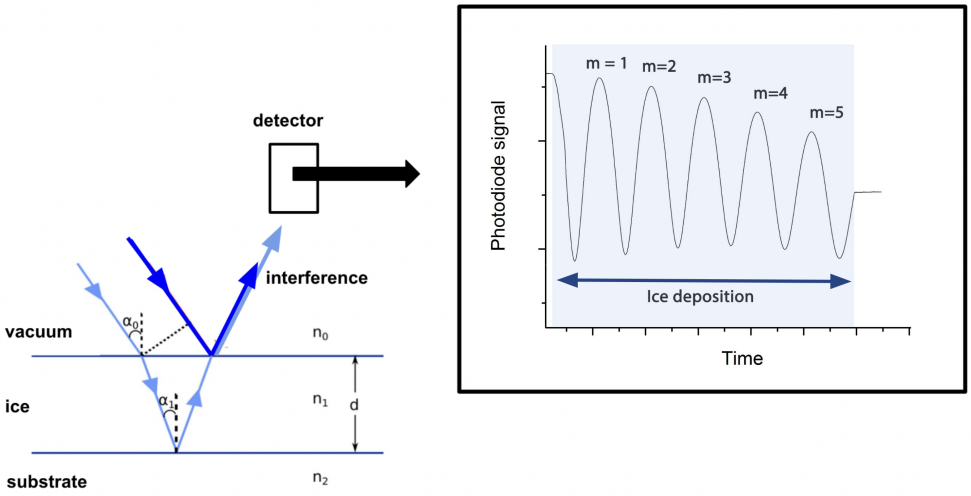

Figure 2.4: Interference of light in the ice sample (based on Chapter 5.

For the refractive index measurements, two laser beams with the same wavelength hitting the ice under different incident angles are employed (see Beltrán et al. 2015). The ice is grown at a constant rate while the interference pattern of both laser beams are recorded, as illustrated in Figure 2.4. The refractive index of the deposited ice is related to the incidence angle and the period of the oscillation patterns by (Tempelmeyer and Mills Jr, 1968):

$$n = \sqrt{\frac{\sin^2\theta_0 - \gamma^2 \sin^2\theta_1}{1-\gamma^2}}, \tag{2.3}$$

where $\gamma = \frac{T_1}{T_0}$ with T_1 and T_0 the period of the interference signals generated by the two laser beams that hit the ice surface at angles θ_1 and θ_0, respectively.

To measure the ice refractive index on IRASIS, the substrate is rotated by 90°. The laser beam is split with a 50:50 cube beam splitter and the resulting beams are pointed to the substrate using a few mirrors. The laser beams hit the ice surface at typical angles of $\sim 5°$ and $\sim 45°$. The produced interference patterns are recorded using individual photodetectors (Thorlabs PDA36A2). During the ice deposition, the pressure in the chamber is kept as constant as possible, since the deposition rate will influence the period of the interference fringes. This is usually performed by filling the dosing line with a pressure of ~ 100 mbar of gas and setting the leak valve at a

fixed position. The pressure in the dosing line is high enough to maintain a constant pressure in the chamber during the ice deposition. For depositing vapors from liquids, a glass tube containing the liquid is connected to one of the dosing lines of the system and filled with the vapor. Thus, the pressure in the dosing line is equal to the vapor pressure of the liquid. During the deposition, the glass tube is immersed in a water bath at a constant temperature to diminish variations in the sample temperature (and thus the vapor pressure of the liquid). Before filling the dosing line with vapor, the liquid sample is purified through at least three freeze-thaw cycles. The refractive index of the pure ice sample is calculated using Equation 2.3. The uncertainty in the refractive index of a given ice is calculated through the standard deviation of a collection of measurements performed under similar conditions. In our measurements, this typically amounts to $\leq 5\%$ of the refractive index values.

2.2.2 Apparent band strength measurements

The column density of a molecule in a pure ice can be written as :

$$N = \frac{d\,\rho\,N_{\mathrm{A}}}{M}, \tag{2.4}$$

where d is the ice thickness (in cm), ρ is the ice density (in g cm^{-3}), N_{A} is the Avogadro's number, and M is the molar mass (in g mol^{-1}) of the molecule. Combining equations 2.4 and 2.1 allows for writing the A values of absorption features as:

$$A = \frac{2.3\,M}{\rho\,d\,N_{\mathrm{A}}} \int_{\nu} \mathrm{abs}_{\nu}\,\mathrm{d}\nu. \tag{2.5}$$

Thus, recording the absorption spectrum of an ice sample with a known thickness and density allows for deriving the apparent band strength values of the molecular absorption features. During a typical measurement, the ice thickness and infrared spectrum are monitored during the ice deposition. The growth rate of the integrated absorbance of a band and the ice thickness is measured during ice deposition and used to calculate the apparent band strength using an analogous of Equation 2.5:

$$A = \frac{2.3\,M\,\alpha}{\rho\;\;N_A\,\beta}, \tag{2.6}$$

where α is the growth rate of the integrated absorbance band (band area), and β is the growth rate of the ice thickness, which is calculated during the maxima and minima of the laser interference pattern using equation 2.2. The growth rates of the thickness and

integrated absorbance are used in place of the single measurements of thickness and integrated absorbance of the deposited ice. This provides more robust measurements, that are less susceptible to fluctuations when compared to measurements acquired for a single thickness and integrated absorbance values. In Chapters 4 and 5 this method is used to calculate the apparent band strengths of pure CH_3NH2 and CH_3CN ices, respectively.

2.3 OASIS

The measurements presented in Chapter 6 of this thesis are acquired on the OASIS setup (Kofman et al. 2018; Kofman et al. 2019; He et al. 2022). In the last years, the OASIS setup has been mainly employed for measuring the UV-visible spectrum of molecules embedded in ice matrix and the refractive index of pure ices in the 250 - 750 nm range. The refractive index measurements are based on the interference technique described in the previous section. However, instead of using two laser beams, a laser beam and the broadband light of a Xe arc lamp are employed, allowing for measuring the refractive index in the the 250 - 750 nm range (He et al., 2022). In Chapter 6 of this thesis, the interference signal generated during and after the growth of CO ice is analyzed to gain insights into morphology transformations happening in μm-thick CO ice. During the ice deposition, changes in the optical path of the light inside the ice result in an interference pattern. After the ice deposition, changes in the interference signal after the ice growth indicate changes in the optical properties of the ice or the ongoing of structural transformations (e.g., changes in thickness, morphology). The changes in the interference signal after the growing CO ice samples under different experimental conditions (temperature, deposition speed, and ice thickness) are analyzed to understand morphological changes taking place in these ices.

The experimetnal setup consists of a stainless steel vacuum chamber pumped by a turbomolecular pump (Leybold 350 iX turbovac) to pressures of $\sim 5 \times 10^{-8}$ mbar. The pressure in the main chamber is monitored with a Pfeiffer PKR 360 C full-range gauge. An aluminum mirror is located in the center of the chamber and used as a substrate to grow the ice samples. This mirror is thermally connected to a closed-cycle helium cryocooler and can reach temperatures as low as 7.5 K. The temperature is measured by a silicon diode (S950-SM-Cryogenic Control Systems) connected to a Lakeshore 330 temperature controller. During the measurements, a HeNe laser beam (632.8 nm) hits the substrate at angles or around 2° - 4° and is reflected to a photodetector (Thorlabs PDA36A2), where the light signal is detected. The light from the Xe-arc lamp hits the

growing ice at angles of 45° and is collected by an Andor 303i Shamrock spectrometer with a 10 μm slit and detected in a thermo-electrically cooled CCD (Andor iDus DV420 OE). The interference pattern originated from the individual light sources are recorded and analyzed. A schematic picture of OASIS is shown in Figure 2.5.

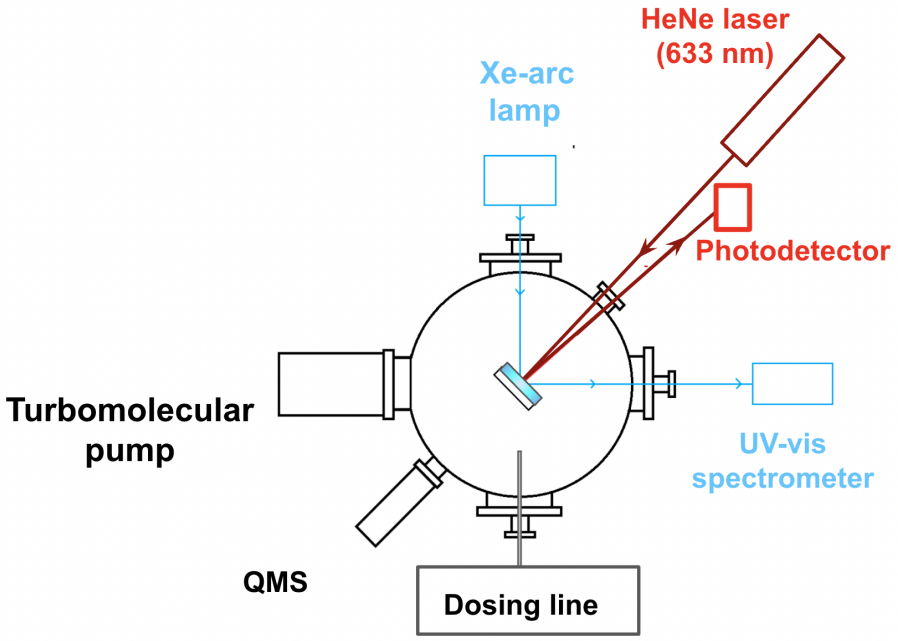

Figure 2.5: Schematic view of the OASIS setup (adapted from He et al. 2022).

The gas used to grow the ice samples is kept in a dosing line and admitted into the chamber through a 1/4" swagelok tube pointed away from the substrate. Thus, the sample is grown by background deposition. The dosing line is typically filled to a pressure of 100 mbar and the gas flow into the chamber is controlled using a leak valve. During the ice deposition, the leak valve is constantly adjusted to maintain a constant gas pressure inside the chamber.

The column density of the ice sample is estimated from the impingement rate of molecules onto the substrate when the chamber is filled to a certain pressure of gas during a certain amount of time, t:

$$N = \frac{\int^t P \, \mathrm{d}t'}{\sqrt{2 \, \pi \, m \, k \, T}}, \tag{2.7}$$

where P and T are the gas pressure and temperature inside the chamber, respectively,

m is the molecular mass of the deposited molecule, and k is the Boltzmann constant.

2.4 The Leiden Ice Database for Astrochemistry

The spectroscopic data acquired on the HV setup and on IRASIS are publicly available through the Leiden Ice Database for Astrochemistry (LIDA). The interface of the database has functionalities that allow for displaying the infrared spectra of samples at different temperatures and visualize the different vibrational modes of a molecules. The broadband refractive index of pure ices at different temperatures recorded on OASIS are also available from LIDA. In addition to the laboratory data, LIDA also has two online astronomy oriented tools. The SPECFY tool allows to create synthetic spectra of ices observed toward protostars by using template spectra of young stars, from the literature and available through the database, and the laboratory data of ice analogs. The second tool is a complex refractive index calculator, that uses the laboratory infrared spectrum of interstellar ice analogs to calculate the mid-infrared refractive index of the sample. An overview of the current data available from the database, its functionalities, online tools, and examples on how to use them for support interstellar ice research is presented in Rocha et al. (2022).

References

Beltrán, M. D., Molina, R. L., Aznar, M. Á. S., et al., 2015, Sensors, 15, 25123
He, J., Diamant, S. J., Wang, S., et al., 2022, ApJ, 925, 179
Kofman, V, Witlox, M., Bouwman, J, et al., 2018, Review of Scientific Instruments, 89, 053111
Kofman, V., He, J., Kate, I. L. ten, et al., 2019, ApJ, 875, 131
Rachid, M. G., Brunken, N., de Boe, D., et al., 2021, A&A, 653, A116
Rocha, W. R. M., Rachid, M. G., Olsthoorn, B., et al., 2022, A&A, 668, A63
Tempelmeyer, K. and Mills Jr, D., 1968, Journal of Applied Physics, 39, 2968
Terwisscha van Scheltinga, J. (Nov. 2021). "Ice and gas in protostellar clouds and planet-forming disks: a combined laboratory and observational study". PhD thesis. University of Leiden, Netherlands.
Yarnall, Y. Y. and Hudson, R. L., 2022, ApJL, 931, L4

3

Infrared spectra of complex organic molecules in astronomically relevant ice mixtures: II Acetone

Complex organic molecules (COMs) have been largely identified through their characteristic rotational transitions in the gas of interstellar and circumstellar regions. Although these species are formed in the icy mantles that cover dust grains, the most complex species that has been unambiguously identified in the solid phase to date is methanol (CH_3OH). With the upcoming launch of the James Webb Space Telescope (JWST), this situation may change. The higher sensitivity, the spectral and spatial resolution of the JWST will allow for the probing of the chemical inventory of ice in star-forming regions. To identify features of solid-state molecules in astronomical spectra, laboratory infrared spectra of COMs within astronomically relevant conditions are required. This chapter is part of a series of laboratory studies focusing on the infrared spectra of frozen COMs embedded in ice matrices. These reflect the environmental conditions in which COMs are thought to be found. This work is aimed at characterizing the infrared features of acetone mixed in ice matrices containing H_2O, CO_2, CO, CH_4, and CH_3OH for temperatures ranging between 15 - 160 K. Changes in the band positions and shapes due to variations in the temperature, ice composition, and morphology are reported. This work also points out the IR features that are considered the best promising tracers when searching for interstellar acetone-containing ices. Acetone-containing ices were grown at 15 K under high-vacuum conditions and infrared (IR) spectra (500 - 4000 cm^{-1}/20 - 2.5 μm, 0.5 cm^{-1} resolution) in transmission mode were recorded using a Fourier transform infrared spectrometer. Spectra of the ices at higher temperatures are acquired during the heating of the sample (at a rate of 25 K hr^{-1}) up to 160 K. The changes in the infrared features due to ice composition, morphology, and temperature were measured. A large set of IR spectra of acetone-containing ices is presented and made available as a basis for interpreting current and future infrared astronomical spectra. The peak position and full width at half maximum (FWHM) of selected acetone bands have been measured for different ice mixtures and temperatures. The bands that are best suitable for acetone identification in astronomical spectra are the C=O stretching mode, around 1710.3 cm^{-1} (5.847 μm), that lies in the 1715 - 1695 cm^{-1} (5.83 - 5.90 μm) range; the CH_3 symmetric deformation, around 1363.4 cm^{-1} (7.335 μm) that lies in the 1353 - 1373 cm^{-1} (7.28 - 7.39 μm) range; and the CCC antisymmetric stretching, around 1228.4 cm^{-1} (8.141 μm), that lies in the 1224 - 1245 cm^{-1} (8.16 - 8.03 μm) range. The CCC antisymmetric stretching band also exhibits potential as a remote probe of the ice temperature and composition; this feature is the superposition of two components that respond differently to temperature and the presence of CH_3OH. All the spectra are available through the Leiden Ice Database.

M. G. Rachid, J. Terwisscha van Scheltinga, D. Koletzki, and H. Linnartz (2020) published in A&A, 639, A4

3.1 Introduction

The increasing number of molecules detected outside our Solar System directly correlated to the many chemical processes taking place in space. Up through today, more than 225 different molecules have been identified in the interstellar medium (McGuire, 2018). The majority of these species have typical sizes ranging from up to 13 atoms, however, much larger molecules have also been detected in space: such as the fullerenes C_{60}, C_{60}^+, and C_{70}, (Cami et al., 2010; Sellgren et al., 2010; Berné et al., 2013; Campbell et al., 2015; Cordiner et al., 2019). These molecules have been detected across a diversity of environments, diffuse and cold molecular clouds, circumstellar disks and gas shells expelled by stars at the end of their lives) (Ehrenfreund and Charnley, 2000). Most of these species have been identified exclusively through their gas-phase signatures; only some 12 species have been found in the solid state and among these, the only complex organic molecule (COM) that has been definitively detected in the solid phase is methanol (CH_3OH). As it is generally thought that COMs form through surface-induced reactions (Herbst and van Dishoeck, 2009; Linnartz et al., 2015; Öberg, 2016), the lack of solid-state COM identifications calls for further attention.

Infrared observational data have shown that the icy material in cold regions of dark clouds and protoplanetary disks can harbor simple molecules, such as H_2O, CO, CO_2, NH_3, CH_4, and CH_3OH (Gibb et al., 2004; Öberg et al., 2011; Boogert et al., 2015). Laboratory work has shown that many COMs can be formed starting from these simple precursor molecules, either through non-energetic processing, such as atom or radical addition and recombination reactions (Watanabe and Kouchi, 2002; Ioppolo et al., 2011; Fedoseev et al., 2015; Linnartz et al., 2015), or energetic processing, for example, via irradiation by UV photons, cosmic-rays, and electrons (Gerakines et al., 1996; Hudson and Moore, 1999, 2001; Öberg et al., 2009; Duarte et al., 2010). With the upcoming launch of the James Webb Space Telescope (JWST), spatially, and spectroscopically well-resolved infrared spectra of ices in star-forming regions will become available. Within ICE AGE (`http://jwst-iceage.org/`), an early release JWST science program, efforts have been underway to search for the solid-state signatures of larger and more complex species, COMs in particular, that may play a role in the formation of the building blocks of life. In order to identify the infrared features of COMs in astronomical data, reference spectra in simulated space environments are required. Currently, worldwide efforts are made to have these data available in time. This paper deals with the case of ices containing acetone (CH_3COCH_3).

Acetone was detected in the interstellar medium (ISM) for the first time in the hot molecular core Sgr B2 (Combes et al., 1987; Snyder et al., 2002). Since then, it has also been detected in other high mass star forming regions (Friedel et al., 2005; Zou and Weaver, 2017), towards an intermediate-mass protostar (Fuente et al., 2014), the low mass protostar IRAS 16293-2422B (Lykke et al., 2017) and in the disk around the outbursting star V883 Ori (Lee et al., 2019). Acetone is a key molecule to understanding the O-N differentiation in the Orion-KL region. There, large N-bearing molecules and large O-bearing molecules are spatially separated. However, acetone is present in the overlapping between these two chemically different environments, indicating that this species may have a unique formation mechanism, that is expected to follow solid-state routes (Friedel and Snyder, 2008; Zou and Weaver, 2017).

Initially, the formation of acetone in the ISM was proposed to occur by the radiative association of a methyl ion and acetaldehyde in the gas phase that results in the formation of protonated acetone ($CH_3COCH_3^+$) that sequentially recombines with electrons to form neutral acetone (Combes et al., 1987):

$$CH_3^+ + CH_3CHO \rightarrow CH_3COCH_3{}^+ + h\nu$$

$$CH_3COCH_3{}^+ + e^- \rightarrow CH_3COCH_3.$$

Herbst et al. (1990) carried out a theoretical study of acetone formation through ion-molecule reactions and demonstrated that the reaction between the methyl ion and acetaldehyde proposed by Combes et al. (1987) is not efficient enough to account for the observed CH_3COCH_3 abundances in Sgr B2. Instead, the authors proposed that acetone synthesis could involve surface chemistry pathways, a proposition that is also observationally supported by the recent work by Lee et al. (2019).

Garrod et al. (2008) proposed that the solid-state formation of some COMs, including acetone, in hot cores could happen through the reaction between aldehyde-group radicals and primary or secondary radicals in ice grain mantles:

$$CH_3CHO + CH_3 \rightarrow CH_3CO + CH_4,$$

$$CH_3CO + CH_3 \rightarrow CH_3COCH_3.$$

Later, the formation of acetone and acetaldehyde in CO:CH_4 ices irradiated by 5 keV electrons was confirmed by Kaiser et al. (2014). An unambiguous identification

of acetone in the solid state would, therefore, shed further light on its chemical origin in interstellar ice.

Hudson et al. (2018) reported IR spectra of amorphous and crystalline acetone ice, at 10 K and 125 K, respectively. The authors compared their reported data with spectra available in the literature, characterized the changes in shape and band position in the acetone spectra at different temperatures, deposition conditions, and thicknesses, and reported refractive index, density, and band strength values for the vibrational modes for both amorphous and crystalline acetone ices. To further support the interpretation of infrared astronomical data, it is important to extend studies of pure acetone ice to acetone-containing ice mixtures comprising abundant interstellar ice species or species that are precursors of solid-state acetone. Moreover, such spectra need to be recorded for different temperatures and ice growth conditions as the vibrational modes are affected by the chemical composition, temperature, and physical structure of the ice (Palumbo, 2005; Dawes et al., 2007; Öberg et al., 2007; Bossa et al., 2012; Isokoski et al., 2014), causing peak positions, peak shapes (e.g., the full width at half maximum, FWHM), and intensity ratios to vary for different experimental settings. Adding to this, vibrational modes may absorb at wavelengths overlapping with those of similar functional groups from other molecules present in the ice, which will further complicate unambiguous infrared identifications.

This work presents a study of the infrared spectral features of acetone in its pure form and mixed in relevant interstellar ice matrices: H_2O, CO, CH_3OH, CO_2, H_2O:CO_2, H_2O:CH_4, and CO:CH_3OH. The strongest bands of acetone (A $> 10^{-18}$ cm molecule^{-1} from Hudson et al. 2018) have been selected and are characterized in terms of peak position, FWHM, and band intensity ratios. The decision to focus on the strongest bands is based on the fact that those are most suited to act as acetone tracers in astronomical infrared spectra.

The present paper is structured as follows: Section 2 describes the apparatus and the measurement protocols. In Section 3, the results of selected spectral features of acetone in different mixtures are presented and the astronomical importance of the present measurements is discussed. The conclusions are outlined in Section 4. Selected wavelength domains of the infrared spectra of all the samples studied in this work, along with graphs showing the peak position versus FWHM and the calculated apparent band strengths, are summarized in Appendix A. The tables listing peak position and FWHM values for all the studied bands are listed in Appendix B. The integrated absorbance of acetone bands is summarized in Appendix C.

3.2 Methodology

All the measurements were performed in a high-vacuum setup (HV) with a central stainless steel chamber with a base pressure of $\sim 3 \times 10^{-7}$ mbar and which houses a cryogenically cooled IR transparent window (ZnSe) onto which ices are grown. The pressure in the main chamber is measured using a full-range pressure gauge. The liquids and gases used in the preparation of the gas mixtures are acetone (Roth, purity $\geq$ 99.9%), water (Milli-Q, Type I), carbon monoxide (Linde Gas, 99.997%), methane (Linde Gas 99.999%), and methanol (Honeywell, purity $\geq$ 99.9%). The gas samples, pure and mixed, are prepared in a separate mixing line within a 2 L glass bulb typically filled up to a total pressure of 20 mbar. The mixtures are prepared through the sequential freezing of gases in the glass bulb immersed in a liquid N_2 bath. The base pressure in the mixing line is around 1×10^{-4} mbar and measured using two mass-independent pressure gauges that cover the range between 0 - 10 mbar and 0 - 1000 mbar. The estimated error in the mixture ratios obtained by this method is $\leq$ 10%. The gas sample is admitted into the main chamber through an inlet valve and the flow is controlled by a calibrated needle valve that is maintained at the same fixed position for all the experiments. The gases are background deposited onto the cryogenically cooled (15 K) ZnSe window using a closed cycle He cryostat. The sample temperature is monitored using a silicon diode DT-670-CU, PID controlled by a Lake Shore 330 temperature controller, with an absolute accuracy of $\pm$ 2 K and a relative accuracy of $<$ 1 K. In this work, the needle valve has already been calibrated for different pure gases, enabling the calculation of their deposition rate (the band strengths for the quantification were taken from Bouilloud et al. 2015; Hudson et al. 2018). Taking into account the deposition rate on pure gases weighted by their respective fraction in the desired gas mixtures, it becomes possible to determine the deposition rate of the gas mixtures. Consequently, the column density of each component in the ice can be calculated. Once the column density of acetone and the integrated IR absorption of a given vibrational mode are known, it is possible to calculate the apparent band strength of the acetone bands in an ice mixture.

The ice samples are typically grown over a period of 30 minutes, resulting in an ice thickness between 2800 - 3500 ML (1 ML $\sim 1 \times 10^{15}$ molecules cm^{-2}), depending on the composition of the gas mixture. These thick ices are used to minimize the influence of contamination from the background gases, which is mainly water at a measured rate of 30 ML hr^{-1}. During the deposition of the mixtures, the non-saturation of the C=O stretching band of acetone is checked. The infrared beam of a Varian 670-IR infrared

spectrometer is guided perpendicularly through the substrate to obtain the IR spectra of the ice samples in transmission mode. The spectrometer covers a range between 4000 cm^{-1} - 500 cm^{-1} (2.5 - 20 μm) at spectral resolutions as high as 0.1 cm^{-1}. In this work, the spectra are collected using a resolution of 0.5 cm^{-1}. All the recorded spectra are averaged over 128 scans (around 3.5 minutes). After the spectra at 15 K are taken, the sample is heated at a rate of 25 K hr^{-1} until it is completely desorbed from the substrate. During the heating of the sample, spectra are continuously recorded to obtain spectra for different temperature settings. Consequently, an ice spectrum recorded for a specific temperature actually covers a temperature range of $\pm$ 0.8 K from the central value. This is also the reason why spectra were recorded at 0.5 cm^{-1} resolution, as this is an optimum between spectral resolution and time needed to perform a full scan; with increasing scan time the uncertainty of the ice temperature would increase. Apart from temperatures close to a phase transition or desorption temperature, this does not cause any inaccuracies. More experimental details can be found in (Terwisscha van Scheltinga et al., 2018).

3.2.1 Ice samples

Astronomical observations supported by laboratory studies have shown that the molecular constituents of interstellar ice are structured in layers rather than homogeneously mixed. Dust grains are initially covered by layers of water, due to surface reactions of H atoms and O atoms and direct freeze-out of gas-phase H_2O (Cuppen et al., 2010; Linnartz et al., 2015). During this stage CO_2 and CH_4 are also formed (Öberg et al. 2008; Ioppolo et al. 2011; Qasim et al. 2020). As the density increases and temperatures further drop, CO starts to accrete rapidly. Subsequent hydrogenation of CO ultimately results in methanol formation within a CO-rich ice (Boogert et al., 2015; Linnartz et al., 2015). In an attempt to simulate the infrared spectra of acetone in these different ice layers, the mixtures prepared in this work contain acetone mixed with some of the more abundant interstellar ice components: H_2O, CO_2, CO, CH_4, and CH_3OH. Additionally, acetone is mixed in H_2O:CO_2, H_2O:CH_4 , and CO:CH_3OH mixtures. The mixtures are prepared with acetone ratios of 1:5 (i.e., 1 molecule of acetone for 5 matrix molecules) and 1:20. These ratios are relatively high compared to COMs (likely to have been) identified in astronomical data but are expected to provide representative spectra. Table 3.1 shows the composition and mixing ratio of all ice samples studied in this work. For all the investigated ice samples, the spectra were collected between 15 - 200 K. In this work, the spectra were analyzed until the

Table 3.1: Composition, mixing ratios, and temperature range of the analyzed samples. The uncertainty in the mixing ratios due to the preparation of the sample is lower than 10 %

Mixture	1:5	1:20	Temperature range (K)
CH_3COCH_3:H_2O	1:5	1:20	15 - 160
CH_3COCH_3:CO_2	1:5	1:20	15 - 100
CH_3COCH_3:H_2O:CO_2	1:2.5:2.5	1:10:10	15 - 160
CH_3COCH_3:H_2O:CH_4	1:2.5:2.5	1:10:10	15 - 160
CH_3COCH_3:CH_3OH	1:5	1:20	15 - 140
CH_3COCH_3:CO	1:5	1:20	15 - 35
CH_3COCH_3:CH_3OH:CO	1:2.5:2.5	1:10:10	15 - 140

desorption of the major matrix components (T $\sim$ 30 K for CO matrix, T $\sim$ 100 K for CO_2 matrix, T $\sim$ 140 K for all the CH_3OH-containing ices and T $\sim$ 160 K for all the H_2O-containing ices) or until the acetone bands are no longer detectable.

3.2.2 Analysis protocol

All the spectra are baseline-corrected using Origin and the acetone bands are identified by comparison with the results presented by Hudson et al. 2018. From the acetone infrared features visible in the pure ice spectra, the strongest ones (A' $> 10^{-18}$, see Hudson et al. 2018) were selected. From these, only the transitions that have no obvious spectral overlap with bands originating from other abundant ice species are characterized (i.e., peak position and FWHM) using a personal Matlab script. Figure 3.1 shows the infrared spectra of pure CH_3COCH_3 ice (bottom spectra) and the spectra of the other ice components that are used in the analyzed samples: H_2O, CH_3OH, CH_4, CO, and CO_2. The five selected acetone bands analyzed in this work are marked in Figure 3.1 with an asterisk. These bands are: the CO in-plane deformation band around 533 cm^{-1} (18.8 μm); the CCC antisymmetric stretching band around 1228 cm^{-1} (8.14 μm); the CH_3 symmetric deformation band at 1363 cm^{-1} (7.34 μm); the CH_3 antisymmetric deformation band around 1418 cm^{-1} (7.05 μm); and the C=O stretching band around 1710 cm^{-1} (5.85 μm).

The band strength (A) of a vibrational mode can be used to calculate the number of absorbing species that count for an absorption feature. Once it is known, it can be used to derive the column density for a specific molecule from an infrared spectrum. Physically, the integrated absorbance of a vibrational mode is related to the changes in the electron charge distribution upon excitation. Since the electronic configuration of a molecule changes due to the interaction with the surrounding species, the band

strength depends on the composition and morphology of the ice. In order to better derive abundances and upper limits of molecules in astronomical data, it is advantageous to know the band strength of COMs when embedded in ices with compositions similar to those such molecules are expected to be found in. In this work, we derive the apparent band strength (A') of the acetone vibrational modes, when acetone is embedded in different ice matrices. These values of the apparent band strength relative to the values reported by Hudson et al., 2018 are displayed in Appendix A. The estimated errors in this procedure are around 20 %.

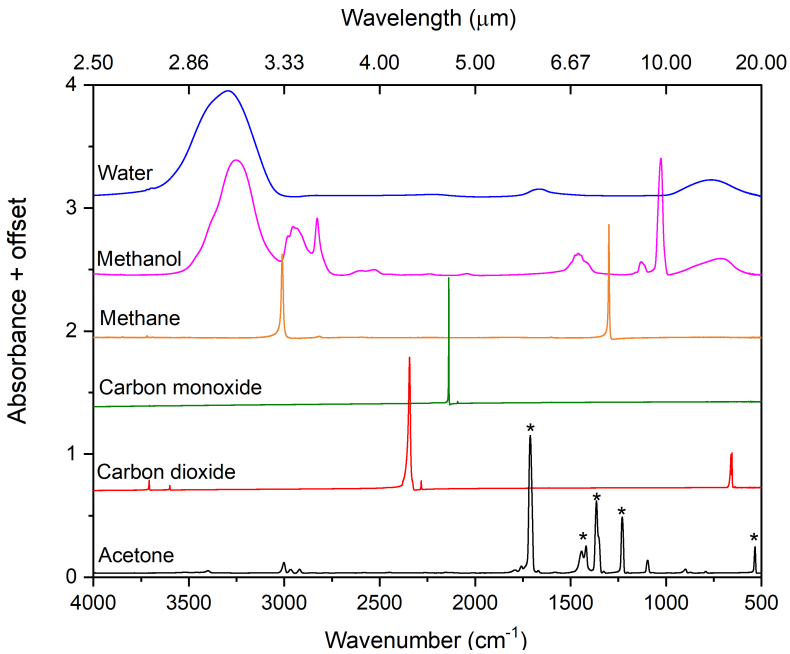

Figure 3.1: Infrared ice spectra of pure CH_3COCH_3 at 15 K (black), CO_2 (red), CO (green), CH_4 (orange), CH_3OH (magenta) and H_2O (blue). The acetone absorption bands marked with an asterisk have been selected for an in-depth study as the most suited acetone tracers for future JWST surveys.

3.3 Results and discussion

This section presents a number of representative infrared spectra of acetone embedded in different ice mixtures and at different temperatures. The overall clear differences in the different mixing ratios and temperature settings provide an analytical tool for

astronomical ice characterization.

Figures 3.2 through 3.5 show the C=O stretching and the CCC antisymmetric stretching of acetone for temperatures ranging from 15 - 160 K, in pure ice and mixtures with an acetone percentage of 20%. For improved visualization, the spectra at different temperatures are offset and it should be noted that the panel showing acetone in pure form (left panel in all figures) is displayed at a different scale compared to the panels presenting the ice mixture spectra. Similar figures displaying the spectra of the other acetone bands are given in Appendix A. All the spectra are available in full from the Leiden Ice Database (`https://icedb.strw.leidenuniv.nl/`). Spectra that were recorded at intermediate temperatures and not listed here are available upon request.

3.3.1 Pure acetone ice

Table 3.2 lists the infrared bands of acetone that have been selected as the best-suited tracers of acetone ice in space. As expected, the peak position values for pure acetone ice are close to those reported by Hudson et al. (2018) for amorphous acetone ice at 10 K. The pure acetone ice remains amorphous between 15 and 90 K and there are no significant changes seen in the peak positions and band shapes. At 93 K, there is an abrupt sharpening of all the investigated bands, characteristic for the transition to crystalline acetone. The peak positions of the acetone bands also change after crystallization. A compilation of all the acetone features at different temperatures can be found in Appendix B. From 100 K up to 140 K, the bandwidths show no appreciable changes. When the pure acetone ice is heated to temperatures above 140 K, the intensity of the acetone bands starts decreasing and drops below the detection sensitivity of our IR technique when the sample reaches 148 K. This desorption temperature is close to the value presented by Hudson et al. 2018, who reported that acetone thermally desorbs around 150 K.

3.3.2 Peak position of acetone features in ice mixtures

The C=O stretching vibrational mode, around 1710 cm^{-1} (5.85 μm), is the strongest acetone band (A = 2.67×10^{-17} cm $molecule^{-1}$). This mode is partially superimposed on the OH bending mode of water as well as other molecules detected in astrophysical ices, such as the N-H bending mode of ammonia (Bouilloud et al., 2015; Boogert et al., 2015). However, since this mode is strong, it is easily identified even in the diluted mixtures (see Figures 3.A.7 and 3.A.8). In H_2O, CO_2, and CO matrices, at low temperatures, this vibrational mode is present as a single feature while in CH_3OH-

Table 3.2: Peak position of the pure acetone ice bands studied in this work. The acetone band position and strengths for the amorphous ice at 10 K (Hudson et al., 2018) are shown for comparison.

Vibrational mode	Peak position (cm^{-1})		A'[**]
	15 K [*]	10 K [**]	(10^{-18} cm $molec^{-1}$)
CO in-plane deformation	532.7	533.6	2.13
CCC antisymmetric stretching	1228.4	1228.9	7.35
CH_3 symmetric deformation	1363.4	1364.4	13.9
CH_3 antisymmetric deformation	1417.9	1418.9	9.19
C=O stretching	1710.3	1711.4	26.7

[*] This work
[**] From Hudson et al. 2018

containing ices, it appears as a two-component feature, which is likely due to the formation of binary complexes with methanol (Han and Kim, 1996).

A point worth stressing is that multi-component peaks, such as the ones showing up with an increase in temperature or when acetone is embedded in certain ice matrices, are usually associated with the vibrational modes of interacting molecules within the ice structure. In methanol-acetone ices, the formation of acetone dimers, trimers, and tetramers induces the appearance of specific absorption bands (Kollipost et al., 2015). When the sample is warmed, molecules are reoriented inside the ice structure, adopting the most energetically favorable configurations, that is, some arrangements of molecules are more likely than others. The intensity of the peaks associated with these dominant configurations at a specific temperature appears enhanced in the spectra. Unfortunately, contrary to the gas phase, little is known about the exact orientations of molecules in amorphous ices, an issue that is even more significant in the case of mixed ices. The data presented here reflect these processes and will prove helpful in identifying COMs in interstellar ices, however, the specific explanation of the spectroscopic behavior is outside the scope of this work. We refer to Zhang et al. 1993; Han and Kim 1996; Kollipost et al. 2015, where the assignment of some of the multi-component infrared bands of acetone in different solid and liquid matrices is investigated.

The shape and FWHM of the acetone bands in the H_2O-containing mixtures are very similar. In the CH_3COCH_3:H_2O:CO_2 and CH_3COCH_3:H_2O:CH_4 ices, the analyzed bands exhibit similar shifts, broadening, and splitting patterns. For example, the peak positions for the acetone bands in these mixtures usually vary less than 2 cm^{-1} at 15 K for ices with the same acetone ratio (see Appendix B). In these H_2O-rich ices, the C=O stretching appears as a broad feature, shifted towards lower frequencies

with respect to the pure acetone ice. The largest shifts towards lower frequencies are observed for the CH_3COCH_3:H_2O:CO_2 ices: 1699.9 cm^{-1} (5.88 μm) and 1695.6 cm^{-1} (5.90 μm) for the samples at 1:5 and 1:20 dilution ratios, respectively, and for the CH_3COCH_3:H_2O:CH_4 (1:10:10) ice, where this mode appears at 1697.5 cm^{-1}. In the CO matrix, this band exhibits the largest shifts towards higher wavenumbers and is found at 1715.9 cm^{-1} (5.83 μm) and 1717.3 cm^{-1} (5.82 μm) for the 1:5 and 1:20 mixture ratios, respectively. By warming the ices to temperatures higher than 120 K, the carbonyl band mode sharpens and appears as a three-component feature in the CH_3OH-containing ices, similar to the pure acetone ice. In all the H_2O-containing ices, the peak sharpening and splitting are not observed, while in the CH_3COCH_3:CO and CH_3COCH_3:CO_2 ices, the matrix is mostly desorbed before 120 K is reached.

The data collected in this work shows that the C=O stretching peak position of acetone varies significantly, depending on the ice matrix and temperature. In the studied 15 K ices, the acetone carbonyl stretching mode lays between 1695 - 1717 cm^{-1} (5.89 - 5.82 μm). These peak shifts that occur due to matrix effects, which add further diagnostic value, should be taken into account when trying to assign peaks in astronomical spectra.

The CH_3 antisymmetric deformation mode of acetone, around 1418 cm^{-1} (7.05 μm), overlaps with the CH_3 bending modes of methanol (Bouilloud et al., 2015). At temperatures higher than 100 K, this band narrows but still overlaps with the CH_3OH bands (Figures 3.A.2 and 3.A.10). This makes the detection of this feature in astronomical data very unlikely if CH_3OH is present, especially at low temperatures when the bands are broader. The CH_3 symmetric deformation mode of acetone, between 1380-1335 cm^{-1} (7.25 - 7.49 μm), however, can be relatively easily identified. This vibrational mode appears as a two-component feature or as a feature with a shoulder in all spectra. For pure acetone ice and the CH_3OH-containing ices, the shoulder at lower wavenumbers (around 1352 cm^{-1}) narrows when the crystallization of acetone-methanol matrix takes place, revealing that it is composed of two other components, which are around 1349.2 cm^{-1} and 1361.3 cm^{-1} (Figures 3.A.4 and 3.A.12). For the pure ice, these features appear at 100 K, and for the CH_3OH-bearing ices (ratio 1:5) these features appear at temperatures higher than 120 K. For the CH_3COCH_3:CO:CH_3OH(1:10:10) ice, the splitting of the CH_3 antisymmetric deformation mode is also observed at high temperatures. In the CH_3COCH_3:CO_2 mixtures a weak feature, close to 1380 cm^{-1} (7.24 μm), is observed. This feature disappears at temperatures higher than 90 K.

The CCC antisymmetric stretching band of acetone, around 1230 cm^{-1} (8.1 μm)

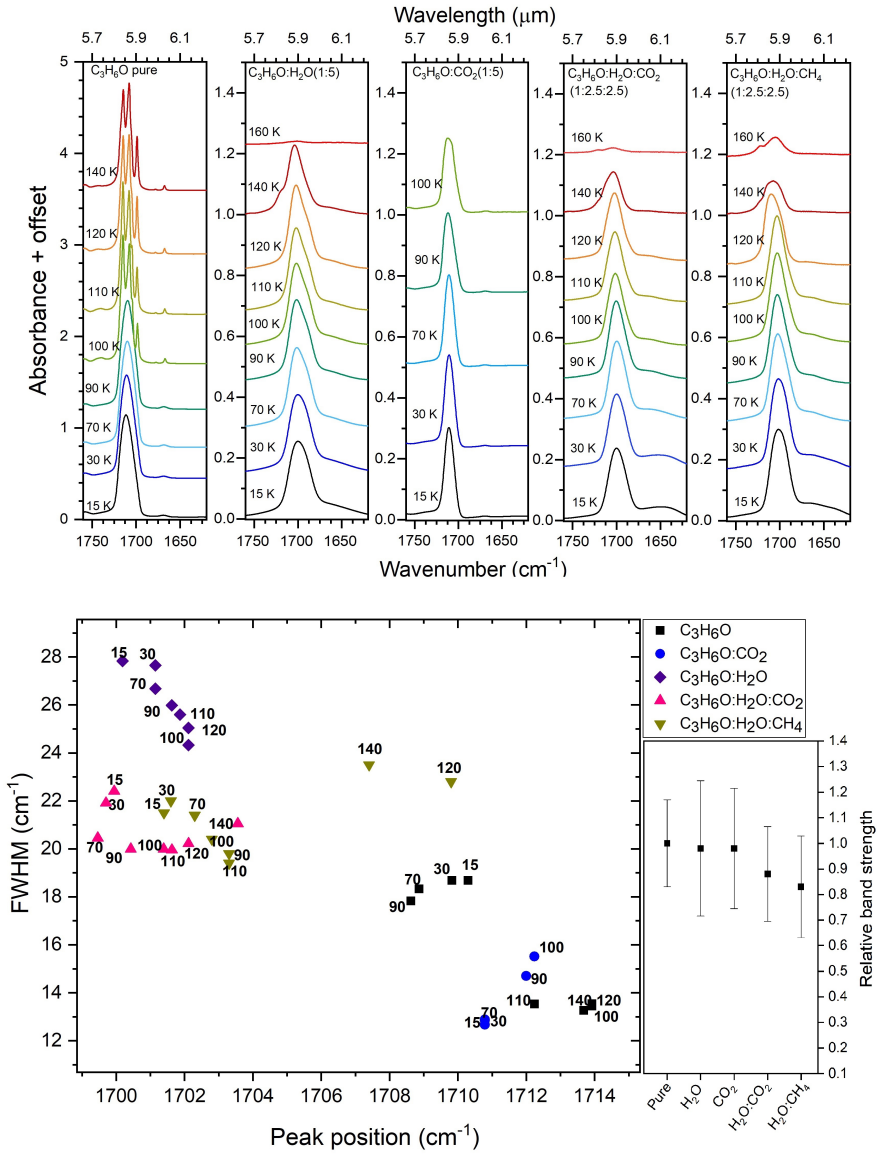

Figure 3.2: Upper panel: infrared spectra in the range of 1760 - 1630 cm^{-1} (5.68 - 6.13 μm) showing the C=O stretching band of acetone in pure and mixed ices. The spectra at different temperatures are offset for improved visualization. Bottom left: peak position vs. FWHM plot for the C=O stretching band in different ice matrices, represented by the different colors, and for different temperatures, indicated by the numbers in the graph. Bottom right: apparent band strength for the acetone C=O stretching band at 15 K in the various matrices divided by the band strength for pure acetone from Hudson et al. (2018).

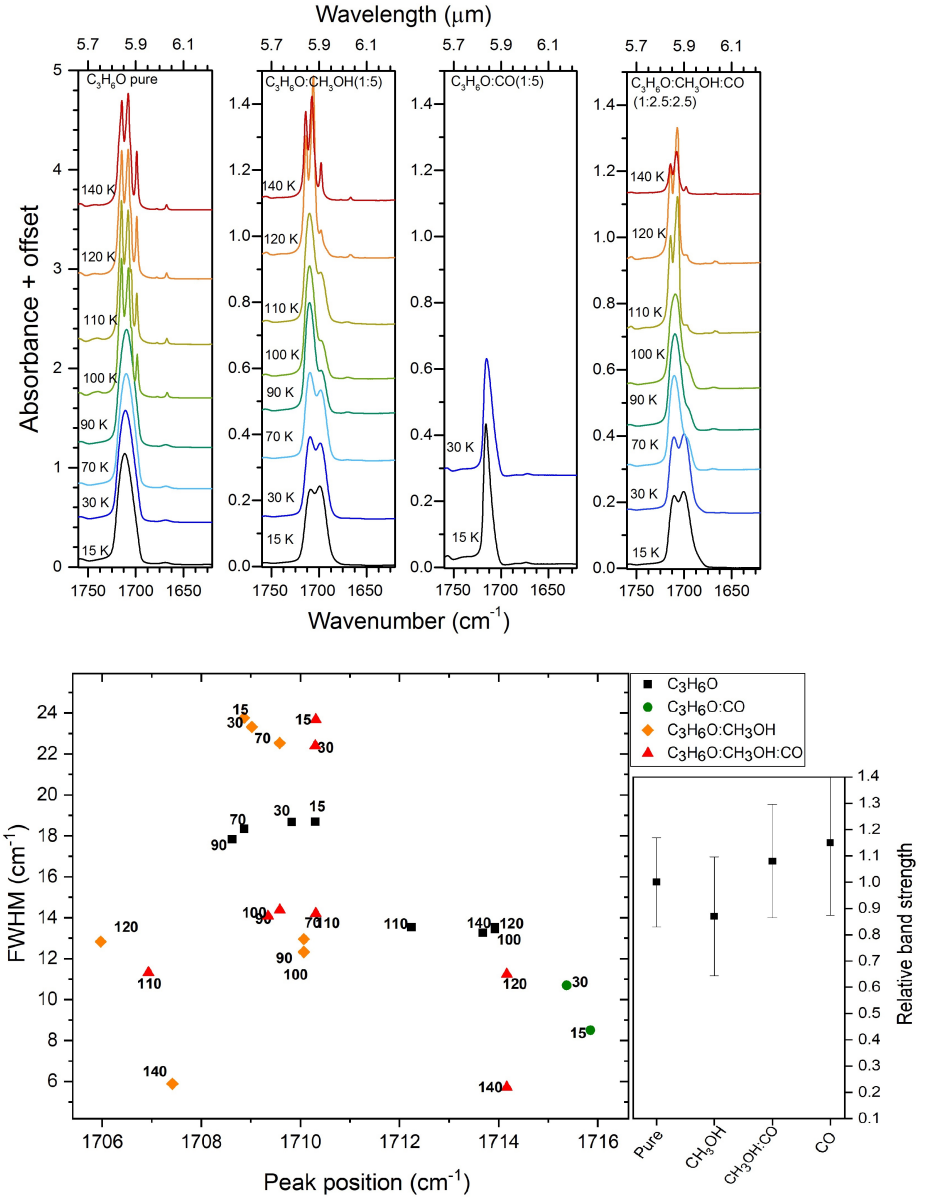

Figure 3.3: Upper panel: infrared spectra in the range of 1760 - 1630 cm^{-1} (5.68 - 6.13 μm) showing the C=O stretching band of acetone in pure and mixed ices. The spectra at different temperatures are offset for improved visualization. Bottom left: peak position vs. FWHM plot for the C=O stretching band in different ice matrices, represented by the different colors, and for different temperatures, indicated by the numbers in the graph. Bottom right: apparent band strength for the acetone C=O stretching band at 15 K in the various matrices divided by the band strength for pure acetone from Hudson et al. (2018).

holds much potential as a tracer of acetone in interstellar ices (Figures 3.4 and 3.5). The 1230 cm^{-1} band does not overlap with bands of the matrix components studied in this work. This feature is also one of the few bands of acetone that do not overlap with the infrared bands of acetaldehyde (CH_3CHO) (Terwisscha van Scheltinga et al., 2018), a possible precursor of solid acetone in interstellar ices (Garrod et al., 2008). In CO and CO_2 matrices this band appears at wavenumbers closer to the value of pure acetone (1228.4 cm^{-1}). In H_2O-containing ices, this feature is shifted to higher wavenumbers: between 1240 - 1245 cm^{-1}. In the CH_3OH-containing ices, this band appears as a two-component feature at 15 K, at 1226.0 cm^{-1} and 1238.1 cm^{-1} for the 1:5 mixture and 1225.5 cm^{-1}, and 1238.1 cm^{-1} for the 1:20 mixture (see Figures 3.4, 3.5, 3.A.11, and 3.A.12).

The CCC antisymmetric stretching band is composed of two components that become visible upon narrowing when the ice is heated to temperatures higher than 100 K. In the pure acetone ice and the methanol-containing mixtures, the component at higher wavenumber increases in strength with respect to the component at lower wavenumber, when warming the ices at temperatures higher than 100 and 110 K, for the pure ice and the methanol-containing mixtures, respectively. In water-rich matrices, the CCC antisymmetric band of acetone appears as a broad feature. As the sample is heated, the peak at low wavenumbers increases in intensity compared to the peak at high wavenumbers, the opposite of what is observed for the methanol-containing mixtures. In this way, the difference in the intensity between the two peaks that compose the CCC antisymmetric stretching band may add further insights into the composition of the ice. In ices where CH_3OH is an abundant component, the different intensities of the peaks composing the CCC antisymmetric stretching band can be related to the ice temperature.

In pure acetone ice, the deformation of the carbonyl group gives rise to a band at 532.7 cm^{-1} (18.77 μm). The position of this band is highly affected by the presence of CO_2 and H_2O, and shifts to higher wavenumbers: 535.6 cm^{-1} (18.67 μm) and 547.0 cm^{-1} (18.28 μm) for CO_2 and H_2O, respectively. This effect is more pronounced in the 1:20 mixtures, where this mode is located at 536.1 cm^{-1}. This trend is probably related to the fact that acetone can interact as an electron donor in the presence of a Lewis acid, as observed by Cha et al. 1999. The profile of the CO deformation mode makes this band a good acetone tracer candidate when acetone is in a water-poor environment, since in the CH_3COCH_3:H_2O(1:20) ice, this band is hard to detect because of a low signal-to-noise ratio (SNR).

3.3.3 FWHM of acetone bands in ice mixtures

In all the H_2O-containing ice samples, the acetone peaks remain broad until 140 K, that is, the moment when the water matrix prohibits the acetone to crystallize. From this temperature onwards, a decrease in the intensity of the acetone peaks is observed, indicating that acetone starts to desorb. In the CH_3OH containing ices, the sharpening and splitting of the acetone bands are observed when reaching temperatures between 110 - 120 K. The band sharpening and splitting may be due to a delayed crystallization of acetone. It is also possible that a thermal induced re-orientation of molecules creates a more organized environment for the acetone molecules and breaks some hydrogen bonds between methanol and acetone, making the peaks sharper. The acetone desorption in these samples happens gradually in the range between 140 - 150 K.

The CO and CO_2-containing ice mixtures were analyzed until their desorption temperature. When this temperature is reached, a decrease in the acetone peak intensity is observed along with matrix desorption. This decrease may be associated with co-desorption, making the quantitative analysis of the intensity of acetone peaks not ideal. However, other findings can be reported about the shape of the acetone peaks in the remaining ice that may be useful. In the CH_3COCH_3:CO ices, all the acetone features are sharper than in the pure acetone ice at 15 K (see Appendix B). From 20 K, the FWHM of the peaks starts to increase. The C=O stretching mode, for example, broadens from 8.5 cm^{-1} at 15 K to 10.7 cm^{-1} at 30 K in the CH_3COCH_3:CO(1:5) mixture and from 6.8 cm^{-1} at 15 K to 9.7 cm^{-1} at 30 K in the CH_3COCH_3:CO(1:20) mixture. When heating the remaining ice to temperatures above 88 K, the acetone bands become sharper, indicating the onset of acetone crystallization. The (1:5) mixture is the only sample for which characteristic crystalline acetone peaks are observed at temperatures lower than 90 K. In the (1:20) mixture, the crystallization of the remaining acetone ice is found around 97 K. In the CH_3COCH_3:CO_2 samples, the CO_2 desorption occurs between 90 - 100 K. The presence of abundant CO_2 in the sample at temperatures between 90 - 100 K makes the crystalline features of acetone appear at temperatures between 101 - 105 K.

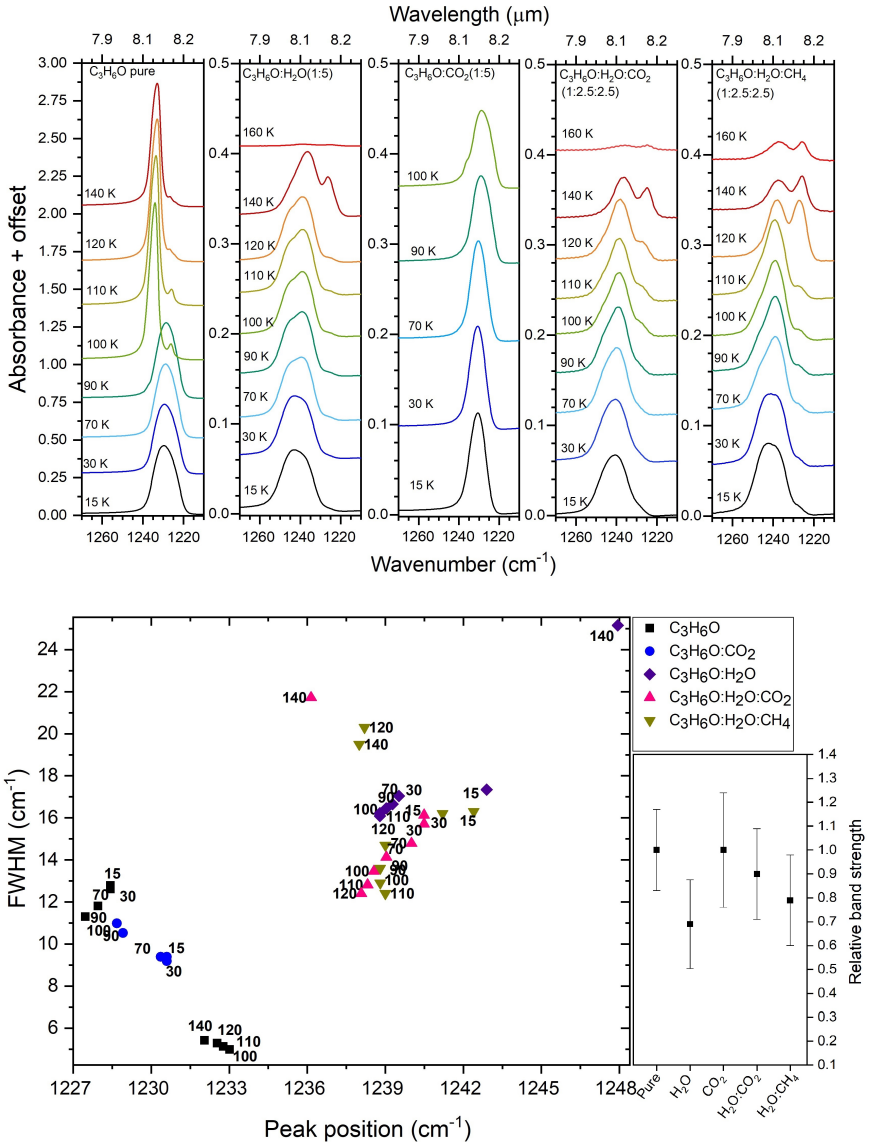

Figure 3.4: Upper panel: infrared spectra in the range of 1270 - 1210 cm^{-1} (7.87 - 8.26 μm) showing the CCC antisymmetric stretching band of acetone in different ice mixtures, from left to right: pure CH_3COCH_3, CH_3COCH_3:H_2O(1:5), CH_3COCH_3:CO_2(1:5), CH_3COCH_3:H_2O:CO_2(1:2.5:2.5), and CH_3COCH_3:H_2O:CH_4(1:2.5:2.5). The spectra at different temperatures are offset for improved visualization. Bottom left: peak position vs. FWHM plot for the CCC antisymmetric stretching band in different ice matrices, represented by the different colors, and for different temperatures, indicated by the numbers in the graph. Bottom right: apparent band strength for the acetone CCC antisymmetric stretching band at 15 K in the various matrices divided by the band strength for pure acetone from Hudson et al. (2018).

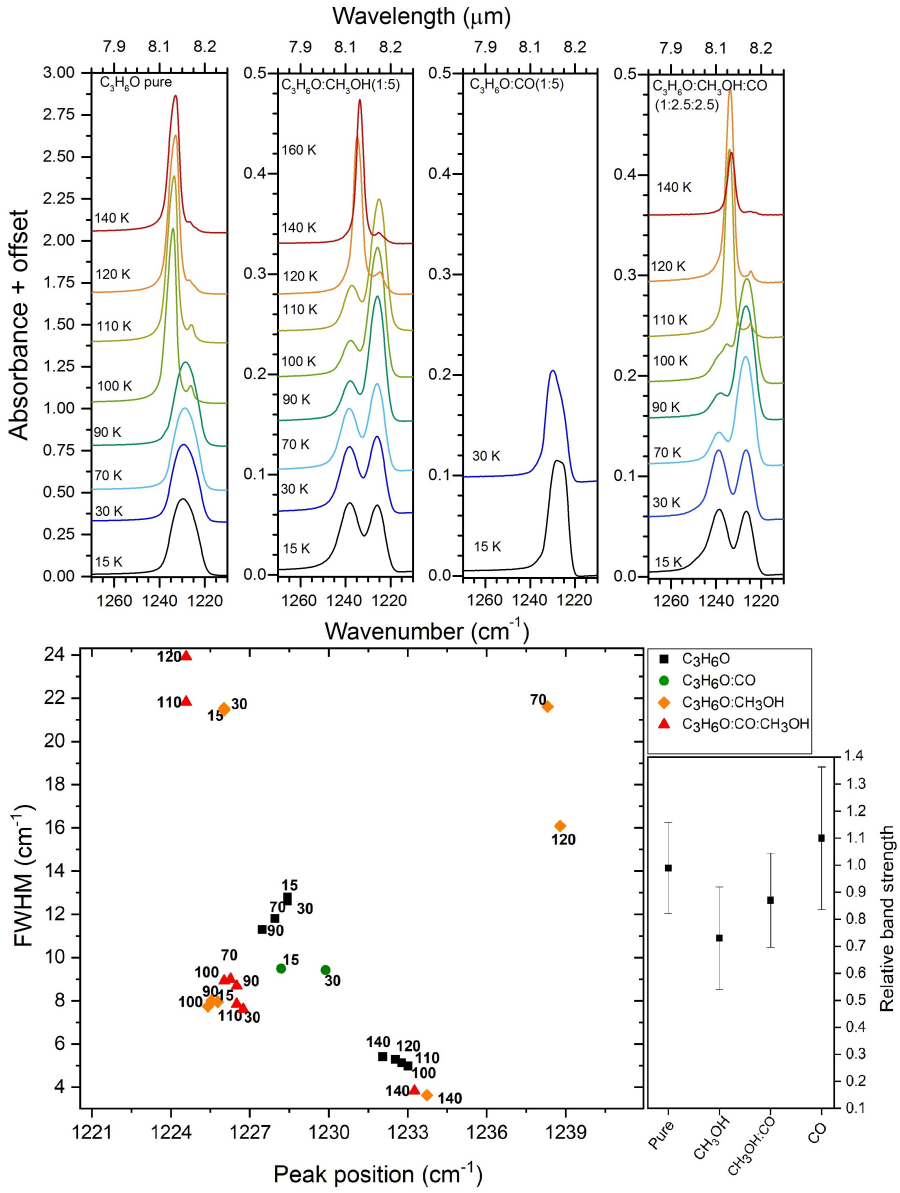

Figure 3.5: Upper panel: infrared spectra in the range of 1270 - 1210 cm^{-1} (7.87 - 8.26 μm) showing the CCC antisymmetric stretching band of acetone in pure and mixed ices. The spectra at different temperatures are offset for improved visualization. Bottom left: peak position vs. FWHM plot for the CCC antisymmetric stretching band in different ice matrices, represented by the different colors, and for different temperatures, indicated by the numbers in the graph. Bottom right: apparent band strength for the acetone CCC antisymmetric stretching band at 15 K in the various matrices divided by the band strength for pure acetone from Hudson et al. (2018).

3.4 Conclusions

Our knowledge of the composition of ices outside of our Solar System may drastically change with the upcoming JWST observations. In order to identify features of frozen COMs in astronomical data, laboratory infrared spectra are necessary for comparison. This work provides an extensive collection of infrared spectra of acetone (CH_3COCH_3) in astronomically relevant ice mixtures, at temperatures ranging from 10 K up to 160 K. The strongest acetone bands are characterized in terms of peak position, FWHM, and band intensity ratios. The bands that are most promising for acetone detection of solid acetone in astronomical data are the CCC antisymmetric stretching band around 1228 cm^{-1} (8.14 μm), the CH_3 symmetric deformation band around 1363 cm^{-1} (7.34 μm) and the C=O stretching band, around 1710 cm^{-1} (5.85 μm). The main conclusions are summarized below:

1. The acetone C=O stretching band is found in the range of 1715.9 - 1695.6 cm^{-1} (5.83 - 5.90 μm) for the analyzed acetone-containing ice mixtures. This mode shifts towards higher wavenumbers in the CO and CO_2 containing mixtures and to lower wavenumbers in the H_2O-rich mixtures.

2. The CH_3 symmetric deformation is found in the range of 1353 - 1373 cm^{-1} (7.28 - 7.39 μm). This band is present as a two-component feature in H_2O, CO_2, CO, H_2O:CO_2 and H_2O:CH_4 ice matrices. The two components become less discernible in the CH_3OH containing ices.

3. The CCC antisymmetric stretching is found in the range of 1224 - 1245 cm^{-1} and shifts towards higher wavenumbers in the H_2O-containing samples. This band is composed of two components and the different intensities of the two components offer a tool for determining the temperature of interstellar ice and for further determining their composition.

References

Berné, O., Mulas, G., and Joblin, C., 2013, A&A, 550, L4
Boogert, A. C. A, Gerakines, P. A., and Whittet, D. C., 2015, ARA&A, 53, 541
Bossa, J.-B., Isokoski, K, Valois, M. de, et al., 2012, A&A, 545, A82
Bouilloud, M, Fray, N, Bénilan, Y, et al., 2015, MNRAS, 451, 2145
Cami, J., Bernard-Salas, J., Peeters, E., et al., 2010, Science, 329, 1180
Campbell, E. K., Holz, M., Gerlich, D., et al., 2015, Nat., 523, 322
Cha, D. K., Kloss, A. A., Tikanen, A. C., et al., 1999, PCCP, 1, 4785
Combes, F, Gerin, M, Wootten, A, et al., 1987, A&A, 180, L13

Cordiner, M., Linnartz, H, Cox, N., et al., 2019, ApJL, 875, L28
Cuppen, H., Ioppolo, S, Romanzin, C, et al., 2010, PCCP, 12, 12077
Dawes, A., Mukerji, R. J., Davis, M. P., et al., 2007, J. Chem. Phys., 126, 244711
Duarte, E. S., Domaracka, A., Boduch, P., et al., 2010, A&A, 512, A71
Ehrenfreund, P. and Charnley, S. B., 2000, ARA&A, 38, 427
Fedoseev, G., Cuppen, H. M., Ioppolo, S., et al., 2015, MNRAS, 448, 1288
Friedel, D. and Snyder, L., 2008, ApJ, 672, 962
Friedel, D. N., Snyder, L., Remijan, A. J., et al., 2005, ApJL, 632, L95
Fuente, A, Cernicharo, J, Caselli, P, et al., 2014, A&A, 568, A65
Garrod, R. T., Weaver, S. L. W., and Herbst, E., 2008, ApJ, 682, 283
Gerakines, P., Schutte, W., and Ehrenfreund, P, 1996, A&A, 312, 289
Gibb, E., Whittet, D., Boogert, A., et al., 2004, ApJS, 151, 35
Han, S. W. and Kim, K., 1996, J. Phys. Chem., 100, 17124
Herbst, E., Giles, K., and Smith, D., 1990, ApJ, 358, 468
Herbst, E. and van Dishoeck, E. F., 2009, ARA&A, 47, 427
Hudson, R. L., Gerakines, P. A., and Ferrante, R. F., 2018, Spectrochimica Acta Part A: Molecular and Biomolecular Spectroscopy, 193, 33
Hudson, R. and Moore, M., 1999, Icarus, 140, 451
Hudson, R. and Moore, M., 2001, Journal of Geophysical Research: Planets, 106, 33275
Ioppolo, S, Van Boheemen, Y, Cuppen, H., et al., 2011, MNRAS, 413, 2281
Isokoski, K., Bossa, J.-B., Triemstra, T., et al., 2014, PCCP, 16, 3456
Kaiser, R. I., Maity, S., and Jones, B. M., 2014, PCCP, 16, 3399
Kollipost, F., Domanskaya, A. V., and Suhm, M. A., 2015, J. Phys. Chem. A, 119, 2225
Lee, J.-E., Lee, S., Baek, G., et al., 2019, Nat. Astronomy, 3, 314
Linnartz, H., Ioppolo, S., and Fedoseev, G., 2015, Int. Rev. Phys. Chem., 34, 205
Lykke, J. M., Coutens, A, Jørgensen, J. K., et al., 2017, A&A, 597, A53
McGuire, B. A., 2018, ApJS, 239, 17
Öberg, K. I., 2016, Chem. Rev., 116, 9631
Öberg, K. I., Boogert, A. A., Pontoppidan, K. M., et al., 2008, ApJ, 678, 1032
Öberg, K. I., Boogert, A. A., Pontoppidan, K. M., et al., 2011, ApJ, 740, 109
Öberg, K. I., Fraser, H. J., Boogert, A. A., et al., 2007, A&A, 462, 1187
Öberg, K. I., Garrod, R. T., Dishoeck, E. F. van, et al., 2009, A&A, 504, 891
Palumbo, M. E. (2005). "The morphology of interstellar water ice". *Journal of Physics: Conference Series*. Vol. 6. IOP Publishing, 211.
Qasim, D., Fedoseev, G., Chuang, K. J., et al., 2020, Nature Astronomy, 4, 781
Sellgren, K., Werner, M. W., Ingalls, J. G., et al., 2010, ApJL, 722, L54
Snyder, L. E., Lovas, F. J., Mehringer, D. M., et al., 2002, ApJ, 578, 245
Terwisscha van Scheltinga, J, Ligterink, N., Boogert, A., et al., 2018, A&A, 611, A35
Watanabe, N. and Kouchi, A., 2002, ApJL, 571, L173
Zhang, X. K., Lewars, E. G., March, R. E., et al., 1993, J. Phys. Chem., 97, 4320
Zou, L. and Weaver, S. L. W., 2017, ApJ, 849, 139

Appendix A
IR spectra and apparent band strengths

This section presents the IR spectra of the selected vibrational modes of acetone (Table 3.2) in pure and mixed ices (upper panels). The peak position versus FWHM for the investigated bands in different ices is displayed in the bottom left panel of each figure. The corresponding values are listed in the Tables in Appendix B. The relative apparent band strengths (in

relation to the values for pure acetone ice at 10 K reported by Hudson et al. 2018) are displayed in the bottom right panel.

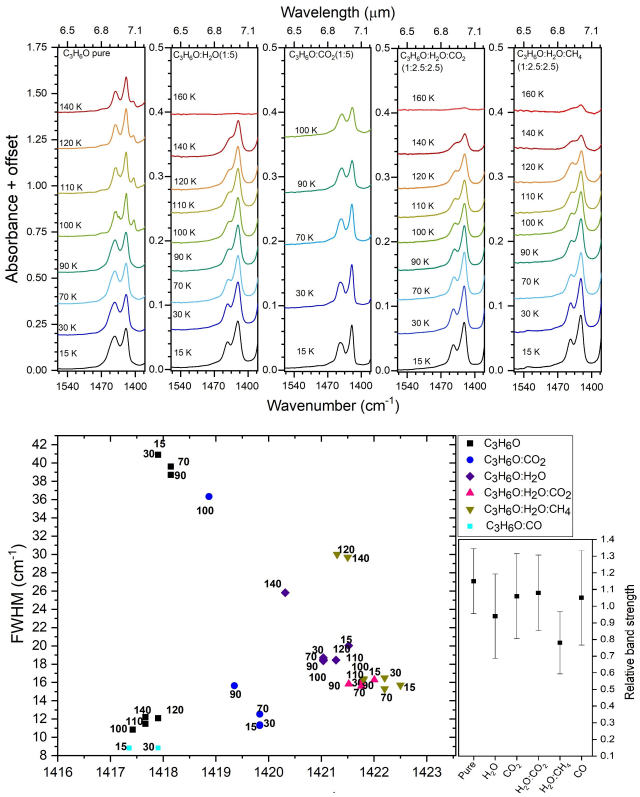

Figure 3.A.1: Upper panel: IR spectra in the 1550 - 1390 cm^{-1} (6.45 - 7.19 μm) range showing the CH_3 antisymmetric deformation band of acetone in pure and mixed ices. The spectra at different temperatures are offset for improved visualization. Bottom left: peak position vs. FWHM plot for the CH_3 antisymmetric deformation band in different ice matrices, represented by the different colors, and for different temperatures, indicated by the numbers in the graph. Bottom right: apparent band strength for the CH_3 antisymmetric deformation band at 15 K in the various matrices divided by the band strength for pure acetone from Hudson et al. (2018). **Note:** The peak position, FWHM, and relative band strength for the CH_3 antisymmetric deformation band in C_3H_6O:CO (1:5) ice are also shown. The IR profile for this mixture is shown in Figure 3.A.2.

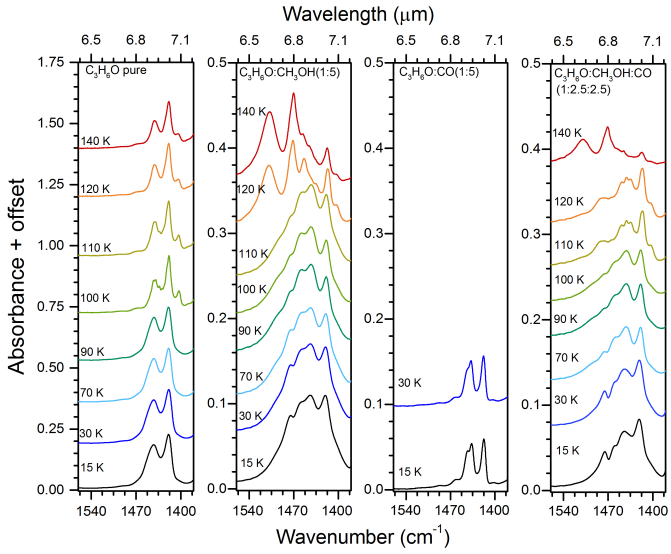

Figure 3.A.2: IR spectra in the 1550 - 1390 cm^{-1} (6.45 - 7.19 μm) range showing the CH_3 antisymmetric deformation band of acetone in pure and mixed ices. The spectra at different temperatures are offset for improved visualization. Since the FWHM of the CH_3 antisymmetric deformation band was not measured in the methanol-containing mixtures (due to the overlap with the methanol CH_3 bending mode), the peak position vs. FWHM plot for this acetone feature in CO matrix is displayed with the data in Figure 3.A.1.

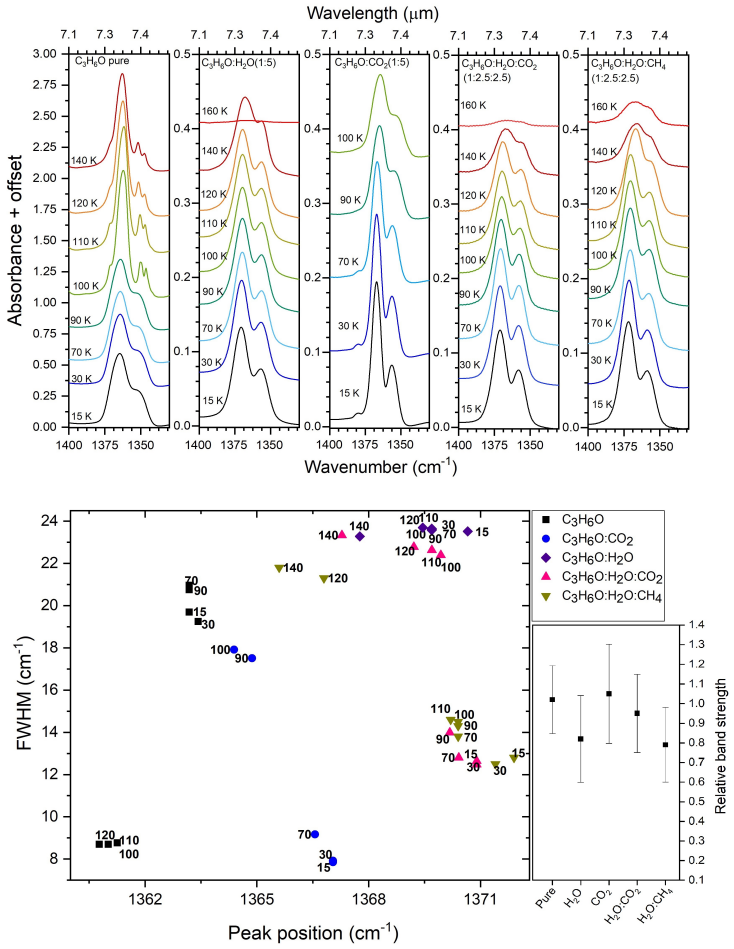

Figure 3.A.3: Upper panel: IR spectra in the 1400 - 1300 cm^{-1} (7.10 - 7.69 μm) range showing the CH_3 symmetric deformation band of acetone in pure and mixed ices. The spectra at different temperatures are offset for improved visualization. Bottom left: peak position vs. FWHM plot for the CH_3 symmetric deformation band in different ice matrices, represented by the different colors, and for different temperatures, indicated by the numbers in the graph. Bottom right: apparent band strength for the acetone CH_3 symmetric deformation band at 15 K in the various matrices divided by the band strength for pure acetone from Hudson et al. (2018).

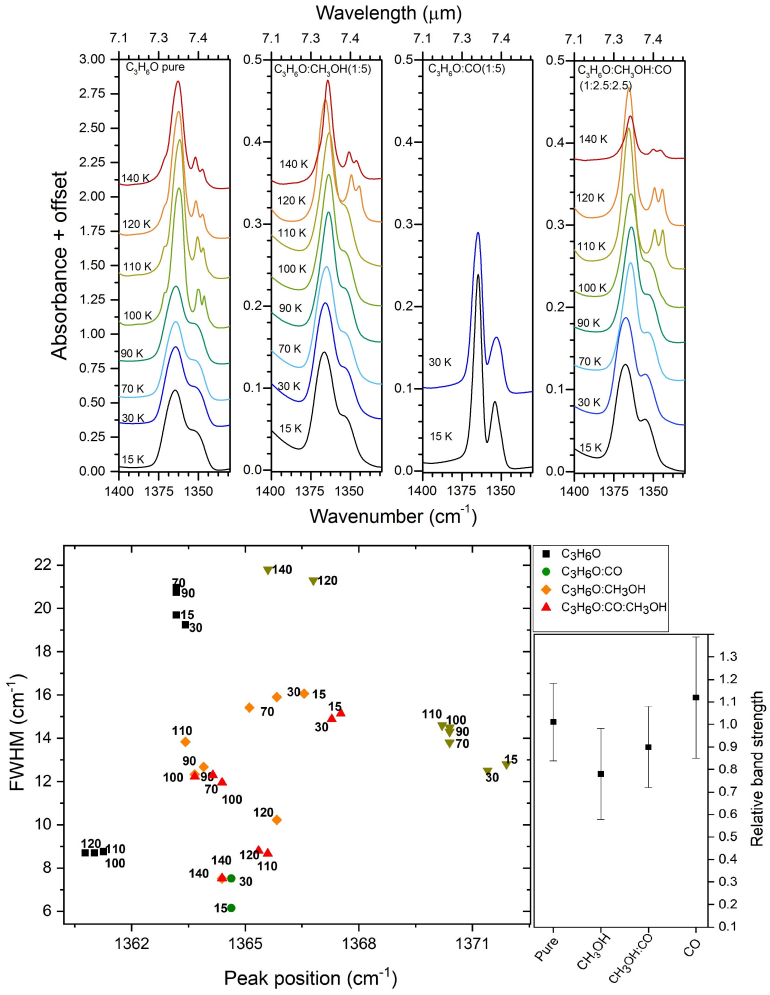

Figure 3.A.4: Upper panel: IR spectra in the 1400 - 1300 cm^{-1} (7.10 - 7.69 μm) range showing the CH_3 symmetric deformation band of acetone in pure and mixed ices. The spectra at different temperatures are offset for improved visualization. Bottom left: peak position vs. FWHM plot for the CH_3 symmetric deformation band in different ice matrices, represented by the different colors, and for different temperatures, indicated by the numbers in the graph. Bottom right: apparent band strength for the acetone CH_3 symmetric deformation band at 15 K in the various matrices divided by the band strength for pure acetone from Hudson et al. (2018).

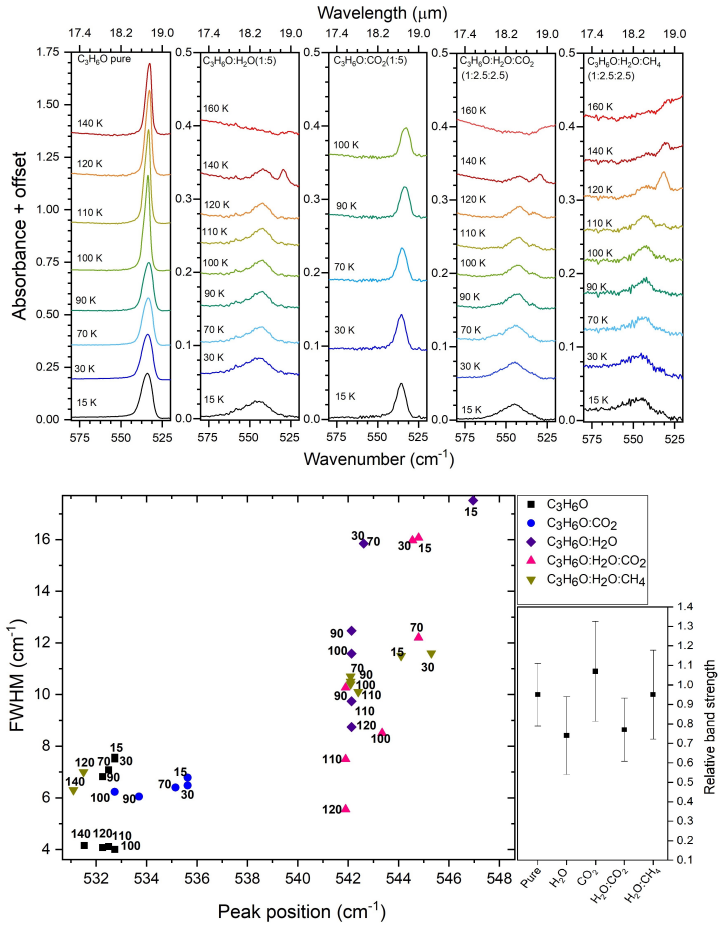

Figure 3.A.5: Upper panel: IR spectra in the 520 - 580 cm^{-1} (19.2 - 17.2 μm) range showing the CO in-plane deformation band of acetone in pure and mixed ices. The spectra at different temperatures are offset for improved visualization. Bottom left: peak position vs. FWHM plot for the CO in-plane deformation band in different ice matrices, represented by the different colors, and for different temperatures, indicated by the numbers in the graph. Bottom right: apparent band strength for the acetone CO in-plane deformation band at 15 K in the various matrices divided by the band strength for pure acetone from Hudson et al. (2018).

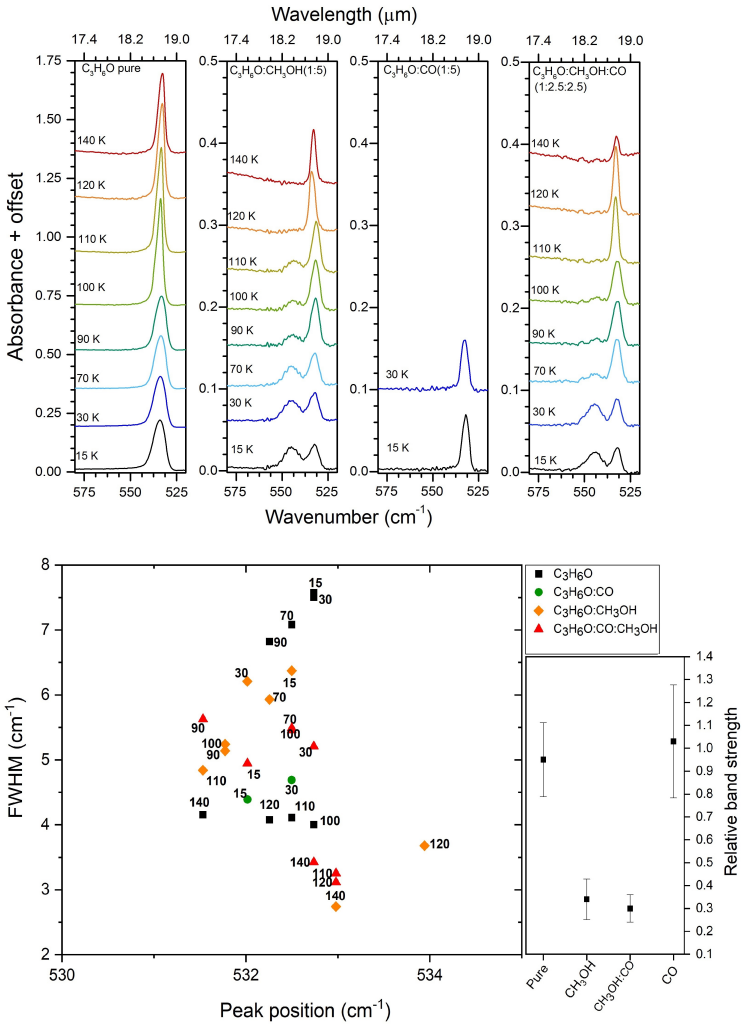

Figure 3.A.6: Upper panel: IR spectra in the 520 - 580 cm^{-1} (19.2 - 17.2 μm) range showing the CO in-plane deformation band of acetone in pure and mixed ices. The spectra at different temperatures are offset for improved visualization. Bottom left: peak position vs. FWHM plot for the CO in-plane deformation band in different ice matrices, represented by the different colors, and for different temperatures, indicated by the numbers in the graph. Bottom right: apparent band strength for the acetone CO in-plane deformation band at 15 K in the various matrices divided by the band strength for pure acetone from Hudson et al. (2018).

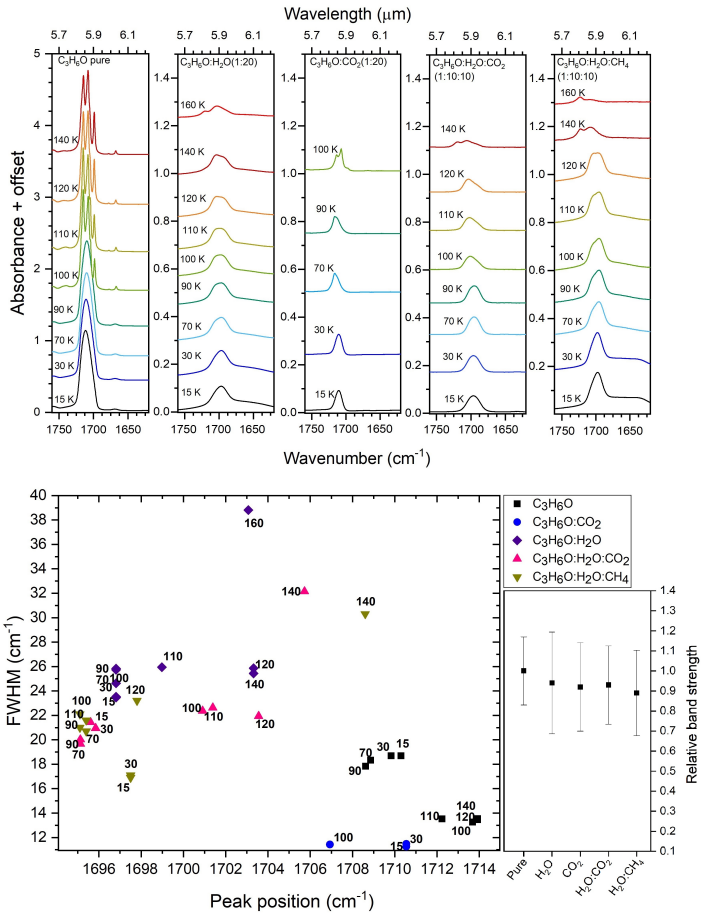

Figure 3.A.7: Upper panel: IR spectra in the 1760 - 1630 cm^{-1} (5.68 - 6.13 μm) range showing the C=O stretching band of acetone in pure and mixed ices. The spectra at different temperatures are offset for improved visualization. Bottom left: peak position vs. FWHM plot for the C=O stretching band in different ice matrices, represented by the different colors, and for different temperatures, indicated by the numbers in the graph. Bottom right: apparent band strength for the acetone C=O stretching band at 15 K in the various matrices divided by the band strength for pure acetone from Hudson et al. (2018).

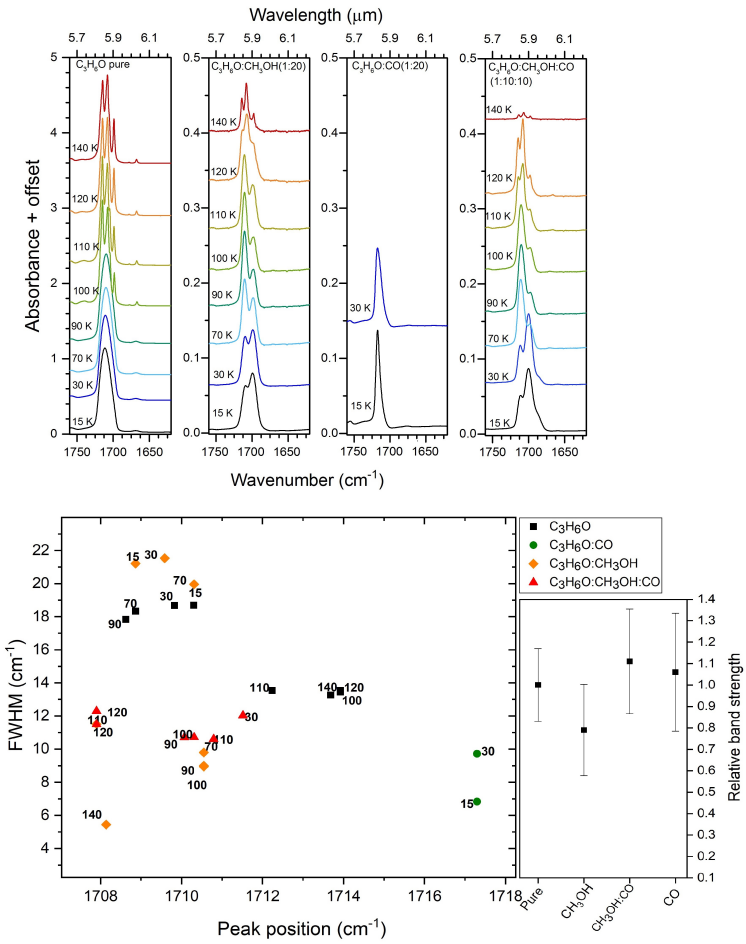

Figure 3.A.8: Upper panel: IR spectra in the 1760 - 1630 cm^{-1} (5.68 - 6.13 μm) range showing the C=O stretching band of acetone in pure and mixed ices. The spectra at different temperatures are offset for improved visualization. Bottom left: peak position vs. FWHM plot for the C=O stretching band in different ice matrices, represented by the different colors, and for different temperatures, indicated by the numbers in the graph. Bottom right: apparent band strength for the acetone C=O stretching band at 15 K in the various matrices divided by the band strength for pure acetone from Hudson et al. (2018).

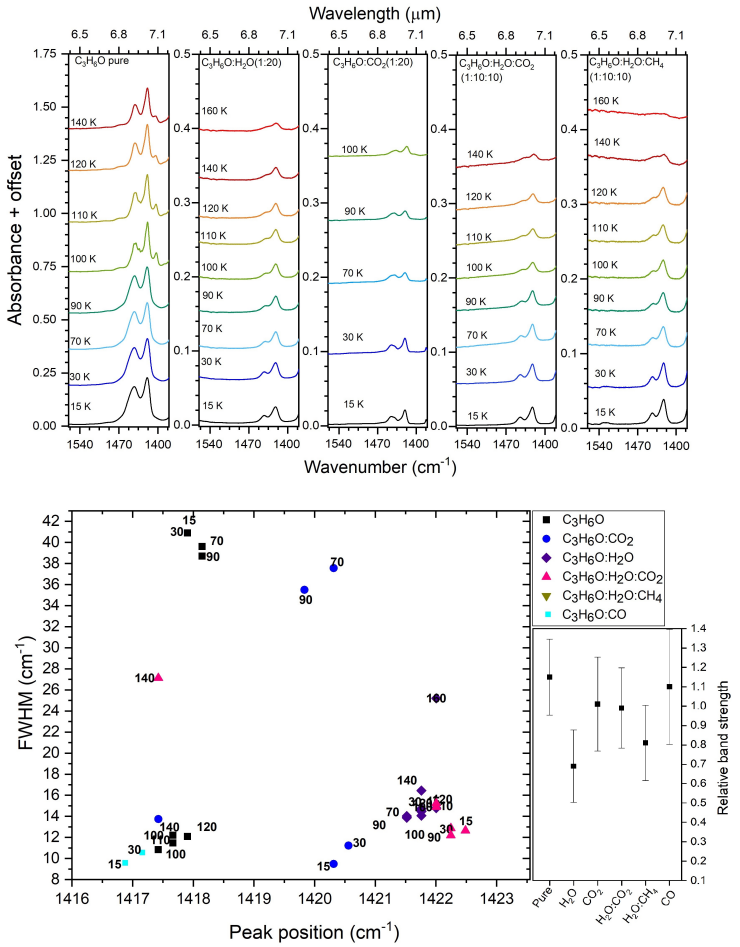

Figure 3.A.9: Upper panel: IR spectra in the 1550 - 1390 cm^{-1} (6.45 - 7.19 μm) range showing the CH_3 antisymmetric deformation band of acetone in pure and mixed ices. The spectra at different temperatures are offset for improved visualization. Bottom left: peak position vs. FWHM plot for the CH_3 antisymmetric deformation band in different ice matrices, represented by the different colors, and for different temperatures, indicated by the numbers in the graph. Bottom right: apparent band strength for the acetone CH_3 antisymmetric deformation band at 15 K in the various matrices divided by the band strength for pure acetone from Hudson et al. (2018).

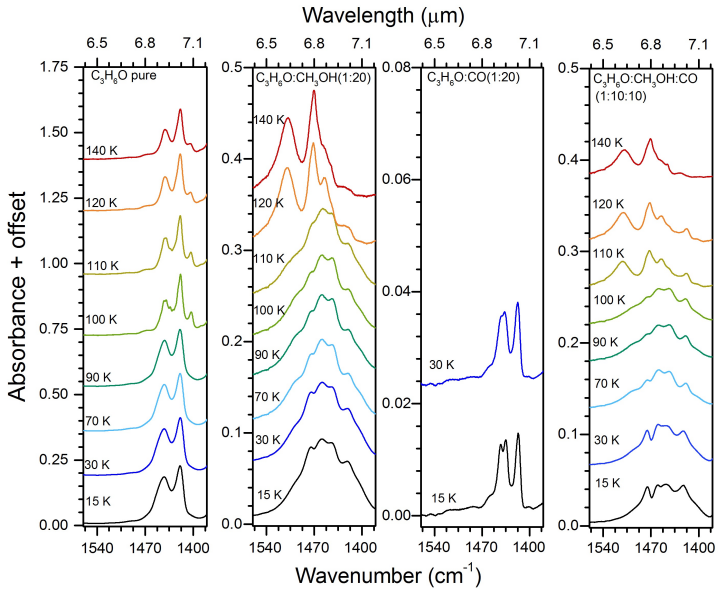

Figure 3.A.10: IR spectra in the 1550 - 1390 cm^{-1} (6.45 - 7.19 μm) range showing the CH_3 antisymmetric deformation band of acetone in pure and mixed ices. The spectra at different temperatures are offset for improved visualization. Since the FWHM of the CH_3 antisymmetric deformation band was not measured in the methanol-containing mixtures (due to the overlap with the methanol CH_3 bending mode), the peak position vs. FWHM plot for this acetone feature in CO matrix is displayed with the data in Figure 3.A.9.

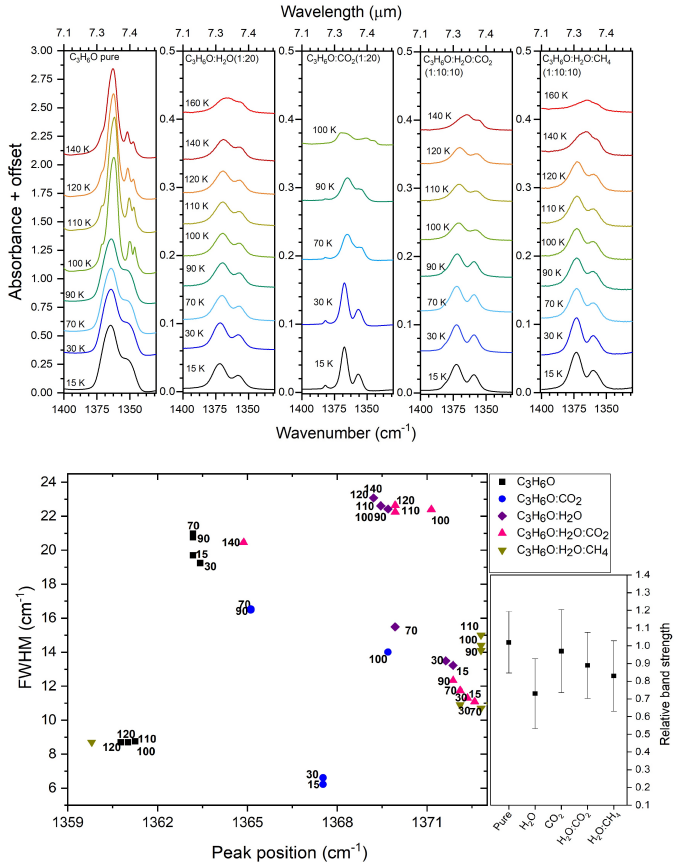

Figure 3.A.11: Upper panel: IR spectra in the 1400 - 1300 cm^{-1} (7.10 - 7.69 μm) range showing the CH_3 symmetric deformation band of acetone in pure and mixed ices. The spectra at different temperatures are offset for improved visualization. Bottom left: peak position vs. FWHM plot for the CH_3 symmetric deformation band in different ice matrices, represented by the different colors, and for different temperatures, indicated by the numbers in the graph. Bottom right: apparent band strength for the acetone CH_3 symmetric deformation band at 15 K in the various matrices divided by the band strength for pure acetone from Hudson et al. (2018).

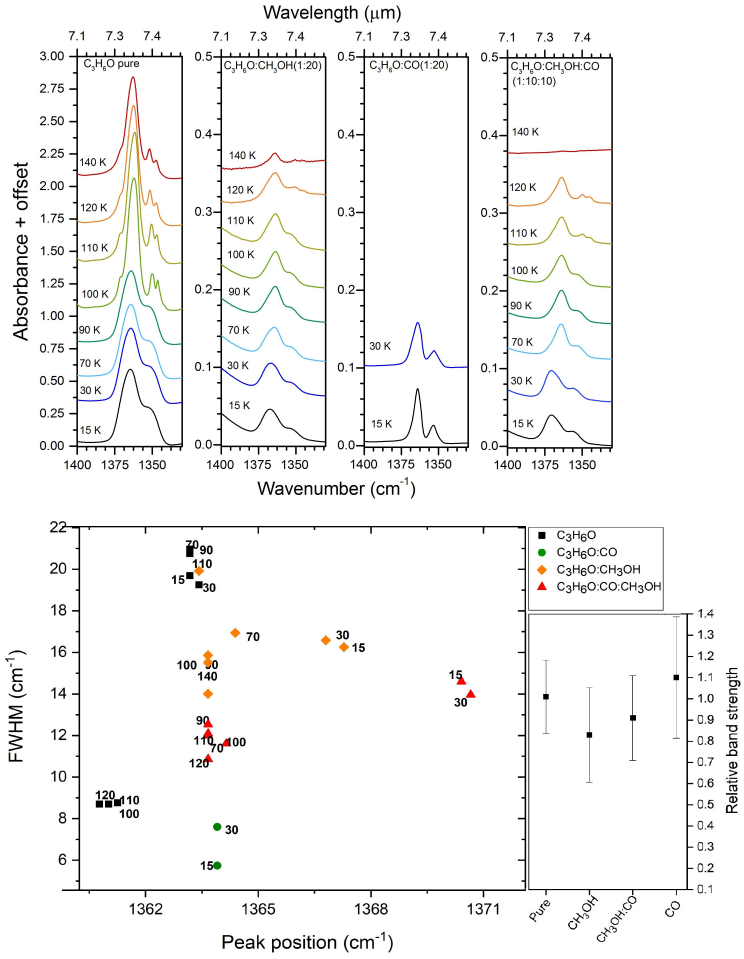

Figure 3.A.12: Upper panel: IR spectra in the 1400 - 1300 cm^{-1} (7.10 - 7.69 μm) range showing the CH_3 symmetric deformation band of acetone in pure and mixed ices. The spectra at different temperatures are offset for improved visualization. Bottom left: peak position vs. FWHM plot for the CH_3 symmetric deformation band in different ice matrices, represented by the different colors, and for different temperatures, indicated by the numbers in the graph. Bottom right: apparent band strength for the acetone CH_3 symmetric deformation band at 15 K in the various matrices divided by the band strength for pure acetone from Hudson et al. (2018).

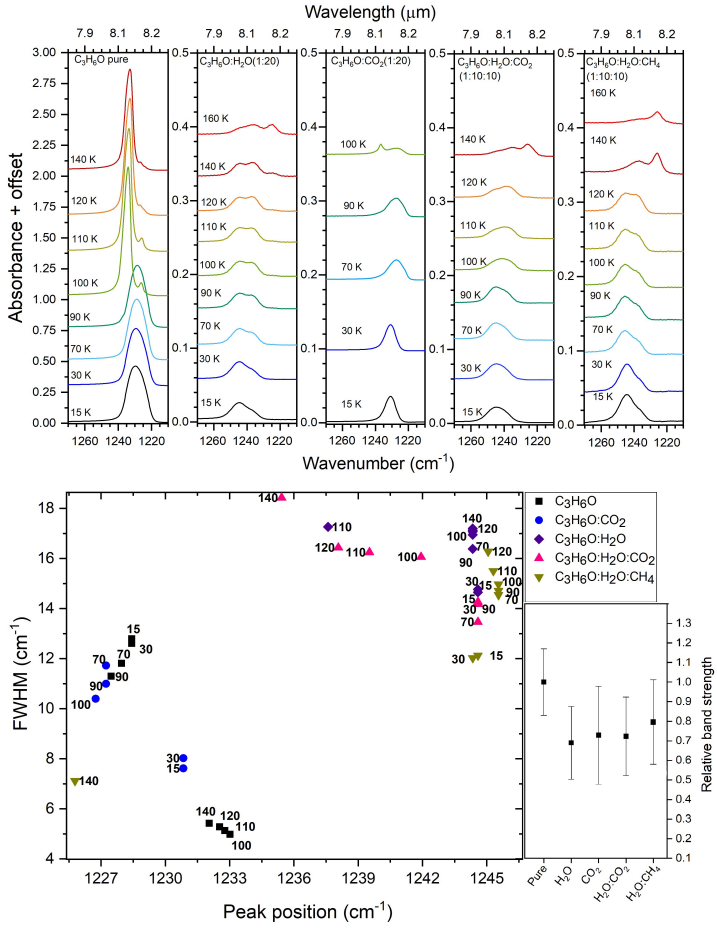

Figure 3.A.13: Upper panel: IR spectra in the 1270 - 1210 cm^{-1} (7.87 - 8.26 μm) range showing the CCC antisymmetric stretching band of acetone in pure and mixed ices. The spectra at different temperatures are offset for improved visualization. Bottom left: peak position vs. FWHM plot for the CCC antisymmetric stretching band in different ice matrices, represented by the different colors, and for different temperatures, indicated by the numbers in the graph. Bottom right: apparent band strength for the acetone CCC antisymmetric stretching band at 15 K in the various matrices divided by the band strength for pure acetone from Hudson et al. (2018).

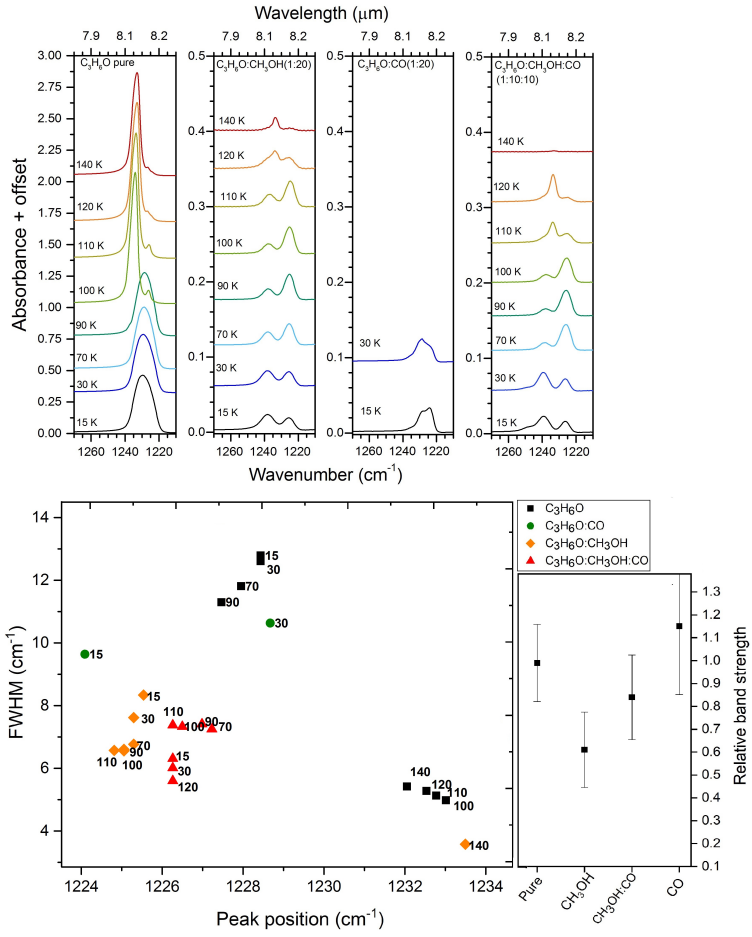

Figure 3.A.14: Upper panel: IR spectra in the 1270 - 1210 cm^{-1} (7.87 - 8.26 μm) range showing the CCC antisymmetric stretching band of acetone in pure and mixed ices. The spectra at different temperatures are offset for improved visualization. Bottom left: peak position vs. FWHM plot for the CCC antisymmetric stretching band in different ice matrices, represented by the different colors, and for different temperatures, indicated by the numbers in the graph. Bottom right: apparent band strength for the acetone CCC antisymmetric stretching band at 15 K in the various matrices divided by the band strength for pure acetone from Hudson et al. (2018).

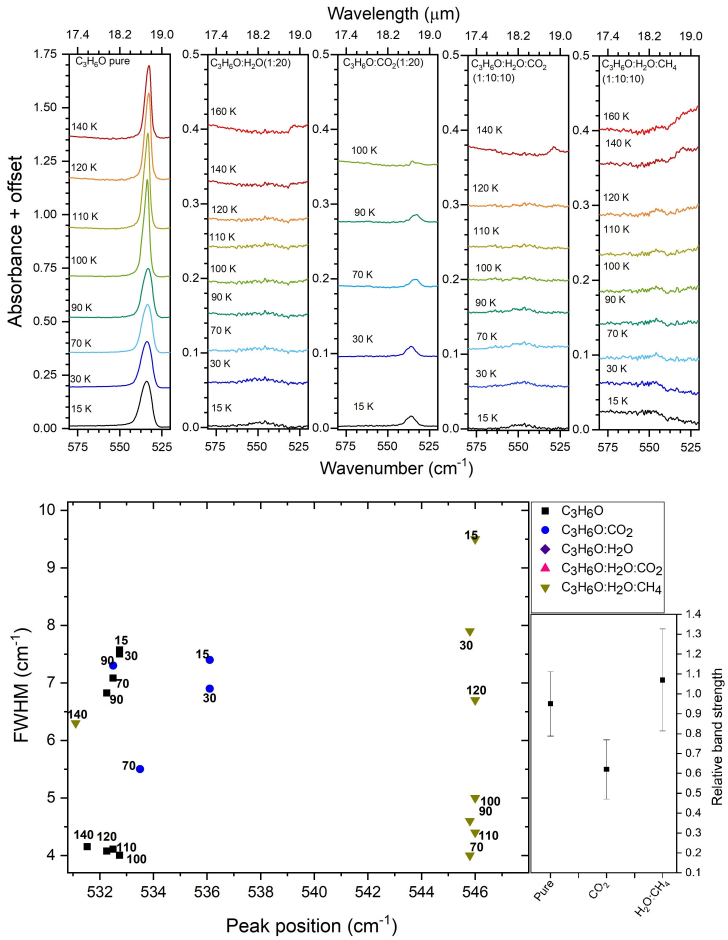

Figure 3.A.15: Upper panel: IR spectra in the 520 - 580 cm^{-1} (19.2 - 17.2 μm) range showing the CO in-plane deformation band of acetone in pure and mixed ices. The spectra at different temperatures are offset for improved visualization. Bottom left: peak position vs. FWHM plot for the CO in-plane deformation band in different ice matrices, represented by the different colors, and for different temperatures, indicated by the numbers in the graph. Bottom right: apparent band strength for the acetone CO in-plane deformation band at 15 K in the various matrices divided by the band strength for pure acetone from Hudson et al. (2018).

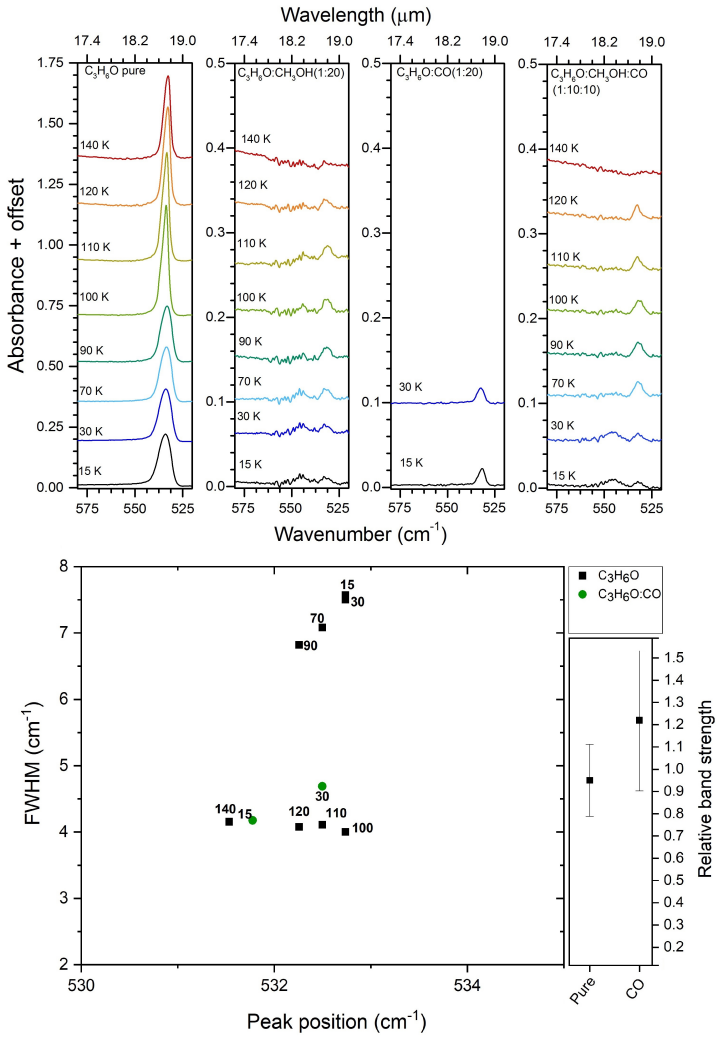

Figure 3.A.16: Upper panel: IR spectra in the 520 - 580 cm^{-1} (19.2 - 17.2 μm) range showing the CO in-plane deformation band of acetone in pure and mixed ices. The spectra at different temperatures are offset for improved visualization. Bottom left: peak position vs. FWHM plot for the CO in-plane deformation band in different ice matrices, represented by the different colors, and for different temperatures, indicated by the numbers in the graph. Bottom right: apparent band strength for the acetone CO in-plane deformation band at 15 K in the various matrices divided by the band strength for pure acetone from Hudson et al. (2018).

Appendix B

Ice band parameters

In this section, the peak position and the FWHM of the acetone bands discussed in the text and shown in Appendix A are presented in tables. The tables display the peak position for a given vibrational mode in the different ice matrices used in this work and at different temperatures, ranging from 15 K up to the matrix desorption temperature.

One asterisk (*) denotes that the FWHM is the value for a blending of two or more peaks. The general uncertainty of the peak position is about 0.5 cm^{-1} for all the measurements and the typical error of the FWHM values amounts to 0.8 cm^{-1}.

Table 3.B.1: Peak position and FWHM of the acetone CO-stretch mode for pure acetone and mixtures with acetone ratio 1:5 and for temperatures ranging from 15 K up to 140 K.

Mixture	T (K)	Peak position (cm^{-1})	Peak position (μm)	FWHM (cm^{-1})	FWHM (μm)
CH_3COCH_3	15	1710.3	5.847	18.7	0.0640
CH_3COCH_3:CO		1715.9	5.828	8.5	0.0289
CH_3COCH_3:CO_2		1710.8	5.845	12.9	0.0440
CH_3COCH_3:H_2O		1700.2	5.882	27.8	0.0965
CH_3COCH_3:CH_3OH		1699.5	5.884	-	-
		1708.9	5.851	23.8	0.0819*
CH_3COCH_3:H_2O:CO_2		1699.9	5.882	22.4	0.0776
CH_3COCH_3:H_2O:CH_4		1701.6	5.877	22.0	0.076
CH_3COCH_3:CH_3OH:CO		1700.4	5.881	-	-
		1710.3	5.847	23.7	0.0815*
CH_3COCH_3	30	1709.8	5.848	18.7	0.064
CH_3COCH_3:CO		1715.4	5.829	10.7	0.0364
CH_3COCH_3:CO_2		1710.8	5.845	12.7	0.0433
CH_3COCH_3:H_2O		1701.1	5.878	27.7	0.0959
CH_3COCH_3:CH_3OH		1698.7	5.887	-	-
		1709.0	5.851	23.3	0.080*
CH_3COCH_3:H_2O:CO_2		1699.7	5.883	21.9	0.0759
CH_3COCH_3:H_2O:CH_4		1701.4	5.877	21.5	0.074
CH_3COCH_3:CH_3OH:CO		1699.9	5.882	-	-
		1710.6	5.846	23.1	0.0794*
CH_3COCH_3	70	1708.9	5.852	18.3	0.0628
CH_3COCH_3:CO_2		1710.8	5.845	12.8	0.0439
CH_3COCH_3:H_2O		1701.1	5.878	26.7	0.092
CH_3COCH_3:CH_3OH		1698.5	5.887	-	-
		1709.6	5.849	22.5	0.0776*
CH_3COCH_3:H_2O:CO_2		1699.5	5.884	20.5	0.0709*
CH_3COCH_3:H_2O:CH_4		1702.3	5.874	21.4	0.074
CH_3COCH_3:CH_3OH:CO		1710.3	5.847	14.2	0.0486
CH_3COCH_3	90	1708.6	5.853	17.8	0.0611
CH_3COCH_3:CO_2		1712.0	5.841	14.7	0.0503
CH_3COCH_3:H_2O		1701.6	5.877	26.0	0.0901
CH_3COCH_3:CH_3OH		1710.1	5.848	12.3	0.0422*
CH_3COCH_3:H_2O:CO_2		1700.4	5.881	20.0	0.0692
CH_3COCH_3:H_2O:CH_4		1702.8	5.873	20.4	0.07O
CH_3COCH_3:CH_3OH:CO		1709.6	5.849	14.4	0.0493
CH_3COCH_3	100	1697.5	5.891	-	-
		1706.7	5.859	-	-
		1713.9	5.835	13.5	0.0463*
CH_3COCH_3:CO_2		1712.2	5.840	15.5	0.0532
CH_3COCH_3:H_2O		1701.9	5.876	25.6	0.0888
CH_3COCH_3:CH_3OH		1710.1	5.848	12.3	0.0422
CH_3COCH_3:H_2O:CO_2		1701.4	5.877	20.0	0.0691
CH_3COCH_3:H_2O:CH_4		1703.3	5.871	19.8	0.068
CH_3COCH_3:CH_3OH:CO		1709.3	5.850	14.1	0.0482
CH_3COCH_3	110	1697.8	5.890	-	-
		1706.9	5.858	-	-
		1713.9	5.835	13.5	0.0463*

Table 3.B.1: (continued).

CH_3COCH_3:CO_2		-	-	-	-
CH_3COCH_3:H_2O		1702.1	5.875	25.0	0.0868
CH_3COCH_3:CH_3OH		1710.1	5.847	13.0	0.0442
CH_3COCH_3:H_2O:CO_2		1701.6	5.877	20.0	0.0689
CH_3COCH_3:H_2O:CH_4		1703.3	5.871	19.4	0.067
CH_3COCH_3:CH_3OH:CO		1706.9	5.858	11.3	0.0387
		1714.2	5.834	-	-
CH_3COCH_3	120	1698.0	5.889	-	-
		1706.9	5.858	-	-
		1713.9	5.835	13.5	0.0460*
CH_3COCH_3:H_2O		1702.1	5.875	24.3	0.0843*
CH_3COCH_3:CH_3OH		1706.0	5.862	12.8	0.0439*
		1713.7	5.835	5.7	0.0196
CH_3COCH_3:H_2O:CO_2		1702.1	5.875	20.2	0.0698
CH_3COCH_3:H_2O:CH_4		1709.8	5.849	22.8	0.078
CH_3COCH_3:CH_3OH:CO		1706.9	5.859	-	-
		1714.2	5.834	11.2	0.0384
CH_3COCH_3	140	1698.0	5.889	-	-
		1706.9	5.858	-	-
		1713.7	5.835	13.3	0.0453*
CH_3COCH_3:H_2O		1703.8	5.869	21.7	0.0749*
CH_3COCH_3:CH_3OH		1698.0	5.889	-	-
		1707.4	5.857	5.9	0.0202*
		1714.2	5.834	11.8	0.0402*
CH_3COCH_3:H_2O:CO_2		1703.6	5.870	21.1	0.0724
CH_3COCH_3:H_2O:CH_4		1707.4	5.857	23.5	0.081
CH_3COCH_3:CH_3OH:CO		1707.9	5.855	-	-
		1714.2	5.834	5.7	0.0196

Table 3.B.2: Peak position and FWHM of the acetone CH_3 asymmetric deformation mode for pure acetone and mixtures with acetone ratio 1:5 and for temperatures ranging from 15 K up to 140 K.

Mixture	T	Peak position		FWHM	
	(K)	(cm^{-1})	(μm)	(cm^{-1})	(μm)
CH_3COCH_3	15	1417.9	7.0527	40.9	0.199*
		1441.0	6.9394	-	-
CH_3COCH_3:CO		1417.4	7.0551	8.7	0.0434
		1436.7	6.9604	15.1	0.0776*
CH_3COCH_3:CO_2		1419.8	7.0431	11.4	0.0563
		1444.2	6.9243	-	-
CH_3COCH_3:H_2O		1421.5	7.0347	20.0	0.100*
		1442.7	6.9313	-	-
CH_3COCH_3:H_2O:CO_2		1422.0	7.0323	16.3	0.0804
		1444.4	6.9232	-	-
CH_3COCH_3:H_2O:CH_4		1422.5	7.0299	15.7	0.078
		1443.0	6.930	14.2	0.0682
CH_3COCH_3	30	1417.9	7.0527	40.9	0.199*
		1441.3	6.9382	-	-
CH_3COCH_3:CO		1417.9	7.0527	8.7	0.0433
		1437.7	6.9557	14.2	0.0740
CH_3COCH_3:CO_2		1419.8	7.0431	11.3	0.0559
		1443.9	6.9255	-	-
CH_3COCH_3:H_2O		1421.0	7.0371	18.7	0.0923
		1441.3	6.9382	-	-
CH_3COCH_3:H_2O:CO_2		1421.8	7.0335	16.1	0.0792*
		1444.2	6.9243	-	-
CH_3COCH_3:H_2O:CH_4		1422.2	7.0314	15.3	0.076
		1442.7	6.9315	14.3	
CH_3COCH_3	70	1418.1	7.0515	39.6	0.193*
		1441.0	6.9394	-	-
CH_3COCH_3:CO_2		1419.8	7.0431	12.5	0.0621
		1441.8	6.9359	-	-
CH_3COCH_3:H_2O		1421.0	7.0371	18.7	0.0923
		1441.3	6.9382	-	-
CH_3COCH_3:H_2O:CO_2		1421.8	7.0335	15.6	0.0770*
		1442.3	6.9336	-	-
CH_3COCH_3:H_2O:CH_4		1422.2	7.0314	16.5	0.082
		1442.5	6.9324	14.3	0.0706
CH_3COCH_3	90	1418.1	7.0515	38.7	0.189*
		1440.8	6.9406	-	-
CH_3COCH_3:CO_2		1419.4	7.0455	15.6	0.0774
		1440.6	6.9417	-	-
CH_3COCH_3:H_2O		1421.0	7.0371	18.5	0.0911
		1439.5	6.9469	-	-

CH_3COCH_3:H_2O:CO_2		1421.5	7.0347	15.8	0.0781*
		1442.0	6.9348	-	-
CH_3COCH_3:H_2O:CH_4		1421.8	7.0333	16.3	0.081
		1441.3	6.9381	14.4	0.0693
CH_3COCH_3		1401.8	7.1339	-	-
		1417.4	7.0551	10.8	0.0538
	100	1438.4	6.9522	-	-
CH_3COCH_3:CO_2		1418.9	7.0479	36.3	0.177*
		1440.1	6.9440	-	-
CH_3COCH_3:H_2O		1421.0	7.0371	18.4	0.0906
		1439.1	6.9486	-	-
CH_3COCH_3:H_2O:CO_2		1420.8	7.0383	-	-
		1440.1	6.9440	17.2	0.0849*
CH_3COCH_3:H_2O:CH_4		1421.8	7.0333	16.4	0.081
		1441.3	6.9382	14.2	0.0683
CH_3COCH_3		1402.2	7.1315	-	-
		1417.7	7.0539	11.5	0.0569
	110	1439.0	6.9495	-	-
CH_3COCH_3:H_2O		1421.3	7.0359	18.5	0.0910
		1440.0	6.9445	-	-
CH_3COCH_3:H_2O:CO_2		1420.8	7.0383	-	-
		1440.1	6.9440	18.8	0.0925*
CH_3COCH_3:H_2O:CH_4		1421.8	7.0333	16.4	0.081
		1441.3	6.9382	14.4	0.0693
CH_3COCH_3		1402.5	7.1302	-	-
		1417.9	7.0527	12.1	0.0599
	120	1438.6	6.9510	-	-
CH_3COCH_3:H_2O		1421.0	7.0371	18.5	0.0913
		1439.5	6.9466	-	-
CH_3COCH_3:H_2O:CO_2		1420.6	7.0395	-	-
		1439.8	6.9452	19.7	0.0971*
CH_3COCH_3:H_2O:CH_4		1421.3	7.0358	30.0	0.149
		1439.6	6.9463	18.0	0.0868
CH_3COCH_3		1404.9	7.1180	-	-
		1417.7	7.0539	12.2	0.0607
	140	1439.8	6.9452	-	-
CH_3COCH_3:H_2O		1420.3	7.0407	25.8	0.127
CH_3COCH_3:H_2O:CO_2		1420.3	7.0407	-	-
		1431.2	6.9873	29.4	0.144*
CH_3COCH_3:H_2O:CH_4		1421.5	7.0348	29.7	0.147

Table 3.B.3: Peak position and FWHM of the acetone CH_3 symmetric deformation mode for pure acetone and mixtures with acetone ratio 1:5 and for temperatures ranging from 15 K up to 140 K.

Mixture	T	Peak position		FWHM	
	(K)	(cm^{-1})	(μm)	(cm^{-1})	(μm)
CH_3COCH_3		1363.4	7.3345	19.2	0.0640
CH_3COCH_3:CO		1354.0	7.3854	7.7	0.0420
		1364.6	7.3280	6.2	0.0330
CH_3COCH_3:CO_2	15	1356.4	7.3723	-	-
		1367.0	7.3151	7.8	0.0420
CH_3COCH_3:H_2O		1356.9	7.3696	-	-
		1370.7	7.2958	23.5	0.127*
CH_3COCH_3:CH_3OH		1366.6	7.3176	16.1	0.0861
CH_3COCH_3:H_2O:CO_2		1358.1	7.3631	-	-
		1370.9	7.2945	12.6	0.0640
CH_3COCH_3:H_2O:CH_4		1358.8	7.3594	10.6	0.0574
		1371.9	7.2892	12.8	0.0680
CH_3COCH_3:CH_3OH:CO		1355.2	7.3788	-	-
		1367.5	7.3125	15.1	0.0810
CH_3COCH_3		1363.2	7.3358	19.7	0.106
CH_3COCH_3:CO		1353.1	7.3907	-	-
		1364.6	7.3280	7.5	0.0404
CH_3COCH_3:CO_2	30	1356.2	7.3736	-	-
		1367.0	7.3151	7.9	0.0424
CH_3COCH_3:H_2O		1356.4	7.3723	-	-
		1369.7	7.3009	23.6	0.127*
CH_3COCH_3:CH_3OH		1365.8	7.3215	15.9	0.0853
CH_3COCH_3:H_2O:CO_2		1358.1	7.3631	-	-
		1370.9	7.2945	12.5	0.0664
CH_3COCH_3:H_2O:CH_4		1358.8	7.3594	10.6	0.0574
		1371.4	7.2918	12.5	0.0664
CH_3COCH_3:CH_3OH:CO		1355.0	7.3801	-	-
		1367.3	7.3138	14.9	0.0796
CH_3COCH_3		1363.2	7.3358	20.8	0.112
CH_3COCH_3:CO_2		1356.0	7.3749	-	-
	70				

		1366.6	7.3176	9.2	0.0491
CH_3COCH_3:H_2O		1356.4	7.3723	-	-
		1369.7	7.3009	23.6	0.127*
CH_3COCH_3:CH_3OH		1365.1	7.3254	15.4	0.0827
CH_3COCH_3:H_2O:CO_2		1357.9	7.3644	-	-
		1370.4	7.2970	12.8	0.0682
CH_3COCH_3:H_2O:CH_4		1357.4	7.367	10.4	0.0564
		1370.4	7.2971	13.8	0.0735
CH_3COCH_3:CH_3OH:CO		1353.8	7.3867	-	-
		1364.4	7.3293	12.0	0.0642
CH_3COCH_3		1363.2	7.3358	21.0	0.113
CH_3COCH_3:CO_2		1364.9	7.3267	17.5	0.0944*
CH_3COCH_3:H_2O	90	1356.4	7.3723	-	-
		1369.7	7.3009	23.6	0.127*
CH_3COCH_3:CH_3OH		1363.9	7.3319	12.7	0.0681
CH_3COCH_3:H_2O:CO_2		1357.6	7.3657	-	-
		1370.2	7.2983	14.0	0.0746
CH_3COCH_3:H_2O:CH_4		1357.4	7.367	10.4	0.0564
		1370.4	7.2971	14.3	0.0761
CH_3COCH_3:CH_3OH:CO		1353.7	7.3869	-	-
		1363.7	7.3332	12.2	0.0657
CH_3COCH_3		1345.3	7.4330	7.7	0.0424*
		1349.2	7.4118	-	-
	100	1361.3	7.3462	8.8	0.0472
CH_3COCH_3:CO_2		1364.4	7.3293	17.9	0.0966*
CH_3COCH_3:H_2O		1356.4	7.3723	-	-
		1369.7	7.3009	23.6	0.127*
CH_3COCH_3:CH_3OH		1363.7	7.3332	12.3	0.0662
CH_3COCH_3:H_2O:CO_2		1356.9	7.3696	-	-
		1369.9	7.2996	22.4	0.120*
CH_3COCH_3:H_2O:CH_4		1357.4	7.367	10.3	0.0559
		1370.4	7.2971	14.5	0.0772
CH_3COCH_3:CH_3OH:CO		1364.1	7.3306	12.3	0.0661
CH_3COCH_3		1345.6	7.4317	7.5	0.0413*
		1349.2	7.4118	-	-
		1361.0	7.3475	8.7	0.0471
CH_3COCH_3:H_2O	110	1356.4	7.3723	-	-
		1369.7	7.3009	23.6	0.127*
CH_3COCH_3:CH_3OH		1363.4	7.3345	13.8	0.0745
CH_3COCH_3:H_2O:CO_2		1356.7	7.3710	-	-
		1369.7	7.3009	22.6	0.1215*
CH_3COCH_3:H_2O:CH_4		1357.4	7.367	10.2	0.0553
		1370.2	7.2982	14.6	0.0777
CH_3COCH_3:CH_3OH:CO		1344.1	7.4397	-	-
		1349.0	7.4131	-	-
		1365.6	7.3228	8.7	0.047
CH_3COCH_3		1346.1	7.4290	7.3	0.0404*
		1349.4	7.4105	-	-
		1360.8	7.3488	8.7	0.0470
CH_3COCH_3:H_2O	120	1356.4	7.3723		-
		1369.5	7.3022	23.7	0.127*
CH_3COCH_3:CH_3OH		1344.4	7.4384	-	-
		1349.2	7.4118	-	-
		1365.8	7.3215	10.2	0.0548
CH_3COCH_3:H_2O:CO_2		1356.7	7.3710	-	-
		1369.2	7.3035	22.8	0.122*
CH_3COCH_3:H_2O:CH_4		1366.8	7.3163	21.3	0.1140
CH_3COCH_3:CH_3OH:CO		1344.1	7.4397	-	-
		1349.2	7.4118	-	-
		1365.4	7.3241	8.8	0.0472
CH_3COCH_3		1346.6	7.4264	-	-
		1350.9	7.4025	-	-
		1361.7	7.3436	9.3	0.0499
CH_3COCH_3:H_2O	140	1356.4	7.3723	-	-
		1367.8	7.3112	23.3	0.125*
CH_3COCH_3:CH_3OH		1346.1	7.4290	-	-
		1350.9	7.4025	-	-
		1364.4	7.3293	7.5	0.0404
CH_3COCH_3:H_2O:CO_2		1356.7	7.3710	-	-
		1367.3	7.3138	23.3	0.125*
CH_3COCH_3:H_2O:CH_4		1365.6	7.3228	21.8	0.1169
CH_3COCH_3:CH_3OH:CO		1345.6	7.4317	-	-
		1349.9	7.4078	-	-
		1364.4	7.3293	7.5	0.0404

3.4. Appendix B

Table 3.B.4: Peak position and FWHM of the acetone CCC asymmetric stretch mode for pure acetone and mixtures with acetone ratio 1:5 and for temperatures ranging from 15 K up to 140 K.

Mixture	T	Peak position		FWHM	
	(K)	(cm^{-1})	(μm)	(cm^{-1})	(μm)
CH_3COCH_3		1228.4	8.1404	12.8	0.0640
CH_3COCH_3:CO		1228.2	8.1420	9.5	0.0630
CH_3COCH_3:CO_2	15	1230.6	8.1261	9.4	0.0620
CH_3COCH_3:H_2O		1242.9	8.0457	17.3	0.112
CH_3COCH_3:CH_3OH		1226.0	8.1565	21.5	0.142*
		1238.1	8.0770	-	-
CH_3COCH_3:H_2O:CO_2		1240.5	8.0614	16.1	0.105
CH_3COCH_3:H_2O:CH_4		1242.4	8.0489	16.3	0.1056
CH_3COCH_3:CH_3OH:CO		1226.5	8.1532	7.8	0.052
		1238.6	8.0739	10.2	0.0662
CH_3COCH_3		1228.4	8.1404	12.6	0.0836
CH_3COCH_3:CO		1229.9	8.1309	9.4	0.0624
CH_3COCH_3:CO_2	30	1230.6	8.1261	9.2	0.0606
CH_3COCH_3:H_2O		1239.5	8.0676	17.0	0.110
CH_3COCH_3:CH_3OH		1226.0	8.1565	21.4	0.141*
		1238.3	8.0755	-	-
CH_3COCH_3:H_2O:CO_2		1240.5	8.0614	15.7	0.102
CH_3COCH_3:H_2O:CH_4		1241.2	8.0567	16.2	0.1051
CH_3COCH_3:CH_3OH:CO		1226.7	8.1516	7.6	0.0506
		1238.8	8.0723	9.1	0.0594
CH_3COCH_3		1228.0	8.1436	11.8	0.0784
CH_3COCH_3:CO_2		1230.4	8.1277	9.4	0.0620
CH_3COCH_3:H_2O	70	1239.5	8.0676	17.0	0.110*
CH_3COCH_3:CH_3OH		1226.0	8.1565	-	-
		1238.3	8.0755	21.6	0.142
CH_3COCH_3:H_2O:CO_2		1240.0	8.0645	14.8	0.0960
CH_3COCH_3:H_2O:CH_4		1239.0	8.071	14.7	0.0958
CH_3COCH_3:CH_3OH:CO		1226.5	8.1532	8.7	0.0577
		1238.6	8.0739		-
CH_3COCH_3		1227.5	8.1468	11.3	0.0750
CH_3COCH_3:CO_2		1228.9	8.1373	10.5	0.0697
CH_3COCH_3:H_2O	90	1239.3	8.0692	16.7	0.108
CH_3COCH_3:CH_3OH		1225.8	8.1581	7.9	0.0528
		1237.8	8.0786	-	-
CH_3COCH_3:H_2O:CO_2		1239.0	8.0708	14.1	0.0918
CH_3COCH_3:H_2O:CH_4		1238.8	8.0723	13.6	0.0886
CH_3COCH_3:CH_3OH:CO		1226.3	8.1548	9.0	0.0598
		1237.8	8.0786	-	-
CH_3COCH_3		1233.0	8.1102	5.0	0.0327
CH_3COCH_3:CO_2		1228.7	8.1389	11.0	0.0728
CH_3COCH_3:H_2O	100	1239.0	8.0708	16.5	0.107
CH_3COCH_3:CH_3OH		1225.5	8.1597	8.0	0.0532
		1237.6	8.0802	-	-
CH_3COCH_3:H_2O:CO_2		1238.6	8.0739	13.5	0.0876
CH_3COCH_3:H_2O:CH_4		1238.8	8.0723	12.9	0.0840
CH_3COCH_3:CH_3OH:CO		1226.0	8.1565	8.9	0.0593
		1235.2	8.0960	-	-
CH_3COCH_3		1232.8	8.1118	5.1	0.0337
CH_3COCH_3:H_2O		1238.8	8.0723	16.2	0.105
CH_3COCH_3:CH_3OH	110	1225.4	8.1606	7.7	0.0516
		1237.1	8.0833	-	-
CH_3COCH_3:H_2O:CO_2		1238.3	8.0755	12.8	0.0835
CH_3COCH_3:H_2O:CH_4		1239.0	8.071	12.4	0.0808
CH_3COCH_3:CH_3OH:CO		1224.6	8.1661	21.8	0.143
CH_3COCH_3		1232.5	8.1134	5.3	0.0347
CH_3COCH_3:H_2O		1238.8	8.0723	16.1	0.104
CH_3COCH_3:CH_3OH	120	1224.6	8.1661	-	-
		1234.9	8.0975	4.5	0.0294
CH_3COCH_3:H_2O:CO_2		1238.1	8.0770	12.4	0.0808
CH_3COCH_3:H_2O:CH_4		1238.2	8.0762	20.35	
CH_3COCH_3:CH_3OH:CO		1224.6	8.1661	23.9	0.157
CH_3COCH_3		1232.0	8.1166	5.4	0.0357
CH_3COCH_3:H_2O		1226.3	8.1548	-	-
	140	1247.9	8.0132	25.2	0.165*
CH_3COCH_3:CH_3OH		1233.7	8.1055	3.6	0.0238
CH_3COCH_3:H_2O:CO_2		1224.8	8.1645	-	-
		1236.1	8.0896	21.7	0.143*
CH_3COCH_3:H_2O:CH_4		1238.0	8.077	19.5	0.1272
CH_3COCH_3:CH_3OH:CO		1233.3	8.1086	3.8	0.0252

Table 3.B.5: Peak position and FWHM of the acetone CO in-plane deformation mode for pure acetone and mixtures with acetone ratio 1:5 and for temperatures ranging from 15 K up to 140 K.

Mixture	T	Peak position		FWHM	
	(K)	(cm^{-1})	(μm)	(cm^{-1})	(μm)
CH_3COCH_3	15	532.7	18.77	7.6	0.266
CH_3COCH_3:CO		532.0	18.79	4.4	0.155
CH_3COCH_3:CO_2		535.6	18.67	6.8	0.236
CH_3COCH_3:H_2O		547.0	18.28	17.5	0.588
CH_3COCH_3:CH_3OH		532.5	18.78	6.4	0.224
CH_3COCH_3:H_2O:CO_2		544.8	18.36	16.1	0.539
CH_3COCH_3:H_2O:CH_4		544.1	18.38	11.5	0.388
CH_3COCH_3:CH_3OH:CO		532.0	18.80	4.9	0.174
CH_3COCH_3	30	532.7	18.77	7.5	0.264
CH_3COCH_3:CO		532.5	18.78	4.7	0.165
CH_3COCH_3:CO_2		535.6	18.67	6.5	0.226
CH_3COCH_3:H_2O		542.6	18.43	15.8	0.533
CH_3COCH_3:CH_3OH		532.0	18.80	6.2	0.219
CH_3COCH_3:H_2O:CO_2		544.6	18.36	16.0	0.536
CH_3COCH_3:H_2O:CH_4		545.3	18.78	11.6	0.3901
CH_3COCH_3:CH_3OH:CO		532.7	18.77	5.2	0.184
CH_3COCH_3	70	532.5	18.78	7.1	0.249
CH_3COCH_3:CO_2		535.1	18.69	6.4	0.228
CH_3COCH_3:H_2O		542.6	18.43	15.8	0.533
CH_3COCH_3:CH_3OH		532.3	18.79	5.9	0.209
CH_3COCH_3:H_2O:CO_2		544.8	18.36	12.2	0.411
CH_3COCH_3:H_2O:CH_4		542.1	18.45	10.7	0.3641
CH_3COCH_3:CH_3OH:CO		532.5	18.78	5.5	0.192
CH_3COCH_3	90	532.3	18.79	6.8	0.240
CH_3COCH_3:CO_2		533.7	18.74	6.0	0.213
CH_3COCH_3:H_2O		542.1	18.44	12.5	0.422
CH_3COCH_3:CH_3OH		531.8	18.81	5.2	0.185
CH_3COCH_3:H_2O:CO_2		541.9	18.45	10.3	0.347
CH_3COCH_3:H_2O:CH_4		542.1	18.45	10.4	0.3539
CH_3COCH_3:CH_3OH:CO		531.5	18.81	5.6	0.198
CH_3COCH_3	100	532.7	18.77	4.0	0.141
CH_3COCH_3:CO_2		532.7	18.77	6.2	0.219
CH_3COCH_3:H_2O		542.1	18.44	11.6	0.392
CH_3COCH_3:CH_3OH		531.8	18.81	5.1	0.181
CH_3COCH_3:H_2O:CO_2		543.3	18.40	8.5	0.289
CH_3COCH_3:H_2O:CH_4		542.1	18.45	10.5	0.3573
CH_3COCH_3:CH_3OH:CO		532.5	18.78	5.5	0.194
CH_3COCH_3	110	532.5	18.78	4.1	0.141
CH_3COCH_3:H_2O		542.1	18.44	9.7	0.330
CH_3COCH_3:CH_3OH		531.5	18.81	4.8	0.171
CH_3COCH_3:H_2O:CO_2		541.9	18.45	7.5	0.254
CH_3COCH_3:H_2O:CH_4		542.4	18.44	10.1	0.3433
CH_3COCH_3:CH_3OH:CO		533.0	18.76	3.3	0.114
CH_3COCH_3	120	532.3	18.79	4.1	0.143
CH_3COCH_3:H_2O		542.1	18.44	8.7	0.296
CH_3COCH_3:CH_3OH		533.9	18.73	3.7	0.129
CH_3COCH_3:H_2O:CO_2		541.9	18.45	5.6	0.189
CH_3COCH_3:H_2O:CH_4		531.5	18.81	7.0	0.2478
CH_3COCH_3:CH_3OH:CO		533.0	18.76	3.1	0.110
CH_3COCH_3	140	531.5	18.81	4.2	0.147
CH_3COCH_3:H_2O		541.9	18.45	-	-
		529.6	18.88	-	-
CH_3COCH_3:CH_3OH		533.0	18.76	2.7	0.097
CH_3COCH_3:H_2O:CO_2		-	-	-	-
CH_3COCH_3:H_2O:CH_4		531.1	18.83	6.3	0.2233
CH_3COCH_3:CH_3OH:CO		532.7	18.77	3.4	0.129

Table 3.B.6: Peak position and FWHM of the acetone CO stretch mode for pure acetone and mixtures with acetone ratio 1:20 and for temperatures ranging from 15 K up to 140 K.

Mixture	T	Peak position		FWHM unit	
	(K)	(cm^{-1})	(μm)	(cm^{-1})	(μm)
CH_3COCH_3	15	1710.3	5.8469	18.7	0.0640
CH_3COCH_3:CO		1717.3	5.8231	6.8	0.0232
CH_3COCH_3:CO_2		1710.6	5.8461	11.5	0.0392
CH_3COCH_3:H_2O		1696.8	5.8934	23.5	0.0813
CH_3COCH_3:CH_3OH		1699.5	5.8842	-	-
		1708.9	5.8518	21.2	0.0731*

CH_3COCH_3:H_2O:CO_2		1695.6	5.8976	21.4	0.0745
CH_3COCH_3:H_2O:CH_4		1697.5	5.9810	17.1	0.0593
CH_3COCH_3:CH_3OH:CO		1700.2	5.8817	20.4	0.0704*
		1711.1	5.8444	-	-
CH_3COCH_3		1709.8	5.8485	18.7	0.0640
CH_3COCH_3:CO		1717.3	5.8231	9.7	0.0330
CH_3COCH_3:CO_2	30	1710.6	5.8461	11.3	0.0384
CH_3COCH_3:H_2O		1696.8	5.8934	23.5	0.0816
CH_3COCH_3:CH_3OH		1699.0	5.8859	-	-
		1709.6	5.8494	21.5	0.0742*
CH_3COCH_3:H_2O:CO_2		1695.8	5.8968	21.0	0.0728
CH_3COCH_3:H_2O:CH_4		1697.5	5.8910	16.9	0.0586
CH_3COCH_3:CH_3OH:CO		1699.9	5.8825	-	-
		1711.5	5.8428	12.0	0.0416
CH_3COCH_3		1708.9	5.8518	18.3	0.0628
CH_3COCH_3:CO_2		1716.6	5.8255	11.3	0.0384
CH_3COCH_3:H_2O	70	1696.8	5.8934	24.6	0.0853*
CH_3COCH_3:CH_3OH		1698.5	5.8876		-
		1710.3	5.8469	20.0	0.0680*
CH_3COCH_3:H_2O:CO_2		1695.1	5.8993	19.7	0.0684
CH_3COCH_3:H_2O:CH_4		1695.4	5.8983	20.7	0.0720
CH_3COCH_3:CH_3OH:CO		1698.3	5.8884	-	-
		1710.8	5.8452	10.6	0.0362
CH_3COCH_3		1708.6	5.8527	17.8	0.0611
CH_3COCH_3:CO_2		1716.3	5.8264	12.4	0.0422
CH_3COCH_3:H_2O	90	1696.8	5.8934	25.7	0.0891
CH_3COCH_3:CH_3OH		1698.0	5.8892	-	-
		1710.6	5.8461	9.0	0.0308
CH_3COCH_3:H_2O:CO_2		1695.1	5.8993	20.0	0.0697
CH_3COCH_3:H_2O:CH_4		1695.1	5.8994	21.0	0.0731
CH_3COCH_3:CH_3OH:CO		1697.5	5.8909	-	-
		1710.1	5.8477	10.7	0.0367
CH_3COCH_3		1697.5	5.8909	-	-
		1706.7	5.8593	-	-
		1713.9	5.8346	13.5	0.0463*
CH_3COCH_3:CO_2	100	1706.9	5.8585	11.4	0.0391*
		1713.7	5.8354	-	-
CH_3COCH_3:H_2O		1696.8	5.8934	25.8	0.0895*
CH_3COCH_3:CH_3OH		1698.0	5.8892	-	-
		1710.6	5.8461	9.0	0.0306*
CH_3COCH_3:H_2O:CO_2		1700.9	5.8792	22.4	0.0775
CH_3COCH_3:H_2O:CH_4		1695.4	5.8983	21.6	0.0751
CH_3COCH_3:CH_3OH:CO		1698.0	5.8892	-	-
		1710.3	5.8469	10.7	0.0367
CH_3COCH_3		1697.8	5.8901	-	-
		1706.9	5.8585	-	-
		1713.9	5.8346	13.5	0.0463*
CH_3COCH_3:H_2O	110	1699.0	5.8859	25.9	0.0898
CH_3COCH_3:CH_3OH		1699.2	5.8851	-	-
		1710.6	5.8461	9.8	0.0335
CH_3COCH_3:H_2O:CO_2		1701.4	5.8775	22.6	0.0783
CH_3COCH_3:H_2O:CH_4		1695.1	5.8994	22.1	0.0769
CH_3COCH_3:CH_3OH:CO		1698.3	5.8884	-	-
		1707.9	5.8551	12.3	0.0420*
		1714.2	5.8337	-	-
CH_3COCH_3		1698.0	5.8892	-	-
		1706.9	5.8585	-	-
		1713.9	5.8346	13.5	0.0460*
CH_3COCH_3:H_2O	120	1703.3	5.8709	25.9	0.0895
CH_3COCH_3:CH_3OH		1707.4	5.8568	19.5	0.0669
CH_3COCH_3:H_2O:CO_2		1703.6	5.8701	21.9	0.0759
CH_3COCH_3:H_2O:CH_4		1697.8	5.8900	23.2	0.0805
CH_3COCH_3:CH_3OH:CO		1698.0	5.8892	-	-
		1707.9	5.8551	11.5	0.0393*
		1714.4	5.8329	-	-
CH_3COCH_3		1698.0	5.8892	-	-
		1706.9	5.8585	-	-
		1713.7	5.8354	13.3	0.0453*
CH_3COCH_3:H_2O	140	1703.3	5.8709	25.4	0.0880
CH_3COCH_3:CH_3OH		1697.8	5.8901	-	-
		1708.1	5.8543	5.4	0.0187
		1714.2	5.8337	-	-
CH_3COCH_3:H_2O:CO_2		1705.7	5.8626	32.1	0.110
CH_3COCH_3:H_2O:CH_4		1708.6	5.8527	30.3	0.1038
CH_3COCH_3:CH_3OH:CO		-	-	-	-

Table 3.B.7: Peak position and FWHM of the acetone CH_3 asymmetric deformation mode for pure acetone and mixtures with acetone ratio 1:20 and for temperatures ranging from 15 K up to 140 K.

Mixture	T	Peak position		FWHM	
	(K)	(cm^{-1})	(μm)	(cm^{-1})	(μm)
CH_3COCH_3	15	1417.9	7.0527	40.9	0.199*
		1441.0	6.9394	-	-
CH_3COCH_3:CO		1416.9	7.0575	9.5	0.0475
		1435.0	6.9685	17.3	0.0885*
		1443.7	6.9267	-	-
CH_3COCH_3:CO_2		1420.3	7.0407	9.5	0.0469
		1445.4	6.9186	-	-
CH_3COCH_3:H_2O		1422.0	7.0323	14.8	0.0730
		1445.3	6.9192	-	-
CH_3COCH_3:H_2O :CO_2		1422.5	7.0299	12.7	0.0624
		1444.4	6.9232	-	-
CH_3COCH_3:H_2O:CH_4		1422.7	7.0289	12.1	0.0593
		1443.0	6.929	-	-
CH_3COCH_3	30	1417.9	7.0527	40.9	0.199*
		1441.3	6.9382	-	-
CH_3COCH_3:CO		1417.4	7.0551	10.6	0.0527
		1436.7	6.9604	17.1	0.0912
CH_3COCH_3:CO_2		1420.6	7.0395	11.2	0.0556
		1444.9	6.9209	-	-
CH_3COCH_3:H_2O		1421.8	7.0335	14.5	0.0716
		1442.0	6.9348	-	-
CH_3COCH_3:H_2O :CO_2		1422.2	7.0311	12.9	0.0635
		1444.4	6.9232	-	-
CH_3COCH_3:H_2O:CH_4		1422.7	7.0289	12.0	0.0593
		1443.2	6.929	-	-
CH_3COCH_3	70	1418.1	7.0515	39.6	0.193*
		1441.0	6.9394	-	-
CH_3COCH_3:CO_2		1420.3	7.0407	37.5	0.183*
		1439.4	6.9475	-	-
CH_3COCH_3:H_2O		1421.5	7.0347	14.0	0.0693
		1439.9	6.9450	-	-
CH_3COCH_3:H_2O :CO_2		1422.2	7.0311	-	-
		1442.3	6.9336	12.2	0.0601
CH_3COCH_3:H_2O:CH_4		1423.2	7.0264	13.8	0.0681
		1441.2	6.9387	-	-
CH_3COCH_3	90	1418.1	7.0515	38.7	0.189*
		1440.8	6.9406	-	-
CH_3COCH_3:CO_2		1419.8	7.0431	35.5	0.173*
		1439.6	6.9464	-	-
CH_3COCH_3:H_2O		1421.5	7.0347	13.9	0.0685
		1439.5	6.9467	-	-
CH_3COCH_3:H_2O :CO_2		1422.2	7.0311	12.2	0.0602
		1441.0	6.9359	-	-
CH_3COCH_3:H_2O:CH_4		1423.4	7.0254	13.9	0.0686
		1443.0	6.93	-	-
CH_3COCH_3	100	1401.8	7.1339	-	-
		1417.4	7.0551	10.8	0.0538
CH_3COCH_3:CO_2		1417.4	7.0551	13.7	0.0682
		1437.2	6.9580	-	-
CH_3COCH_3:H_2O		1421.8	7.0335	14.1	0.0695
CH_3COCH_3:H_2O :CO_2		1422.0	7.0323	14.9	0.0735
		1439.6	6.9464	-	-
CH_3COCH_3:H_2O:CH_4		1423.4	7.0254	14.0	0.0691
		1441.0	6.9396	-	-
CH_3COCH_3	110	1402.2	7.1315	-	-
		1417.7	7.0539	11.5	0.0569
		1438.6	6.9510	-	-
CH_3COCH_3:H_2O		1421.8	7.0335	14.7	0.0727
CH_3COCH_3:H_2O :CO_2		1422.0	7.0323	-	-
		1439.6	6.9464	14.8	0.0731
CH_3COCH_3:H_2O:CH_4		1423.4	7.0254	14.5	0.0716
		1441.0	6.9396	-	-
CH_3COCH_3	120	1402.5	7.1302	-	-
-		1417.9	7.0527	12.1	0.0599
CH_3COCH_3:H_2O		1421.8	7.0335	14.5	0.0715
CH_3COCH_3:H_2O :CO_2		1422.0	7.0323	15.2	0.0752
		1437	6.9557	-	-
CH_3COCH_3:H_2O:CH_4		1423.4	7.0254	14.1	0.0696
		1438.9	6.9498	-	-
CH_3COCH_3	140	1404.9	7.1180	-	-
		1417.7	7.0539	12.2	0.0607
		1439.8	6.9452	-	-
CH_3COCH_3:H_2O		1421.8	7.0335	16.4	0.0812

CH_3COCH_3:H_2O:CO_2		1417.4	7.0551	27.1	0.133*
		1437.5	6.9566	-	-
CH_3COCH_3:H_2O:CH_4		1421.3	7.0358	29.5	0.1460
		1438.6	6.9512	-	-
CH_3COCH_3	160	-	-	-	-
CH_3COCH_3:H_2O		1422.0	7.0323	25.2	0.124
CH_3COCH_3:H_2O :CO_2		-	-	-	-

Table 3.B.8: Peak position and FWHM of the acetone CH_3 symmetric deformation mode for pure acetone and mixtures with acetone ratio 1:20 and for temperatures ranging from 15 K up to 160 K.

Mixture	T (K)	Peak position		FWHM	
		cm^{-1})	μm	cm^{-1}	μm
CH_3COCH_3	19	1363.4	7.3345	19.2	0.0640
CH_3COCH_3:CO		1353.3	7.3893	6.1	0.0332
		1363.9	7.3319	5.7	0.0308
CH_3COCH_3:CO_2		1356.9	7.3696	6.6	0.0358
		1367.5	7.3125	6.2	0.0333
CH_3COCH_3:H_2O		1358.1	7.3631	-	-
		1371.9	7.2894	13.2	0.180
CH_3COCH_3:CH_3OH		1367.3	7.3138	16.3	0.0870*
CH_3COCH_3:H_2O:CO_2		1359.3	7.3566	-	-
		1372.6	7.2855	11.1	0.0588
CH_3COCH_3:H_2O:CH_4		1359.8	7.354	10.7	0.0579
		1373.1	7.2828	10.9	0.0578
CH_3COCH_3:CH_3OH:CO		1356.7	7.3710	-	-
		1370.4	7.2971	14.6	0.0779
CH_3COCH_3	30	1363.2	7.3358	19.7	0.106
CH_3COCH_3:CO		1352.8	7.3920	8.1	0.0408
		1363.9	7.3319	7.6	0.0440
CH_3COCH_3:CO_2		1356.7	7.3710	-	-
		1367.5	7.3125	6.6	0.0353
CH_3COCH_3:H_2O		1358.1	7.3631	-	-
		1371.6	7.2906	13.5	0.0717
CH_3COCH_3:CH_3OH		1366.8	7.3164	16.6	0.0888
CH_3COCH_3:H_2O:CO_2		1359.1	7.3579	-	-
		1372.3	7.2868	11.3	0.0600
CH_3COCH_3:H_2O:CH_4		1360.3	7.3513	10.5	0.0567
		1372.8	7.2843	10.7	0.0568
CH_3COCH_3:CH_3OH:CO		1356.4	7.3723	-	-
		1370.7	7.2958	14.0	0.0745
CH_3COCH_3	70	1363.2	7.3358	20.8	0.112
CH_3COCH_3:CO_2		1365.1	7.3254	16.5	0.0888
CH_3COCH_3:H_2O		1357.2	7.3683	-	-
		1369.9	7.2996	15.5	0.0826
CH_3COCH_3:CH_3OH		1364.4	7.3293	16.9	0.0909
CH_3COCH_3:H_2O:CO_2		1359.1	7.3579	-	-
		1372.1	7.2881	11.7	0.0623
CH_3COCH_3:H_2O:CH_4		1359.6	7.3551	10.5	0.0568
		1372.8	7.284	13.3	0.0706
CH_3COCH_3:CH_3OH:CO		1354.3	7.3841	-	-
		1364.1	7.3306	11.6	0.0623
CH_3COCH_3	90	1363.2	7.3358	21.0	0.113
CH_3COCH_3:CO_2		1365.1	7.3254	16.5	0.0892
CH_3COCH_3:H_2O		1356.9	7.3696	-	-
		1369.7	7.3009	22.4	0.120*
CH_3COCH_3:CH_3OH		1363.7	7.3332	15.9	0.0852
CH_3COCH_3:H_2O:CO_2		1359.1	7.3579	-	-
		1371.9	7.2894	12.3	0.0656
CH_3COCH_3:H_2O:CH_4		1359.8	7.354	10.3	0.0557
		1372.8	7.284	14.1	0.0748
CH_3COCH_3:CH_3OH:CO		1354.3	7.3841	-	-
		1363.7	7.3332	12.0	0.0644
CH_3COCH_3	100	1345.3	7.4330	7.7	0.0424*
		1349.2	7.4118	-	-
		1361.3	7.3462	8.8	0.0472
CH_3COCH_3:CO_2		1351.1	7.4012	-	-
		1369.7	7.3009	14.0	0.0750
CH_3COCH_3:H_2O		1356.9	7.3696	-	-
		1369.7	7.3009	22.5	0.120
CH_3COCH_3:CH_3OH		1363.7	7.3332	15.5	0.0834*
CH_3COCH_3:H_2O:CO_2		1358.4	7.3618	-	-
		1371.1	7.2932	22.4	0.1200
CH_3COCH_3:H_2O:CH_4		1360.3	7.351	10.3	0.0556
		1372.8	7.284	14.4	0.0764
CH_3COCH_3:CH_3OH:CO		1354.5	7.3831	-	-

		1363.7	7.3332	12.5	0.0674
CH_3COCH_3		1345.6	7.4317	7.5	0.0413*
		1349.2	7.4118	-	-
		1361.0	7.3475	8.7	0.0471
CH_3COCH_3:H_2O	110	1356.9	7.3696	-	-
		1369.5	7.3022	22.6	0.121*
CH_3COCH_3:CH_3OH		1363.4	7.3345	19.9	0.107
CH_3COCH_3:H_2O:CO_2		1358.1	7.3631	-	-
		1369.9	7.2996	22.2	0.119*
CH_3COCH_3:H_2O:CH_4		1359.8	7.354	9.5	0.0514
		1372.8	7.284	15.0	0.0796
CH_3COCH_3:CH_3OH:CO		1349.9	7.4078	-	-
		1363.7	7.3332	12.1	0.0650
CH_3COCH_3		1346.1	7.4290	7.3	0.0404*
		1349.4	7.4105	-	-
		1360.8	7.3488	8.7	0.0470
CH_3COCH_3:H_2O	120	1356.7	7.3710	-	-
		1369.5	7.3022	22.6	0.121*
CH_3COCH_3:CH_3OH		1363.7	7.3332	24.6	0.133*
CH_3COCH_3:H_2O:CO_2		1356.9	7.3696	-	-
		1369.9	7.2996	22.6	0.121*
CH_3COCH_3:H_2O:CH_4		1372.6	7.285	15.6	0.0828
		1359.8	7.354	8.7	0.0470
CH_3COCH_3:CH_3OH:CO		1345.1	7.4344	-	-
		1349.7	7.4091	-	-
		1363.7	7.3332	10.9	0.0583
CH_3COCH_3		1346.6	7.4264	-	-
		1350.9	7.4025	-	-
		1361.7	7.3436	9.3	0.0499
CH_3COCH_3:H_2O	140	1356.7	7.3710	-	-
		1369.2	7.3035	23.1	0.124*
CH_3COCH_3:CH_3OH		1363.7	7.3332	14.0	0.0753
CH_3COCH_3:H_2O:CO_2		1356.4	7.3723	-	-
		1364.9	7.3267	20.5	0.110*
CH_3COCH_3:H_2O:CH_4		1366.1	7.320	-	
CH_3COCH_3:CH_3OH:CO		-	-	-	-
CH_3COCH_3		-	-	-	-
CH_3COCH_3:H_2O		1357.5	7.3666	-	-
	160	1367.0	7.3151	23.3	0.125
CH_3COCH_3:CH_3OH		-	-	-	-
CH_3COCH_3:H_2O:CO_2		-	-	-	-
CH_3COCH_3:H_2O:CH_4			-	-	-
CH_3COCH_3:CH_3OH:CO		-	-	-	-

Table 3.B.9: Peak position and FWHM of the acetone CCC asymmetric stretch mode for pure acetone and mixtures with acetone ratio 1:20 and for temperatures ranging from 15 K up to 160 K.

Mixture	T	Peak position		FWHM	
	(K)	(cm^{-1})	(μm)	(cm^{-1})	(μm)
CH_3COCH_3		1228.4	8.1404	12.8	0.0640
CH_3COCH_3:CO		1224.1	8.1693	9.6	0.0641*
	15	1231.3	8.1216	-	-
CH_3COCH_3:CO_2		1230.8	8.1245	7.6	0.0502
CH_3COCH_3:H_2O		1244.6	8.0348	14.6	0.0947
CH_3COCH_3:CH_3OH		1225.5	8.1597	8.3	0.0554
		1238.1	8.0770	9.7	0.0635
CH_3COCH_3:H_2O:CO_2		1244.6	8.0348	14.2	0.0919
CH_3COCH_3:H_2O:CH_4		1244.6	8.035	12.1	0.0781
CH_3COCH_3:CH_3OH:CO		1226.3	8.1548	6.3	0.0419
		1239.3	8.0692	9.0	0.0588
CH_3COCH_3		1228.4	8.1404	12.6	0.0836
CH_3COCH_3:CO		1228.7	8.1389	10.6	0.0706
CH_3COCH_3:CO_2	30	1230.8	8.1245	8.0	0.0529
CH_3COCH_3:H_2O		1244.6	8.0348	14.8	0.0956
CH_3COCH_3:CH_3OH		1225.3	8.1613	7.6	0.0507
		1238.3	8.075	9.2	0.06
CH_3COCH_3:H_2O:CO_2		1244.6	8.035	14.2	0.092
CH_3COCH_3:H_2O:CH_4		1244.3	8.037	12.0	0.0775
CH_3COCH_3:CH_3OH:CO		1226.3	8.1548	6.0	0.0400
		1239.5	8.0676	7.7	0.0500
CH_3COCH_3		1228.0	8.14	11.8	0.078
CH_3COCH_3:CO_2		1227.2	8.1484	11.7	0.0778
CH_3COCH_3:H_2O	70	1244.3	8.0364	16.4	0.1062
CH_3COCH_3:CH_3OH		1225.3	8.1613	6.8	0.0450
		1238.1	8.0770	8.1	0.0527

CH_3COCH_3:H_2O:CO_2		1244.6	8.0348	13.5	0.0870
CH_3COCH_3:H_2O:CH_4		1245.5	8.029	14.5	0.0935
CH_3COCH_3:CH_3OH:CO		1227.2	8.1484	7.2	0.0478
		1239.5	8.0677	8.43	0.048
CH_3COCH_3		1227.5	8.1468	11.3	0.0750
CH_3COCH_3:CO_2		1227.2	8.1484	11.0	0.0729
CH_3COCH_3:H_2O	90	1237.7	8.0793	-	-
		1244.3	8.0364	17.0	0.1100
CH_3COCH_3:CH_3OH		1225.1	8.1629	6.6	0.0440
		1238.1	8.0770	8.0	0.0521
CH_3COCH_3:H_2O:CO_2		1244.6	8.0348	14.3	0.0923
CH_3COCH_3:H_2O:CH_4		1245.5	8.029	14.7	0.0948
CH_3COCH_3:CH_3OH:CO		1227.0	8.1499	7.4	0.0491
		1239.0	8.0710	7.4	0.049
CH_3COCH_3		1233.0	8.1102	5.0	0.0327
CH_3COCH_3:CO_2		1226.7	8.1516	-	-
	100	1236.9	8.0849	4.3	0.0282
CH_3COCH_3:H_2O		1237.2	8.0827	-	-
		1244.3	8.0364	17.1	0.111
CH_3COCH_3:CH_3OH		1225.1	8.1629	6.6	0.0437
		1237.8	8.0786	8.0	0.0524
CH_3COCH_3:H_2O:CO_2		1241.9	8.0520	16.1	0.1042
CH_3COCH_3:H_2O:CH_4		1245.5	8.029	15.0	
CH_3COCH_3:CH_3OH:CO		1226.5	8.1533	7.3	0.0490
		1239.0	8.0710	8.9	0.0579
CH_3COCH_3		1232.8	8.1118	5.1	0.0337
CH_3COCH_3:H_2O		1237.6	8.0803	-	-
	110	1237.6	8.0802	17.3	0.112
CH_3COCH_3:CH_3OH		1224.8	8.1645	6.6	0.0438
		1236.6	8.0865	9.0	0.0591
CH_3COCH_3:H_2O:CO_2		1239.5	8.0676	16.3	0.105
CH_3COCH_3:H_2O:CH_4		1245.3	8.030	15.5	
CH_3COCH_3:CH_3OH:CO		1226.3	8.1549	7.4	0.0492
		1234.9	8.0978	5.3	0.0352
CH_3COCH_3		1232.5	8.1134	5.3	0.0347
CH_3COCH_3:H_2O		1237.4	8.0818	-	-
	120	1244.3	8.0364	17.1	0.111
CH_3COCH_3:CH_3OH		1225.3	8.1613	19.3	0.127*
		1233.7	8.1055	-	-
CH_3COCH_3:H_2O:CO_2		1238.1	8.0770	16.4	0.107
CH_3COCH_3:H_2O:CH_4		1245.1	8.031	16.3	
CH_3COCH_3:CH_3OH:CO		1226.3	8.1548	5.6	0.0372
		1234.7	8.0991	4.5	0.0297
CH_3COCH_3		1232.0	8.1166	5.4	0.0357
CH_3COCH_3:H_2O		1237.4	8.0818	-	-
	140	1244.3	8.0364	17.2	0.112
CH_3COCH_3:CH_3OH		1233.5	8.1070	3.6	0.0235
CH_3COCH_3:H_2O:CO_2		-	-	-	-
		-	-	-	-
CH_3COCH_3:H_2O:CH_4		1225.8	8.158	7.1	0.0472
CH_3COCH_3		-	-	-	-
CH_3COCH_3:H_2O	160	1224.6	8.1661	-	-
		1235.7	8.0928	24.9	0.163

Table 3.B.10: Peak position and FWHM of the acetone CO in-plane deformation mode for pure acetone and mixtures with acetone ratio 1:20 and for temperatures ranging from 15 K up to 120 K. For higher temperatures this band is not visible.

Mixture	T	Peak position		FWHM	
	(K)	(cm^{-1})	(μm)	(cm^{-1})	(μm)
CH_3COCH_3		532.7	18.77	7.6	0.266
CH_3COCH_3:CO		531.8	18.80	4.2	0.147
CH_3COCH_3:CO_2	15	536.1	18.65	7.4	0.257
CH_3COCH_3:H_2O		-	-	-	-
CH_3COCH_3:CH_3OH		-	-	-	-
CH_3COCH_3:H_2O:CO_2		-	-	-	-
CH_3COCH_3:H_2O:CH_4		546.0	18.31	9.5	0.319
CH_3COCH_3:CH_3OH:CO		-	-	-	-
CH_3COCH_3		532.7	18.77	7.5	0.264
CH_3COCH_3:CO		532.5	18.78	4.7	0.165
CH_3COCH_3:CO_2	30	536.1	18.65	6.9	0.238
CH_3COCH_3:H_2O		-	-	-	-
CH_3COCH_3:CH_3OH		-	-	-	-
CH_3COCH_3:H_2O:CO_2		-	-	-	-
CH_3COCH_3:H_2O:CH_4		545.8	18.32	7.9	0.265
CH_3COCH_3:CH_3OH:CO		-	-	-	-
CH_3COCH_3		532.5	18.78	7.1	0.249

70

CH_3COCH_3:CO_2		533.5	18.74	5.5	0.194
CH_3COCH_3:H_2O		-	-	-	-
CH_3COCH_3:CH_3OH		-	-	-	-
CH_3COCH_3:H_2O:CO_2		-	-	-	-
CH_3COCH_3:H_2O:CH_4		545.8	18.32	4.0	0.134
CH_3COCH_3:CH_3OH:CO		532.3	18.79	4.4	0.154
CH_3COCH_3	90	532.3	18.79	6.8	0.240
CH_3COCH_3:CO_2		532.5	18.78	7.3	0.257
CH_3COCH_3:H_2O		-	-	-	-
CH_3COCH_3:CH_3OH		-	-	-	-
CH_3COCH_3:H_2O:CO_2		-	-	-	-
CH_3COCH_3:H_2O:CH_4		545.8	18.32	4.6	0.154
CH_3COCH_3:CH_3OH:CO		532.3	18.79	4.7	0.167
CH_3COCH_3	100	532.7	18.77	4.0	0.141
CH_3COCH_3:H_2O		-	-	-	-
CH_3COCH_3:CH_3OH		-	-	-	-
CH_3COCH_3:H_2O:CO_2		-	-	-	-
CH_3COCH_3:H_2O:CH_4		546.0	18.31	5.0	0.168
CH_3COCH_3:CH_3OH:CO		532.0	18.80	4.6	0.162
CH_3COCH_3	110	532.5	18.80	4.1	0.141
CH_3COCH_3:H_2O:CH_4		546.0	18.31	4.4	0.148
CH_3COCH_3:CH_3OH:CO		532.5	18.78	4.1	0.146
CH_3COCH_3	120	532.3	18.79	4.1	0.143
CH_3COCH_3:H_2O:CH_4		546.0	18.31	6.7	0.224
CH_3COCH_3:CH_3OH:CO		532.5	18.78	2.9	0.103

Appendix C

Integrated absorbance values

In this section, the integrated absorbance of the analyzed acetone bands are presented in tables. The tables contain the integrated absorbance of the acetone bands normalized in relation to the C=O stretch mode of the respective mixture at 15 K.

All the measurements are taken from baseline-corrected spectra and for the C=O stretch band of acetone, water subtraction is also performed, since the O-H bending mode of water (around 1667 cm^{-1}) overlaps with this mode. For modes that present two or more overlapping components, the values listed below refers to the absorbance integrated over all the components.

Table 3.C.1: Integrated absorbance ratios of selected transitions in pure acetone ice.

Temperature (K)	C=O stretch (5.847 μm)	CH_3 assym. deformation (7.053 μm)	CH_3 symm. deformation (7.335 μm)	CCC asymm. stretch (8.141 μm)	CO in-plane deformation (18.77 μm)
15	1.00	0.40	0.53	0.27	0.08
30	1.00	0.40	0.53	0.27	0.08
70	1.01	0.39	0.52	0.28	0.08
90	1.02	0.38	0.52	0.28	0.07
100	0.89	0.31	0.62	0.30	0.09
110	0.90	0.31	0.61	0.30	0.09
120	0.91	0.30	0.61	0.30	0.09
140	0.79	0.26	0.49	0.25	0.07

3.4. Appendix C

Table 3.C.2: Integrated absorbance ratios of selected transitions in CH_3COCH_3:H_2O(1:5)

Temperature (K)	C=O stretch (5.847 μm)	CH_3 assym. deformation (7.053 μm)	CH_3 symm. deformation (7.335 μm)	CCC asymm. stretch (8.141 μm)	CO in-plane deformation (18.77 μm)
15	1.00	0.33	0.44	0.19	0.060
30	1.04	0.33	0.45	0.20	0.059
70	1.03	0.31	0.44	0.19	0.055
90	1.02	0.30	0.43	0.19	0.044
100	1.02	0.29	0.43	0.19	-
110	1.02	0.29	0.42	0.18	-
120	1.01	0.27	0.42	0.19	-
140	0.86	0.24	0.40	0.20	-

Table 3.C.3: Integrated absorbance ratios of selected transitions in CH_3COCH_3:CO_2(1:5)

Temperature (K)	C=O stretch (5.847 μm)	CH_3 assym. deformation (7.053 μm)	CH_3 symm. deformation (7.335 μm)	CCC asymm. stretch (8.141 μm)	CO in-plane deformation (18.77 μm)
15	1.00	0.37	0.56	0.28	0.087
30	1.01	0.37	0.56	0.28	0.084
70	1.05	0.38	0.57	0.30	0.067
90	1.00	0.32	0.51	0.27	0.044
100	1.00	0.30	0.48	0.25	0.044

Table 3.C.4: Integrated absorbance ratios of selected transitions in CH_3COCH_3:CO (1:5)

Temperature (K)	C=O stretch (5.847 μm)	CH_3 assym. deformation (7.053 μm)	CH_3 symm. deformation (7.335 μm)	CCC asymm. stretch (8.141 μm)	CO in-plane deformation (18.77 μm)
15	1.00	0.31	0.51	0.26	0.07
30	0.99	0.34	0.50	0.25	0.07

Table 3.C.5: Integrated absorbance ratios of selected transitions in CH_3COCH_3:CH_3OH(1:5)

Temperature (K)	C=O stretch (5.847 μm)	CH_3 assym. deformation (7.053 μm)	CH_3 symm. deformation (7.335 μm)	CCC asymm. stretch (8.141 μm)	CO in-plane deformation (18.77 μm)
15	1.00	-	0.47	0.23	0.031
30	0.98	-	0.47	0.23	0.037
70	0.96	-	0.46	0.23	0.043
90	0.92	-	0.46	0.23	0.054
100	0.92	-	0.46	0.23	0.054
110	0.98	-	0.50	0.24	0.052
120	1.01	-	0.46	0.18	0.038
140	0.64	-	0.30	0.12	0.011

Table 3.C.6: Integrated absorbance ratios of selected transitions in CH_3COCH_3:H_2O(1:20)

Temperature (K)	C=O stretch (5.847 μm)	CH_3 assym. deformation (7.053 μm)	CH_3 symm. deformation (7.335 μm)	CCC asymm. stretch (8.141 μm)	CO in-plane deformation (18.77 μm)
15	1.00	0.25	0.40	0.19	-
30	1.06	0.26	0.42	0.20	-
70	0.97	0.24	0.42	0.21	-
90	1.00	0.22	0.41	0.20	-
100	0.98	0.22	0.41	0.20	-
110	0.98	0.24	0.41	0.20	-
120	0.94	0.22	0.41	0.19	-
140	0.88	0.21	0.39	0.19	-

Table 3.C.7: Integrated absorbance ratios of selected transitions in CH_3COCH_3:CO_2(1:20)

Temperature (K)	C=O stretch (5.847 μm)	CH_3 assym. deformation (7.053 μm)	CH_3 symm. deformation (7.335 μm)	CCC asymm. stretch (8.141 μm)	CO in-plane deformation (18.77 μm)
15	1.00	0.38	0.55	0.27	-
30	0.99	0.48	0.69	0.38	-
70	0.99	0.41	0.61	0.39	-
90	1.01	0.34	0.51	0.27	-
100	1.13	0.30	0.34	0.15	-

Table 3.C.8: Integrated absorbance ratios of selected transitions in CH_3COCH_3:CO(1:20)

Temperature (K)	C=O stretch (5.847 μm)	CH_3 assym. deformation (7.053 μm)	CH_3 symm. deformation (7.335 μm)	CCC asymm. stretch (8.141 μm)	CO in-plane deformation (18.77 μm)
15	1.00	0.36	0.54	0.30	0.09
30	1.09	0.35	0.55	0.29	0.09

Table 3.C.9: Integrated absorbance ratios of selected transitions in CH_3COCH_3:CH_3OH(1:20)

Temperature (K)	C=O stretch (5.847 μm)	CH_3 assym. deformation (7.053 μm)	CH_3 symm. deformation (7.335 μm)	CCC asymm. stretch (8.141 μm)	CO in-plane deformation (18.77 μm)
15	1.00	-	0.55	0.21	-
30	0.99	-	0.57	0.21	-
70	1.01	-	0.64	0.21	-
90	0.92	-	0.66	0.22	-
100	0.91	-	0.67	0.22	-
110	1.00	-	0.75	0.24	-
120	1.06	-	0.71	0.19	-
140	0.48	-	0.37	0.06	-

Table 3.C.10: Integrated absorbance ratios of selected transitions in CH_3COCH_3:H_2O:CO_2(1:2.5:2.5)

Temperature (K)	C=O stretch (5.847 μm)	CH_3 assym. deformation (7.053 μm)	CH_3 symm. deformation (7.335 μm)	CCC asymm. stretch (8.141 μm)	CO in-plane deformation (18.77 μm)
15	1.00	0.43	0.56	0.28	0.07
30	1.00	0.42	0.56	0.27	0.07
70	0.98	0.40	0.56	0.26	0.05
90	0.97	0.38	0.54	0.24	-
100	0.92	0.36	0.51	0.23	-
110	0.90	0.35	0.50	0.23	-
120	0.89	0.32	0.48	0.22	-
140	0.58	0.20	0.33	0.18	-

Table 3.C.11: Integrated absorbance ratios of selected transitions in CH_3COCH_3:H_2O:CO_2(1:10:10)

Temperature (K)	C=O stretch (5.847 μm)	CH_3 assym. deformation (7.053 μm)	CH_3 symm. deformation (7.335 μm)	CCC asymm. stretch (8.141 μm)	CO in-plane deformation (18.77 μm)
15	1.00	0.37	0.50	0.20	-
30	1.01	0.39	0.54	0.22	-
70	0.99	0.33	0.49	0.21	-
90	0.99	0.28	0.45	0.25	-
100	0.85	0.24	0.38	0.21	-
110	0.84	0.22	0.37	0.20	-
120	0.81	0.22	0.37	0.21	-
140	0.56	0.17	0.34	0.18	-

3.4. Appendix C

Table 3.C.12: Integrated absorbance ratios of selected transitions in CH_3COCH_3:H_2O:CH_4(1:2.5:2.5)

Temperature (K)	C=O stretch (5.847 μm)	CH_3 assym. deformation (7.053 μm)	CH_3 symm. deformation (7.335 μm)	CCC asymm. stretch (8.141 μm)	CO in-plane deformation (18.77 μm)
15	1.00	0.32	0.49	0.26	0.09
30	1.00	0.30	0.48	0.26	0.08
70	1.04	0.47	0.47	0.24	0.06
90	1.05	0.27	0.46	0.23	0.05
100	1.05	0.25	0.44	0.23	0.04
110	1.04	0.24	0.23	0.23	0.05
120	1.02	0.23	0.44	0.23	0.07
140	0.51	0.11	0.22	0.13	0.05

Table 3.C.13: Integrated absorbance ratios of selected transitions in CH_3COCH_3:H_2O:CH_4(1:10:10)

Temperature (K)	C=O stretch (5.847 μm)	CH_3 assym. deformation (7.053 μm)	CH_3 symm. deformation (7.335 μm)	CCC asymm. stretch (8.141 μm)	CO in-plane deformation (18.77 μm)
15	1.00	0.31	0.49	0.26	0.10
30	1.04	0.33	0.48	0.27	0.08
70	1.18	0.29	0.48	0.24	0.05
90	1.17	0.28	0.46	0.24	0.04
100	1.20	0.27	0.44	0.24	0.04
110	1.17	0.27	0.45	0.23	0.03
120	1.16	0.25	0.43	0.23	0.04
140	0.74	0.17	0.35	0.22	0.02

Table 3.C.14: Integrated absorbance ratios of selected transitions in CH_3COCH_3:CO:CH_3OH(1:2.5:2.5)

Temperature (K)	C=O stretch (5.847 μm)	CH_3 assym. deformation (7.053 μm)	CH_3 symm. deformation (7.335 μm)	CCC asymm. stretch (8.141 μm)	CO in-plane deformation (18.77 μm)
15	1.00	-	0.43	0.22	0.022
30	0.97	-	0.43	0.22	0.029
70	0.87	-	0.41	0.22	0.050
90	0.86	-	0.41	0.23	0.051
100	0.85	-	0.41	0.23	0.047
110	0.80	-	0.41	0.19	0.041
120	0.80	-	0.40	0.19	0.037
140	0.24	-	0.13	0.05	0.022

Table 3.C.15: Integrated absorbance ratios of selected transitions in CH_3COCH_3:CO:CH_3OH(1:10:10)

Temperature (K)	C=O stretch (5.847 μm)	CH_3 assym. deformation (7.053 μm)	CH_3 symm. deformation (7.335 μm)	CCC asymm. stretch (8.141 μm)	CO in-plane deformation (18.77 μm)
15	1.00	-	0.43	0.21	-
30	0.96	-	0.42	0.20	-
70	0.79	-	0.47	0.20	-
90	0.79	-	0.46	0.20	-
100	0.79	-	0.45	0.20	-
110	0.82	-	0.47	0.17	-
120	0.83	-	0.44	0.16	-
140	0.07	-	0.08	-	-

4

Infrared spectra of complex organic molecules in astronomically relevant ice mixtures: IV Methylamine

In the near future, high spatial and spectral infrared (IR) data of star-forming regions obtained by the James Webb Space Telescope (JWST) may reveal new solid-state features of various species, including more intriguing classes of chemical compounds. The identification of Complex Organic Molecules (COMs) in the upcoming data will only be possible when laboratory IR ice spectra of these species under astronomically relevant conditions are available for comparison. For this purpose, systematic series of laboratory measurements are performed, providing high-resolution IR spectra of COMs. Here, spectra of pure methylamine (CH_3NH_2) and methylamine-containing ices are discussed. The work is aimed at characterizing the mid-IR (500 - 4000 cm^{-1}, 20 - 2.5 μm) spectra of methylamine in pure and mixed ices to provide accurate spectroscopic data of vibrational bands that are most suited to trace this species in interstellar ices. Fourier Transform InfraRed (FTIR) spectroscopy is used to record spectra of CH_3NH_2 in the pure form and mixed with H_2O, CH_4, and NH_3, for temperatures ranging from 15 to 160 K. The IR spectra in combination with HeNe laser (632.8 nm) interference data of pure CH_3NH_2 ice were used to derive the IR band strengths of methylamine in pure and mixed ices. The refractive index of amorphous methylamine ice at 15 K was determined as being 1.30 $\pm$ 0.01. Accurate spectroscopic information and band strength values are systematically presented for a large set of methylamine-containing ices and different temperatures. Selected bands are characterized and their use as methylamine tracers are discussed. The selected bands include the following: the CH_3 antisymmetric stretch band at 2881.3 cm^{-1} (3.471 μm), the CH_3 symmetric stretching band at 2791.9 cm^{-1} (3.582 μm), the CH_3 antisymmetric deformation bands, at 1455.0 and 1478.6 cm^{-1} (6.873 μm and 6.761 μm), the CH_3 symmetric deformation band at 1420.3 cm^{-1} (7.042 μm), and the CH_3 rock at 1159.2 cm^{-1} (8.621 μm). Using the laboratory data recorded in this work and ground-based spectra of ices toward YSOs (Young Stellar Objects), upper limits for the methylamine ice abundances are derived. In some of these YSOs, the CH_3NH_2 abundance is less than 4% relative to H_2O.

M. G. Rachid, N. Brunken, D. de Boe, G. Fedoseev, A. C. A. Boogert and H. Linnartz (2021) published in A&A, 653, A116

4.1 Introduction

Amino acids are key molecules to life on Earth. Whereas such species have been found in meteorites, already more than half a century ago (Kvenvolden et al., 1970), the simplest amino acid, glycine (NH_2CH_2COOH) still has not been unambiguously detected in the interstellar medium (ISM). Its formation pathways in the gas phase and the solid state have been a matter of ongoing debate (Elsila et al., 2007). A direct consequence of this has been that several molecules, regarded as potential glycine precursors, have become a target in new surveys with the ultimate goal being to point out sources that may host glycine at a detectable level. Recent examples include the search for amino acetonitrile (NH_2CH_2CN) by Belloche et al., 2008, methanimine (CH_2NH) by Suzuki et al., 2016, hydroxylamine (NH_2OH) by McGuire et al., 2015, and methylamine (CH_3NH_2) by Ohishi et al., 2019. Such species are expected to have a solid state origin and in this respect, methylamine is of special interest, as in recent laboratory work by Ioppolo et al. (2020), it was shown to form nonthermally, under dark cloud conditions (i.e., without impacting UV photons) in a chain of solid-state reactions that also leads to glycine. Fully in line with these experiments was the recent detection of both species in the comet 67P/Churyumov-Gerasimenko (Altwegg et al., 2016), whose composition is considered to reflect the chemical material of the prestellar core from which our Solar System originated (Mumma and Charnley, 2011). For these reasons, we aim in this study to provide high-resolution solid-state infrared (IR) spectra of methylamine ice, both pure and embedded in astronomically relevant ice matrices. These data are currently lacking and these allow one to search for frozen methylamine in the ISM, also adding further options to optimize the search for interstellar glycine.

The first CH_3NH_2 detection dates back to 1974 when it was identified toward Sgr B2 and Orion A (Kaifu et al., 1974; Fourikis et al., 1974). Since then, methylamine has also been detected in other high mass star-forming regions (Bøgelund et al., 2019; Ohishi et al., 2019) and our own Solar System, in the material from the comets Wild 2 and 67P/Churyumov–Gerasimenko (Glavin et al., 2008; Goesmann et al., 2015; Altwegg et al., 2016). Also recently, Ohishi et al. 2019 used the radio telescope Nobeyama to search for methylamine toward several hot molecular cores, which resulted in the detection of a new CH_3NH_2 source, G10.47+0.03, the richest methylamine source up to date.

Several interstellar reaction pathways toward methylamine have been proposed, both in the gas phase and in the solid state. In the gas phase, CH_3NH_2 can be

formed by the reaction of a methyl radical cation with ammonia, followed by dissociative recombination (Leung et al., 1984; Herbst, 1985; Maeda and Ohno, 2006). The photolysis of gaseous mixtures containing CH_4, NH_3, and H_2O is also effective to form methylamine (Gardner and McNesby, 1980; Ogura et al., 1988; Ogura et al., 1989). Gardner and McNesby (1980) demonstrated that the condensation of a gaseous CH_4:NH_3:H_2O mixture followed by UV irradiation provided a solid-state channel resulting in the formation of methylamine. This solid-phase reaction has been included in a gas-grain chemical network by Garrod et al. (2008), who pointed out that the CH_3 and NH_2 radicals can be formed on the ice grains by UV or cosmic rays (CR), indicating that methylamine can be formed at very early stages inside dark molecular clouds. Additionally, Theulé et al. (2011) demonstrated that the hydrogenation of HCN can lead to the formation of CH_3NH_2 at 15 K. The mechanism for this synthesis involves multiple hydrogenation steps, possibly passing through the intermediate methanimine (CH_2NH). The electron irradiation of CH_4:NH_3 ices was also shown to form methylamine in the solid phase (Kim and Kaiser, 2011; Förstel et al., 2017).

Similar to NH_3, methylamine can act as an electron donor at low temperatures, forming salts and complexes in the solid state (Bossa et al., 2009; Bossa et al., 2010; Kayi et al., 2011; Noble et al., 2014). Bossa et al. (2009) showed that CH_3NH_2 thermally reacts with CO_2 at temperatures between 50 K and 70 K, forming methylammonium methylcarbamate ($[CH_3NH_3^+][CH_3NHCOO^-]$), which can be converted to glycine (Gly) under UV photolysis:

$$CO_2 + 2\,CH_3NH_2 \rightarrow [CH_3NH_3^+][CH_3NHCOO^-]$$

$$[CH_3NH_3^+][CH_3NHCOO^-] \xrightarrow{h\nu} CH_3NH_2 + \text{Gly}.$$

More recently, Mahjoub and Hodyss (2018) also showed that methylamine can thermally react with carbonyl sulfide (OCS) in the solid phase to form the methylammonium methylthiocarbamate salt $[CH_3NH_3^+][CH_3NHOCS^-]$. The salt formation by nitrogen-bearing molecules is of great importance since these reactions can increase their sublimation temperatures, "locking" these species on ices at relatively high temperatures (Bossa et al., 2009).

Many solid-state routes have been shown to result in CH_3NH_2 formation, and given its relevance as an amino acid precursor, it is essential to study this species' solid-state spectral features. The mid-IR spectrum of solid CH_3NH_2 has been reported in the literature in pure form and isolated in Ar and Kr matrices (Durig et al., 1968; Wolff, 1970; Durig and Zheng, 2001). The infrared spectra of some CH_3NH_2-containing ices

are reported in previous works (Bossa et al., 2009; Kayi et al., 2011; Vinogradoff et al., 2013), but a systematic study of the mid-infrared spectrum of methylamine recorded for different astrochemical relevant conditions is still lacking. To address this sparsity of laboratory data, we present the spectra of methylamine in mixtures containing H_2O, CH_4, and NH_3 for temperatures ranging from 15 K up to 160 K. The molecules used in the studied samples are amongst the most abundant detected species in water-rich interstellar ices (Boogert et al., 2015), moreover, CH_4 and NH_3 are expected to be solid-state precursors of methylamine (Kim and Kaiser, 2011; Förstel et al., 2017; Ioppolo et al., 2020). The chosen ice compositions aim to simulate the conditions in which methylamine is expected to be present in icy dust grains. This permits tracking changes in the spectral appearance of vibrational modes with alterations in the ice morphology. The IR bands that carry the highest potential as tracers of methylamine in interstellar ice are selected for in-depth spectral surveys. These IR features are characterized in terms of peak position and full width at half maximum (FWHM), and their relative band strengths in ices at 15 K are derived.

The data presented here are part of a series of laboratory experiments supporting upcoming observations with the James Webb Space Telescope (JWST) within the framework of "ICE AGE", a JWST ERS program. The Mid-InfraRed instrument (MIRI) on board JWST will provide infrared spectra of star-forming regions between 5 and 28.5 μm. These data allow one to identify new species in ices and increase our insight into the morphology and thermal history of ices in space. The secure assignment of the solid-state features in JWST spectra will only be possible when combined with laboratory spectra of ices recorded for similar astrophysical conditions. The data presented here will be publicly available from `https://icedb.strw.leidenuniv.nl/`, and spectra of ices recorded for intermediate temperatures can be supplied upon request.

This manuscript is organized in the following way: section 2 provides information on the measurements and applied methodology, including details on the band strength measurements. Section 3 presents the overall IR spectra and focuses on bands that might be useful for the astronomical identification of solid CH_3NH_2. This is illustrated in Section 4 discussing the potential of these IR features for tracing solid CH_3NH_2. The final section summarizes this work with a conclusion. The essential data resulting from this work are available in the Appendices. Appendix A presents the IR spectra of pure and mixed CH_3NH_2 ices as well as graphical representations of the relative band strengths and peak position versus FWHM for the selected bands. Appendix B provides data on the peak position and FWHM for these CH_3NH_2 bands in different

ice samples. Appendix C provides the integrated absorbance of the analyzed bands.

4.2 Methodology

The experiments have been performed with two setups. The infrared spectra were recorded with our HV (High Vacuum) setup. Details of this system and methodology are available from Terwisscha van Scheltinga et al. 2018 and Rachid et al. 2020. Over the last year, this setup has been fully upgraded, replacing the high vacuum by an UHV system. The new IRASIS (InfraRed Absorption Setup for Ice Spectroscopy) system allows for recording IR ice spectra and simultaneously performing laser interference measurements to determine ice thickness. For both setups, all relevant experimental information is provided below.

The infrared measurements of the pure CH_3NH_2 ice and CH_3NH_2 mixed in H_2O, NH_3, and CH_4 ices are conducted with the HV setup in a high vacuum stainless steel chamber that operates with a base pressure of $\sim 3 \times 10^{-7}$ mbar. Inside the chamber, an IR transparent zinc selenide (ZnSe) window is mounted on a copper holder connected to a cold finger and is maintained at 15 K by a closed-cycle He cryostat. Pure or premixed gases, contained in a 2L glass bulb with a total pressure of 20 mbar, are admitted into the chamber through a precalibrated needle valve and background deposited onto the substrate. The ices are grown for approximately 30 minutes, which results in ices with total column densities of 1 - 3 $\sim 10^{18}$ molecules cm^{-2}. After deposition, the ice is heated at a rate of 25 K hr^{-1} until its complete sublimation. During both the deposition and ice heating, mid-IR spectra (20 - 2.5 μm, 500 - 4000 cm^{-1} at resolution 0.5 cm^{-1}, averaged over 256 scans) are acquired continuously using a Varian 670 Fourier transform spectrometer. During a single-spectrum acquisition period, the ice is heated by roughly 3.5 K. Apart from temperatures close to crystallization or the thermal desorption point, this barely affects band profiles.

The gas mixtures are prepared in a separate mixing system by the sequential addition of gases or vapor components in a 2L glass bulb. This is done by adding a certain gas/vapor into the glass balloon and freezing this component by immersing the balloon in a liquid nitrogen bath. The freezing of a component gas ensures that this component cannot diffuse into the volume from which the upcoming component is added. For all measurements, the bulb is prepared by filling it with a total pressure of 20 mbar. For gaseous mixtures, each component's partial pressure in the mixture corresponds to the desired ratio in the ice sample. The estimated error in each component ratio following this method is ≤ 10 %. The gases and liquids used for preparing the gaseous mixtures are CH_3NH_2 (Sigma Aldrich, anhydrous ≥ 99.99 %), H_2O (Milli-Q,

Type I), CH_4 (Linde Gas 99.995%), and NH_3 (Sigma Aldrich, anhydrous $\geq$ 99.99 %).

The measurements of the methylamine band strengths are performed in the new experimental setup, IRASIS. This setup allows for the simultaneous acquisition of infrared spectra and laser interference measurements of the growing ice. Figure 4.1 shows a schematic picture of IRASIS. The central stainless chamber is kept at ultra-high vacuum (base pressure $\sim 2 \times 10^{-9}$ mbar) by a turbomolecular pump (Turbovac i350) prepumped by a rotary vane pump supplied with an oil filter. Compared to the previous HV setup, the measurements performed on IRASIS are less sensitive to water ice growth caused by background gas deposition. In the center of the chamber, a Germanium (Ge) substrate is attached to the tip of the cryostat's cold finger. The cryostat head system is mounted onto a rotatable platform, which allows the sample's rotation by 360°. The ice is deposited on both sides of the substrate, and the thickness on each side is monitored during growth by using a HeNe laser (λ = 632.8 nm) interference pattern. The ice thickness (d) is related to the number of interference fringes (m) by:

$$d = \frac{m\lambda}{2\sqrt{n^2 - sin^2\theta}}, \tag{4.1}$$

where λ is the wavelength of the laser, n is the refractive index of the ice, and θ is the incident angle of the laser beam (Tempelmeyer and Mills Jr, 1968). Since the Ge substrate is opaque for the light at 632.8 nm, each laser beam probes only the ice growing on one side of the substrate. The reflected light beams are measured by two separate photodetectors (Thorlabs PDA36A2) connected to a data acquisition card (National Instruments) that is controlled using a LabView program, which enables simultaneous data acquisition from both detectors. Figure 4.1a shows the experimental configuration for simultaneous acquisition of infrared spectra and laser interference measurements (in the measurements described here $\theta_0 = 45° \pm 3°$ and $\theta_1 = 42° \pm 3°$).

The refractive index of pure methylamine ice at 15 K is derived by a double-laser interference technique that employs two laser beams hitting the ice sample (in the same spot) at different angles and generating two interference patterns (for details, see Tempelmeyer and Mills Jr (1968), Romanescu et al. (2010), Beltrán et al. (2015), and Hudson et al. (2017)). The period of the interference patterns and the incidence angles of the two laser beams are related to the refractive index of the ice by:

$$n = \sqrt{\frac{\sin^2\theta_0 - \gamma^2 \sin^2\theta_1}{1 - \gamma^2}}, \tag{4.2}$$

where $\gamma = \frac{T_1}{T_0}$ is the ratio between the two periods T_1 and T_0 of the interference

signals generated by the two laser beams (see Figure 4.2), impacting on the substrate at angles θ_1 and θ_0, respectively.

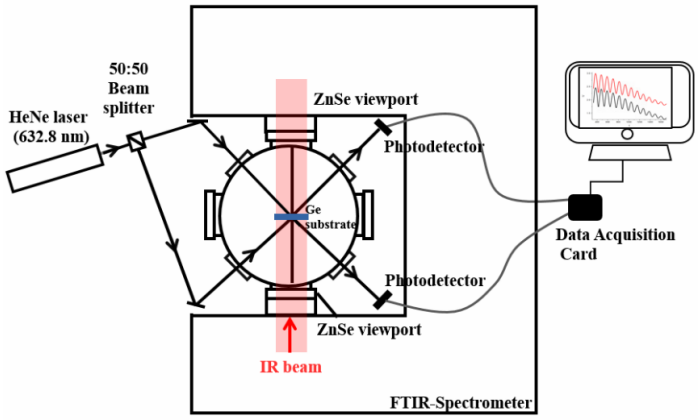

(a)

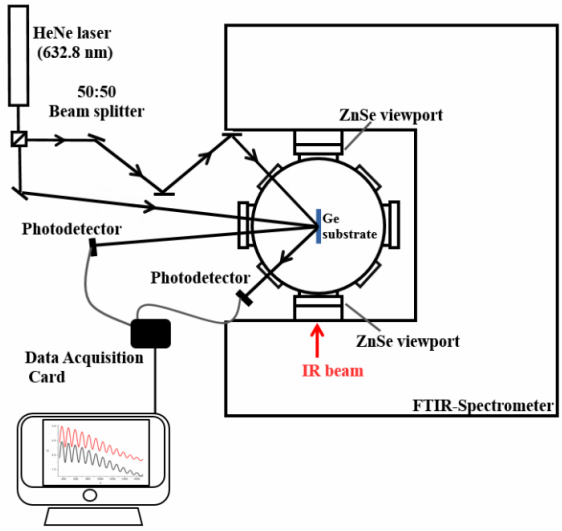

(b)

Figure 4.1: Schematic picture of the new IRASIS setup. a) Configuration in which the IR and thickness measurements are performed simultaneously. The laser beam impinges on the substrate at an angle of 45 ± 3° on one side of the substrate and 42 ± 3° on the other side. b) Configuration for refractive index measurements only: the substrate is rotated by 90° and the laser hits the substrate at two different angles (for this work $\theta_0 = 5.8° \pm 0.5°$ and $\theta_1 = 50.0° \pm 0.5°$).

Since the refractive index measurements are more sensitive to the accuracy in the incident angle around 50°, these measurements are performed using a different optical configuration, in which the sample holder is rotated by 90° (Figure 4.1b). In this configuration, the uncertainty in the angle is smaller, as the angle can be determined by measuring the laser beam over larger distances from the substrate. In this work, the laser beams hit the substrate at angles 5.8° ± 0.5° and 50.0° ± 0.5° (Figure 4.1b).

4.2.1 Ice samples

Under interstellar ice conditions, CH_4 and NH_3 are embedded in a H_2O rich matrix, formed at very early stages of stellar evolution, still in the molecular cloud stage (Boogert et al., 2015; Linnartz et al., 2015; Fedoseev et al., 2015; Qasim et al., 2020). To simulate more realistic astronomical conditions, the studied ices are prepared by mixing methylamine with H_2O, CH_4, and NH_3, in binary, tertiary, and quaternary mixtures containing these molecules.

To analyze the effects of methylamine dilution on the IR spectral features, three different concentrations were prepared: 1:5, 1:10, and 1:20, which means that for each methylamine molecule in the ice sample, there are 5, 10, or 20 molecules of the other ice component(s). The deposition rates (and consequently the column densities) of the different species in the ices are derived by considering the weighted deposition rate of all the species in the gaseous mixture. Based on previous work (Terwisscha van Scheltinga et al., 2018), the uncertainty in this approach is estimated to amount to 10 percent for the accuracy with which a gas mixture can be prepared, and, upon deposition, another 10 percent uncertainty is added to account for changes in the deposition rate of the individual components. This results in propagated uncertainties of 14, 17, and 20 percent in the column densities of the two, three, and four-component ices. For the uncertainty in the ratio between two species in the deposited ice, this number translates into values of 20, 24, and 28 percent, respectively. The IR spectra of all the ice samples are recorded from 15 - 160 K. The desorption of matrix components during the ice heating changes the relative methylamine concentration in the sample, causing methylamine bands to appear stronger or have a different profile because of new intermolecular interactions in the ice. Due to these changes and the fact that we do not have precise information about the new mixing ratio, quantitative analyses of the methylamine bands are made until the majority of the ice matrix components have desorbed. The composition, ice mixing ratio, column density of methylamine in the ice, and temperature range of all studied samples are listed in Table 4.1.

Table 4.1: Characteristics of the analyzed ice samples (composition, mixing ratios, methylamine column density, and temperature range). For more information on the uncertainty of the ice mixtures, see Section 2.1.

Mixture	Mixing ratios	$N_{CH_3NH_2}$ (10^{17} cm^{-2})	Temperature range (K)
CH_3NH_2:H_2O	1:5	4.5 ± 0.6	15 - 150
CH_3NH_2:H_2O	1:10	2.5 ± 0.3	15 - 150
CH_3NH_2:H_2O	1:20	1.3 ± 0.2	15 - 150
CH_3NH_2:CH_4	1:5	3.7 ± 0.5	15 - 45
CH_3NH_2:CH_4	1:10	2.0 ± 0.3	15 - 45
CH_3NH_2:CH_4	1:20	1.0 ± 0.1	15 - 45
CH_3NH_2:NH_3	1:5	4.4 ± 0.6	15 - 115
CH_3NH_2:NH_3	1:10	2.4 ± 0.3	15 - 115
CH_3NH_2:NH_3	1:20	1.3 ±0.2	15 - 115
CH_3NH_2:H_2O:CH_4	1:5:5	2.2 ± 0.4	15 - 150
CH_3NH_2:H_2O:CH_4	1:10:10	1.2 ± 0.2	15 - 150
CH_3NH_2:H_2O:NH_3	1:5:5	2.5 ± 0.4	15 - 150
CH_3NH_2:H_2O:NH_3	1:10:10	1.3 ± 0.2	15 - 150
CH_3NH_2:CH_4:NH_3	1:5:5	2.2 ± 0.4	15 - 115
CH_3NH_2:CH_4:NH_3	1:10:10	1.2 ± 0.2	15 - 115
CH_3NH_2:H_2O:CH_4:NH_3	3:10:10:10	2.3 ± 0.4	15 - 150

4.2.2 Band strength of the methylamine IR features

As described previously, the refractive index of the pure methylamine ice can be derived through a double laser interference technique. Representative data obtained in this way is shown in Figure 4.2. The procedure to obtain the periods of the generated signals (T_0 and T_1 for Equation 4.2) and the position of the constructive interference for thickness measurements (Equation 4.1) are made using a personal Python script. The interference pattern is initially baseline corrected using a Savitzky–Golay filter, followed by the adjust of a sine function, whose periods are employed to calculate n (Equation 4.2). Other methods for deriving the period from an interference pattern consist of measuring the number of fringes in a large interval of time, averaging a large number of individual periods, or adjusting the signal using a multiparameter function containing polynomial terms and a periodic term modulated by an exponential decay. These methods yield refractive index values consistent with the method used in this work within their uncertainties. In this work, the refractive index for pure methylamine ices is measured at 15 K (amorphous) and 123 K (crystalline), being these values 1.30 ± 0.01 and 1.40 ± 0.01, respectively. The later value was measured for calculating the molar refraction of methylamine, necessary for deriving the ice density through the

Lorentz-Lorenz relation, as described below.

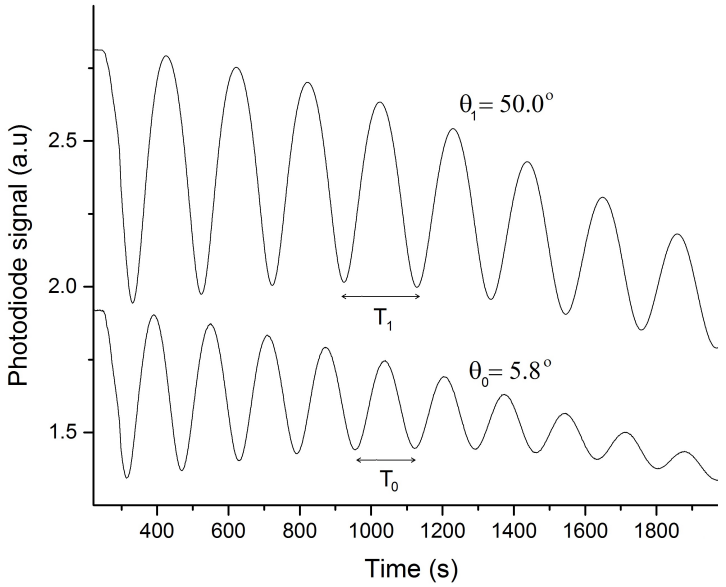

Figure 4.2: Interference pattern obtained during ice growth. In this work, the employed laser beams hit the substrate at angles $\theta_0 = 5.8° \pm 0.5°$ and $\theta_1 = 50.0° \pm 0.5°$.

A pure ice's column density (in molecules per cm^2) as a function of its thickness can be written as:

$$N = \frac{d\ \rho\ N_A}{M}, \tag{4.3}$$

where d is the sample thickness (in cm), ρ is the mass density (in g cm^{-3}), N_A is the Avogadro's number, and M is the ice component's molar mass (in g mol^{-1}). Using Equation 4.3 and the Lambert-Beer law, the band strength (A) of a given IR feature is given by (Yamada and Person, 1964):

$$A = \frac{2.3\ M}{\rho\ d\ N_A} \int_\nu \mathrm{abs}_\nu\ \mathrm{d}\nu, \tag{4.4}$$

where A is given in cm $molecule^{-1}$, and $\int_\nu abs_\nu \mathrm{d}\nu$ is the integrated absorbance of the band (i.e., the band area).

The pure methylamine band strength measurements are performed by growing rel-

atively thin ices (typically 2-4 fringes in the interference pattern) and recording spectra at 1.0 cm^{-1} resolution. The ice thickness and area of the IR bands are monitored simultaneously, and a linear adjustment of the thickness × time and band area × time yields good linear relations (R^2 bigger than 0.98). By using the slope of such linear relations and Equation 4.4, the band strength of a given feature can be calculated as :

$$A = \frac{2.3\ M\ \alpha}{\rho\ \ N_A\ \beta}, \tag{4.5}$$

where α is the variation of integrated band absorbance (band area) in time, and β is the variation of ice thickness in time. In the derivation of the pure ice band strengths, the methylamine mass density (ρ in Equation 4.5) is the main source of uncertainty. To the best of our knowledge, the density of amorphous methylamine ice has not been reported in the literature, only the value for orthorhombic CH_3NH_2 at 123 K is available (Atoji and Lipscomb, 1953). The methylamine density at 15 K can be estimated using the Lorentz–Lorenz relation in a molar version:

$$R_M = \frac{M}{\rho}\left(\frac{n^2-1}{n^2+2}\right), \tag{4.6}$$

where R_M, M, ρ, and n are respectively the molar refraction, the molar mass, the mass density, and the refractive index of the molecule under analysis. The molar refraction can be estimated from the individual chemical bonds' molar refraction (Denbigh, 1940; Hudson et al., 2020) or from equation 4.6 using the density and refractive index for crystalline methylamine at 123 K. Following the second approach, Equation 4.6 yields R_M = 8.86 $cm^3\ mol^{-1}$ when n = 1.40 ± 0.01 and ρ = 0.85 g cm^{-3} (from Atoji and Lipscomb (1953)) are employed. Using this molar refraction value, a pure amorphous methylamine density of 0.66 cm^{-3} is obtained. This density is used in Equation 4.5 for deriving methylamine band strengths, and in the case that a more accurate measurement of the amorphous methylamine density becomes available, the band strengths derived here can be re-scaled. Table 4.2 shows the calculated methylamine band strengths and the wavelength region that is used for the calculation of the band areas. All the spectra are baseline corrected before area calculations.

4.2.3 Relative band strengths

The light absorption profile of a molecule changes depending on the chemical environment surrounding the species. This is well known from studies analyzing the IR band profiles of molecules in different liquid or solid mixtures. Once the band profile

Table 4.2: Calculated IR band strengths (A) of amorphous methylamine ice at 15 K.

Peak position (cm^{-1})	Integrated region (cm^{-1})	Assignment	A (10^{-18} cm $molec^{-1}$)
2881.3	2893 - 2870	CH_3 antisymmetric stretch	2.6 ± 0.5
2791.8	2825 - 2765	CH_3 symmetric stretch	3.8 ± 0.6
1478.6	1500 - 1467	CH_3 antisymmetric def.	1.1 ± 0.2
1455.0	1467 - 1440	CH_3 antisymmetric def.	0.7 ± 0.1
1420.3	1432 - 1407	CH_3 symmetric def.	0.20 ± 0.03
1159.2	1215 - 1130	CH_3 rock	1.5 ± 0.2

changes, the IR t band strengths may change significantly. For a better quantification of methylamine in astrophysical ice analogs, the relative band strengths are calculated. In this work, the relative band strength (η) is the ratio between the apparent band strength of a given band when embedded in an ice mixture and the corresponding band strength in the pure ice:

$$\eta = \frac{A'}{A}, \tag{4.7}$$

where A' is the apparent band strength for a band in a given mixture and A is the band strength of the same band in pure methylamine ice at 15 K. The apparent band strength values and their uncertainties for the methylamine bands are graphically displayed in Appendix A.

4.3 Results and discussion

This section presents a set of representative mid-IR spectra of the methylamine-containing ices analyzed in this work. Changes in the IR absorbance profile of pure methylamine and mixed ices are described, and some ideas concerning the origins of these changes are pointed out. The complete data set is available from the Appendices. In Appendix A, spectra showing the selected methylamine bands in ice mixtures are presented for selected temperatures. The FWHM values versus peak positions are graphically shown for different ice mixtures and temperatures. The relative band strength values (see Equation 4.7) for different matrices are also given. The peak positions and FWHMs of the selected bands are organized in Tables 4.B.1 - 4.B.15, and the integrated absorbance of the methylamine in different ice mixtures is listed in Tables 4.C.1 - 4.C.15 (see notes in Appendix B and C).

This section is organized as follows: firstly, the overall spectra of methylamine ice in amorphous (15 K) and crystalline (101 K) forms are presented. According to data found in the literature, the infrared features are assigned to the corresponding vibrational modes, and the most prominent features in the spectra are described. In the next subsections, profiles of specific methylamine bands are analyzed. These infrared features are selected based on a minimal overlap with bands of abundant molecules detected in water-rich interstellar ices (i.e., CO_2, CH_4, and NH_3).

The actual composition of interstellar ice is far more complex than the mixtures presented here. Also, infrared astronomical data exhibit absorption features from the dust material. Thereby, methylamine features may be hidden by absorption of species other than H_2O, NH_3, and CH_4, in particular molecules with similar functional groups. In order to maintain our analysis feasible, only a few other typically more abundant species, such as methanol, are explicitly taken into account.

4.3.1 Pure methylamine ice

Figure 4.3 shows the spectra of methylamine ice deposited at 15 K (amorphous) and heated to 101 K (crystalline). The pure CH_3NH_2 ice crystallizes around 100 K, and upon heating, this phase transition is spotted by the abrupt sharpening and splitting of the IR absorption bands. These changes are the result of a more organized ice structure, which reduces the diversity of molecular orientations. Table 4.3 lists the peak positions for amorphous (15 K) and crystalline (101 K) methylamine ice measured in this work, along with their tentative assignments (based on the work of Durig and Zheng, 2001) and literature values for methylamine ices.

The 3000 - 2750 cm^{-1} region contains the methylamine ice features assigned to the CH_3 stretching mode and overtones of the CH_3 deformation modes. In pure methylamine, the bands in this region are strong, including the overtone modes, whose intensities are enhanced due to Fermi resonance (Durig et al., 1968; Wolff, 1970; Lavalley and Sheppard, 1972).

The peaks at 1455.0 cm^{-1} and 1478.6 cm^{-1} are assigned to the CH_3 antisymmetric deformation mode. By warming up the ices, the peak positions do not change significantly until the ice crystallizes. Upon the phase transition, both peaks narrow abruptly: the FWHM changes from 16.8 cm^{-1} and 13.8 cm^{-1} at 15 K to 4.7 cm^{-1} and 2.7 cm^{-1} at 100 K for the 1478.6 cm^{-1} and 1455.0 cm^{-1} features, respectively (see Figure 4.3 and Table 4.B.7).

In pure methylamine ice, the symmetric deformation of the CH_3 group appears

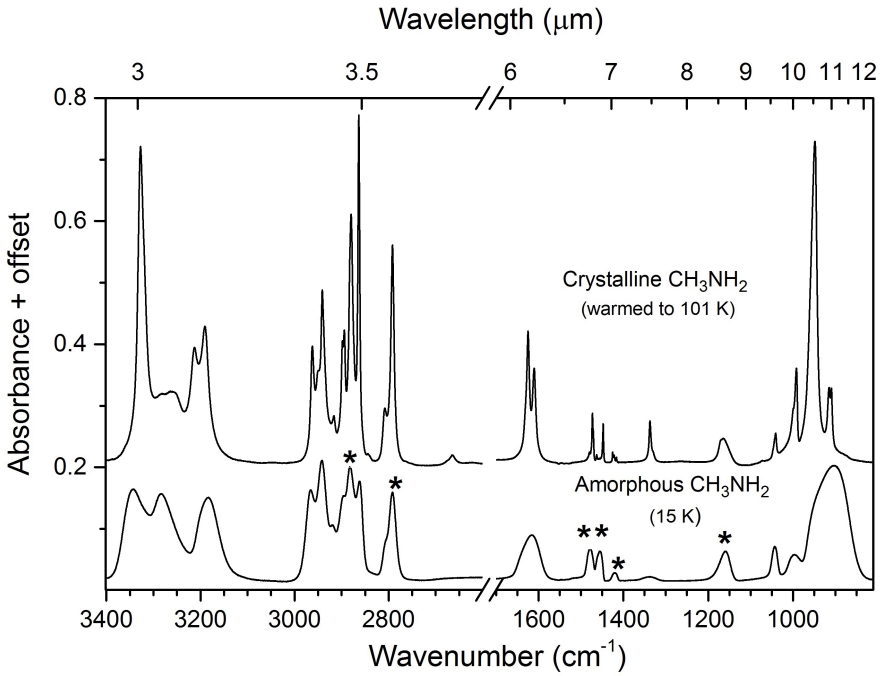

Figure 4.3: Infrared spectra of amorphous (bottom spectrum) and crystalline (top spectrum) methylamine ice acquired with a resolution of 0.5 cm^{-1} in the range from 3400 - 850 cm^{-1}. The methylamine peaks chosen for in-depth characterization are marked with an asterisk.

as a single feature at 1420.3 cm^{-1} (Figure 4.3). As the temperature increases, the peak position and FWHM do not change significantly at temperatures lower than 100 K. At 100 K, the sample crystallizes, and an abrupt narrowing and shift to lower wavenumbers are observed. The narrowing of the CH_3 symmetric deformation band peaks reveals three features, at 1416.5 cm^{-1}, 1422.0 cm^{-1}, and 1425.4 cm^{-1}, with the former feature being the strongest one.

The feature assigned to the methylamine CH_3 rock vibrational mode appears at 1159.2 cm^{-1} in pure methylamine at 15 K and shifts to higher wavenumbers when the ice is heated, peaking at 1164 cm^{-1} at 100 K. The warming of the pure ice causes a slight narrowing of this peak, changing the FWHM from 28.4 cm^{-1} at 15 K to 26.2 cm^{-1} at 100 K. Unlike other methylamine bands, no strong and abrupt sharpening and increase in intensity is observed upon crystallization.

Methylamine presents a strong feature at 903.5 cm^{-1} assigned to the ν_9 mode.

Table 4.3: Vibrational modes of pure methylamine ice.

Mode	Assignment	Amorphous[a] 15 K	Crystalline[a] 101 K	Solid[b] 10 K	Solid[c] 120 K
ν_{10}	NH_2 antisymmetric stretch	3342.8	3327.6	3348	3332
ν_1	NH_2 symmetric stretch	3283.4		3287	3260
		3183.2	3212.8	3189	3191
			3190.6		
		2965.3	2962.4	2969	
ν_{11}	CH_3 antisymmetric stretch	2941.9	2941.1	2945	2942
		2896.0	2898.2	2899	
			2894.1		
ν_2	CH_3 antisymmetric stretch	2881.3	2879.9	2884	2881
		2862.1	2863.3	2865	
ν_3	CH_3 symmetric stretch	2791.8	2791.9	2794	2793
ν_4	NH_2 def.	1616.1	1625.0	1618	1651
			1472.8		
ν_{12}	CH_3 antisymmetric def.	1478.6	1480.1	1479	1500
			1610.5		
ν_5	CH_3 antisymmetric def.	1455.0	1447.8		
			1463.0		
ν_6	CH_3 symmetric def.	1420.3	1425.4	1421	1441
			1422.0		
			1416.5		
ν_{13}	CH_3 rock/NH_2 twist	1339.1	1337.4	1339	1353
ν_7,	CH_3 rock	1159.2	1164.3	1161	1182
ν_8	CN stretch	1043.3	1040.9	1045	1048
ν_{14}	CH_3 rock/NH_2	996.8	991.7	997	1005
ν_9	NH_2 wag	903.5	948.1	931	955
			914.8		
			909.5		

[a] This work
[b] Oba et al., 2014
[c] Durig et al., 1968

Upon crystallization, this feature sharpens and is one of the strong features in the methylamine spectrum. Despite being a strong feature, this peak is not characterized throughout this work, since it overlaps with the broad libration mode of H_2O ice (around 760 cm^{-1}), being not easy to disentangle in a complex ice mixture. Since the goal of this work is characterizing features that present less overlapping with such abundant ice components, the band at 903.5 cm^{-1} was not chosen for a more in-depth investigation.

In the upcoming sections, we describe the morphology of methylamine features in pure and mixed ices in more detail. The features selected for in-depth investigation are the CH_3 rock mode around 1159 cm^{-1}, the CH_3 symmetric deformation

around 1420 cm^{-1}, the CH_3 antisymmetric deformation modes that give rise to the bands around 1455.0 and 1478.6 cm^{-1}, the CH_3 symmetric stretching band, around 2791.8 cm^{-1}, and the CH_3 antisymmetric stretching band, around 2881.3 cm^{-1}. These six peaks are labeled with an asterisk in Figure 4.3.

4.3.2 Mixed methylamine ices

CH_3 rock - 1159.2 cm^{-1}

In the binary CH_3NH_2:H_2O ice mixtures, the band due to the CH_3 rock vibrational modes shifts toward higher wavenumbers, peaking at 1176.8, 1177.5, and 1178.3 cm^{-1} in the 1:5, 1:10, and 1:20 mixtures, respectively (see Tables 4.B.1, 4.B.2, 4.B.3, and Figures 4.4, 4.A.1, and 4.A.2). By warming the CH_3NH_2:H_2O mixtures, this methylamine band narrows by 1 cm^{-1} to 3 cm^{-1}. In the binary mixtures with CH_4, the peak shifts to lower wavenumbers with an increasing CH_4 ratio. However, upon heating of the CH_3NH_2:CH_4 mixtures, the peak position shifts to higher wavenumbers, and the FWHM increases. These shifts can be due to rearrangements inside the ice and hydrogen bonds forming between methylamine molecules. In the CH_3NH_2:CH_4(1:20) ice, this feature is visible but it is too weak for quantitative analysis (Figure 4.A.2).

In the NH_3-containing samples, the methylamine CH_3 rock band overlaps with the strong feature of the ammonia umbrella vibration (around 1070 cm^{-1}), appearing as a weak shoulder in the ammonia feature (see Figures 4.4, 4.A.1, 4.A.2, 4.A.3, and 4.A.4 - in some of the panels, the position of the shoulder, when visible, is marked with a dashed vertical line). This band can be observed as a shoulder in binary mixtures with a ratio 1:5, some of the 1:10 mixtures (including the CH_3NH_2:H_2O:CH_4:NH_3(3:10:10:10) ice) but is almost absent in the 1:20 mixtures. The shoulder becomes more prominent at higher temperatures due to the narrowing of the ammonia band.

CH_3 symmetric deformation - 1420.3 cm^{-1}

In all the mixed ices, the CH_3 symmetric deformation band appears at higher wavenumbers when compared to pure methylamine ice, shifted by around 5 cm^{-1} (see Tables 4.B.4, 4.B.5, and 4.B.6 and Figures 4.5, 4.A.5, 4.A.6, 4.A.7, and 4.A.8). The more substantial shifts are observed for the H_2O containing mixtures, for which this feature appears between 1424 and 1425 cm^{-1}. In all the ice samples, this band does not overlap with any bands from H_2O, CH_4, and NH_3. Also, this feature is distinguishable in all the samples with exception of the CH_3NH_2:CH_4(1:20) ice, where it appears as a weak feature.

The peak intensity of the CH_3 symmetric deformation is enhanced in the water-containing mixtures. From Figures 4.5, 4.A.5, and 4.A.6, it is possible to notice that the peak height of this feature in the H_2O-containing matrices is comparable to the intensity of the CH_3 antisymmetric deformation features, located at 1455.0 and 1478.6 cm^{-1}. In the mixtures without water and pure methylamine ice, the peak height of the CH_3 symmetric deformation is less than half of the intensity of the CH_3 antisymmetric deformation features. The enhancement in strength is also noticed in the apparent band strength of this feature, which is around three times higher in CH_3NH_2:H_2O ice mixtures when compared to the values for pure methylamine ice (see panels displaying the relative band strengths in Figures 4.5, 4.A.5, and 4.A.6).

CH_3 antisymmetric deformation - 1455.0 and 1478.6 cm^{-1}

In the ice mixtures, the feature at 1455 cm^{-1} peaks at higher wavenumbers when compared to the pure methylamine ice, being the most significant shift observed in the water-containing mixtures, in which it peaks between 1462 - 1464 cm^{-1} (see Tables 4.B.7, 4.B.8, and 4.B.9 and the two peaks at higher wavenumbers on the panels of Figures 4.5, 4.A.5, 4.A.7, and 4.A.8). By warming the ice mixtures, this peak position does not shift appreciably, but some notable trends in the binary mixtures are observed. With increasing temperature, the peak around 1455 cm^{-1} narrows in a water environment but becomes broader in CH_4 and NH_3 matrices. In the water-containing three-component ices and the four-component ice, a decrease of FWHM is observed, following the trend for the CH_3NH_2:H_2O ices.

The peak at 1478.6 cm^{-1}, also assigned to the CH_3 antisymmetric deformation mode, behaves differently from the peak at 1455 cm^{-1}. In the two-component ices, this peak appears at higher wavenumbers in the H_2O and NH_3 matrices and lower wavenumbers in the CH_4 matrices (Tables B.7, B.8, and B.9). In all the ice mixtures at 15 K, this feature shifts by a maximum of 2 cm^{-1} from the position in the pure methylamine ice. Upon heating, this peak slightly narrows and shifts toward low wavenumbers in H_2O and NH_3 and becomes broader and shifts toward higher wavenumbers in CH_4. The broadening in the CH_4 matrix is probably due to the re-establishment of methylamine-methylamine interactions and is more pronounced when CH_4 starts to desorb. In the 3 and 4 component mixtures, the changes in FWHM are not very pronounced, changing less than 2 cm^{-1} for all the mixtures with exception of the CH_3NH_2:CH_4:NH_3 ices.

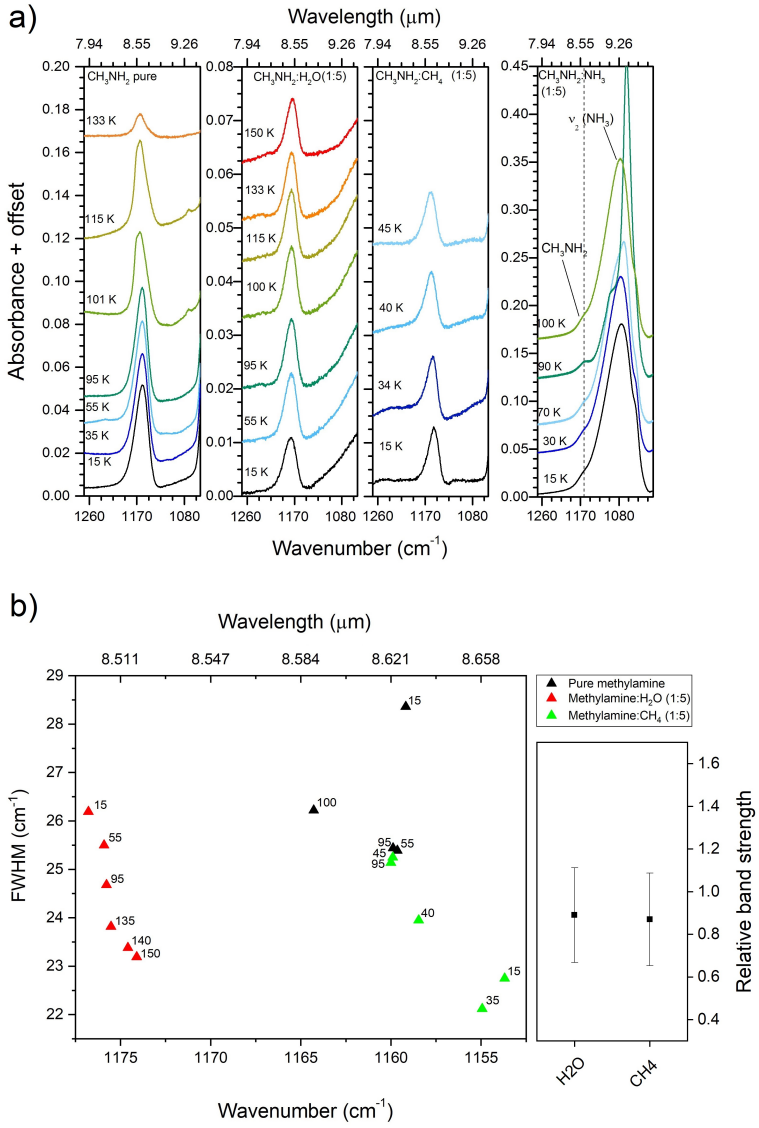

Figure 4.4: a) Infrared profile of the CH_3 rock vibrational mode of CH_3NH_2, around 1159 cm^{-1}, in pure and mixed ices. The first and the last panels are displayed at a different Y-scale. In the last panel, the CH_3NH_2 feature (whose position is indicated by the dashed line) appears as a shoulder in the ammonia ν_2 band (umbrella mode). b) Left panel: peak position vs. FWHM for the CH_3 rock band in the ice mixtures displayed in a). Different mixtures are indicated by different colors, and the ice temperatures are marked in the graph. Right panel: relative band strength of the CH_3 rock vibrational mode in different ice mixtures at 15 K.

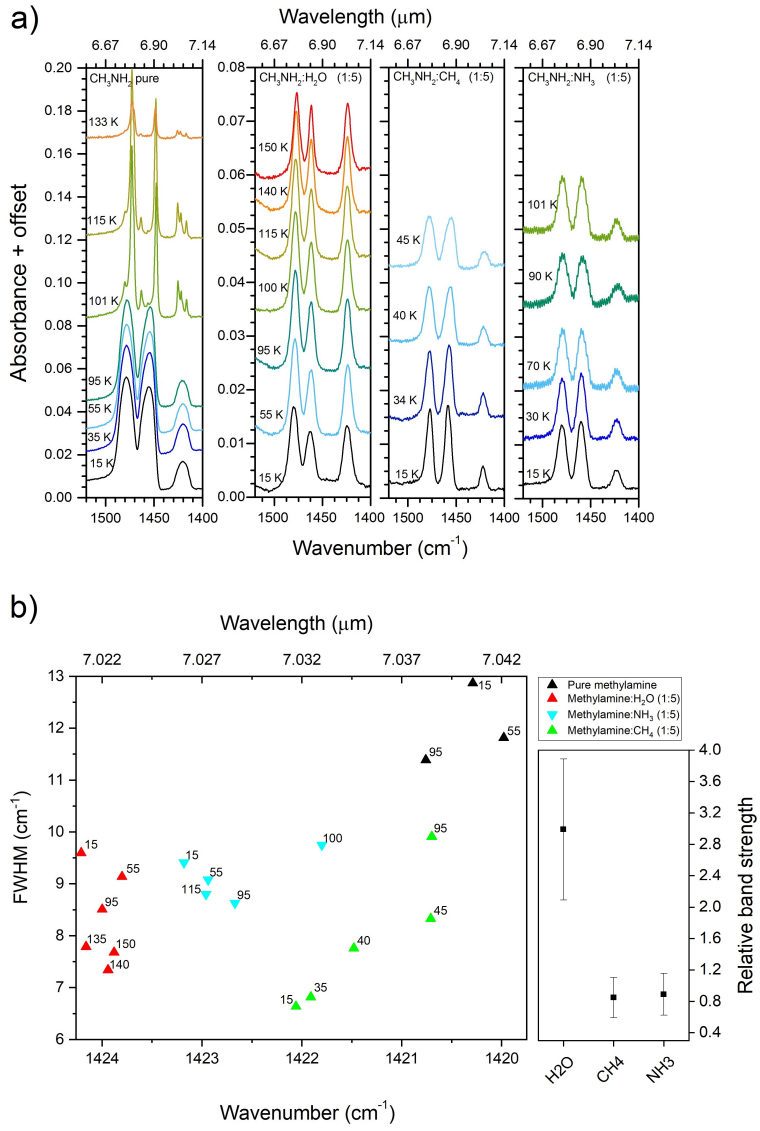

Figure 4.5: a) Infrared profile of the CH_3 antisymmetric deformation mode of CH_3NH_2 (the peaks around 1478.6 cm^{-1} and 1455.0 cm^{-1}) and the CH_3 symmetric deformation mode (around 1420 cm^{-1}), in pure and mixed ices. b) Left panel: peak position vs. FWHM for the CH_3 symmetric deformation band (1420 cm^{-1}) in the ice mixtures displayed in a). Different mixtures are indicated by different colors, and the ice temperatures are marked in the graph. Right panel: relative band strength of the CH_3 symmetric deformation band (1420 cm^{-1}) in different ice mixtures at 15 K. Panels c) and d): same as b) for the CH_3 antisymmetric deformation modes, ν_5 and ν_{12}, at 1455 cm^{-1} and 1478.6 cm^{-1}, respectively.

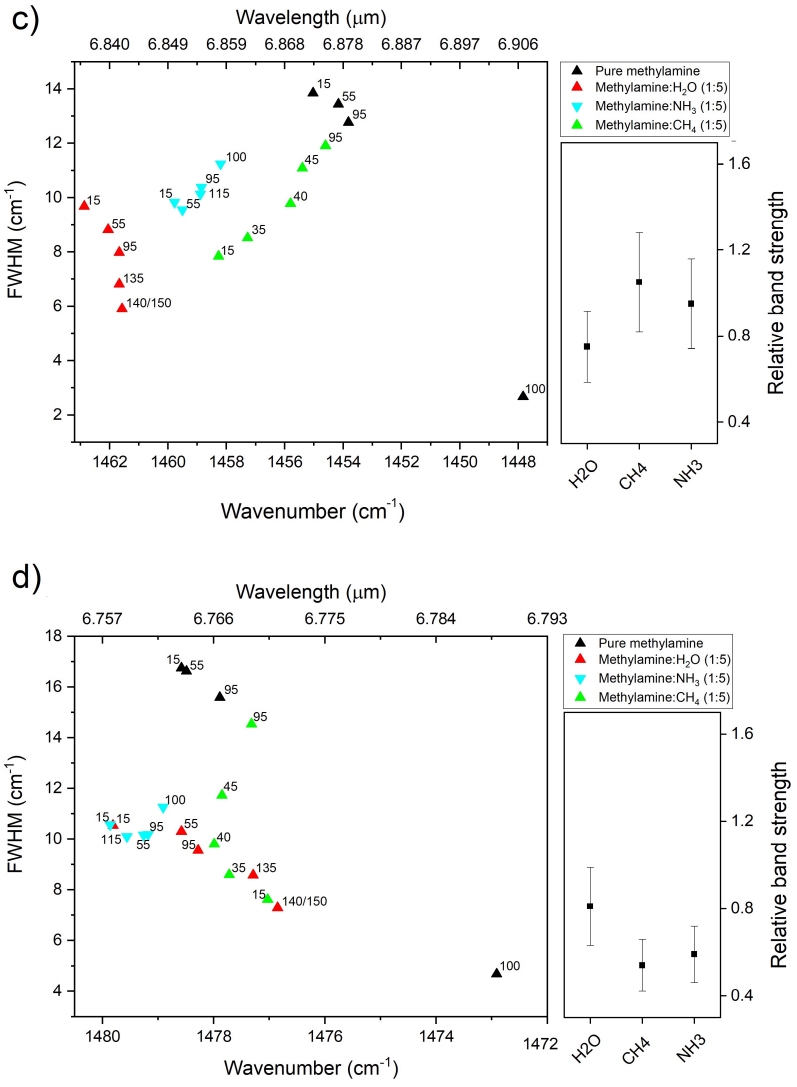

Figure 4.5: Continued.

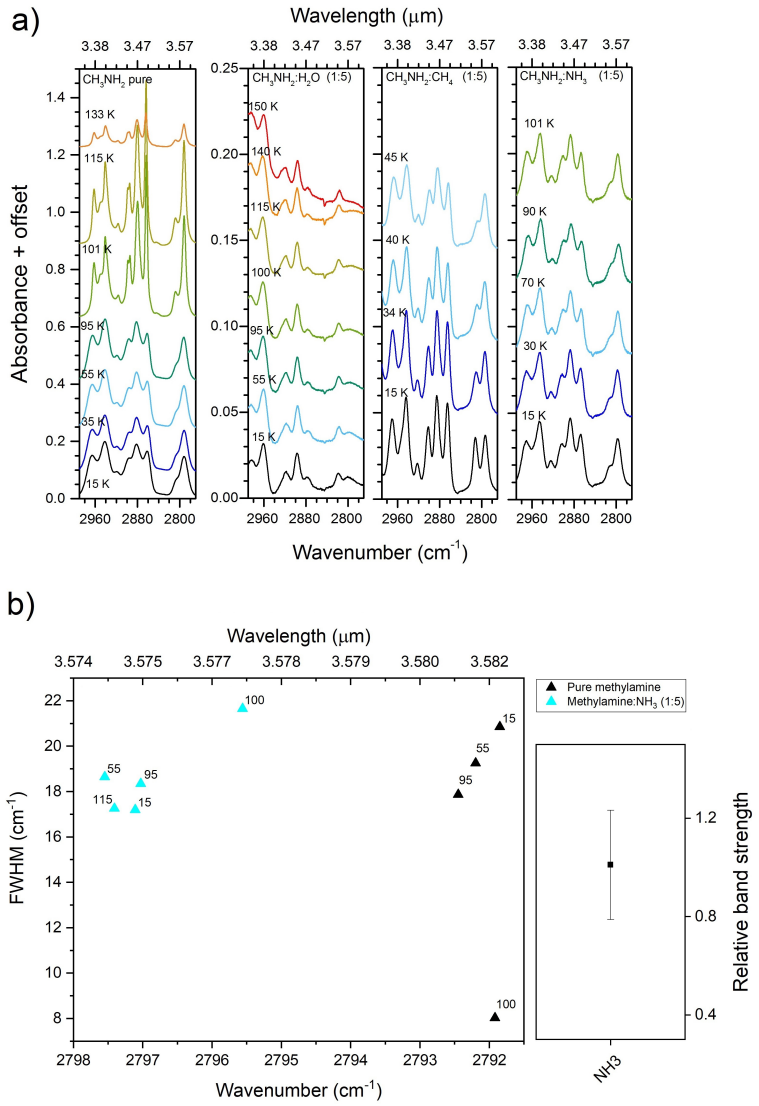

Figure 4.6: a) 2750 - 3000 cm^{-1} spectral region in pure and mixed CH_3NH_2 ices. The CH_3 antisymmetric stretching mode (around 2881 cm^{-1}) and the CH_3 symmetric stretching mode (around 2792 cm^{-1}) are displayed in the panels. b) Left panel: peak position vs. FWHM for the CH_3 symmetric stretching band in pure CH_3NH_2 and CH_3NH_2:NH_3(1:5) ices. Different mixtures are indicated by different colors, and the ice temperatures are marked in the graph. Right panel: relative band strength of the CH_3 symmetric stretching band in pure CH_3NH_2 and CH_3NH_2:NH_3(1:5) ices at 15 K. c) same as b) for the CH_3 antisymmetric stretching band (around 2881 cm^{-1}) in the ice mixtures displayed in a).

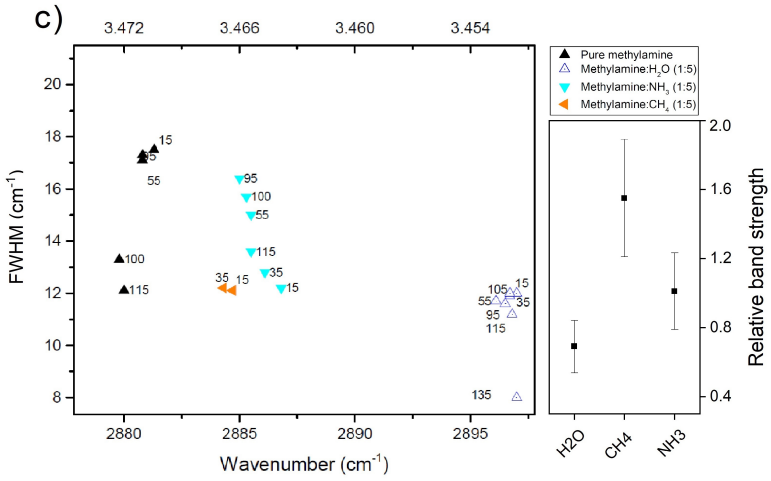

Figure 4.6: Continued.

Finally, the peak position, FWHM, and intensity of both features assigned to CH_3 antisymmetric deformation do not change dramatically after ice matrix crystallization compared to other methylamine bands. These peaks are also detectable even in the most diluted mixtures, offering perspective for use as a methylamine tracer.

The 3000 - 2700 cm^{-1} region

As previously shown, the IR spectrum of pure methylamine ice shows strong bands in the 3000 - 2700 cm^{-1} region (Figure 4.3). As can be seen in the spectra of 1:5 mixtures of methylamine with H_2O, CH_4, and NH_3 (Figure 4.6), bands in this region are blended, but some of the stronger features can be identified. The stretching modes and the overtones of deformation modes in this region have a similar profile as in most of the CH_3-bearing molecules, making it very difficult to look for particularities of the methylamine molecule. Figures 4.6, 4.A.9, 4.A.10, 4.A.11, and 4.A.12 show the spectra in the 3000 - 2750 cm^{-1} region for all analyzed ice mixtures. The features that are chosen for characterization in this region are the CH_3 antisymmetric stretching (2881.3 cm^{-1}) and CH_3 symmetric stretching (2791.8 cm^{-1}) bands. The peak position and FWHM for these bands are measured and presented in Appendix B (Tables B10 to B15).

In pure amorphous methylamine ice, the CH_3 symmetric stretch, around 2791.8 cm^{-1}, seems to have two overlapping components. In all the ice mixtures, the two

components appear as two separate features (see Figure 4.6). The component at higher wavenumbers occurs at the same position as the $\nu_2 + \nu_4$ combination mode of methane (around 2815 cm^{-1}), being difficult to separate (Figure 4.A.11 and 4.A.12). The component at lower wavenumbers (around 2796 cm^{-1}) is visible in all ice spectra, although it appears as a weaker feature in the H_2O matrix.

In H_2O-containing ices, methylamine features in the 3000 - 2750 cm^{-1} region have an overall different profile compared to similar features in non-containing H_2O matrices. This seems to be particular for the CH_3 vibrational modes since such changes are not observed for the other vibrational modes. In CH_3NH_2:H_2O ices, the strongest peak in this region is due to a CH_3 antisymmetric stretching band located at 2898 cm^{-1}. This feature is visible in all the mixtures, and in matrices containing H_2O and CH_4 it partially overlaps with the ν_1 mode of CH_4 (Herrero et al., 2010). This overlap can be noticed in Figures 4.A.11 and 4.A.12, where the 2898 cm^{-1} feature of CH_3NH_2 is wider than in H_2O, CH_4 and NH_3 matrices at temperatures below 50 K (Figures 4.6, 4.A.9 and 4.A.10). Above 50 K, CH_4 starts to desorb and the remaining feature is similar to the 2898 cm^{-1} band observed in the CH_3NH_2:H_2O ices. In H_2O:NH_3:CH_3NH_2 and H_2O:NH_3:CH_3NH_2:CH_4 ices, the bands in the 3000 - 2700 cm^{-1} region are difficult to resolve due to the overlap with broad absorption bands from H_2O:NH_3 hydrates (Moore et al., 2007). Some of the methylamine features are clear in the mixtures with dilution 1:10, but appear as very weak peaks in dilution of 1:20 (Figures 4.A.11, and 4.A.12).

A particularity of the ices in which methylamine is mixed in water is the appearance of a broad and strong feature centered around 2760 cm^{-1}. Figure 4.7 shows the feature in all the CH_3NH_2:H_2O ice mixtures at 15 K. The appearance of such a broad profile is also noticed in the CH_3NH_2:CH_4 containing ices and in the CH_3NH_2:H_2O:NH_3 matrices, though this last is less perceptible due to the overlap with the broad ammonia hydrate feature centered around 2900 cm^{-1}. The 2760 cm^{-1} feature is visible during the warming up of the ice mixtures and disappears only when methylamine desorbs from the ice. This band is likely due to the interaction of the N-H stretching mode of methylamine with the water O-H stretching mode and is possibly analogous to the ammonia hydrate feature observed in H_2O:NH_3 ices (Dartois and d'Hendecourt, 2001). Since this feature appears in a region of the mid-infrared spectrum that is free from strong absorption from abundant interstellar ice components, this band could indicate the presence of methylamine in H_2O-rich ices. However, other molecules containing an N-H group may show a similar absorption feature when embedded in H_2O matrix, which makes this band a not unambiguous tracer of any particular species.

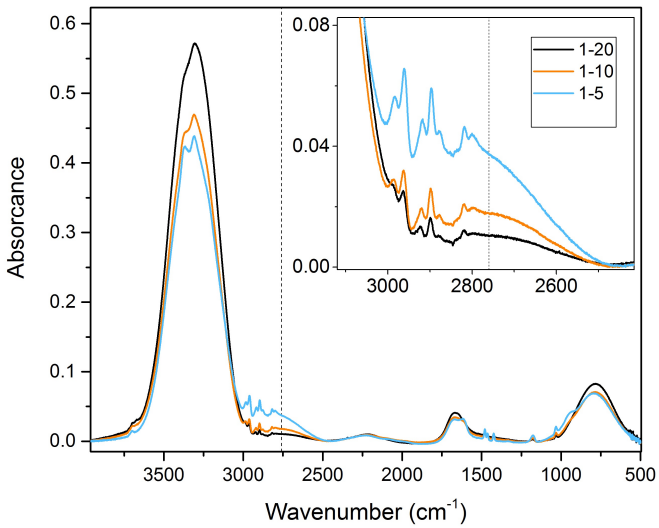

Figure 4.7: Infrared spectra of CH_3NH_2:H_2O at ratios 1:5 (blue), 1:10 (orange), and 1:20 (black) at 15 K. The center of the broad feature at 2760 cm^{-1} is marked with a dashed line. The top panel shows a zoom in the 3100 - 2400 cm^{-1} region of the spectra.

4.4 Astronomical implications

In dense molecular clouds, CH_3NH_2 is likely to be formed in regions that are rich in atomic C, H, and N, that is, in the less dense regions, or early in the cloud's life cycle, when also H_2O, CH_4, and NH_3 are formed (Ioppolo et al., 2020). Using a gas-grain astrochemical kinetic model (Garrod 2013) that involves only non-energetic reactions, Ioppolo et al. (2020) showed that methylamine can be formed by barrierless reactions on the surface of interstellar icy grains during the prestellar core collapse. After the core collapse, the methylamine abundance in the ice mantle reaches 0.65 percent relative to H_2O, which is comparable to the abundance for solid CH_4 in the model. However, significantly higher solid CH_4 abundances (1 - 11 percent relative to H_2O; (Öberg et al., 2008)) are observed toward Young Stellar Objects (YSOs). This suggests that solid methylamine may also be detectable in dense clouds and YSO envelopes, and the data presented here offer a tool to do so.

The challenge for methylamine identification in interstellar ice is related to the fact that most of its strongest modes, explored in the previous sections, overlap with features from other abundant interstellar ice and dust components (e.g., CH_3OH, NH_3, silicates). In a realistic astronomical scenario, even the features that are easily

identified in the laboratory will likely appear blended with bands from other species. The following sections describe the potential of solid methylamine absorption features as tracers of its presence in mid-infrared observations.

4.4.1 CH_3NH_2 in the 3 - 4 μm wavelength range

The methylamine features in the 3400 -2500 cm^{-1} (2.94 - 4.0 μm) region have the advantage of being observable with ground-based telescopes at resolving power R>1000, which is much higher than that for spectra in the 5 - 10 μm range observed with Spitzer/IRS (R $\sim$ 100). Figure 4.8 shows a comparison of the CH_3NH_2:H_2O(1:10) ice spectrum at 15 K with low and high-mass YSO spectra obtained with Keck/NIRSPEC, VLT/ISAAC, and IRTF/SpeX (Boogert et al. 2008, Emerson & Boogert 2021 (in prep)). The peak positions of the methylamine features at 2898 cm^{-1} (3.451 μm), 2796 cm^{-1} (3.576 μm), and the broad feature at 2760 cm^{-1} (3.623 μm) are marked with vertical dashed lines. In H_2O mixtures, the band from the CH_3 antisymmetric stretching mode at 2898 cm^{-1} is the strongest methylamine feature in this region. It appears close to the CH_3 stretching bands from other organic molecules (e.g., acetaldehyde, ethanol) and the ν_1 mode of CH_4 observed in CH_4:H_2O ices, as discussed on the previous section. Still, at the high resolving power, this relatively narrow absorption feature is best suited to constrain the methylamine abundance. On the other hand, while the methylamine CH_3 antisymmetric stretching feature at 2796 cm^{-1} peaks at wavenumbers lower than most of the CH_3 stretching vibrations of abundant ice species, its strength is significantly suppressed in H_2O matrices.

The broad feature at 2760 cm^{-1} is observed in CH_3NH_2:H_2O ice samples with a methylamine abundance as low as 5% relative to H_2O and is in a spectral region where few abundant interstellar ice molecules have absorption peaks. As can be seen from Figure 4.8, such a broad feature centered at 2760 cm^{-1} is not promptly identified in the YSO spectra. We find that abundance estimates from this shallow band are strongly limited by the baseline choice, and stronger constraints are obtained from the CH_3 antisymmetric stretching mode at 2898 cm^{-1}. In an alternative scenario where methylamine is embedded in an apolar ice environment, the 2760 cm^{-1} feature would be absent. This seems an unlikely scenario since the formation routes of methylamine may well pass through NH_2 and CH_3 radicals in a H_2O matrix (Garrod, 2013; Ioppolo et al., 2020).

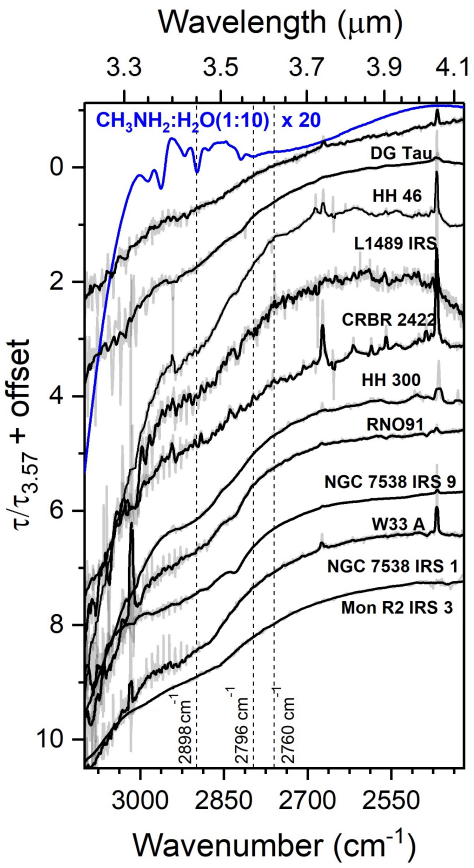

Figure 4.8: Comparison between the IR profile of YSOs and the absorption spectra of the CH_3NH_2:H_2O(1:10) ice at 15 K (top blue curve). All the YSO spectra are normalized in relation to the optical depth at 2800 cm^{-1} (3.57 μm). The gray lines are the original spectra and the black lines are the smoothed spectra. The smoothing uses a 15-point boxcar, that corresponds to a window of 4 - 6 cm^{-1} in the analyzed spectra. The position of the methylamine bands at 2898 cm^{-1}, 2796 cm^{-1}, and the feature at 2760 cm^{-1} are marked with dashed lines.

4.4.2 CH_3NH_2 in the 5 - 8 μm wavelength range

In the 1700 - 1250 cm^{-1} ($\sim$ 5.9 - 8.0 μm) range, airborne and space-based observations revealed a series of ice absorption features (Soifer et al., 1979; Schutte et al., 1996). Among the likely carriers of these features are many hydrocarbons and oxygen-bearing species, such as methanol (CH_3OH), formaldehyde (H_2CO), formic acid (HCOOH), acetaldehyde (CH_3CHO), ethanol (CH_3CH_2OH), the formate ion ($HCOO^-$) and others

(Tielens et al., 1984; Schutte et al., 1996; Keane et al., 2001; Knez et al., 2005; Boogert et al., 2008; Bottinelli et al., 2010; Öberg et al., 2011; Boogert et al., 2015). Some N-bearing molecules have also been proposed as possible carriers, for example, NH_3, NH_4^+ (Schutte and Khanna, 2003), HCN, and a few suggestions for larger molecules, such as acetonitrile (CH_3CN), urea (H_2NCONH_2) and formamide ($HCONH_2$; Raunier et al. 2004).

Figure 4.9 shows a comparison of the infrared spectra of methylamine-containing ices with the mid-IR spectra of YSOs obtained by Spitzer/IRS (Boogert et al., 2008). As can be seen from the figure, the NH_2 deformation mode and the CH_3 symmetric deformation mode of methylamine, around 1613 cm^{-1} and 1424 cm^{-1}, respectively, coincide with the strong features observed in the YSOs. Methylamine could thus be one of the species that contribute to both of these features. However, because the observed features result from a blending of many absorbing species, it is not possible to significantly constrain the methylamine abundance. Future JWST observations at a resolving power of R $\sim$ 1000 - 3000, more than an order of magnitude better than Spitzer, will be better suited to search for weak substructures, possibly providing better ice abundance constraints.

4.4.3 CH_3NH_2 in the 8 - 13 μm wavelength range

In the 1200 - 800 cm^{-1} ($\sim$ 8 - 12.5 μm) region, the methylamine bands also overlap with features from abundant interstellar ice molecules. The CH_3 rock band, around 1159 cm^{-1} in pure methylamine, overlaps with the umbrella mode of NH_3 at 1070 cm^{-1}, appearing as weak shoulders in the laboratory spectra. Since ammonia is an abundant interstellar ice species, the band around 1159 cm^{-1} may not be suitable for methylamine identification. However, the presence of a shoulder at higher wavenumbers in the ammonia umbrella feature may be an indication of methylamine, but this again requires a high resolving power.

Methylamine also presents a strong peak around 903.5 cm^{-1} ($\sim$ 11.07 μm), assigned to the ν_9 mode, that was not characterized in this work due to the overlap with the libration band of H_2O ice. This peak appears in the same region as the broad torsion mode band of CH_3OH (around 700 cm^{-1}) and a feature around 902.5 cm^{-1} (11.08 μm) observed in some YSOs that has been assigned to crystalline silicates Do-Duy et al., 2020. Investigations concerning COMs that can contribute to the astronomical feature around 11.08 μm should consider methylamine as a carrier candidate.

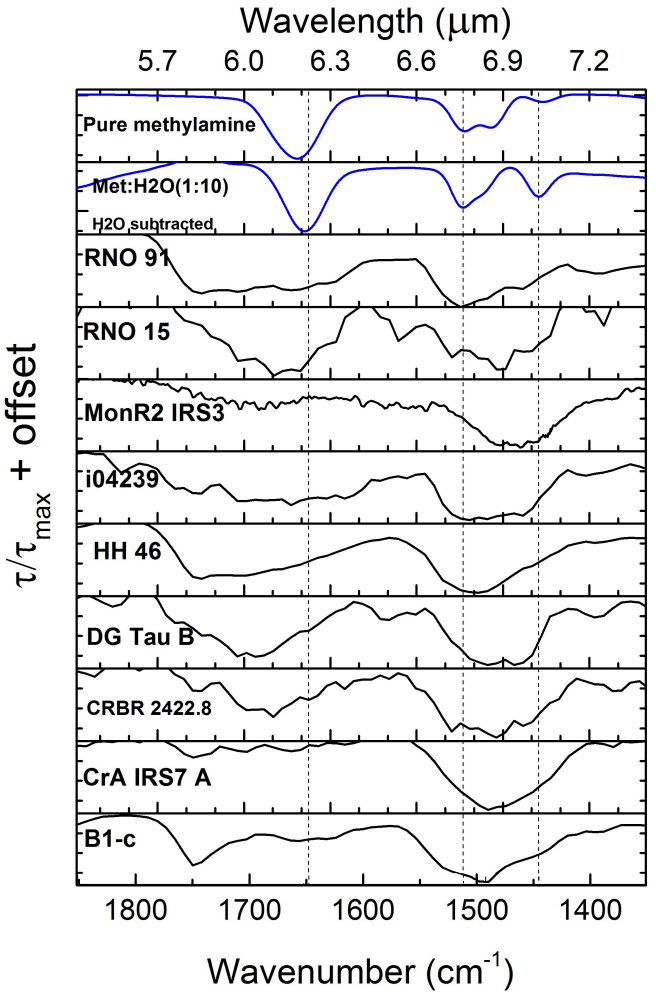

Figure 4.9: Comparison between laboratory spectra of methylamine-containing ices and some Spitzer/IRS spectra of YSOs (with H_2O subtracted) in the 5.4 - 7.4 μm range (Boogert et al., 2008). The two top panels show the spectra of pure methylamine ice at 15 K and the H_2O subtracted CH_3NH_2:H_2O(1:10) ice spectra at 15 K. The vertical dashed lines mark the peak positions of the bands in this mixture. The laboratory spectra are convolved with a Gaussian profile with FWHM corresponding to the Spitzer/IRS resolution (R = 100). Both the laboratory and YSO spectra are normalized with respect to the 1612.9 cm^{-1} (6.2 μm) feature for better visualization.

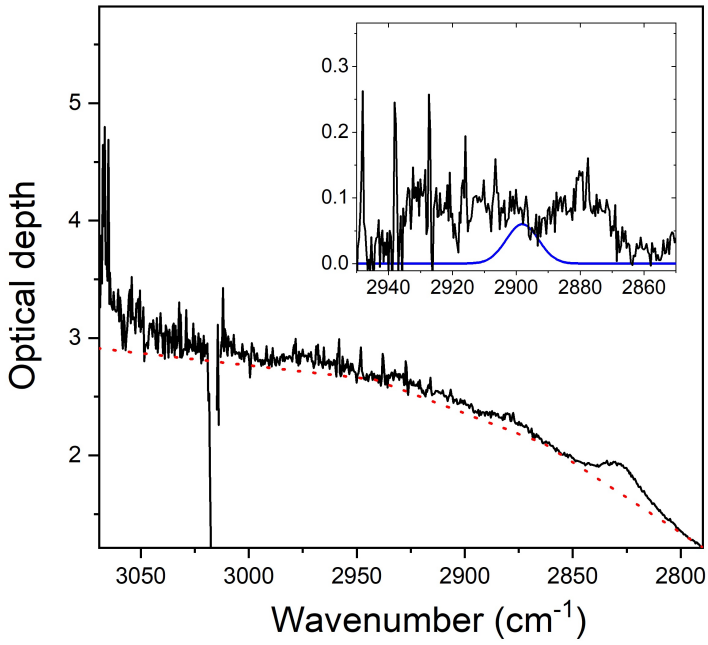

Figure 4.10: Example of the adjustment of a local baseline in the W33A spectrum (red dotted line). The top right panel shows the subtracted spectra in the 2850 cm^{-1} - 2950 cm^{-1} region and the adjusted Gaussian feature (blue) expected from CH_3NH_2 in an H_2O matrix.

4.4.4 CH_3NH_2 abundances

With the currently available observations of YSO envelopes, the best estimate of the methylamine abundance is obtained from the 3000 - 2700 cm^{-1} region (Figure 4.8). No distinct feature due to methylamine is detected in the ground-based spectra, and the tightest upper limit can be obtained from the feature around CH_3 antisymmetric stretching mode (around 2898 cm^{-1} in CH_3NH_2:H_2O ices). The column density upper limit (N) of methylamine can be estimated from the FWHM and the band strength (A') of the 2898 cm^{-1} feature:

$$N \leq \frac{\tau_\nu \times FWHM}{A'}, \tag{4.8}$$

where A' = 1.48×10^{-18} is the band strength for the 2898 cm^{-1} feature and FWHM = 11.8 cm^{-1} (adopting the value for the CH_3NH_2:H_2O(1:10) ice mixture, see Appendix A), and τ_ν is the optical depth of the peak in the YSO spectra. For obtaining the optical depth, a local baseline is subtracted from the region around the 2898 cm^{-1},

and τ_ν is taken as the maximum optical depth that is consistent with the absence of a peak centered at 2898 cm^{-1} (with FWHM = 11.8 cm^{-1}) in the YSO spectra. Figure 4.10 shows an example of this procedure. The derived methylamine upper limits are shown in Table 4.4 along with predicted values and the abundance observed in the Comet 67P.

Table 4.4: Methylamine upper limits using the CH_3 antisymmetric stretching band at 2898 cm^{-1}. The methylamine abundances detected in the comet 67P/Churyumov-Gerasimenko and the predicted abundance for gas-grain astrochemical models of prestellar cores are also presented for comparison.

Source	N(CH_3NH_2) 10^{17} cm^{-2}	(% H_2O)
CRBR2422.8-342	$\leq$ 6.7	16
L1489 IRS	$\leq$2.3	5.3
HH46	$\leq$8.4	10
DG Tau	$\leq$1.7	7.4
RNO91	$\leq$2.5	5.9
HH300	$\leq$2.1	8.0
Mon R2 IRS 3	$\leq$0.8	5.3
NGC 7538 IRS 1	$\leq$0.8	3.1
NGC 7538 IRS 9	$\leq$1.7	2.6
W33 A	$\leq$4.2	3.4
Comet 67P[a,b]	-	0.16
Model[c]	-	0.65

[a]Le Roy et al. (2015) [b]Altwegg et al. (2016)
[c]Ioppolo et al. (2020)

As can be seen in Table 4.4, the methylamine upper limits values range from 2.6 to 16 percent in relation to water. The higher upper limits obtained for CRBR2422.8-342 and HH46 are a consequence of the lower S/N in the spectral region in comparison with some other objects (e.g., NGC 7538 IRS 1, NGC 7538 IRS 9, W33 A). For the YSO spectra with higher S/N, the abundance of methylamine is constrained to less than a few percent relative to H_2O, which is at the level of tentatively detected COMs (Öberg et al., 2011; Terwisscha van Scheltinga et al., 2018). Still, the calculated values are higher than the methylamine abundance of 0.65 relative to H_2O from the gas-grain model presented by Ioppolo et al. (2020). This indicates that current IR observations of ices around YSOs are not sensitive enough to probe the solid methylamine budget, and are so unable to significantly constrain the accuracy of methylamine formation

models. Observations at higher spectral resolution and sensitivity across the full 3 -10 μm wavelength range with the JWST mission toward a wider variety of dense clouds and YSO targets should provide tighter constraints on the presence of COMs in the ices. The JWST early release program ICE AGE (McClure et al., 2018) targets a search for COM ice features in the wavelength domain studied here. The data presented in this work will support the interpretation of future data, helping to understand the chemical inventory of ices in star-forming regions.

4.5 Conclusions

This work reports a set of systematically measured infrared spectra of methylamine-containing ices in astronomically relevant conditions. The following methylamine features are selected for peak position and FWHM characterization in the studied ices: the CH_3 antisymmetric stretching band around 2881.3 cm^{-1} (3.453 μm), the CH_3 symmetric stretching band around 2791.8 cm^{-1} (3.582 μm), the CH_3 antisymmetric deformation bands around 1455.0 cm^{-1} and 1478.6 cm^{-1} (6.873 μm and 6.761 μm), the CH_3 symmetric deformation band around 1420.3 cm^{-1} (7.042 μm), and the CH_3 rock around 1159.2 cm^{-1} (8.621 μm). The mid-IR band strengths of pure methylamine ice (in the transmission mode) for the selected vibrational modes and the refractive index at 632.8 nm are, to the best of our knowledge, reported here for the first time. The relative band strengths of methylamine in the ice mixtures are also derived. These values are essential for estimating methylamine abundances in astronomical IR spectra. The main conclusions of this work are summarized below:

1. The interaction of methylamine with the H_2O matrix induces substantial changes in the methylamine absorption profile, such as an enhancement in the strength of the CH_3 antisymmetric stretching (at 2898 cm^{-1}) in relation to other methylamine features in the 3000 - 2700 cm^{-1} region, an enhancing in the CH_3 symmetric deformation mode (1425 cm^{-1}) strength, and the appearance of a broad and strong feature centered at 2760 cm^{-1}. This last feature appears in a region where few abundant interstellar ice species absorb, and therefore may also offer a tool to search for the presence of methylamine in interstellar ice.

2. The comparison of the methylamine-containing ices with mid-infrared spectra of some YSOs shows that despite some overlap between laboratory and astronomical data, no feature can be unambiguously assigned to methylamine. The methylamine bands are hard to be used as tracers due to blending with bands

from other molecules. Even the bands that are distinguishable in the laboratory ice data and are characterized in this work have limited use to identify methylamine.

3. From the work presented here, upper limits for methylamine are derived based on the CH_3 antisymmetric stretching mode (at 2898 cm^{-1} in CH_3NH_2:H_2O ices). In some of these YSOs, the methylamine abundance with respect to water is less than 4%.

Given the complexity of an IR spectra, final assignments are only made by identifying a collection of features that reflect the peak position, bandwidths, and intensities reported in reference laboratory spectra. With the upcoming JWST observations of ices, weaker solid-state features, not present in the available ice data, may be revealed. Within the ICE AGE program, several targets are envisaged to search for COM ice features in the wavelength domain studied here. The data presented in this work will support the interpretation of future JWST spectra, helping to understand the chemical inventory of ices in star-forming regions.

References

Altwegg, K., Balsiger, H., Bar-Nun, A., et al., 2016, Science advances, 2, e1600285
Atoji, M and Lipscomb, W., 1953, Acta Crystallographica, 6, 770
Belloche, A, Menten, K., Comito, C., et al., 2008, A&A, 492, 769
Beltrán, M. D., Molina, R. L., Aznar, M. Á. S., et al., 2015, Sensors, 15, 25123
Bøgelund, E. G., McGuire, B. A., Hogerheijde, M. R., et al., 2019, A&A, 624, A82
Boogert, A. C. A, Gerakines, P. A., and Whittet, D. C., 2015, ARA&A, 53, 541
Boogert, A. C. A., Pontoppidan, K. M., Knez, C., et al., 2008, ApJ, 678, 985
Bossa, J.-B., Duvernay, F., Theulé, P., et al., 2009, A&A, 506, 601
Bossa, J.-B., Borget, F., Duvernay, F., et al., 2010, Journal of Physical Organic Chemistry, 23, 333
Bottinelli, S., Boogert, A. A., Bouwman, J., et al., 2010, ApJ, 718, 1100
Dartois, E and d'Hendecourt, L, 2001, A&A, 365, 144
Denbigh, K., 1940, Transactions of the Faraday Society, 36, 936
Do-Duy, T., Wright, C. M., Fujiyoshi, T., et al., 2020, MNRAS, 493, 4463
Durig, J. R. and Zheng, C., 2001, Structural Chemistry, 12, 137
Durig, J., Bush, S., and Baglin, F., 1968, J. Chem. Phys., 49, 2106
Elsila, J. E., Dworkin, J. P., Bernstein, M. P., et al., 2007, ApJ, 660, 911
Fedoseev, G., Ioppolo, S., Zhao, D., et al., 2015, MNRAS, 446, 439
Förstel, M., Bergantini, A., Maksyutenko, P., et al., 2017, ApJ, 845, 83
Fourikis, N, Takagi, K, and Morimoto, M, 1974, ApJ, 191, L139
Gardner, E. P. and McNesby, J. R., 1980, Journal of Photochemistry, 13, 353
Garrod, R. T., 2013, ApJ, 765, 60
Garrod, R. T., Weaver, S. L. W., and Herbst, E., 2008, ApJ, 682, 283
Glavin, D. P., Dworkin, J. P., and Sandford, S. A., 2008, Meteoritics & Planetary Science, 43, 399
Goesmann, F., Rosenbauer, H., Bredehöft, J. H., et al., 2015, Science, 349, 2.689
Herbst, E, 1985, ApJ, 292, 484

Herrero, V. J., Gálvez, Ó., Maté, B., et al., 2010, PCCP, 12, 3164
Hudson, R. L., Loeffler, M. J., Ferrante, R. F., et al., 2020, ApJ, 891, 22
Hudson, R., Loeffler, M., and Gerakines, P., 2017, J. Chem. Phys., 146, 024304
Ioppolo, S, Fedoseev, G, Chuang, K.-J., et al., 2020, Nat. Astronomy, 1
Kaifu, N, Morimoto, M, Nagane, K, et al., 1974, ApJ, 191, L135
Kayi, H., Kaiser, R. I., and Head, J. D., 2011, PCCP, 13, 11083
Keane, J., Tielens, A., Boogert, A., et al., 2001, A&A, 376, 254
Kim, Y. S. and Kaiser, R. I., 2011, ApJ, 729, 68
Knez, C., Boogert, A. C. A., Pontoppidan, K. M., et al., 2005, ApJL, 635, L145
Kvenvolden, K., Lawless, J., Pering, K., et al., 1970, Nat., 228, 923
Lavalley, J. and Sheppard, N, 1972, Spectrochimica Acta Part A: Molecular Spectroscopy, 28, 2091
Le Roy, L., Altwegg, K., Balsiger, H., et al., 2015, A&A, 583, A1
Leung, C. M., Herbst, E., and Huebner, W. F., 1984, ApJS, 56, 231
Linnartz, H., Ioppolo, S., and Fedoseev, G., 2015, Int. Rev. Phys. Chem., 34, 205
Maeda, S and Ohno, K, 2006, ApJ, 640, 823
Mahjoub, A. and Hodyss, R., 2018, ApJ, 869, 98
McClure, M. K., Boogert, A., Linnartz, H., et al. (2018). "The IceAge ERS Program: Probing Building blocks of Life During the JWST Era". *American Astronomical Society Meeting Abstracts# 232.* Vol. 232, 302.
McGuire, B. A., Carroll, P. B., Dollhopf, N. M., et al., 2015, ApJ, 812, 76
Moore, M. H., Ferrante, R., Hudson, R., et al., 2007, Icarus, 190, 260
Mumma, M. J. and Charnley, S. B., 2011, ARA&A, 49,
Noble, J., Theule, P, Duvernay, F, et al., 2014, PCCP, 16, 23604
Oba, Y., Chigai, T., Osamura, Y., et al., 2014, Meteoritics & Planetary Science, 49, 117
Öberg, K. I., Boogert, A. A., Pontoppidan, K. M., et al., 2008, ApJ, 678, 1032
Öberg, K. I., Boogert, A. A., Pontoppidan, K. M., et al., 2011, ApJ, 740, 109
Ogura, K, Migita, C., and Yamada, T, 1989, Journal of Photochemistry and Photobiology A: Chemistry, 49, 53
Ogura, K., Migita, C. T., and Yamada, T., 1988, Chemistry Letters, 17, 1563
Ohishi, M., Suzuki, T., Hirota, T., et al., 2019, Publications of the Astronomical Society of Japan, 71, 86
Qasim, D, Fedoseev, G, Chuang, K.-J., et al., 2020, Nat. Astronomy, 4, 781
Rachid, M. G., Terwisscha van Scheltinga, J, Koletzki, D, et al., 2020, A&A, 639, A4
Raunier, S., Chiavassa, T., Duvernay, F., et al., 2004, A&A, 416, 165
Romanescu, C., Marschall, J., Kim, D., et al., 2010, Icarus, 205, 695
Schutte, W. and Khanna, R., 2003, A&A, 398, 1049
Schutte, W., Tielens, A., Whittet, D., et al., 1996, A&A, 315, L333
Soifer, B., Puetter, R., Russell, R., et al., 1979, ApJ, 232, L53
Suzuki, T., Ohishi, M., Hirota, T., et al., 2016, ApJ, 825, 79
Tempelmeyer, K. and Mills Jr, D., 1968, Journal of Applied Physics, 39, 2968
Terwisscha van Scheltinga, J, Ligterink, N., Boogert, A., et al., 2018, A&A, 611, A35
Theulé, P., Borget, F., Mispelaer, F., et al., 2011, A&A, 534, A64
Tielens, A. G. G. M., Allamandola, L. J., Bregman, J, et al., 1984, ApJ, 287, 697
Vinogradoff, V., Duvernay, F., Danger, G., et al., 2013, A&A, 549, A40
Wolff, H, 1970, J. Chem. Phys., 52, 2800
Yamada, H. and Person, W. B., 1964, J. Chem. Phys., 41, 2478

Appendix A

This section presents the infrared spectra of pure and mixed methylamine ices. The spectra are focused on selected bands: the CH_3 antisymmetric stretch band around

2881.3 cm^{-1} (3.471 μm), the CH_3 symmetric stretch band around 2791.9 cm^{-1} (3.582 μm), the CH_3 antisymmetric deformation bands, at 1455.0 and 1478.6 cm^{-1} (6.873 μm and 6.761 μm), the CH_3 symmetric deformation band at 1420.3 cm^{-1} (7.042 μm), and the CH_3 rock at 1159.2 cm^{-1} (8.621 μm). Graphs displaying the peak position vs. FWHM for the bands and the relative band strengths are displayed at the bottom of each figure. The FWHM and peak position values displayed in the graphs are available from the Tables in Appendix B.

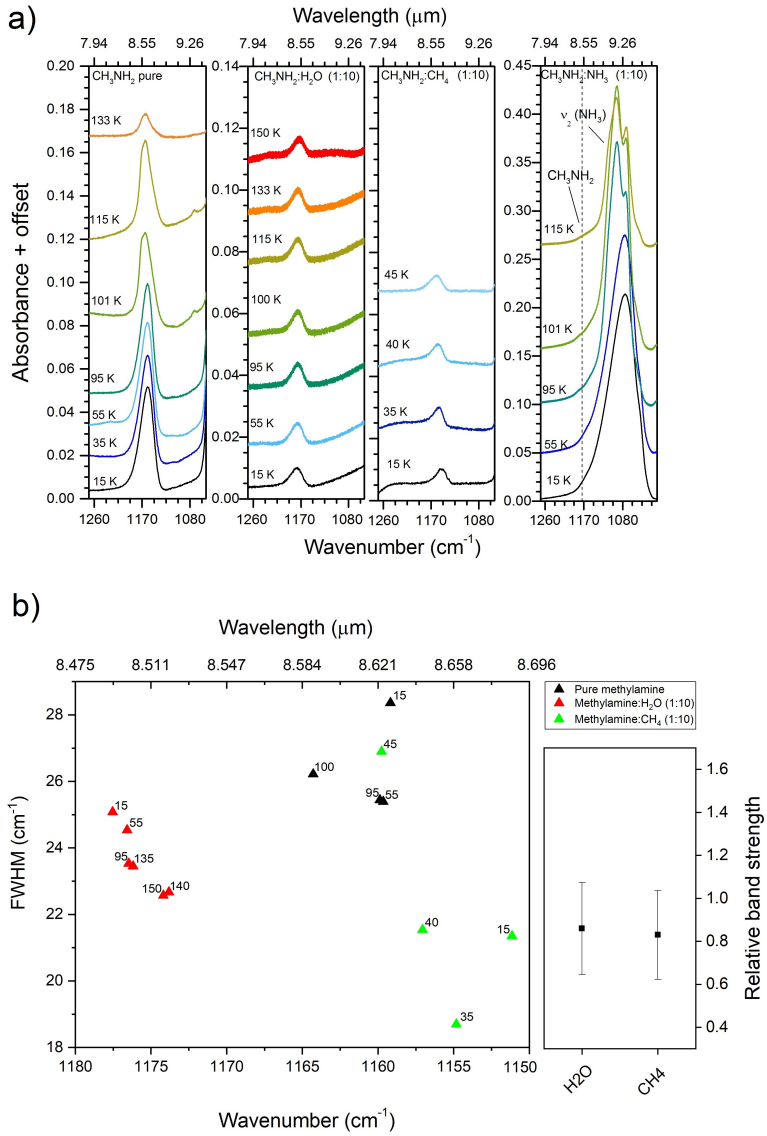

Figure 4.A.1: a) IR profile of the CH_3 rock vibrational mode of CH_3NH_2, around 1159 cm^{-1}, in pure and mixed ices. The first and the last panels are displayed at a different Y-scale. In the last panel the CH_3NH_2 feature (whose position is indicated by the dashed line) appears as a shoulder in the ammonia ν_2 band (umbrella mode). b) Left panel: peak position vs. FWHM for the CH_3 rock band in the ice mixtures displayed in a) Different mixtures are indicated by different colors, and the different temperatures are marked in the graph. Right panel: relative band strength of the CH_3 rock vibrational mode in different ice mixtures at 15 K.

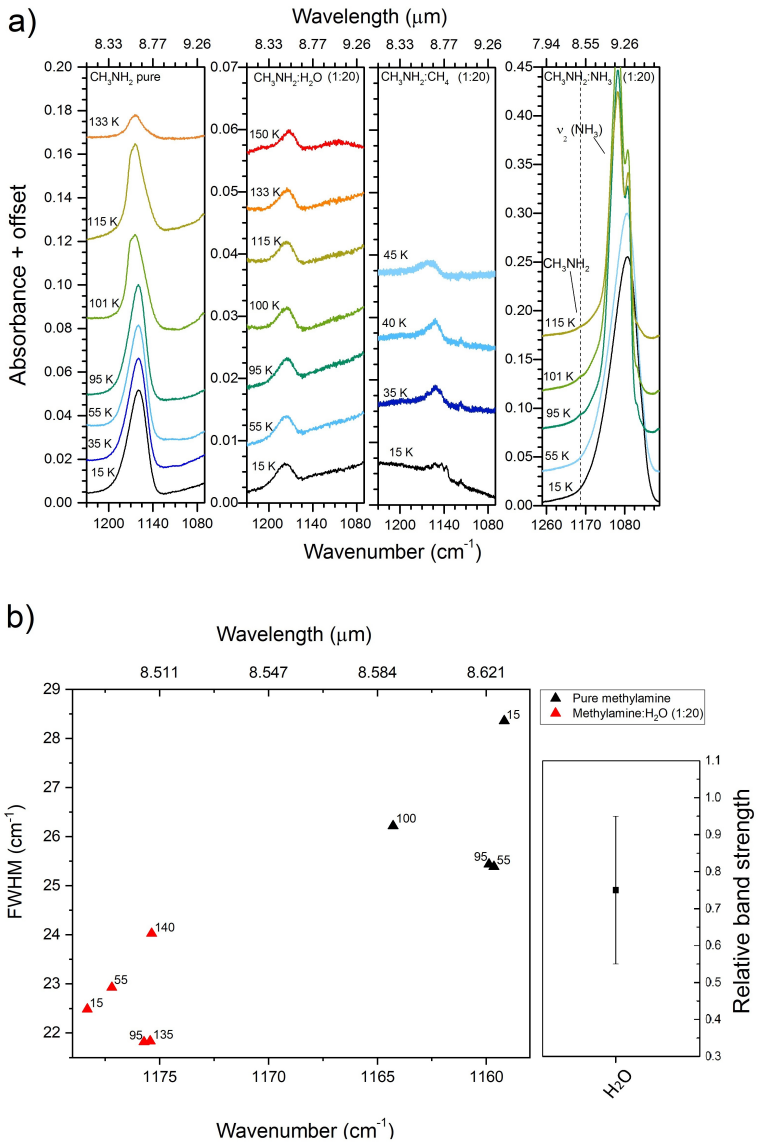

Figure 4.A.2: a) IR profile of the CH_3 rock vibrational mode of CH_3NH_2, around 1159 cm^{-1}, in pure and mixed ices. The first and the last panels are displayed at a different Y-scale. In the last panel the CH_3NH_2 feature (whose position is indicated by the dashed line) appears as a shoulder in the ammonia ν_2 band (umbrella mode). b) Left panel: peak position vs. FWHM for the CH_3 rock band in the ice mixtures displayed in in a) Different mixtures are indicated by different color and the different temperatures are marked in the graph. Right panel: relative band strength of the CH_3 rock vibrational mode at 15 K.

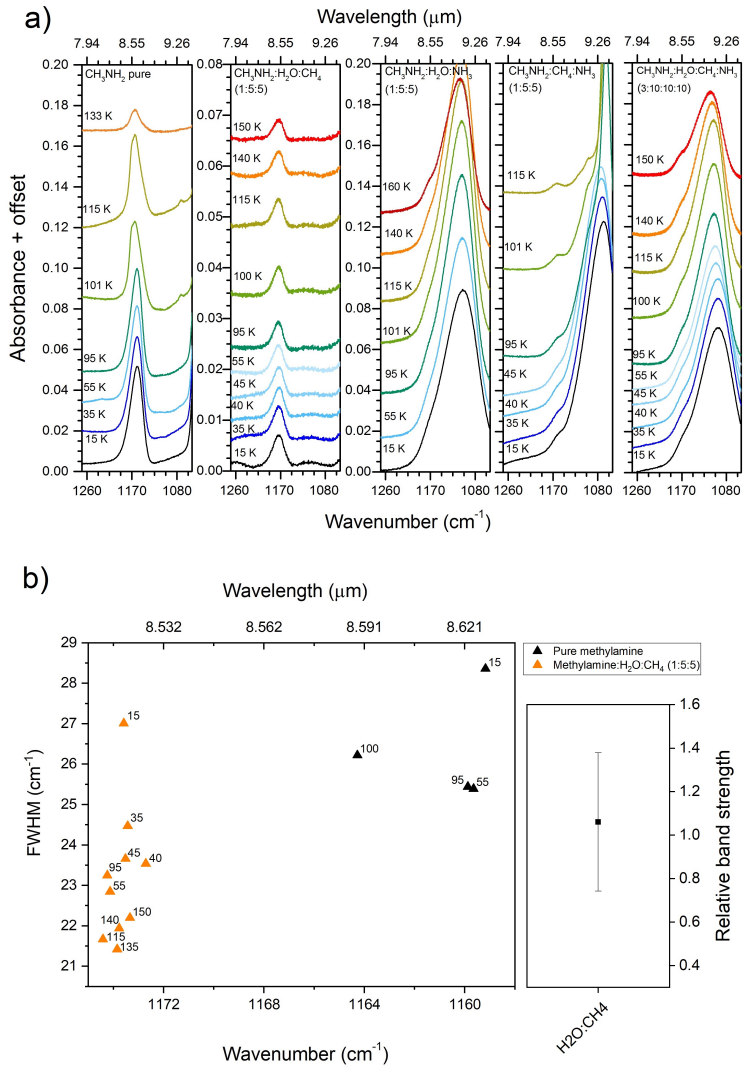

Figure 4.A.3: a) IR profile of the CH_3 rock vibrational mode of CH_3NH_2, around 1159 cm^{-1}, in pure and mixed ices. The panels are displayed at a different Y-scale. In the last three panels, the CH_3NH_2 feature appears as a shoulder in the ammonia ν_2 band (umbrella mode). b) Left panel: peak position vs. FWHM for the CH_3 rock band in the ice mixtures displayed in a) Different mixtures are indicated by different colors, and the different temperatures are marked in the graph. Right panel: relative band strength of the CH_3 rock vibrational mode at 15 K.

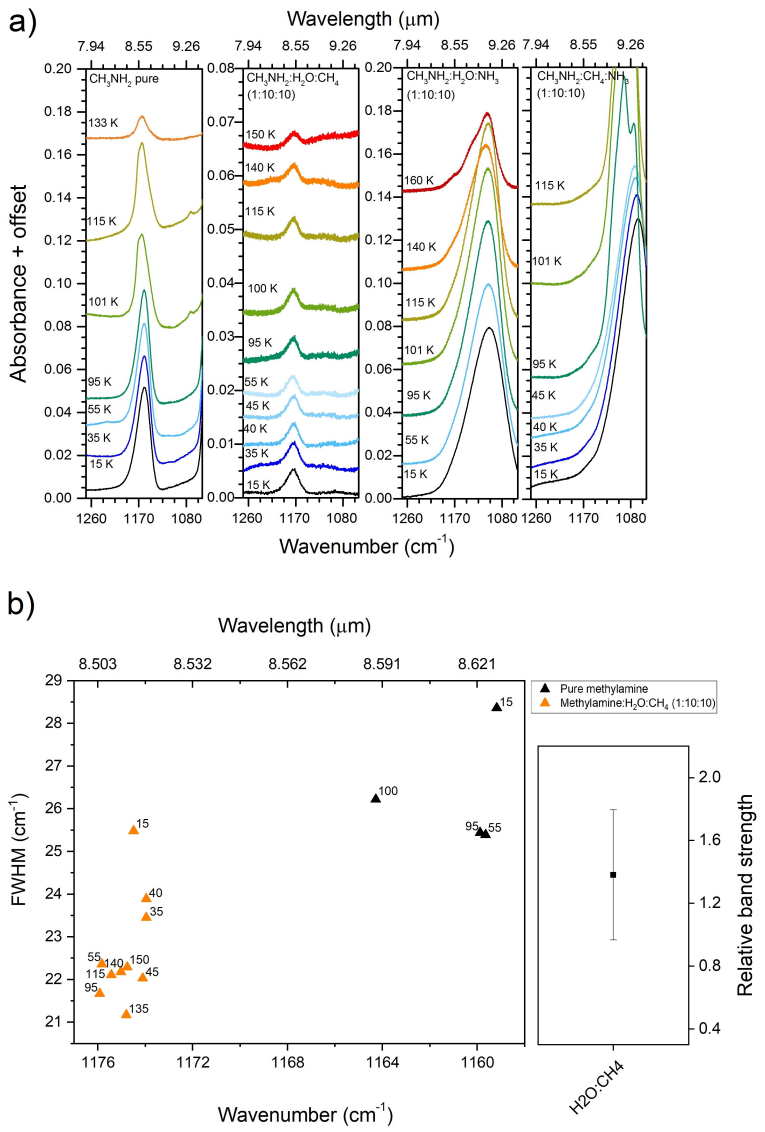

Figure 4.A.4: a) IR profile of the CH_3 rock vibrational mode of CH_3NH_2, around 1159 cm^{-1}, in pure and mixed ices. The last three panels are displayed at a different scale because the CH_3NH_2 feature appears as a shoulder in the band of the ammonia ν_2 mode (umbrella). b) Left panel: peak position vs. FWHM for the CH_3 rock band in the ice mixtures displayed in a) Different mixtures are indicated by different colors, and the different temperatures are marked in the graph. Right panel: relative band strength of the CH_3 rock vibrational mode at 15 K.

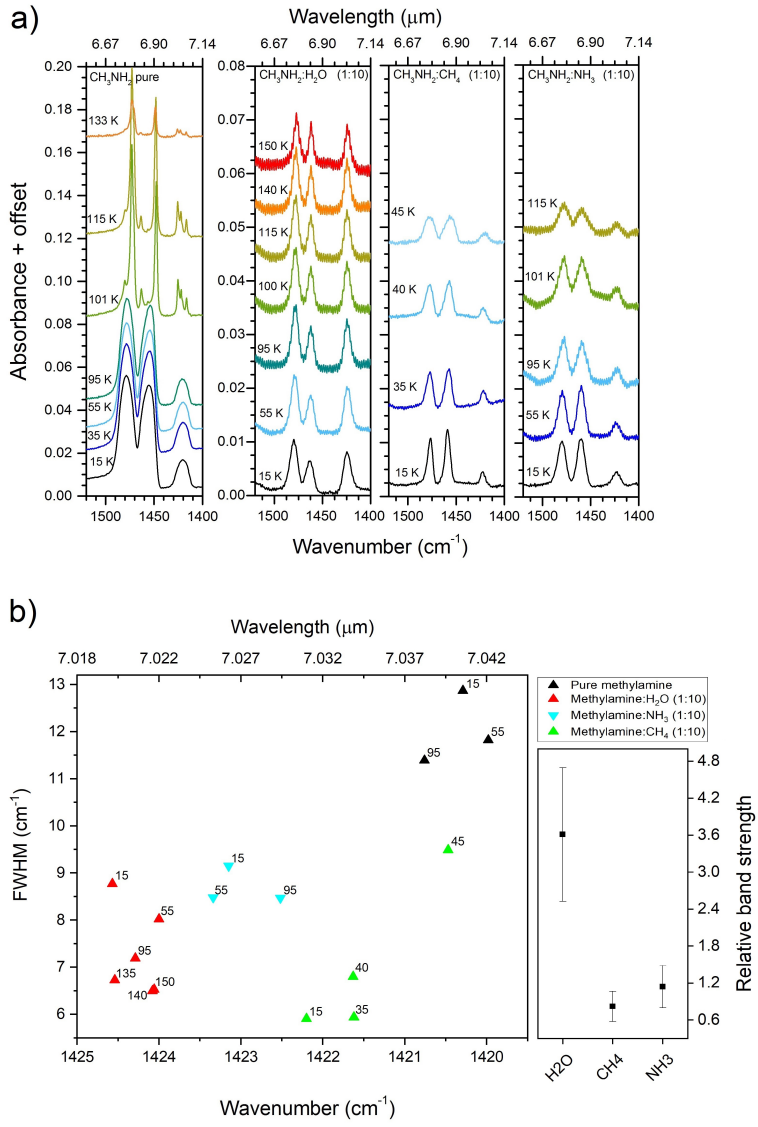

Figure 4.A.5: a) IR profile of the CH_3 antisymmetric deformation mode of CH_3NH_2 (around 1479 cm^{-1} and 1455 cm^{-1}) and the CH_3 symmetric deformation mode (around 1420 cm^{-1}), in pure and mixed ices. b) Left panel: peak position vs. FWHM for the CH_3 symmetric deformation band in the ice mixtures displayed in a) Different mixtures are indicated by different colors, and the different temperatures are marked in the graph. Right panel: relative band strength of the CH_3 symmetric deformation band (1420 cm^{-1}) in different ice mixtures at 15 K. Panels c) and d): same as b) for the CH_3 antisymmetric deformation modes, ν_5 and ν_{12}, at 1455 cm^{-1} and 1478.6 cm^{-1}, respectively.

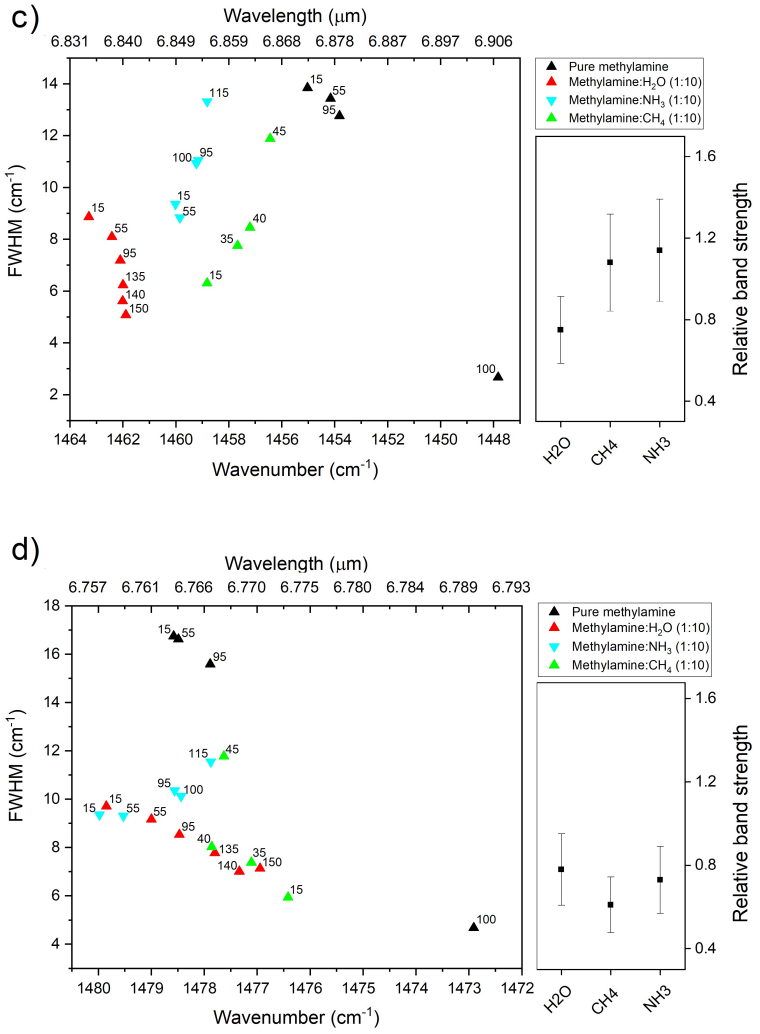

Figure 4.A.5: Continued.

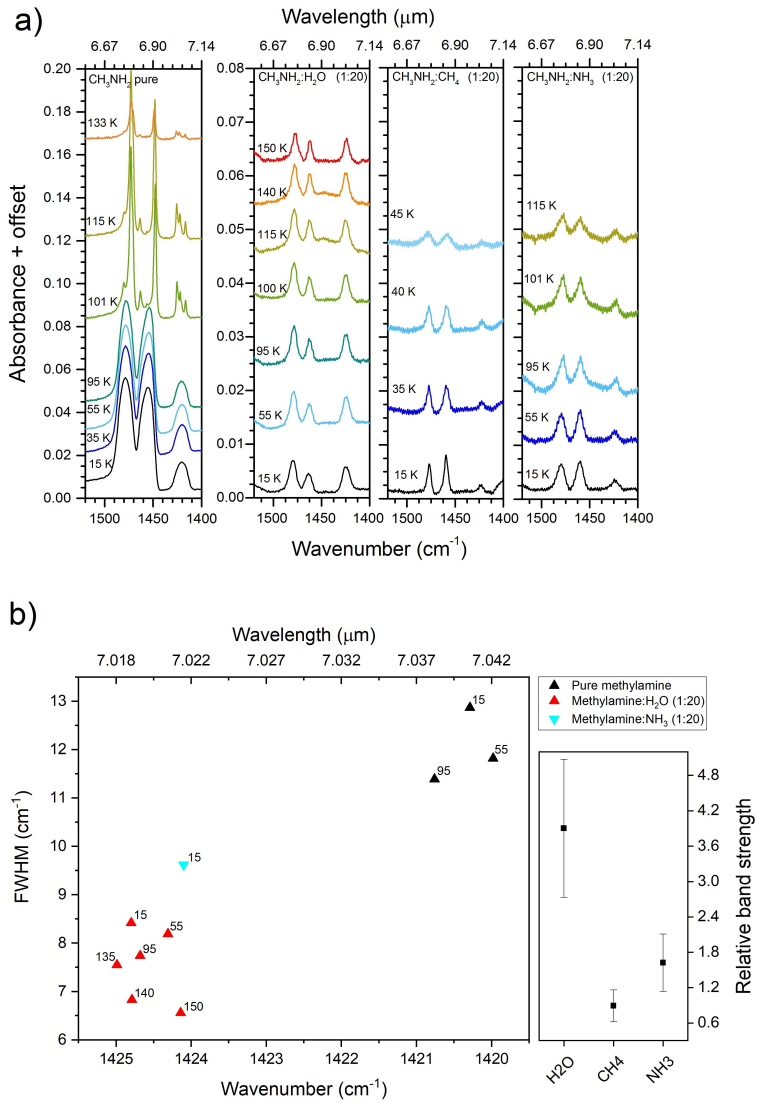

Figure 4.A.6: a) IR profile of the CH_3 antisymmetric deformation mode of CH_3NH_2 (around 1479 cm^{-1} and 1455 cm^{-1}) and the CH_3 symmetric deformation mode (around 1420 cm^{-1}), in pure and mixed ices. b) Left panel: peak position vs. FWHM for the CH_3 symmetric deformation band in the ice mixtures displayed in a) Different mixtures are indicated by different colors, and the different temperatures are marked in the graph. Right panel: relative band strength of the CH_3 symmetric deformation band (1420 cm^{-1}) in different ice mixtures at 15 K. Panels c) and d): same as b) for the CH_3 antisymmetric deformation modes, ν_5 and ν_{12}, at 1455 cm^{-1} and 1478.6 cm^{-1}, respectively.

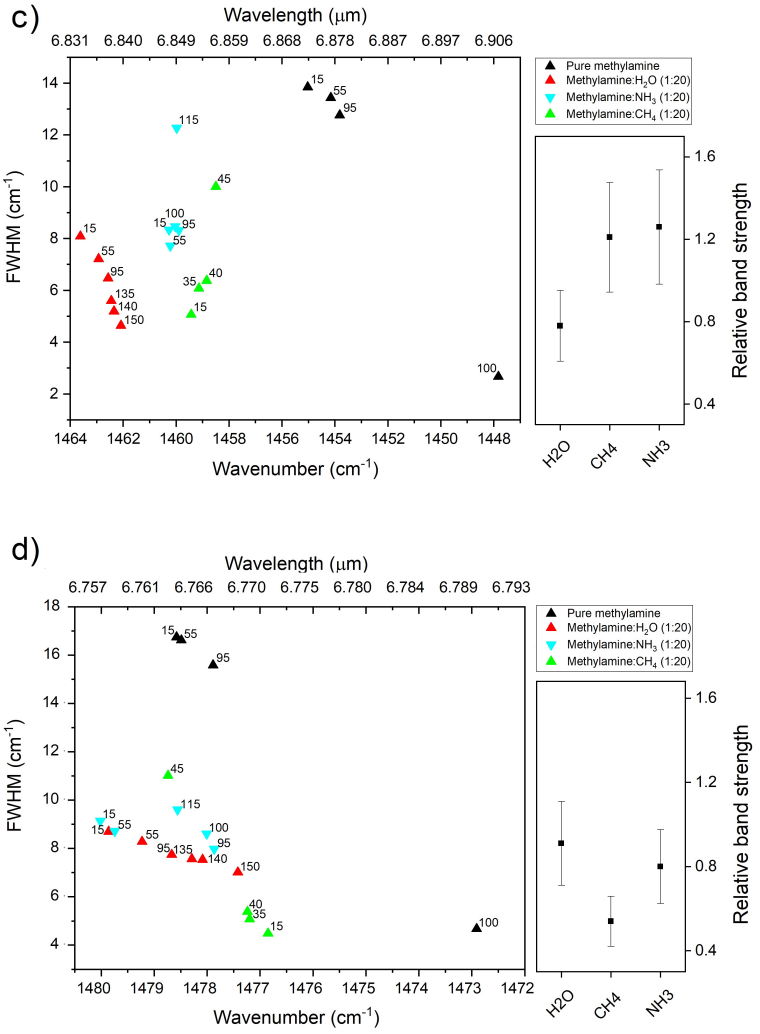

Figure 4.A.6: Continued.

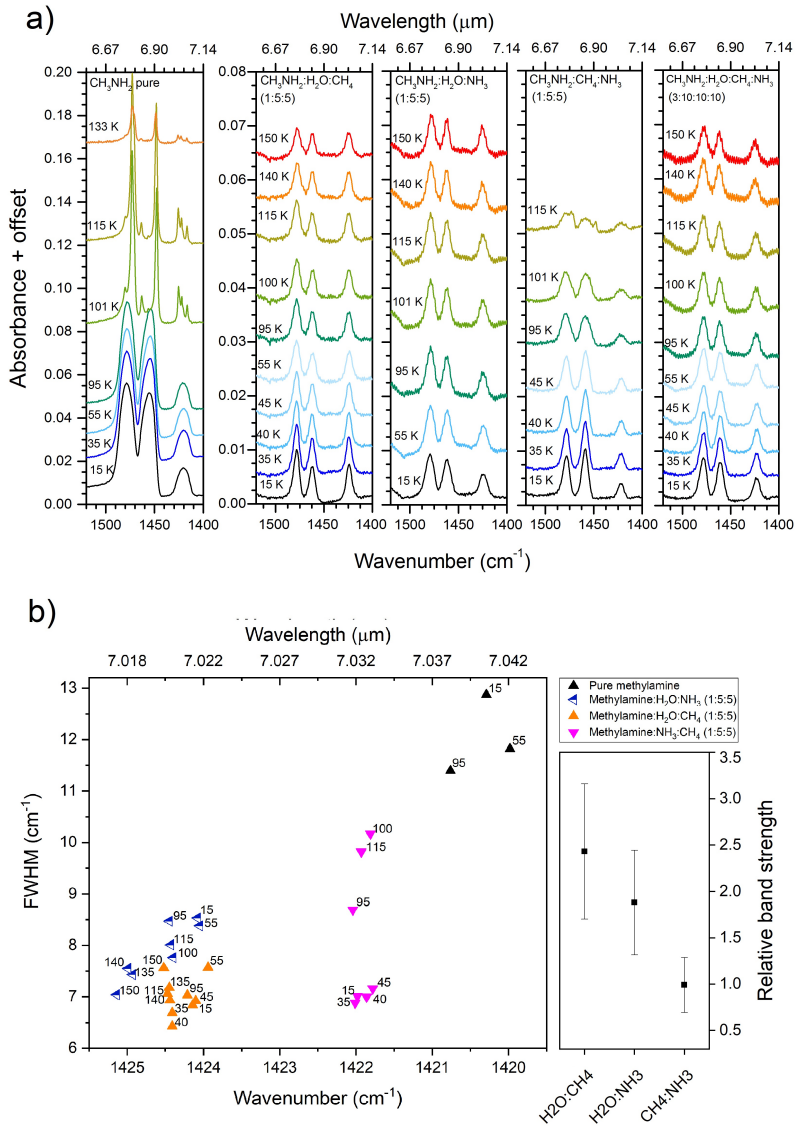

Figure 4.A.7: a) IR profile of the CH_3 antisymmetric deformation mode of CH_3NH_2 (around 1479 cm^{-1} (ν_{12} mode) and 1455 cm^{-1} (ν_5)) and the CH_3 symmetric deformation mode (around 1420 cm^{-1}), in pure and mixed ices. b) Left panel: peak position vs. FWHM for the CH_3 symmetric deformation band (1420 cm^{-1}) in the ice mixtures displayed in a) Different mixtures are indicated by different colors, and the different temperatures are marked in the graph. Right panel: relative band strength of the CH_3 symmetric deformation band in different ice mixtures at 15 K. Panels c) and d): same as b) for the CH_3 antisymmetric deformation modes, ν_5 and ν_{12}, at 1455 cm^{-1} and 1478.6 cm^{-1}, respectively.

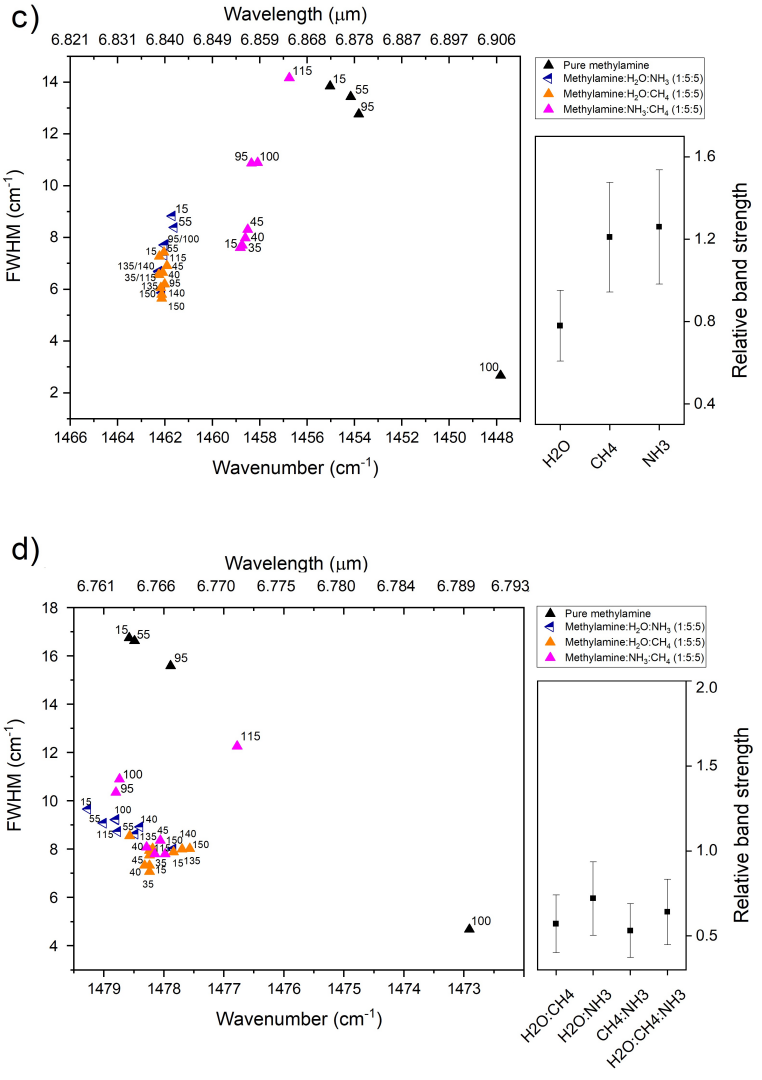

Figure 4.A.7: Continued.

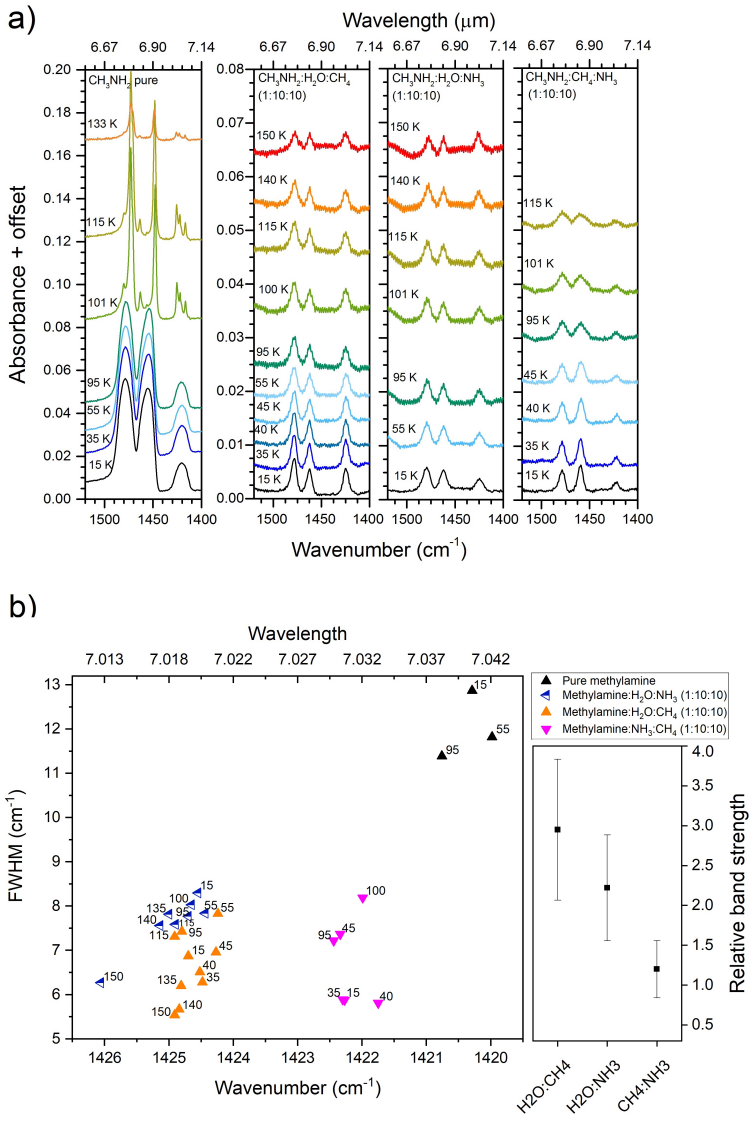

Figure 4.A.8: a) IR profile of the CH_3 antisymmetric deformation mode of CH_3NH_2 (around 1479 cm^{-1} and 1455 cm^{-1}) and the CH_3 symmetric deformation mode (around 1420 cm^{-1}), in pure and mixed ices. b) Left panel: peak position vs. FWHM for the CH_3 symmetric deformation band in the ice mixtures displayed in a) Different mixtures are indicated by different colors, and the different temperatures are marked in the graph. Right panel: relative band strength of the CH_3 symmetric deformation band (1420 cm^{-1}) in different ice mixtures at 15 K. Panels c) and d): same as b) for the CH_3 antisymmetric deformation modes, ν_5 and ν_{12}, at 1455 cm^{-1} and 1478.6 cm^{-1}, respectively.

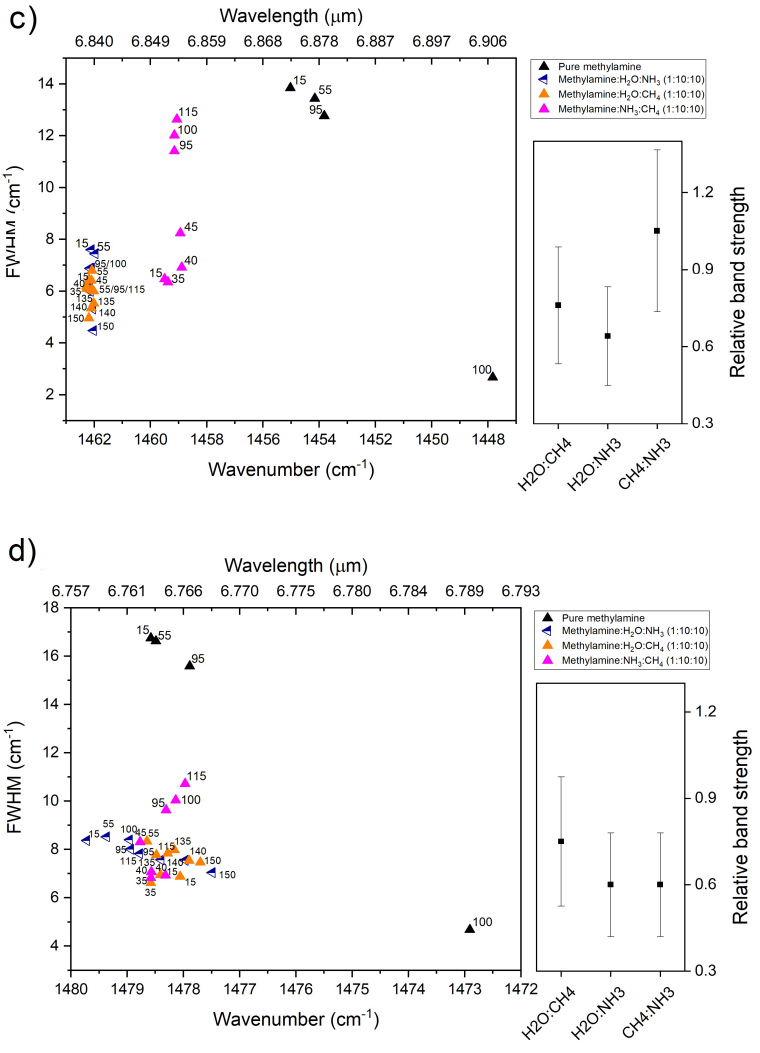

Figure 4.A.8: Continued.

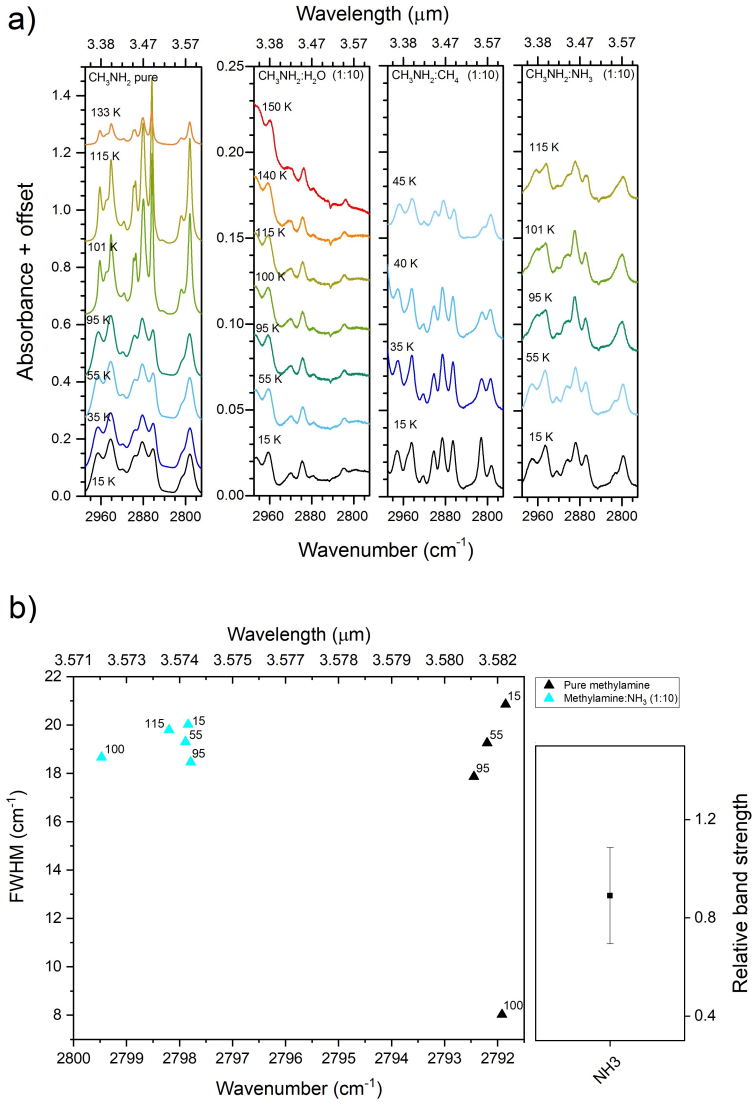

Figure 4.A.9: a) 2750 - 3000 cm^{-1} spectral region in pure and mixed CH_3NH_2 ices. The CH_3 antisymmetric stretching mode (around 2881 cm^{-1}) and the CH_3 symmetric stretching mode (around 2792 cm^{-1}) are displayed in the panels. b) Left panel: Peak position vs. FWHM for the CH_3 symmetric stretch band in the ice mixtures displayed in a) Different mixtures are indicated by different colors, and the different temperatures are marked in the graph. Right panel: Relative band strength of CH_3 antisymmetric stretch of CH_3NH_2:NH_3 (1:10) at 15 K. c) same as b) for the CH_3 antisymmetric stretch band (around 2881 cm^{-1}) in the ice mixtures displayed in a).

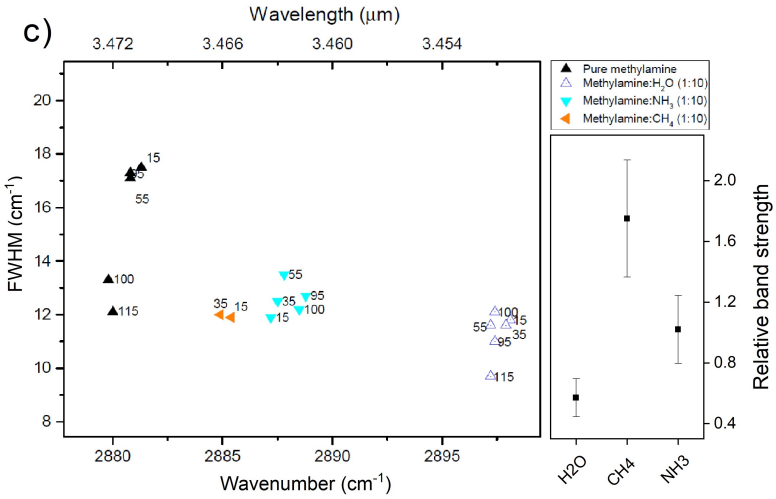

Figure 4.A.9: Continued.

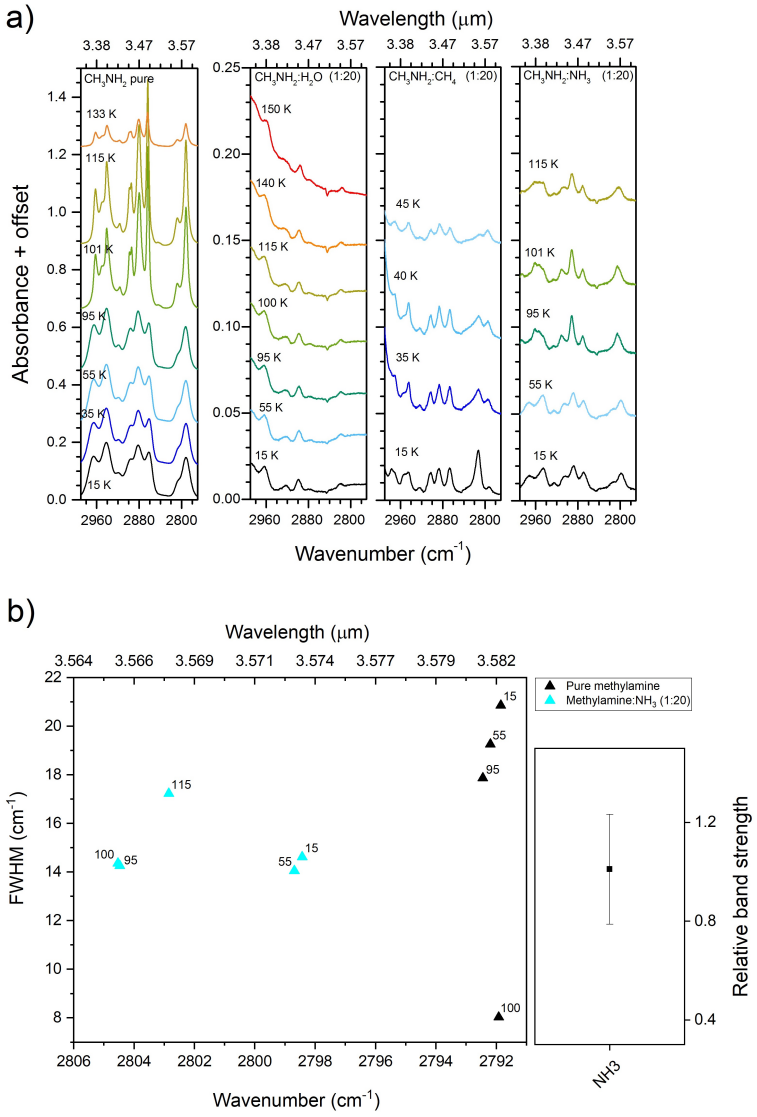

Figure 4.A.10: a) 2750 - 3000 cm^{-1} spectral region in pure and mixed CH_3NH_2 ices. The CH_3 antisymmetric stretching mode (around 2881 cm^{-1}) and the CH_3 symmetric stretching mode (around 2792 cm^{-1}) are displayed in the panels. b) Left panel: Peak position vs. FWHM for the CH_3 symmetric stretch band in pure and CH_3NH_2:NH_3 (1:10) ices. Right panel: Relative band strength of the CH_3 symmetric stretch mode in different ice mixtures at 15 K. c) same as b) for the CH_3 antisymmetric stretch band (around 2881 cm^{-1}) in the ice mixtures displayed in a).

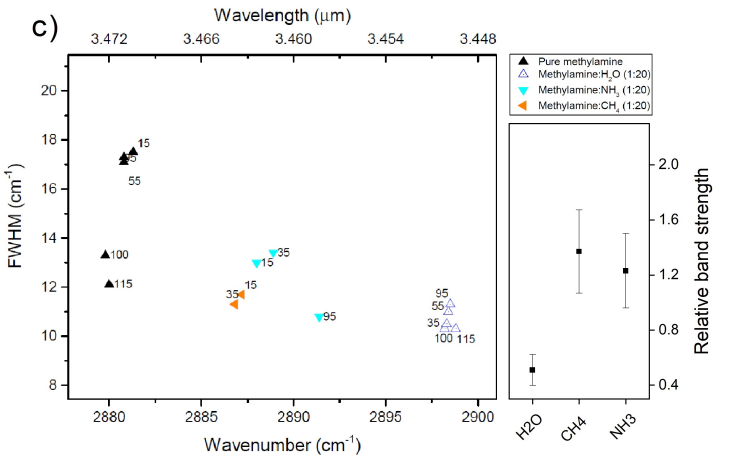

Figure 4.A.10: Continued.

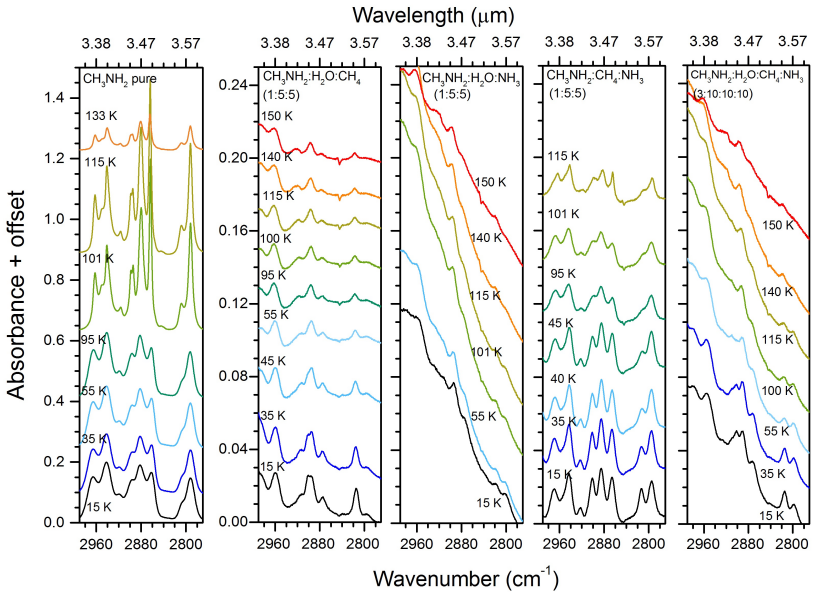

Figure 4.A.11: 2750 - 3000 cm^{-1} spectral region in pure and mixed CH_3NH_2 ices in which methylamine is diluted in a 1:10 ratio. The CH_3 antisymmetric stretching mode (around 2881 cm^{-1}) and the CH_3 symmetric stretching mode (around 2792 cm^{-1}) are displayed in the panels.

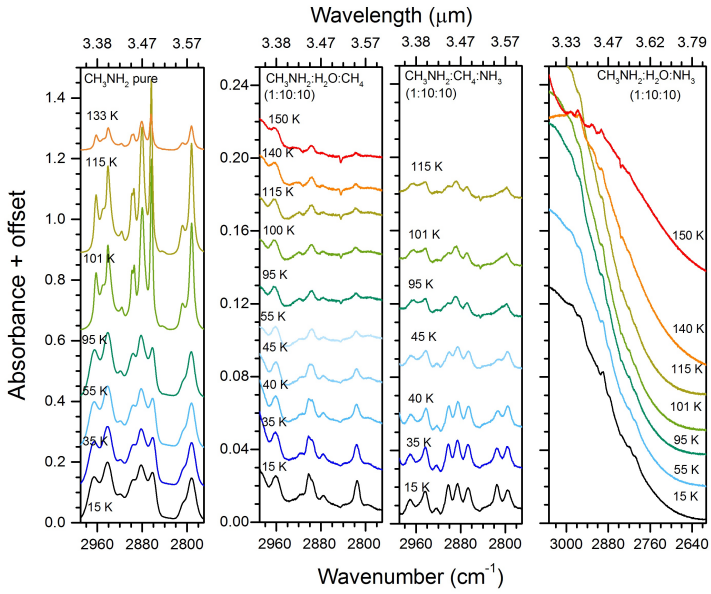

Figure 4.A.12: 2750 - 3000 cm^{-1} spectral region in pure and mixed CH_3NH_2 ices in which methylamine is diluted in a 1:20 ratio. The CH_3 antisymmetric stretching mode (around 2881 cm^{-1}) and the CH_3 symmetric stretching mode (around 2792 cm^{-1}) are displayed in the panels.

Appendix B

This section presents the peak position and FWHM of the methylamine features. Each table is composed of the measured peak position and FWHM for a given band in the mixtures with the same methylamine ratio and the pure ice for comparison. The peak position is measured for temperatures up to the desorption temperature of the methylamine ice matrix components (e.g., in the binary mixtures with CH_4, the peak position and FWHM are calculated up to 55 K). The general uncertainty of peak positions is 0.5 cm^{-1} for all the measurements, and the typical error of the FWHM values amounts to a maximum of 1 cm^{-1}.

In the cases that the CH_3 antisymmetric deformation modes (around 1455 cm^{-1} and 1479 cm^{-1}) overlap, the band profile is decomposed in two component features and the FWHM and peak position is calculated for each of the individual components. The absorption profile between 2800 - 2900 cm^{-1} was decomposed into Gaussian features for the calculation of peak position and FWHM for the CH_3 antisymmetric stretch

feature (2881.3 cm^{-1}). Also, in cases where the bands are weak or blended with matrix bands, the FWHM is not determined, a rough peak position is given and marked with an asterisk (*). The resulting uncertainty is much larger than the peak positions that are derived for features that do not overlap.

Table 4.B.1: Peak position and FWHM of the CH_3 rock feature of methylamine in pure ice and in the 1:5 binary mixtures from 15 K to 140 K.

Mixture	Temperature (K)	Peak position (cm^{-1})	Peak position (μm)	FWHM (cm^{-1})	FWHM (μm)
CH_3NH_2	15	1159.2	8.627	28.4	0.211
CH_3NH_2:H_2O (1:5)		1176.8	8.498	26.2	0.189
CH_3NH_2:CH_4 (1:5)		1153.7	8.668	22.7	0.170
CH_3NH_2:NH_3 (1:5)		1165*	-	-	-
CH_3NH_2	35	1159.5	8.624	27.7	0.206
CH_3NH_2:H_2O (1:5)		1176.5	8.5	26.0	0.188
CH_3NH_2:CH_4 (1:5)		1154.9	8.659	22.1	0.166
CH_3NH_2:NH_3 (1:5)		-	-	-	-
CH_3NH_2	55	1159.6	8.624	25.4	0.189
CH_3NH_2:H_2O (1:5)		1175.9	8.504	25.5	0.184
CH_3NH_2:CH_4 (1:5)		1160.0	8.621	25.2	0.187
CH_3NH_2:NH_3 (1:5)		-	-	-	-
CH_3NH_2	95	1159.9	8.621	25.4	0.188
CH_3NH_2:H_2O (1:5)		1175.8	8.505	24.7	0.179
CH_3NH_2:NH_3 (1:5)		-	-	-	-
CH_3NH_2	115	1164.3	8.589	26.4	0.195
CH_3NH_2:H_2O (1:5)		1175.6	8.506	24.0	0.174
CH_3NH_2:NH_3 (1:5)		-	-	-	-
CH_3NH_2	135	-	-	-	-
CH_3NH_2:H_2O (1:5)		1175.5	8.507	23.8	0.172
CH_3NH_2:NH_3 (1:5)		-	-	-	-
CH_3NH_2	140	-	-	-	-
CH_3NH_2:H_2O (1:5)		1174.6	8.513	23.4	0.169

Table 4.B.2: Peak position and FWHM of the CH_3 rock feature of pure methylamine and mixtures in which methylamine is diluted in a ratio of 1:10 and for temperatures ranging from 15 K to 140 K.

Mixture	Temperature (K)	Peak position (cm^{-1})	Peak position (μm)	FWHM (cm^{-1})	FWHM (μm)
CH_3NH_2	15	1159.2	8.627	28.4	0.211
CH_3NH_2:H_2O (1:10)		1177.5	8.493	25.1	0.181
CH_3NH_2:CH_4 (1:10)		1153.7	8.668	22.7	0.171
CH_3NH_2:NH_3 (1:10)		1161*	-	-	-
CH_3NH_2:H_2O:CH_4 (1:5:5)		1173.6	8.521	27.0	0.196
CH_3NH_2:H_2O:NH_3 (1:5:5)		-	-	-	-
CH_3NH_2:CH_4:NH_3 (1:5:5)		-	-	-	-
CH_3NH_2:H_2O:CH_4:NH_3 (3:10:10:10)		-	-	-	-
CH_3NH_2	35	1159.5	8.624	27.7	0.206
CH_3NH_2:H_2O (1:10)		1176.0	8.503	24.7	0.179
CH_3NH_2:CH_4 (1:10)		1154.8	8.660	18.7	0.140
CH_3NH_2:NH_3 (1:10)		-	-	-	-
CH_3NH_2:H_2O:CH_4 (1:5:5)		1173.4	8.522	24.5	0.178
CH_3NH_2:H_2O:NH_3 (1:5:5)		-	-	-	- -
CH_3NH_2:CH_4:NH_3 (1:5:5)		-	-	-	- -
CH_3NH_2:H_2O:CH_4:NH_3 (3:10:10:10)		-	-	-	-
CH_3NH_2	55	1159.6	8.624	25.4	0.189
CH_3NH_2:H_2O (1:10)		1176.6	8.499	24.5	0.177
CH_3NH_2:CH_4 (1:10)		1160.0	8.621	27.0	0.201
CH_3NH_2:NH_3 (1:10)		-	-	-	-
CH_3NH_2:H_2O:CH_4 (1:5:5)		1177.2	8.495	22.9	0.165
CH_3NH_2:H_2O:NH_3 (1:5:5)		-	-	-	-
CH_3NH_2:CH_4:NH_3 (1:5:5)		-	-	-	-
CH_3NH_2:H_2O:CH_4:NH_3 (3:10:10:10)		-	-	-	-
CH_3NH_2	95	1159.9	8.621	25.4	0.189
CH_3NH_2:H_2O (1:10)		1176.5	8.50	23.5	0.170
CH_3NH_2:NH_3 (1:10)		-	-	-	-
CH_3NH_2:H_2O:CH_4 (1:5:5)		1174.2	8.516	23.2	0.169
CH_3NH_2:H_2O:NH_3 (1:5:5)		-	-	-	-
CH_3NH_2:CH_4:NH_3 (1:5:5)		-	-	-	-

CH_3NH_2:H_2O:CH_4:NH_3 (3:10:10:10)		-	-	-	-
CH_3NH_2	115	1164.3	8.589	26.4	0.195
CH_3NH_2:H_2O (1:10)		1176.3	8.501	23.4	0.169
CH_3NH_2:NH_3 (1:10)		-	-	-	-
CH_3NH_2:H_2O:CH_4 (1:5:5)		1174.4	8.515	21.7	0.157
CH_3NH_2:H_2O:NH_3 (1:5:5)		-	-	-	-
CH_3NH_2:CH_4:NH_3 (1:5:5)		-	-	-	-
CH_3NH_2:H_2O:CH_4:NH_3 (3:10:10:10)		-	-	-	-
CH_3NH_2	135	-	-	-	-
CH_3NH_2:H_2O (1:10)		1176.2	8.502	23.4	0.169
CH_3NH_2:NH_3 (1:10)		-	-	-	-
CH_3NH_2:H_2O:CH_4 (1:5:5)		1173.8	8.519	21.4	0.155
CH_3NH_2:H_2O:NH_3 (1:5:5)		-	-	-	- -
CH_3NH_2:H_2O:CH_4:NH_3 (3:10:10:10)		-	-	-	-
CH_3NH_2	140	-	-	-	-
CH_3NH_2:H_2O (1:10)		1174.2	8.516	22.6	0.164
CH_3NH_2:H_2O:CH_4 (1:5:5)		1173.8	8.519	21.9	0.159
CH_3NH_2:H_2O:NH_3 (1:5:5)		-	-	-	-
CH_3NH_2:H_2O:CH_4:NH_3 (3:10:10:10)		-	-	-	-

Table 4.B.3: Peak position and FWHM of the CH_3 rock feature of methylamine in pure ice and mixtures in which methylamine is diluted in a ratio of 1:20 and for temperatures ranging from 15 K to 140 K.

Mixture	Temperature (K)	Peak position (cm^{-1})	(μm)	FWHM (cm^{-1})	(μm)
CH_3NH_2	15	1159.2	8.627	28.4	0.211
CH_3NH_2:H_2O (1:20)		1178.3	8.487	22.5	0.162
CH_3NH_2:CH_4 (1:20)		-	-	-	-
CH_3NH_2:NH_3 (1:20)		-	-	-	-
CH_3NH_2:H_2O:CH_4 (1:10:10)		1174.5	8.514	25.5	0.185
CH_3NH_2:H_2O:NH_3 (1:10:10)		-	-	-	-
CH_3NH_2:CH_4:NH_3 (1:10:10)		-	-	-	-
CH_3NH_2	35	1159.5	8.624	27.7	0.206
CH_3NH_2:H_2O (1:20)		1178.0	8.489	22.7	0.164
CH_3NH_2:CH_4 (1:20)		1152*	-	-	-
CH_3NH_2:NH_3 (1:20)		-	-	-	-
CH_3NH_2:H_2O:CH_4 (1:10:10)		1174.0	8.518	23.4	0.170
CH_3NH_2:H_2O:NH_3 (1:10:10)		-	-	-	-
CH_3NH_2:CH_4:NH_3 (1:10:10)		-	-	-	-
CH_3NH_2	55	1159.6	8.624	25.4	0.189
CH_3NH_2:H_2O (1:20)		1177.2	8.495	22.9	0.165
CH_3NH_2:CH_4 (1:20)		-	-	-	-
CH_3NH_2:NH_3 (1:20)		-	-	-	-
CH_3NH_2:H_2O:CH_4 (1:10:10)		1175.8	8.505	22.4	0.162
CH_3NH_2:H_2O:NH_3 (1:10:10)		-	-	-	-
CH_3NH_2:CH_4:NH_3 (1:10:10)		-	-	-	-
CH_3NH_2	95	1159.9	8.621	25.4	0.189
CH_3NH_2:H_2O (1:20)		1175.7	8.506	21.8	0.1577
CH_3NH_2:NH_3 (1:20)		-	-	-	-
CH_3NH_2:H_2O:CH_4 (1:10:10)		1175.9	8.504	21.7	0.157
CH_3NH_2:H_2O:NH_3 (1:10:10)		-	-	-	-
CH_3NH_2:CH_4:NH_3 (1:10:10)		-	-	-	-
CH_3NH_2	115	1164.3	8.589	26.4	0.195
CH_3NH_2:H_2O (1:20)		1175.4	8.508	21.8	0.158
CH_3NH_2:CH_4 (1:20)		-	-	-	-
CH_3NH_2:NH_3 (1:20)		-	-	-	-
CH_3NH_2:H_2O:CH_4 (1:10:10)		1175.4	8.508	22.1	0.160
CH_3NH_2:H_2O:NH_3 (1:10:10)		-	-	-	-
CH_3NH_2:CH_4:NH_3 (1:10:10)		-	-	-	-
CH_3NH_2	135	1164.3	8.589	22.8	0.168
CH_3NH_2:H_2O (1:20)		1175.4	8.508	21.8	0.158
CH_3NH_2:H_2O:CH_4 (1:10:10)		1174.8	8.512	21.2	0.154
CH_3NH_2:H_2O:NH_3 (1:10:10)		-	-	-	-
CH_3NH_2	140	-	-	-	-
CH_3NH_2:H_2O (1:20)		1175.4	8.508	24.0	0.174
CH_3NH_2:H_2O:CH_4 (1:10:10)		1175.0	8.511	22.2	0.161
CH_3NH_2:H_2O:NH_3 (1:10:10)		-	-	-	-

Table 4.B.4: Peak position and FWHM of the CH_3 symmetric deformation feature of methylamine in pure ice and in the 1:5 binary mixtures at temperatures from 15 K to 140 K.

Mixture	Temperature (K)	Peak position (cm^{-1})	(μm)	FWHM (cm^{-1})	(μm)
CH_3NH_2	15	1420.3	7.041	12.9	0.064
CH_3NH_2:H_2O (1:5)		1424.2	7.021	9.6	0.047
CH_3NH_2:CH_4 (1:5)		1422.1	7.032	6.6	0.033
CH_3NH_2:NH_3 (1:5)		1423.2	7.026	9.4	0.046
CH_3NH_2	35	1420.2	7.041	12.4	0.061
CH_3NH_2:H_2O (1:5)		1423.8	7.023	9.1	0.045
CH_3NH_2:CH_4 (1:5)		1421.9	7.033	6.8	0.034
CH_3NH_2:NH_3 (1:5)		1423.0	7.027	9.3	0.046
CH_3NH_2	55	1420.0	7.042	11.8	0.059
CH_3NH_2:H_2O (1:5)		1423.8	7.023	9.10	0.045
CH_3NH_2:CH_4 (1:5)		1420.7	7.039	9.0	0.045
CH_3NH_2:NH_3 (1:5)		1422.9	7.028	9.1	0.045
CH_3NH_2	95	1420.8	7.038	11.4	0.056
CH_3NH_2:H_2O (1:5)		1424.0	7.022	8.5	0.042
CH_3NH_2:NH_3 (1:5)		1422.7	7.029	8.6	0.042
CH_3NH_2	115	1425.6	7.015	2.1	0.010
		1422.4	7.030	3.6	0.018
		1416.7	7.059	2.2	0.011
CH_3NH_2:H_2O (1:5)		1424.2	7.021	7.8	0.038
CH_3NH_2:NH_3 (1:5)		1423.0	7.027	8.8	0.043
CH_3NH_2	135	-	-	-	-
CH_3NH_2:H_2O (1:5)		1424.2	7.021	7.8	0.038
CH_3NH_2	140	-	-	-	-
CH_3NH_2:H_2O (1:5)		1423.9	7.023	7.3	0.036

Table 4.B.5: Peak position and FWHM of the CH_3 symmetric deformation of pure methylamine and mixtures in which methylamine is diluted in a ratio of 1:10 and for temperatures ranging from 15 K to 140 K.

Mixture	Temperature (K)	Peak position (cm^{-1})	(μm)	FWHM (cm^{-1})	(μm)
CH_3NH_2	15	1420.3	7.041	12.9	0.064
CH_3NH_2:H_2O (1:10)		1424.6	7.020	8.8	0.043
CH_3NH_2:CH_4 (1:10)		1422.2	7.031	5.9	0.029
CH_3NH_2:NH_3 (1:10)		1423.1	7.027	9.1	0.045
CH_3NH_2:H_2O:CH_4 (1:5:5)		1424.1	7.022	6.8	0.034
CH_3NH_2:H_2O:NH_3 (1:5:5)		1424.1	7.022	8.5	0.042
CH_3NH_2:CH_4:NH_3 (1:5:5)		1422.0	7.032	7.0	0.035
CH_3NH_2:H_2O:CH_4:NH_3 (3:10:10:10)		1423.1	7.027	7.50	0.037
CH_3NH_2	35	1420.2	7.041	12.4	0.061
CH_3NH_2:H_2O (1:10)		1424.3	7.021	8.4	0.041
CH_3NH_2:CH_4 (1:10)		1421.6	7.034	5.9	0.029
CH_3NH_2:NH_3 (1:10)		1423.2	7.026	8.9	0.044
CH_3NH_2:H_2O:CH_4 (1:5:5)		1424.4	7.020	6.7	0.033
CH_3NH_2:H_2O:NH_3 (1:5:5)		-	-	-	-
CH_3NH_2:CH_4:NH_3 (1:5:5)		1422.0	7.032	6.9	0.034
CH_3NH_2:H_2O:CH_4:NH_3 (3:10:10:10)		1423.0	7.026	7.8	0.039
CH_3NH_2	55	1420.0	7.042	11.8	0.059
CH_3NH_2:H_2O (1:10)		1424.0	7.022	8.0	0.039
CH_3NH_2:CH_4 (1:10)		-	-	-	-
CH_3NH_2:NH_3 (1:10)		1423.3	7.026	8.5	0.042
CH_3NH_2:H_2O:CH_4 (1:5:5)		1423.9	7.023	7.6	0.037
CH_3NH_2:H_2O:NH_3 (1:5:5)		1424.0	7.022	8.4	0.041
CH_3NH_2:CH_4:NH_3 (1:5:5)		1421.8	7.033	7.8	0.039
CH_3NH_2:H_2O:CH_4:NH_3 (3:10:10:10)		1423.0	7.027	8.4	0.041
CH_3NH_2	95	1420.8	7.038	11.4	0.056
CH_3NH_2:H_2O (1:10)		1424.3	7.021	7.2	0.035
CH_3NH_2:NH_3 (1:10)		1422.5	7.030	8.5	0.042
CH_3NH_2:H_2O:CH_4 (1:5:5)		1424.2	7.021	7.0	0.035
CH_3NH_2:H_2O:NH_3 (1:5:5)		1424.4	7.020	8.5	0.042
CH_3NH_2:CH_4:NH_3 (1:5:5)		1422.0	7.032	8.7	0.043
CH_3NH_2:H_2O:CH_4:NH_3 (3:10:10:10)		1423.4	7.025	8.0	0.039
CH_3NH_2	115	1425.6	7.015	2.1	0.010
		1422.4	7.030	3.6	0.018
		1416.7	7.059	2.2	0.011
CH_3NH_2:H_2O (1:10)		1424.4	7.020	7.0	0.035
CH_3NH_2:NH_3 (1:10)		-	-	-	-
CH_3NH_2:H_2O:CH_4 (1:5:5)		1424.5	7.020	7.1	0.035
CH_3NH_2:H_2O:NH_3 (1:5:5)		1424.4	7.020	8.0	0.039

CH_3NH_2:CH_4:NH_3 (1:5:5)		1421.9	7.033	9.8	0.048
CH_3NH_2:H_2O:CH_4:NH_3 (3:10:10:10)		1423.7	7.024	8.0	0.039
CH_3NH_2	135	-	-		-
CH_3NH_2:H_2O (1:10)		1424.5	7.020	6.7	0.033
CH_3NH_2:H_2O:CH_4 (1:5:5)		1424.4	7.020	7.2	0.035
CH_3NH_2:H_2O:NH_3 (1:5:5)		1425.0	7.018	7.4	0.036
CH_3NH_2:H_2O:CH_4:NH_3 (3:10:10:10)		1424.7	7.019	8.6	0.042
CH_3NH_2	140	-	-		-
CH_3NH_2:H_2O (1:10)		1424.1	7.022	6.5	0.032
CH_3NH_2:H_2O:CH_4 (1:5:5)			-		-
CH_3NH_2:H_2O:NH_3 (1:5:5)		1425.0	7.018	7.5	0.037
CH_3NH_2:H_2O:CH_4:NH_3 (3:10:10:10)		1424.7	7.019	8.5	0.042

Table 4.B.6: Peak position and FWHM of the CH_3 symmetric deformation of pure methylamine and mixtures in which methylamine is diluted in a ratio of 1:20 and for temperatures ranging from 15 K to 140 K.

Mixture	Temperature (K)	Peak position (cm^{-1})	(μm)	FWHM (cm^{-1})	(μm)
CH_3NH_2	15	1420.3	7.041	12.9	0.064
CH_3NH_2:H_2O (1:20)		1424.8	7.019	8.4	0.041
CH_3NH_2:CH_4 (1:20)		-	-	-	-
CH_3NH_2:NH_3 (1:20)		1424.1	7.022	9.6	0.047
CH_3NH_2:H_2O:CH_4 (1:10:10)		1424.7	7.019	6.9	0.034
CH_3NH_2:H_2O:NH_3 (1:10:10)		1424.5	7.020	8.3	0.041
CH_3NH_2:CH_4:NH_3 (1:10:10)		1422.3	7.031	5.9	0.029
CH_3NH_2	55	1420.0	7.042	11.8	0.059
CH_3NH_2:H_2O (1:20)		1424.3	7.021	8.2	0.040
CH_3NH_2:CH_4 (1:20)		-	-	-	-
CH_3NH_2:NH_3 (1:20)		-	-	-	-
CH_3NH_2:H_2O:CH_4 (1:10:10)		1424.2	7.021	7.8	0.038
CH_3NH_2:H_2O:NH_3 (1:10:10)		1424.4	7.020	7.8	0.038
CH_3NH_2:CH_4:NH_3 (1:10:10)		1422.3	7.031	7.3	0.036
CH_3NH_2	95	1420.8	7.038	11.4	0.056
CH_3NH_2:H_2O (1:20)		1424.7	7.019	7.7	0.038
CH_3NH_2:NH_3 (1:20)		-	-	-	-
CH_3NH_2:H_2O:CH_4 (1:10:10)		1424.8	7.019	7.4	0.036
CH_3NH_2:H_2O:NH_3 (1:10:10)		1424.7	7.019	7.8	0.038
CH_3NH_2:CH_4:NH_3 (1:10:10)		1422.4	7.030	7.2	0.036
CH_3NH_2	115	1425.6	7.015	2.1	0.010
		1422.4	7.030	3.6	0.018
		1416.7	7.059	2.2	0.011
CH_3NH_2:H_2O (1:20)		-	-	-	-
CH_3NH_2:NH_3 (1:20)		1424.9	7.018	7.6	0.037
CH_3NH_2:H_2O:CH_4 (1:10:10)		1424.9	7.018	7.3	0.036
CH_3NH_2:H_2O:NH_3 (1:10:10)		-	-	-	-
CH_3NH_2:CH_4:NH_3 (1:10:10)		-	-	-	-
CH_3NH_2	135	-	-	-	-
CH_3NH_2:H_2O (1:20)		1425.0	7.018	7.6	0.037
CH_3NH_2:H_2O:CH_4 (1:10:10)		1424.8	7.019	6.2	0.031
CH_3NH_2:H_2O:NH_3 (1:10:10)		1425.0	7.018	7.8	0.038
CH_3NH_2	140	-	-	-	-
CH_3NH_2:H_2O (1:20)		1424.8	7.019	6.8	0.033
CH_3NH_2:H_2O:CH_4 (1:10:10)		1424.8	7.019	5.7	0.028
CH_3NH_2:H_2O:NH_3 (1:10:10)		1425.1	7.017	7.6	0.037

Table 4.B.7: Peak position and FWHM of the two bands assigned to CH_3 antisymmetric deformation modes of methylamine in pure ice and in the 1:5 binary mixtures at temperatures from 15 K to 140 K.

Mixture	Temperature (K)	Peak position (cm^{-1})	(μm)	FWHM (cm^{-1})	(μm)
CH_3NH_2	15	1455.0	6.873	13.8	0.065
		1478.6	6.763	16.7	0.076
CH_3NH_2:H_2O (1:5)		1462.9	6.836	9.7	0.045
		1479.8	6.758	10.5	0.048
CH_3NH_2:CH_4 (1:5)		1458.3	6.857	7.8	0.037
		1477.0	6.770	7.6	0.035
CH_3NH_2:NH_3 (1:5)		1459.8	6.850	9.8	0.046
		1479.9	6.757	10.6	0.048

CH_3NH_2	35	1454.5	6.875	13.5	0.064
		1478.5	6.764	16.7	0.076
CH_3NH_2:H_2O (1:5)		1462.1	6.839	9.2	0.043
		1478.9	6.762	10.4	0.048
CH_3NH_2:CH_4 (1:5)		1457.3	6.862	8.5	0.040
		1477.7	6.767	8.6	0.039
CH_3NH_2:NH_3 (1:5)		1459.6	6.851	9.7	0.046
		1479.7	6.758	10.3	0.047
CH_3NH_2	55	1454.2	6.877	13.4	0.063
		1478.5	6.764	16.6	0.076
CH_3NH_2:H_2O (1:5)		1462.0	6.840	8.8	0.041
		1478.6	6.763	10.3	0.047
CH_3NH_2:CH_4 (1:5)		1455.3	6.871	11.1	0.052
		1477.7	6.767	11.8	0.054
CH_3NH_2:NH_3 (1:5)		1459.5	6.852	9.5	0.045
		1479.6	6.759	10.1	0.046
CH_3NH_2	95	1453.8	6.879	12.8	0.061
		1477.9	6.766	15.6	0.071
CH_3NH_2:H_2O (1:5)		1461.7	6.841	8.0	0.037
		1478.3	6.765	9.6	0.044
CH_3NH_2:NH_3 (1:5)		1458.9	6.854	10.4	0.049
		1479.2	6.760	10.2	0.047
CH_3NH_2	115	1448.3	6.905	3.0	0.014
		1472.5	6.791	5.1	0.024
CH_3NH_2:H_2O (1:5)		-	-	-	-
CH_3NH_2:NH_3 (1:5)		1458.9	6.854	-	-
		1479.3	6.760	10.2	0.047
CH_3NH_2	135	-	-	-	-
CH_3NH_2:H_2O (1:5)		1461.7	6.841	6.8	0.032
		1477.3	6.769	8.6	0.039
CH_3NH_2	140	-	-	-	-
CH_3NH_2:H_2O (1:5)		1461.6	6.842	5.9	0.028
		1476.8	6.771	7.3	0.033

Table 4.B.8: Peak position and FWHM of the two bands assigned to CH_3 antisymmetric deformation modes of methylamine in pure ice and in the 1:10 mixtures at temperatures from 15 K to 140 K.

Mixture	Temperature	Peak position		FWHM	
	(K)	(cm^{-1})	(μm)	(cm^{-1})	(μm)
CH_3NH_2	15	1455.0	6.873	13.8	0.065
		1478.6	6.763	16.7	0.076
CH_3NH_2:H_2O (1:10)		1463.3	6.834	8.9	0.042
		1479.8	6.758	9.7	0.044
CH_3NH_2:CH_4 (1:10)		1458.8	6.855	6.3	0.030
		1476.4	6.773	5.9	0.027
CH_3NH_2:NH_3 (1:10)		1460.0	6.849	9.4	0.044
		1480.0	6.757	9.4	0.043
CH_3NH_2:H_2O:CH_4 (1:5:5)		1462.2	6.839	7.3	0.034
		1478.2	6.765	7.3	0.033
CH_3NH_2:H_2O:NH_3 (1:5:5)		1461.7	6.841	8.8	0.041
		1479.3	6.760	9.7	0.044
CH_3NH_2:CH_4:NH_3 (1:5:5)		1458.8	6.855	7.6	0.036
		1478.0	6.766	7.8	0.036
CH_3NH_2:H_2O:CH_4:NH_3 (3:10:10:10)		1460.8	6.846	8.4	0.039
		1478.3	6.765	8.7	0.040
CH_3NH_2	35	1454.5	6.875	13.5	0.064
		1478.5	6.764	16.7	0.076
CH_3NH_2:H_2O (1:10)		1462.9	6.836	8.5	0.040
		1479.5	6.759	9.4	0.043
CH_3NH_2:CH_4 (1:10)		1457.7	6.860	7.8	0.037
		1477.1	6.770	7.4	0.034
CH_3NH_2:NH_3 (1:10)		1459.7	6.851	9.7	0.046
		1479.7	6.758	9.3	0.042
CH_3NH_2:H_2O:CH_4 (1:5:5)		1462.3	6.839	6.6	0.031
		1478.2	6.765	7.1	0.032
CH_3NH_2:H_2O:NH_3 (1:5:5)		1461.6	6.842	8.6	0.040
		1479.1	6.761	9.3	0.043
CH_3NH_2:CH_4:NH_3 (1:5:5)		1458.7	6.855	7.7	0.036
		1478.1	6.765	7.8	0.036
CH_3NH_2:H_2O:CH_4:NH_3 (3:10:10:10)		1461.0	6.845	8	0.037
CH_3NH_2	55	1454.2	6.877	13.4	0.063
		1478.5	6.764	16.6	0.076
CH_3NH_2:H_2O (1:10)		1462.4	6.838	8.1	0.038
		1479.0	6.761	9.2	0.042
CH_3NH_2:CH_4 (1:10)		1456.3	6.867	12.0	0.057
		1477.6	6.768	11.9	0.055
CH_3NH_2:NH_3 (1:10)		1459.8	6.850	8.8	0.041

		1479.5	6.759	9.3	0.042
CH_3NH_2:H_2O:CH_4 (1:5:5)		1462.0	6.840	7.4	0.035
		1478.6	6.763	8.5	0.039
CH_3NH_2:H_2O:NH_3 (1:5:5)		1461.6	6.842	8.4	0.039
		1479.0	6.761	9.1	0.042
CH_3NH_2:CH_4:NH_3 (1:5:5)		1458.5	6.856	8.3	0.039
CH_3NH_2:H_2O:CH_4:NH_3 (3:10:10:10)		1460.9	6.845	8.5	0.040
		1478.0	6.766	9.5	0.043
CH_3NH_2		1453.8	6.879	12.8	0.061
		1477.9	6.766	15.6	0.071
CH_3NH_2:H_2O (1:10)		1462.1	6.839	7.2	0.034
		1478.5	6.764	8.5	0.039
CH_3NH_2:NH_3 (1:10)		1459.2	6.853	11.0	0.052
		1478.6	6.763	10.4	0.048
CH_3NH_2:H_2O:CH_4 (1:5:5)		1462.0	6.840	6.2	0.029
	95	1478.2	6.765	7.9	0.036
		-		-	
CH_3NH_2:H_2O:NH_3 (1:5:5)		1462.0	6.840	7.7	0.036
CH_3NH_2:CH_4:NH_3 (1:5:5)		1458.3	6.857	10.9	0.051
		1478.8	6.762	9.2	0.042
CH_3NH_2:H_2O:CH_4:NH_3 (3:10:10:10)		1461.3	6.843	8.0	0.037
		1478.3	6.765	9.0	0.041
CH_3NH_2		1448.3	6.905	3.0	0.014
		1472.5	6.791	5.1	0.024
CH_3NH_2:H_2O (1:10)		1462.2	6.839	6.9	0.032
		1478.3	6.765	8.5	0.039
CH_3NH_2:NH_3 (1:10)		1458.8	6.855	13.3	0.062
		1477.9	6.766	11.5	0.053
CH_3NH_2:H_2O:CH_4 (1:5:5)		1462.2	6.839	6.6	0.031
	115	1478.2	6.765	8	0.037
CH_3NH_2:H_2O:NH_3 (1:5:5)		1462.0	6.840	7.3	0.034
		1478.8	6.762	8.7	0.040
CH_3NH_2:CH_4:NH_3 (1:5:5)		1456.7	6.865	14.2	0.067
		1476.8	6.771	12.3	0.056
CH_3NH_2:H_2O:CH_4:NH_3 (3:10:10:10)		1461.6	6.842	7.7	0.036
		1478.4	6.764	9.0	0.041
CH_3NH_2		-	-	-	-
CH_3NH_2:H_2O (1:10)		1462.0	6.840	6.2	0.029
		1477.8	6.767	7.8	0.036
CH_3NH_2:H_2O:CH_4 (1:5:5)	135	1462.2	6.839	6.1	0.029
		1478.2	6.765	8.0	0.037
CH_3NH_2:H_2O:NH_3 (1:5:5)		1462.3	6.839	6.7	0.031
		1478.5	6.764	8.6	0.039
CH_3NH_2:H_2O:CH_4:NH_3 (3:10:10:10)		1462.1	6.839	7.5	0.035
		1478.5	6.764	9.1	0.042
CH_3NH_2		-	-	-	-
CH_3NH_2:H_2O (1:10)		1462.0	6.840	5.6	0.026
		1477.3	6.769	7.0	0.032
CH_3NH_2:H_2O:CH_4 (1:5:5)	140	1462.1	6.839	5.8	0.027
		1477.9	6.766	7.5	0.034
CH_3NH_2:H_2O:NH_3 (1:5:5)		1462.3	6.839	6.7	0.031
		1478.4	6.764	8.9	0.041
CH_3NH_2:H_2O:CH_4:NH_3 (3:10:10:10)		1462.1	6.839	7.4	0.035
		1478.4	6.764	8.9	0.041

Table 4.B.9: Peak position and FWHM of the two bands assigned to CH_3 antisymmetric deformation modes of methylamine in pure ice and in the 1:20 binary mixtures at temperatures from 15 K to 140 K.

Mixture	Temperature	Peak position		FWHM	
	(K)	(cm^{-1})	(μm)	(cm^{-1})	(μm)
CH_3NH_2		1455.0	6.873	13.8	0.065
		1478.6	6.763	16.7	0.076
CH_3NH_2:H_2O (1:20)		1463.6	6.832	8.1	0.038
		1479.9	6.757	8.7	0.040
CH_3NH_2:CH_4 (1:20)	15	1459.4	6.852	5.1	0.024
		1476.8	6.771	4.5	0.021
CH_3NH_2:NH_3 (1:20)		1460.3	6.848	8.3	0.039
		1480.0	6.757	9.1	0.042
CH_3NH_2:H_2O:CH_4 (1:10:10)		1462.2	6.839	6.5	0.030
		1478.1	6.765	6.9	0.032
CH_3NH_2:H_2O:NH_3 (1:10:10)		1462.1	6.839	7.6	0.036
		1479.7	6.758	8.4	0.038
CH_3NH_2:CH_4:NH_3 (1:10:10)		1459.5	6.852	6.5	0.031
		1478.3	6.765	6.9	0.032
CH_3NH_2		1454.5	6.875	13.5	0.064
		1478.5	6.764	16.7	0.076
CH_3NH_2:H_2O (1:20)		1463.3	6.834	7.8	0.036
		1479.5	6.759	8.5	0.039

		-	-	-	
CH_3NH_2:CH_4 (1:20)		1478.6	6.763	6.6	0.030
		1477.2	6.770	5.1	0.023
		-	-	-	-
CH_3NH_2:NH_3 (1:20)		1459.6	6.851	9.6	0.045
		1479.8	6.758	9.0	0.041
CH_3NH_2:H_2O:CH_4 (1:10:10)		1462.3	6.839	6.1	0.029
		-	-	-	-
CH_3NH_2:H_2O:NH_3 (1:10:10)		-	-		-
		-	-	-	-
CH_3NH_2:CH_4:NH_3 (1:10:10)		1459.4	6.852	6.3	0.030
		1478.6	6.763	6.8	0.031
CH_3NH_2		1454.2	6.877	13.4	0.063
		1478.5	6.764	16.6	0.076
CH_3NH_2:H_2O (1:20)		1462.9	6.836	7.2	0.034
		1479.2	6.760	8.3	0.038
CH_3NH_2:CH_4 (1:20)		1458.5	6.856	10.1	0.047
CH_3NH_2:NH_3 (1:20)		1460.2	6.848	7.7	0.036
		1479.7	6.758	8.7	0.040
CH_3NH_2:H_2O:CH_4 (1:10:10)	55	1462.1	6.839	6.8	0.032
		1478.6	6.763	8.3	0.038
CH_3NH_2:H_2O:NH_3 (1:10:10)		1462.0	6.840	7.4	0.035
		1479.4	6.759	8.5	0.039
CH_3NH_2:CH_4:NH_3 (1:10:10)		1458.9	6.854	6.9	0.032
		1478.4	6.764	9.0	0.041
CH_3NH_2		1453.8	6.879	12.8	0.061
		1477.9	6.766	15.6	0.071
CH_3NH_2:H_2O (1:20)		1462.6	6.837	6.5	0.030
		1478.7	6.763	7.7	0.035
CH_3NH_2:NH_3 (1:20)		1459.9	6.850	8.3	0.039
		1477.9	6.766	8.0	0.037
CH_3NH_2:H_2O:CH_4 (1:10:10)		1462.1	6.839	6.1	0.029
	95	1478.5	6.764	7.8	0.036
CH_3NH_2:H_2O:NH_3 (1:10:10)		1462.1	6.839	6.9	0.032
		1478.9	6.762	8.0	0.037
CH_3NH_2:CH_4:NH_3 (1:10:10)		1458.9	6.854	8.2	0.039
		1478.3	6.765	9.6	0.044
CH_3NH_2		1448.3	6.905	3.0	0.014
		1472.5	6.791	5.1	0.024
CH_3NH_2:H_2O (1:20)		1462.5	6.838	6.0	0.028
		1478.4	6.764	7.3	0.033
CH_3NH_2:NH_3 (1:20)		1460.0	6.849	12.3	0.058
	115	1748.6	5.719	9.6	0.031
CH_3NH_2:H_2O:CH_4 (1:10:10)		1462.1	6.839	6	0.028
		1478.3	6.765	7.8	0.036
CH_3NH_2:H_2O:NH_3 (1:10:10)		1462.2	6.839	6.2	0.029
		1478.8	6.762	7.8	0.036
CH_3NH_2:CH_4:NH_3 (1:10:10)		1459.1	6.854	12.0	0.056
		1478	6.766	10.7	0.049
CH_3NH_2		-	-	-	-
CH_3NH_2:H_2O (1:20)		1462.4	6.838	5.6	0.026
		1478.3	6.765	7.6	0.035
CH_3NH_2:H_2O:CH_4 (1:10:10)	135	1462.0	6.840	5.5	0.026
		1478.2	6.765	8.0	0.037
CH_3NH_2:H_2O:NH_3 (1:10:10)		1462.1	6.839	6.0	0.028
		1478.4	6.764	7.6	0.035
CH_3NH_2		-	-	-	-
CH_3NH_2:H_2O (1:20)		1462.3	6.839	5.2	0.024
	140	1478.1	6.765	7.5	0.034
CH_3NH_2:H_2O:CH_4 (1:10:10)		1462.1	6.839	5.3	0.025
		1477.9	6.766	7.5	0.034
CH_3NH_2:H_2O:NH_3 (1:10:10)		1462.0	6.840	5.3	0.025
		1478.0	6.766	7.5	0.034

Table 4.B.10: Peak position and FWHM of the CH_3 symmetric stretch feature of methylamine in pure ice and in the 1:5 binary mixtures at temperatures from 15 K to 135 K.

Mixture	Temperature (K)	Peak position (cm^{-1})	Peak position (μm)	FWHM (cm^{-1})	FWHM (μm)
CH_3NH_2		2791.8	3.582	20.9	0.027
CH_3NH_2:H_2O (1:5)	15	2800*	3.571*	-	-
CH_3NH_2:CH_4 (1:5)		2792.9*	3.580*	-	-
CH_3NH_2:NH_3 (1:5)		2797.1	3.575	17.2	0.022
CH_3NH_2		2791.5	3.582	20.6	0.026
CH_3NH_2:H_2O (1:5)	35	-	-	-	-
CH_3NH_2:CH_4 (1:5)		2793.9*	3.579*	-	-
CH_3NH_2:NH_3 (1:5)		-	-	-	-
CH_3NH_2		2792.2	3.581	19.3	0.025
CH_3NH_2:H_2O (1:5)	55	-	-	-	-

CH_3NH_2:CH_4 (1:5)		-	-	-	-
CH_3NH_2:NH_3 (1:5)		2797.5	3.575	18.6	0.024
CH_3NH_2	95	2792.4	3.581	17.9	0.023
CH_3NH_2:H_2O (1:5)		-	-	-	-
CH_3NH_2:NH_3 (1:5)		2797.0	3.575	18.3	0.023
CH_3NH_2	115	2791.9	3.582	8.8	0.011
CH_3NH_2:H_2O (1:5)		2796.8	3.575	-	-
CH_3NH_2:NH_3 (1:5)		2797.4	3.575	17.3	0.022
CH_3NH_2	135	-	-	-	-
CH_3NH_2:H_2O (1:5)		2794.4	3.579	28.9	-

Table 4.B.11: Peak position and FWHM of the CH_3 symmetric stretch of pure methylamine and mixtures in which methylamine is diluted in a ratio of 1:10 and for temperatures ranging from 15 K to 115 K.

Mixture	Temperature (K)	Peak position (cm^{-1})	(μm)	FWHM (cm^{-1})	(μm)
CH_3NH_2	15	2791.8	3.582	20.9	0.027
CH_3NH_2:H_2O (1:10)		2802*	3.569*	-	-
CH_3NH_2:CH_4 (1:10)		2791.9*	3.582*		-
CH_3NH_2:NH_3 (1:10)		2797.8	3.574	20.0	0.026
CH_3NH_2:H_2O:CH_4 (1:5:5)		-	-	-	-
CH_3NH_2:H_2O:NH_3 (1:5:5)		-	-	-	-
CH_3NH_2:CH_4:NH_3 (1:5:5)		2794.7*	3.578*		-
CH_3NH_2:H_2O:CH_4:NH_3 (3:10:10:10)		2797.8*	3.574*		-
CH_3NH_2	35	2791.5	3.582	20.6	0.026
CH_3NH_2:H_2O (1:10)		-	-	-	-
CH_3NH_2:CH_4 (1:10)		-	-	-	-
CH_3NH_2:NH_3 (1:10)		2797.8	3.574	19.5	0.025
CH_3NH_2	55	2792.2	3.581	19.3	0.025
CH_3NH_2:H_2O (1:10)		2802.6	3.568	48.1	0.061
CH_3NH_2:CH_4 (1:10)		-	-	-	-
CH_3NH_2:NH_3 (1:10)		2797.9	3.574	18.5	0.024
CH_3NH_2	95	-	-		-
CH_3NH_2:H_2O (1:10)		2803.7	3.267	48.3	0.061
CH_3NH_2:NH_3 (1:10)		2797.8	3.574	18.5	0.024
CH_3NH_2:H_2O:CH_4 (1:5:5)		-	-	-	-
CH_3NH_2:H_2O:NH_3 (1:5:5)		2798.2	3.574	19.8	0.025
CH_3NH_2	115	2791.9	3.582	8.8	0.011
CH_3NH_2:H_2O (1:10)		-	-	-	-
CH_3NH_2:NH_3 (1:10)		2798.2	3.574	19.8	0.025
CH_3NH_2:H_2O:CH_4 (1:5:5)		-	-	-	-

Table 4.B.12: Peak position and FWHM of the CH_3 symmetric stretch of pure methylamine and mixtures in which methylamine is diluted in a ratio of 1:20 and for temperatures ranging from 15 K to 115 K.

Mixture	Temperature (K)	Peak position (cm^{-1})	(μm)	FWHM (cm^{-1})	(μm)
CH_3NH_2	15	2791.8	3.582	20.9	0.027
CH_3NH_2:H_2O (1:20)		-	-	-	-
CH_3NH_2:CH_4 (1:20)		2792.4*	3.581*	-	-
CH_3NH_2:NH_3 (1:20)		2798.4	3.573	14.6	0.019
CH_3NH_2:H_2O:CH_4 (1:10:10)		-	-	-	-
CH_3NH_2:H_2O:NH_3 (1:10:10)		-	-	-	-
CH_3NH_2:CH_4:NH_3 (1:10:10)		-	-	-	-
CH_3NH_2	35	2791.5	3.582	20.6	0.026
CH_3NH_2:H_2O (1:20)		-	-	-	-
CH_3NH_2:CH_4 (1:20)		-	-	-	-
CH_3NH_2:NH_3 (1:20)		2798.5	3.573	14.3	0.018
CH_3NH_2	55	2792.2	3.581	19.3	0.025
CH_3NH_2:H_2O (1:20)		-	-	-	-
CH_3NH_2:CH_4 (1:20)		-	-	-	-
CH_3NH_2:NH_3 (1:20)		2798.7	3.573	14.0	0.018
CH_3NH_2	95	-	-	-	-
CH_3NH_2:H_2O (1:20)		-	-	-	-
CH_3NH_2:NH_3 (1:20)		2804.5	3.566	14.3	0.018
CH_3NH_2	115	2791.9	3.582	8.8	0.011
CH_3NH_2:H_2O (1:20)		-	-	-	-
CH_3NH_2:NH_3 (1:20)		2802.8	3.568	17.2	0.022

Table 4.B.13: Peak position and FWHM of the CH_3 antisymmetric stretch feature of methylamine in pure ice and in the 1:5 binary mixtures from 15 K to 140 K.

Mixture	Temperature (K)	Peak position (cm^{-1})	(μm)	FWHM (cm^{-1})	(μm)
CH_3NH_2	15	2881.3	3.471	17.5	0.0211
CH_3NH_2:H_2O (1:5)		2897.0	3.452	12.0	0.0143
CH_3NH_2:CH_4 (1:5)		2884.7	3.466	12.1	0.0145
CH_3NH_2:NH_3 (1:5)		2886.8	3.464	12.2	0.0146
CH_3NH_2	35	2881.0	3.471	17.4	0.0210
CH_3NH_2:H_2O (1:5)		2896.7	3.452	11.9	0.0142
CH_3NH_2:CH_4 (1:5)		2884.3	3.467	12.2	0.0147
CH_3NH_2:NH_3 (1:5)		2886.1	3.465	12.8	0.0154
CH_3NH_2	55	2880.8	3.471	17.3	0.0208
CH_3NH_2:H_2O (1:5)		2896.1	3.453	11.7	0.0139
CH_3NH_2:CH_4 (1:5)		-	-	-	-
CH_3NH_2:NH_3 (1:5)		2885.5	3.465	15	0.0180
CH_3NH_2	95	2880.8	3.471	17.1	0.0206
CH_3NH_2:H_2O (1:5)		2896.5	3.452	11.6	0.0138
CH_3NH_2:NH_3 (1:5)		2885.0	3.466	16.4	0.0197
CH_3NH_2	100	2879.8	3.472	13.3	0.0160
CH_3NH_2:H_2O (1:5)		2896.7	3.452	12.0	0.0143
CH_3NH_2:NH_3 (1:5)		2885.3	3.466	15.7	0.0189 -
CH_3NH_2	115	2880.0	3.472	12.1	0.0146
CH_3NH_2:H_2O (1:5)		2896.8	3.452	11.2	0.0133
CH_3NH_2:NH_3 (1:5)		2885.5	3.466	13.6	0.0163
CH_3NH_2	140	-	-	-	-
CH_3NH_2:H_2O (1:5)		2897.0	3.452	8.0	0.0095

Table 4.B.14: Peak position and FWHM of the CH_3 antisymmetric stretch of pure methylamine and mixtures in which methylamine is diluted in a ratio of 1:10 and for temperatures ranging from 15 K to 140 K.

Mixture	Temperature (K)	Peak position (cm^{-1})	(μm)	FWHM (cm^{-1})	(μm)
CH_3NH_2	15	2881.3	3.471	17.5	0.021
CH_3NH_2:H_2O (1:10)		2898.1	3.451	11.8	0.014
CH_3NH_2:CH_4 (1:10)		2885.4	3.466	11.9	0.014
CH_3NH_2:NH_3 (1:10)		2887.2	3.464	11.9	0.014
CH_3NH_2:H_2O:CH_4 (1:5:5)		-	-	-	-
CH_3NH_2:H_2O:NH_3 (1:5:5)		-	-	-	-
CH_3NH_2:CH_4:NH_3 (1:5:5)		2885.1	3.466	12.6	0.015
CH_3NH_2:H_2O:CH_4:NH_3 (3:10:10:10)		-	-	-	-
CH_3NH_2	35	2881.0	3.471	17.4	0.021
CH_3NH_2:H_2O (1:10)		2879.9	3.472	11.6	0.014 -
CH_3NH_2:CH_4 (1:10)		2884.9	3.466	12	0.014 -
CH_3NH_2:NH_3 (1:10)		2887.5	3.463	12.5	0.015
CH_3NH_2:H_2O:CH_4 (1:5:5)		-	-	-	-
CH_3NH_2:H_2O:NH_3 (1:5:5)		-	-	-	-
CH_3NH_2:CH_4:NH_3 (1:5:5)		2885.1	3.466	12.4	0.015 -
CH_3NH_2:H_2O:CH_4:NH_3 (3:10:10:10)		-	-	-	-
CH_3NH_2	55	2880.8	3.471	17.3	0.021
CH_3NH_2:H_2O (1:10)		2897.2	3.452	11.6	0.014 -
CH_3NH_2:CH_4 (1:10)		-	-	-	-
CH_3NH_2:NH_3 (1:10)		2887.8	3.463	13.5	0.016
CH_3NH_2:H_2O:CH_4 (1:5:5)		-	-	-	-
CH_3NH_2:H_2O:NH_3 (1:5:5)		-	-	-	-
CH_3NH_2:CH_4:NH_3 (1:5:5)		-	-	-	-
CH_3NH_2:H_2O:CH_4:NH_3 (3:10:10:10)		-	-	-	-
CH_3NH_2	95	2880.8	3.471	17.1	0.021
CH_3NH_2:H_2O (1:10)		2897.4	3.451	11.0	0.013 -
CH_3NH_2:NH_3 (1:10)		2888.8	3.462	12.7	0.015
CH_3NH_2:H_2O:CH_4 (1:5:5)		2884.8	3.466	12.1	0.015 -
CH_3NH_2:H_2O:NH_3 (1:5:5)		-	-	-	-
CH_3NH_2:CH_4:NH_3 (1:5:5)		-	-	-	-
CH_3NH_2:H_2O:CH_4:NH_3 (3:10:10:10)		-	-	-	-
CH_3NH_2	115	2880.0	3.472	12.1	0.015
CH_3NH_2:H_2O (1:10)		2897.4	3.451	11.2	0.013 -
CH_3NH_2:NH_3 (1:10)		2888.5	3.462	12.2	0.015

CH_3NH_2:H_2O:CH_4 (1:5:5)		-	-	-	-
CH_3NH_2:H_2O:NH_3 (1:5:5)		-	-	-	- -
CH_3NH_2:H_2O:CH_4:NH_3 (3:10:10:10)		-	-	-	-
CH_3NH_2	140	-	-	-	-
CH_3NH_2:H_2O (1:10)		2897.2	3.452	9.7	0.012 -
CH_3NH_2:H_2O:CH_4 (1:5:5)		-	-	-	-
CH_3NH_2:H_2O:NH_3 (1:5:5)		-	-	-	-
CH_3NH_2:H_2O:CH_4:NH_3 (3:10:10:10)		-	-	-	-

Table 4.B.15: Peak position and FWHM of the CH_3 antisymmetric stretch of pure methylamine and mixtures in which methylamine is diluted in a ratio of 1:20 and for temperatures ranging from 15 K to 115 K.

Mixture	Temperature (K)	Peak position (cm^{-1})	(μm)	FWHM (cm^{-1})	(μm)
CH_3NH_2	15	2881.3	3.471	17.5	0.021
CH_3NH_2:H_2O (1:20)		2898.2	3.450	10.3	0.012
CH_3NH_2:CH_4 (1:20)		2887.2	3.464	11.7	0.014
CH_3NH_2:NH_3 (1:20)		2888	3.463	13.0	0.016
CH_3NH_2:H_2O:CH_4 (1:10:10)		2887.2	3.464	11.7	0.014
CH_3NH_2:H_2O:NH_3 (1:10:10)		-	-	-	-
CH_3NH_2:CH_4:NH_3 (1:10:10)		2885.9	3.465	11.9	0.014
CH_3NH_2	35	2881.0	3.471	17.4	0.021
CH_3NH_2:H_2O (1:20)		2898.3	3.450	10.5	0.012
CH_3NH_2:CH_4 (1:20)		2886.8	3.464	11.3	0.014
CH_3NH_2:NH_3 (1:20)		2888.9	3.462	13.4	0.016
CH_3NH_2:H_2O:CH_4 (1:10:10)		-		-	
CH_3NH_2:H_2O:NH_3 (1:10:10)		-	-	-	-
CH_3NH_2:CH_4:NH_3 (1:10:10)		2885.7	3.465	11.8	0.014
CH_3NH_2	55	2880.8	3.471	17.3	0.021
CH_3NH_2:H_2O (1:20)		2898.4	3.450	11.0	0.013 -
CH_3NH_2:CH_4 (1:20)		-	-	-	-
CH_3NH_2:NH_3 (1:20)		-	-	-	-
CH_3NH_2:H_2O:CH_4 (1:10:10)		-	-	-	-
CH_3NH_2:H_2O:NH_3 (1:10:10)		-	-	-	-
CH_3NH_2:CH_4:NH_3 (1:10:10)		-	-	-	-
CH_3NH_2	95	2880.8	3.471	17.1	0.021
CH_3NH_2:H_2O (1:20)		2898.5	3.450	11.3	0.013
CH_3NH_2:NH_3 (1:20)		2891.4	3.459	10.8	0.013
CH_3NH_2:H_2O:CH_4 (1:10:10)		-	-	-	-
CH_3NH_2:H_2O:NH_3 (1:10:10)		2891.3	3.459	10.9	0.013
CH_3NH_2	115	2880.0	3.472	12.1	0.015
CH_3NH_2:H_2O (1:20)		2898.8	3.450	10.3	0.012 -
CH_3NH_2:NH_3 (1:20)		-	-	-	-
CH_3NH_2:H_2O:CH_4 (1:10:10)		-	-	-	-
CH_3NH_2:H_2O:NH_3 (1:10:10)		-	-	-	-

Appendix C

The integrated absorbance of the methylamine bands (i.e., the band areas) in different ice mixtures and at selected temperatures is organized in tables available online at the CDS via anonymous ftp to `cdsarc.u-strasbg.fr` (130.79.128.5) or via `http://cdsweb.u-strasbg.fr/cgi-bin/qcat?J/A+A/`. Each table displays the data for one specific mixture. The band's integrated absorption is normalized in relation to the CH_3 antisymmetric deformation mode, around 1478.6 cm^{-1}, from the given mixture at 15 K. The CH_3 antisymmetric deformation mode was chosen for normalization because this feature is distinguishable in all the mixtures and does not overlap with any of the matrix components.

Table 4.C.1: Integrated absorbance ratios of CH_3NH_2 in the CH_3NH_2:H_2O(1:5) mixture.

Temperature (K)	1159.2 cm^{-1} (8.627 μm)	1420.3 cm^{-1} (7.041 μm)	1455.0 cm^{-1} (6.873 μm)	1478.6 cm^{-1} (6.763 μm)	2791.8 cm^{-1} (3.582 μm)	2881.3 cm^{-1} (3.471 μm)
15	1.60	0.67	0.61	1.00	-	1.68
55	1.97	0.77	0.70	1.17	-	1.55
95	1.98	0.73	0.63	1.10	-	1.32
135	1.85	0.70	0.55	0.96	-	1.12
140	1.73	0.65	0.48	0.79	-	1.08

Table 4.C.2: Integrated absorbance ratios of CH_3NH_2 in the CH_3NH_2:H_2O(1:10) mixture.

Temperature (K)	1159.2 cm^{-1} (8.627 μm)	1420.3 cm^{-1} (7.041 μm)	1455.0 cm^{-1} (6.873 μm)	1478.6 cm^{-1} (6.763 μm)	2791.8 cm^{-1} (3.582 μm)	2881.3 cm^{-1} (3.471 μm)
15	1.57	0.69	0.58	1.00	-	1.72
55	1.75	0.70	0.60	1.05	-	1.51
95	1.74	0.63	0.56	1.02	-	1.40
135	1.65	0.61	0.49	0.89	-	1.40
140	1.49	0.59	0.45	0.75	-	1.31

Table 4.C.3: Integrated absorbance ratios of CH_3NH_2 in the CH_3NH_2:H_2O(1:20) mixture.

Temperature (K)	1159.2 cm^{-1} (8.627 μm)	1420.3 cm^{-1} (7.041 μm)	1455.0 cm^{-1} (6.873 μm)	1478.6 cm^{-1} (6.763 μm)	2791.8 cm^{-1} (3.582 μm)	2881.3 cm^{-1} (3.471 μm)
15	1.30	0.74	0.56	1.00	-	1.54
55	1.44	0.79	0.54	1.02	-	1.54
95	1.39	0.75	0.51	0.98	-	1.48
135	1.35	0.73	0.44	0.90	-	1.25
140	1.53	0.86	0.40	0.85	-	1.17

Table 4.C.4: Integrated absorbance ratios of CH_3NH_2 in the CH_3NH_2:CH_4(1:5) mixture.

Temperature (K)	1159.2 cm^{-1} (8.627 μm)	1420.3 cm^{-1} (7.041 μm)	1455.0 cm^{-1} (6.873 μm)	1478.6 cm^{-1} (6.763 μm)	2791.8 cm^{-1} (3.582 μm)	2881.3 cm^{-1} (3.471 μm)
15	2.06	0.27	1.17	1.00	-	5.50
35	2.35	0.29	1.19	1.10	-	5.00
40	2.42	0.27	1.10	1.04	-	4.55
45	2.51	0.24	1.11	1.14	-	4.57

Table 4.C.5: Integrated absorbance ratios of CH_3NH_2 in the CH_3NH_2:CH_4(1:10) mixture.

Temperature (K)	1159.2 cm^{-1} (8.627 μm)	1420.3 cm^{-1} (7.041 μm)	1455.0 cm^{-1} (6.873 μm)	1478.6 cm^{-1} (6.763 μm)	2791.8 cm^{-1} (3.582 μm)	2881.3 cm^{-1} (3.471 μm)
15	2.04	0.30	1.30	1.00	-	7.80
35	2.04	0.30	1.15	0.96	-	8.30
40	2.23	0.30	1.11	0.95	-	5.60
45	2.71	0.34	1.23	1.18	-	5.61

Table 4.C.6: Integrated absorbance ratios of CH_3NH_2 in the CH_3NH_2:NH_3(1:5) mixture.

Temperature (K)	1159.2 cm^{-1} (8.627 μm)	1420.3 cm^{-1} (7.041 μm)	1455.0 cm^{-1} (6.873 μm)	1478.6 cm^{-1} (6.763 μm)	2791.8 cm^{-1} (3.582 μm)	2881.3 cm^{-1} (3.471 μm)
15	-	0.28	1.04	1.00	4.08	4.08
55	-	0.27	0.98	0.92	3.77	4.24
95	-	0.22	0.91	0.87	3.34	4.61
100	-	0.21	0.83	0.84	3.69	4.00
115	-	0.25	0.93	0.88	3.66	-

Table 4.C.7: Integrated absorbance ratios of CH_3NH_2 in the CH_3NH_2:NH_3(1:10) mixture.

Temperature (K)	1159.2 cm^{-1} (8.627 μm)	1420.3 cm^{-1} (7.041 μm)	1455.0 cm^{-1} (6.873 μm)	1478.6 cm^{-1} (6.763 μm)	2791.8 cm^{-1} (3.582 μm)	2881.3 cm^{-1} (3.471 μm)
15	-	0.27	1.05	1.00	3.89	3.62
55	-	0.26	1.00	0.92	3.67	3.62
95	-	0.28	0.93	0.93	0.34	3.38
100	-	0.00	0.84	0.87	3.36	3.34
115	-	0.00	0.64	0.66	2.81	-

Table 4.C.8: Integrated absorbance ratios of CH_3NH_2 in the CH_3NH_2:NH_3(1:20) mixture.

Temperature (K)	1159.2 cm^{-1} (8.627 μm)	1420.3 cm^{-1} (7.041 μm)	1455.0 cm^{-1} (6.873 μm)	1478.6 cm^{-1} (6.763 μm)	2791.8 cm^{-1} (3.582 μm)	2881.3 cm^{-1} (3.471 μm)
15	-	0.38	1.03	1.00	2.66	4.11
55	-	-	0.96	0.97	2.51	4.10
95	-	-	0.83	0.87	3.15	-
100	-	-	0.81	0.95	3.13	-
115	-	-	0.87	0.80	2.76	-

Table 4.C.9: Integrated absorbance ratios of CH_3NH_2 in the CH_3NH_2:H_2O:CH_4(1:5:5) mixture.

Temperature (K)	1159.2 cm^{-1} (8.627 μm)	1420.3 cm^{-1} (7.041 μm)	1455.0 cm^{-1} (6.873 μm)	1478.6 cm^{-1} (6.763 μm)	2791.8 cm^{-1} (3.582 μm)	2881.3 cm^{-1} (3.471 μm)
15	2.47	0.66	0.72	1.00	-	-
35	2.24	0.65	0.63	0.95	-	-
40	2.07	0.59	0.61	0.92	-	-
45	1.96	0.60	0.57	0.89	-	-
55	1.73	0.60	4.58	0.90	-	-
95	1.89	0.52	0.44	0.82	-	-
115	1.70	0.53	0.47	0.83	-	-
133	1.47	0.53	0.42	0.74	-	-
140	1.46	0.50	0.39	0.70	-	-
150	1.29	0.48	0.33	0.59	-	-

Table 4.C.10: Integrated absorbance ratios of CH_3NH_2 in the CH_3NH_2:H_2O:CH_4(1:10:10) mixture.

Temperature (K)	1159.2 cm^{-1} (8.627 μm)	1420.3 cm^{-1} (7.041 μm)	1455.0 cm^{-1} (6.873 μm)	1478.6 cm^{-1} (6.763 μm)	2791.8 cm^{-1} (3.582 μm)	2881.3 cm^{-1} (3.471 μm)
15	2.42	0.78	0.69	1.00	-	-
35	2.20	0.71	0.65	0.98	-	-
40	2.23	0.72	0.64	0.98	-	-
45	1.82	0.70	0.58	0.88	-	-
55	1.74	0.74	0.58	1.00	-	-
95	1.74	0.72	0.49	0.90	-	-
115	1.78	0.63	0.45	0.87	-	-
133	1.51	0.49	0.44	0.85	-	-
140	1.49	0.41	0.41	0.73	-	-
150	1.04	0.29	0.28	0.47	-	-

4.5. Appendix C

Table 4.C.11: Integrated absorbance ratios of CH_3NH_2 in the CH_3NH_2:H_2O:NH_3(1:5:5) mixture.

Temperature (K)	1159.2 cm^{-1} (8.627 μm)	1420.3 cm^{-1} (7.041 μm)	1455.0 cm^{-1} (6.873 μm)	1478.6 cm^{-1} (6.763 μm)	2791.8 cm^{-1} (3.582 μm)	2881.3 cm^{-1} (3.471 μm)
15	-	0.47	0.79	1.00	-	-
55	-	0.49	0.75	0.97	-	-
95	-	0.54	0.72	1.03	-	-
100	-	0.48	0.72	1.04	-	-
115	-	0.51	0.66	0.95	-	-
135	-	0.49	0.62	0.94	-	-
140	-	0.48	0.59	0.93	-	-
150	-	0.47	0.45	0.73	-	-

Table 4.C.12: Integrated absorbance ratios of CH_3NH_2 in the CH_3NH_2:H_2O:NH_3(1:10:10) mixture.

Temperature (K)	1159.2 cm^{-1} (8.627 μm)	1420.3 cm^{-1} (7.041 μm)	1455.0 cm^{-1} (6.873 μm)	1478.6 cm^{-1} (6.763 μm)	2791.8 cm^{-1} (3.582 μm)	2881.3 cm^{-1} (3.471 μm)
15	-	0.49	0.76	1.00	-	-
55	-	0.50	0.71	1.00	-	-
95	-	0.54	0.65	0.92	-	-
100	-	0.56	0.64	0.98	-	-
115	-	0.54	0.57	0.89	-	-
135	-	0.58	0.52	0.80	-	-
140	-	0.60	0.43	0.77	-	-
150	-	0.52	0.34	0.56	-	-

Table 4.C.13: Integrated absorbance ratios of CH_3NH_2 in the CH_3NH_2:CH_4:NH_3(1:5:5) mixture.

Temperature (K)	1159.2 cm^{-1} (8.627 μm)	1420.3 cm^{-1} (7.041 μm)	1455.0 cm^{-1} (6.873 μm)	1478.6 cm^{-1} (6.763 μm)	2791.8 cm^{-1} (3.582 μm)	2881.3 cm^{-1} (3.471 μm)
15	-	0.34	1.21	1.00	-	5.84
35	-	0.35	1.21	0.99	-	6.00
40	-	0.33	1.00	1.10	-	5.67
45	-	0.32	1.10	0.97	-	5.16
95	-	0.25	1.03	1.00	-	4.64
100	-	0.30	0.95	0.98	-	-
115	-	0.21	0.54	0.67	-	-

Table 4.C.14: Integrated absorbance ratios of CH_3NH_2 in the CH_3NH_2:CH_4:NH_3(1:10:10) mixture.

Temperature (K)	1159.2 cm^{-1} (8.627 μm)	1420.3 cm^{-1} (7.041 μm)	1455.0 cm^{-1} (6.873 μm)	1478.6 cm^{-1} (6.763 μm)	2791.8 cm^{-1} (3.582 μm)	2881.3 cm^{-1} (3.471 μm)
15	-	0.30	1.18	1.00	-	6.96
35	-	0.33	1.15	0.95	-	6.96
40	-	0.32	1.14	0.90	-	6.23
45	-	0.32	1.18	0.97	-	5.86
95	-	0.31	1.03	1.12	-	-
100	-	0.34	1.03	1.10	-	-
115	-	-	0.86	0.87	-	-

Table 4.C.15: Integrated absorbance ratios of CH_3NH_2 in the CH_3NH_2:H_2O:CH_4:NH_3(3:10:10:10) mixture.

Temperature (K)	1159.2 cm^{-1} (8.627 μm)	1420.3 cm^{-1} (7.041 μm)	1455.0 cm^{-1} (6.873 μm)	1478.6 cm^{-1} (6.763 μm)	2791.8 cm^{-1} (3.582 μm)	2881.3 cm^{-1} (3.471 μm)
15	-	0.43	0.91	1.00	-	-
35	-	0.48	0.84	0.97	-	-
40	-	0.48	0.81	0.97	-	-
45	-	0.50	0.82	0.99	-	-
55	-	0.49	0.77	0.98	-	-
95	-	0.47	0.70	0.91	-	-
115	-	0.46	0.65	0.90	-	-
133	-	0.50	0.64	0.90	-	-
140	-	0.48	0.61	0.84	-	-
150	-	0.44	0.46	0.76	-	-

5

Infrared spectra of complex organic molecules in astronomically relevant ice mixtures: V. Methyl cyanide (acetonitrile)

The increasing sensitivity and resolution of ground-based telescopes have enabled the detection of gas-phase complex organic molecules (COMs) across a variety of environments. Many of the detected species are expected to form on the icy surface of interstellar grains and transfer later into the gas phase. Therefore, icy material is regarded as a primordial source of complex molecules in the interstellar medium. Upcoming James Webb Space Telescope (JWST) observations of interstellar ices in star-forming regions will reveal infrared (IR) features of frozen molecules with unprecedented resolution and sensitivity. To identify COM features in the JWST data, laboratory IR spectra of ices for conditions that simulate interstellar environments are needed. This work provides laboratory mid-IR spectra of methyl cyanide (CH_3CN, also known as acetonitrile) ice in its pure form and mixed with known interstellar molecules at cryogenic temperatures. The spectroscopic data presented in this work will support the interpretation of JWST ice observations and are made available to the community through the Leiden Ice Database for Astrochemistry (LIDA). Fourier transform IR spectroscopy is used to record the mid-IR spectra (500 - 4000 cm^{-1}/ 20 - 2.5 μm, with a resolution of 1 cm^{-1}) of methyl cyanide (acetonitrile, CH_3CN) mixed with H_2O, CO, CO_2, CH_4, NH_3, H_2O:CO_2, and H_2O:CH_4:NH_3, at temperatures ranging from 15 K - 150 K. The refractive index (at 632.8 nm) of pure amorphous CH_3CN ice at 15 K and the band strength of selected IR transitions are also measured. We present a variety of reference mid-IR spectra of frozen CH_3CN that can be compared to astronomical ice observations. The peak position and full width at half maximum (FWHM) of six absorption bands of frozen methyl cyanide in its pure form and mixed ices, at temperatures between 15 K - 150 K, are characterized. These bands are the following: the CH_3 symmetric stretching at 2940.9 cm^{-1} (3.400 μm), the CN stretching at 2252.2 cm^{-1} (4.440 μm), a peak resulting from a combination of different vibrational modes at 1448.3 cm^{-1} (6.905 μm), the CH_3 antisymmetric deformation at 1410 cm^{-1} (7.092 μm), the CH_3 symmetric deformation at 1374.5 cm^{-1} (7.275 μm), and the CH_3 rock vibration at 1041.6 cm^{-1}(9.600 μm). Additionally, the apparent band strength of these vibrational modes in mixed ices is derived. The laboratory spectra of CH_3CN are compared to observations of interstellar ices toward W33A and three low-mass Young Stellar Objects (YSO). Since an unambiguous identification of solid methyl cyanide toward these objects is not possible, upper limits for the CH_3CN column density are determined as $\leq 2.4 \times 10^{17}$ molecules cm^{-2} for W33A and 5.2×10^{16}, 1.9×10^{17}, and 3.8×10^{16} molecules cm^{-2} for EC92, IRAS 03235, and L1455 IRS3, respectively. With respect to solid H_2O, these values correspond to relative abundances of 1.9, 3.1, 1.3, and 4.1 percent, for W33A, EC92, IRAS 03235, and L1455 IRS3, respectively.

M. G. Rachid, W. R. M. Rocha and H. Linnartz (2022) published in A&A, 665, A89

5.1 Introduction

An increasing number of molecules has been detected in the interstellar medium (ISM) over the past decades, adding to more than 240 species (McGuire, 2022). Listed in this inventory are many organic molecules with more than six atoms, which in astrochemistry are referred to as complex organic molecules (COMs, Herbst and van Dishoeck, 2009). These COMs were identified across a diversity of environments, ranging from cold starless cores (e.g., Scibelli and Shirley, 2020; Jørgensen et al., 2020) to objects in different phases of protostellar evolution (e.g., Remijan et al., 2005; Herbst and van Dishoeck, 2009; Jørgensen et al., 2016; van Gelder et al., 2020), and extragalactic sources (e.g., Henkel et al., 1987; Aladro et al., 2011; Sewiło et al., 2019). Although observations and laboratory studies indicate that these species are mainly formed in interstellar ices (e.g., Elsila et al., 2007; Bisschop et al., 2007; Requena-Torres et al., 2008; Jiménez-Escobar et al., 2016; Chuang et al., 2020, 2021; Ioppolo et al., 2021), the only interstellar COM securely detected in the solid state to date is CH_3OH (Skinner et al., 1992). The lack of icy COM detections is mainly driven by instrumental limitations and spectral overlap of molecular absorption features. Observing missions with the *Infrared Space Observatory* (ISO) and the *Spitzer* Space Telescope allowed systematic observations of ices toward high- and low-mass star-forming regions (e.g., Gibb et al., 2004; Boogert et al., 2008). *Spitzer* also observed ice bands toward quiescent molecular clouds, thus enabling the study of the ice formation in starless cores (Boogert et al., 2011). So far, only the simple and more abundant molecular species have been detected in interstellar ices, such as H_2O, CO_2, CO, CH_4, NH_3, and CH_3OH (Öberg et al., 2011). With the recent launch of the James Webb Space Telescope (JWST), this scenario is expected to change. With the high sensitivity, spatial and spectroscopic resolution of JWST, weak features of frozen molecules may be revealed. To support the upcoming JWST ice observations, laboratory studies aiming at characterizing COMs in relevant astronomical ices have been carried out during the past years (see for example Maté et al. 2017; Urso et al. 2017; Luna et al. 2018; Hudson and Gerakines 2018; Terwisscha van Scheltinga et al. 2018; Scirè et al. 2019; Palumbo et al. 2019; Terwisscha van Scheltinga et al. 2021; Rachid et al. 2020, 2021; Müller et al. 2021; Gerakines et al. 2022). These works are of paramount importance for the correct assignment of features in interstellar ice spectra since the molecular vibrational bands are sensitive to ice composition, temperature, and morphology (e.g., Pontoppidan et al., 2008; Cuppen et al., 2011). Therefore, interpreting astronomical ice observations using laboratory spectra of molecules in realistic astronomical condi-

tions brings not only information about the ice chemical composition, but also the ice matrix and processes taking place in the solid phase in the ISM (Ehrenfreund et al., 1998).

This work is a study of the spectral features of methyl cyanide (or acetonitrile, CH_3CN) in astronomical relevant ices. Methyl cyanide (Figure 5.1) is a symmetric top molecule, which makes it an important species to trace the different physical conditions in the ISM (Loren and Mundy, 1984). Methyl cyanide has been identified across a variety of environments, such as in the galactic diffuse molecular gas (Liszt et al., 2018), in low and high mass star-forming regions (Araya et al., 2005), protoplanetary disks (Öberg et al., 2015; Loomis et al., 2018; Bergner et al., 2018), photodissociation regions (Guzmán et al., 2014), extragalactic sources (Mauersberger et al., 1991) and in our Solar System, in the atmosphere of Titan (Marten et al., 2002), and in the material outgassed by comets (Bockelée-Morvan et al., 2000; Dutrey et al., 1996; Goesmann et al., 2015).

Despite its ubiquitous presence in the ISM, the interstellar formation of methyl cyanide remains a puzzle, and both gas and solid-state mechanisms have been proposed. In the gas phase, the radiative association of HCN and $CH_3{}^+$:

$$HCN + CH_3{}^+ \rightarrow CH_3CNH^+ + h\nu,$$

followed by dissociative recombination:

$$CH_3CNH^+ + e^- \rightarrow CH_3CN + H,$$

can yield CH_3CN (Huntress Jr and Mitchell, 1979; Willacy et al., 1993; Mackay, 1999). In the solid phase, CH_3CN is expected to form through radical-radical reaction:

$$CH_3{}^\bullet + CN^\bullet \rightarrow CH_3CN,$$

or through successive hydrogenation of C_2N (Garrod et al., 2008). Recently, Volosatova et al. (2021) experimentally showed that CH_3CN can also be formed upon X-ray irradiation of CH_4:HCN in matrix isolated ices. To determine the dominant formation pathways in different astronomical conditions, more spatially resolved observations of CH_3CN and laboratory measurements of reaction rate constants are needed. Nevertheless, the gas-phase abundance of methyl cyanide observed in protoplanetary disks indicates that the formation of CH_3CN may happen in the ice phase (Öberg et al.,

2015; Loomis et al., 2018). This assumption is in line with recent observations of methyl cyanide and other COMs in the disk around the young star V883 Ori by Lee et al. (2019). The quick increase in the temperature of V883 Ori's inner disk, caused by outbursts, sublimates the ice mantles covering the dust grains. Consequently, the content of the ice material is injected into the gas phase, providing a unique chance to probe the solid-phase molecular inventory through sensitive millimeter ALMA observations.

In interstellar ices, methyl cyanide can be a precursor of a range of N-bearing COMs. Experimental works about the UV photolysis of CH_3CN and CH_3CN-containing ices were shown to result in a variety of more complex species, among them amino acids, amines, and amides (Hudson et al., 2008; Abdulgalil et al., 2013; Bulak et al., 2021). In a recent study, Bulak et al., 2021 showed that the UV irradiation of CH_3CN in a H_2O environment has the potential to form several COMs containing both oxygen and nitrogen. Thus, CH_3CN is an important piece for unveiling the chemistry taking place in the ISM.

To identify CH_3CN ice signatures in future JWST data, the spectrum of this species in the solid state is needed. The absorption profile of a molecule (e.g., peak positions, bandwidths, and intensities) is sensitive to the ice composition, morphology, and temperature. Therefore, the spectrum of CH_3CN in simulated interstellar ice conditions is necessary. The mid-IR spectra of pure CH_3CN ice in its amorphous and different crystalline forms have been reported in the literature (see, for example, Dello Russo and Khanna (1996), Hudson and Moore (2004), Abdulgalil et al. (2013), and Hudson (2020)). The spectra of CH_3CN mixed with H_2O, CH_3OH, and CH_3CH_2OH in a range of different temperatures have been also investigated (Bhuin et al., 2015; Methikkalam et al., 2017). These studies report changes in the infrared profile of methyl cyanide in different ice mixtures and explore the molecular interactions taking place in the solid phase (e.g., hydrogen bonding). To simulate more realistic interstellar ices, it is necessary to study samples containing known interstellar ice molecules and low concentrations of CH_3CN. Also important is to report the changes in peak position, bandwidth, and strength of CH_3CN features in different ice mixtures to offer astronomers a quick source of spectroscopic parameters.

This work investigates the spectra of CH_3CN mixed with H_2O, CO, CO_2, CH_4, and NH_3, at temperatures ranging from 15 K - 150 K. The position and FWHM of selected CH_3CN bands are characterized and their potential to identify methyl cyanide in astronomical ice observations is discussed. This paper is structured as follows. Section 2 brings the experimental setup and measurement protocols. Section

3 reports the changes in the profile of the selected methyl cyanide bands in different ice mixtures and temperatures. Section 4 explores the potential of methyl cyanide features to trace this species in ice observations and shows the use of the laboratory spectra to interpret astronomical data. Section 5 summarizes the conclusions of the work. The appendices bring the infrared profile, peak position, FWHM, and the integrated absorbance of the characterized methyl cyanide bands in the different ice mixtures and temperatures. The complete data set recorded in this work is available from the Leiden Ice Database for Astrochemistry[1] (LIDA, Rocha et al., 2022).

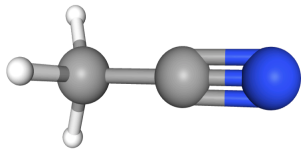

Figure 5.1: Three-dimensional molecular structure of CH_3CN (hydrogen: white; carbon: gray; nitrogen: blue).

5.2 Methodology

All the measurements are performed using IRASIS (InfraRed Absorption Setup for Ice Spectroscopy), a vacuum setup (base pressure $\sim 2 \times 10^{-9}$ mbar) dedicated to acquiring mid-IR spectra and visible refractive index (at 632.8 nm) of ice samples. The analyzed ices are grown by background deposition of a gaseous sample onto a germanium (Ge) substrate kept at 15 K by a closed-cycle helium cryostat. Typically, the ices are grown for $10 - 20$ minutes, which results in a thickness of around $1 - 1.5$ μm on each side of the germanium substrate. After the ice deposition, a Fourier transform infrared spectrometer is used to record the mid-infrared spectrum ($20 - 2.5$ μm, 500 - 4000 cm^{-1}) in transmission mode at resolution 1.0 cm^{-1} and averaging 128 scans. Subsequently, the sample is heated at a rate of 25 K hr^{-1} until its complete desorption. The spectrum of the ice sample is recorded during the heating and it takes around 2 minutes to obtain the complete spectrum. This time interval results in an uncertainty of 1 K in the temperature associated with the spectrum. For all the ice mixtures, a single sample is prepared and studied. For the pure CH_3CN ice, at least three samples are prepared, and since the IR profile of methyl cyanide bands in all the samples is identical, the spectrum of one of them is chosen to be reported. For a detailed description of the setup and methodology see Rachid et al. (2021).

[1] `https://icedb.strw.leidenuniv.nl/`

The changes in the IR profile of methyl cyanide when mixed with different and abundant interstellar ice molecules (H_2O, CO, CO_2, CH_4, and NH_3) are investigated. For this purpose, binary mixtures containing methyl cyanide are prepared at ratios 1:5, 1:10, and 1:20 (i.e., for each CH_3CN molecule in the mixture, there are 5, 10, or 20 molecules of the second component). A three and a four components mixtures are also analyzed: CH_3CN:H_2O:CH_4:NH_3(1:20:2:2) and CH_3CN:H_2O:CO_2(1:5:2). These more complex samples have a composition that is closer to "real" interstellar ices. The gaseous samples are prepared in a separate mixing system by the sequential addition of vapor or gas components to a glass bulb. The liquid components (H_2O and CH_3CN) are purified by at least three freeze-thaw cycles before preparing the mixture. The gaseous mixture in the bulb has a total pressure of 20 mbar, and the partial pressure of each molecular component corresponds to their fraction in the mixture. It is assumed in this work that the ratio of a molecular species in the final ice sample is the same as in the gaseous mixture. The estimated error in the mixture ratios is estimated as 20, 24, and 30 percent for the two, three, and four-component mixtures, respectively (Rachid et al., 2021). The gases and liquids used for preparing the gaseous mixtures are methyl cyanide (acetonitrile, VWR, $\leq$ 10 ppm of water), water (Milli-Q, Type I), carbon monoxide (Linde gas, 99.997%), carbon dioxide (Linde Gas, 99.95%) methane (Linde Gas 99.995%), and ammonia (Sigma Aldrich, anhydrous $\geq$ 99.99 %).

5.2.1 Refractive index and ice thickness

The real part of the refractive index (n) of a solid sample can be measured through a technique that consists in acquiring the interference pattern of two individual laser beams, hitting the growing ice at the same spot but under two different angles (Romanescu et al., 2010; Beltrán et al., 2015). The real refractive index is related to the period of the generated interference patterns by:

$$n = \sqrt{\frac{\sin^2\theta_0 - \gamma^2 \sin^2\theta_1}{1-\gamma^2}}, \tag{5.1}$$

where $\gamma = \frac{T_1}{T_0}$ is the ratio between the periods of the interference patterns, T_1 and T_0, produced by the laser beams hitting the substrate at angles θ_1 and θ_0, respectively. In this work, a red HeNe laser (λ = 632.8 nm) hitting the ice at angles of $\theta_0 = 8.0^\circ \pm 0.5^\circ$ and $\theta_1 = 50.0^\circ \pm 0.5^\circ$ is employed. For this wavelength, the measured refractive index of pure CH_3CN ice at 15 K is n = 1.28 $\pm$ 0.02. The uncertainty in this value is calculated from the standard deviation of five independent measurements. This value

is slightly lower than values found in the literature for amorphous CH_3CN at 15 K, (n = 1.334, Hudson, 2020) and at 30 K (n = 1.31, Moore et al., 2010).

Once the refractive index of the ice is known, its thickness can be measured by recording a single laser interference measurement during the ice deposition. The ice thickness is related to the number of fringes (m) in an interference pattern by:

$$d = \frac{m\lambda}{2\sqrt{n^2 - sin^2\theta}}, \tag{5.2}$$

where λ and θ are the wavelength and incidence angle of the laser light, respectively, and n is the ice's refractive index. The thickness of the pure methyl cyanide ice analyzed in this work is around 2.63 μm (considering both sides of the substrate).

5.2.2 IR band strengths

To derive the band strength of an IR absorption feature (A, in units cm molec^{-1}), it is necessary to know its integrated absorption as well as the number of absorbing species in the pathway of the probing IR beam, given by the column density (N, in units of molecules cm^{-2}, d'Hendecourt and Allamandola 1986). The column density of a species in pure ice is related to the ice thickness and density (assuming that the thickness of the ice is homogeneous in the area probed by the beam) by:

$$N = \frac{d\ \rho\ N_A}{M}, \tag{5.3}$$

where d and ρ are the ice thickness (in cm) and density (in g cm^{-3}), M is the molar mass (in g mol^{-1}) of the molecule being deposited, and N_A is Avogadro's number. This expression can be combined with the Lambert-Beer law to provide the band strength in terms of the ice parameters and integrated absorbance of an absorption band:

$$A = \frac{2.3\ M\ \alpha}{\rho\ \ N_A\ \beta}, \tag{5.4}$$

where M = 41.05 g mol^{-1} is the molecular mass of methyl cyanide, ρ = 0.778 g cm^{-3} is the ice density, from Hudson (2020), α is the growth rate of the integrated absorbance (cm^{-1} s^{-1}), and β is the ice thickness growth (cm s^{-1}). In Equation 5.4, the growth of the ice thickness and integrated absorbance during the ice deposition are used instead of single measurements of thickness and integrated absorbance at a given time. This procedure is valid as long as both growth rates are linear in time, which is the case in our measurements. Using equation 5.4, the refractive index of CH_3CN at 15 K and the

measured growth rate of the ice thickness and integrated absorbance of the CH_3CN features, the band strengths for pure CH_3CN ice at 15 K are obtained (Table 5.1). The uncertainty in the values listed in Table 5.1 is calculated through error propagation of the terms in Equation 5.4. The uncertainties in α and β, follow from the uncertainty in the linear fit of the thickness (or integrated absorbance) with time. These uncertainties amount to a maximum of 4 percent for the ice thickness growth and 10 percent for the integrated absorbance. For the density value, an uncertainty of 10 percent is taken to avoid an underestimation of the uncertainty. The final uncertainty in the band strengths resulting from these assumptions is smaller than 15 percent. These band strengths derived in this work are generally in good agreement with most of the values measured by d'Hendecourt and Allamandola (1986), also shown in Table 5.1, and the CN stretching band strength value derived by Hudson and Moore (2004), A = 2.2 × 10^{-18} cm molecule^{-1}. Small differences in the values derived in previous works can be attributed to variations in the experimental conditions, integration boundaries in the IR spectrum, and baseline correction. The band strength values derived in this work are employed to calibrate the deposition rate of methyl cyanide in the measurements.

Table 5.1: IR band strength of amorphous CH_3CN ice at 15 K derived in this work.

Peak position (cm^{-1})	Integrated region (cm^{-1})	Assignment*	A (10^{-18} cm molec^{-1})	A**
3001.7	3030 - 2975	CH_3 antisymmetric stretching	1.5 ± 0.2	1.5
2940.9	2955 - 2923	CH_3 symmetric stretching	0.53 ± 0.08	0.47
2289.0	2310 - 2270	Combination of modes	0.62 ± 0.09	2.3
2252.2	2265 - 2235	CN stretching	1.9 ± 0.3	
1448.3	1490 - 1435	Combination of modes	2.9 ± 0.4	2.2
1410.0	1434 - 1398.5	CH_3 antisymmetric def.	1.9 ± 0.3	1.4
1374.5	1395 - 1357	CH_3 symmetric def.	1.2 ± 0.2	1.0
1041.6	1100 - 1025	CH_3 rock	1.6 ± 0.2	1.3
919.6	940 - 913.5	C-C stretching	0.35 ± 0.05	0.2

*Band assignments following Milligan and Jacox 1962; Dello Russo and Khanna 1996, and references therein.

** Values from d'Hendecourt and Allamandola 1986. Estimated uncertainties are around 20%.

In the ice mixtures, the apparent band strength of a feature i (A'_i) is derived using the column density of methyl cyanide in the mixture (N_{mix}) and the integrated absorbance of the feature by:

$$A'_i = 2.3 \, \frac{\int_i abs(\nu) \; d\nu}{N_{mix}}, \tag{5.5}$$

where $\int_i abs(\nu) \; d\nu$ is the integrated absorbance of the feature i. We note that the

absorbance is measured on the logarithm base 10 scale and is related to the transmittance (T) of light through the sample by Abs = -log(T). In this work, the column density and deposition rate of methyl cyanide in the ice mixtures (N_{mixt}) are derived in the following way. First, the deposition rate of pure CH_3CN is determined when the leak valve is kept at a fixed position and a bulb filled with 20 mbar of methyl cyanide vapor is connected to the dosing line. This procedure was repeated three times and the average value obtained for the deposition rate of pure CH_3CN was around 4.7 × 10^{15} molecules cm^{-2} s^{-1}. Next, this value is used to derive the CH_3CN deposition rate when a gas mixture containing a total pressure (adding all components) of 20 mbar is employed. This is done by multiplying the deposition rate for the pure CH_3CN by its fraction in the gaseous mixtures:

$$D_{CH_3CN,mixt} = D_{CH_3CN,pure} \times f, \tag{5.6}$$

where $D_{CH_3CN,mixt}$ and $D_{CH_3CN,pure}$ are the deposition rate of CH_3CN when depositing an ice mixture and pure CH_3CN, respectively, and f is the fraction of CH_3CN in the gaseous mixture. As an example, for mixtures in which CH_3CN is diluted in a 1:10 ratio, the deposition rate of CH_3CN would be $D_{CH_3CN,mixt(1:10)} = 4.7 \times 10^{15} \times \frac{1}{11} = 4.3 \times 10^{14}$ molecules cm^{-2} s^{-1}. Here, we assume that the deposition of methyl cyanide is not altered differently by the different gas components. This methodology comes with rather large uncertainties in the mixing ratio, which are estimated to amount to up to 30 percent.

The relative band strengths of methyl cyanide features in ice mixtures (i.e., the apparent band strength normalized with respect to the value for the pure ice) are calculated through the relation:

$$\eta = \frac{A'_i}{A_i}, \tag{5.7}$$

where A_i is the band strength of the feature in pure CH_3CN ice at 15 K derived in this work. The relative band strengths are derived for all the characterized bands in ices at 15 K. In conclusion, it is important to stress that currently it is not possible to reduce the large uncertainties in relative band strengths, which can be as high as 40 percent.

5.3 Results

This section describes the changes in the IR profile of selected methyl cyanide absorption features in the pure form and mixed with known interstellar ice components.

Figure 5.2 shows the IR spectra of pure CH_3CN ice and the other matrix molecules used in this work: H_2O, CO, CO_2, CH_4, and NH_3. Despite the relatively high deposition rates, the solid samples deposited at 15 K are amorphous. This can be concluded from the peak position and broad profile of the IR peaks of the pure methyl cyanide ices, characteristic of its amorphous structure (see Hudson and Moore 2004; Abdulgalil et al. 2013; Bhuin et al. 2015; Hudson 2020; Smith et al. 2021). The crystalline forms of methyl cyanide display a rather different peak profile in the 1500 - 1000 cm^{-1} region, in which the bands assigned to the CH_3 symmetric and antisymmetric deformation modes and the CH_3 rock display multiple components. In the measurements presented here, the peaks characteristics of crystalline CH_3CN are only observed after heating the pure ice to 100 K or temperatures higher than 120 K for mixed ices, as discussed in the following sections. Except for the CO-containing ices, the major components of the mixed ices used in this work are deposited as amorphous ice. This is evident by the comparison of their IR spectra with available literature data (see, for example, Bouilloud et al. 2015 for the profile of amorphous H_2O and the other molecules used in the mixture, Gerakines and Hudson 2015 for the profile of amorphous CH_4 ice, (see Ehrenfreund et al., 1999; Palumbo and Baratta, 2000) for CO_2; Zanchet et al. 2013 for the NH_3 profile, and Ehrenfreund et al. 1997 for the pure CO profile). In the CO-containing ices, CO is likely deposited in a polycrystalline form, as the formation of amorphous CO ice is only possible at temperatures below 8 K (He et al., 2022).

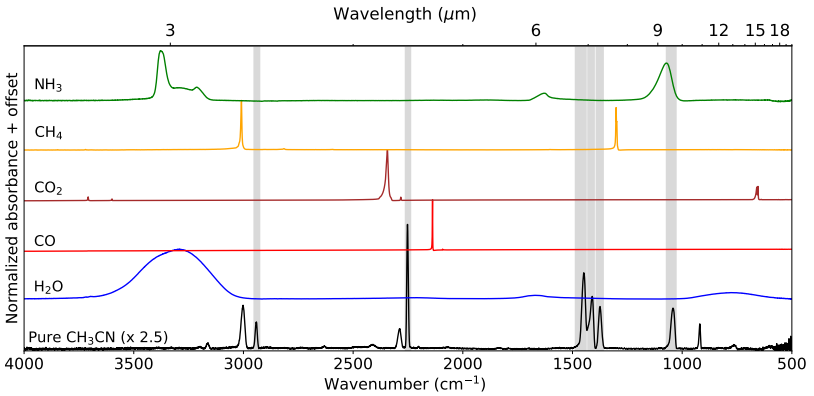

Figure 5.2: Infrared spectra of pure methyl cyanide (CH_3CN) ice and the different molecules present in the ice mixtures analyzed in this work (H_2O, CO, CO_2, CH_4, and NH_3), all at 15 K. The methyl cyanide bands characterized in this work are highlighted by a shaded area.

The CH_3CN absorption bands highlighted by the shaded areas in Figure 5.2 are

selected for peak position and FWHM characterization. These are chosen according to their strength and marginal or no overlap with spectral features of other abundant species. The selected bands are the following: the CH_3 symmetric stretching at 2940.9 cm^{-1} (3.400 μm), the CN stretching at 2252.2 cm^{-1} (4.440 μm), a combination of modes at 1448.3 cm^{-1} (6.905 μm), the CH_3 antisymmetric deformation at 1410 cm^{-1} (7.092 μm), the CH_3 symmetric deformation at 1374.5 cm^{-1} (7.275 μm), and the CH_3 rock at 1041.6 cm^{-1}(9.600 μm). The potential of these bands as tracers of CH_3CN in interstellar ice observations is discussed in Section 5.4. The peak positions, assignments and band strengths measured for the amorphous CH_3CN ice at 15 K are listed in Table 5.1.

The infrared profile of methyl cyanide strongest mid-IR band, the CN stretching, in different ice mixtures and temperatures is shown in Figure 5.3. Similarly, the profiles of the other bands characterized in this work are displayed in figures 5.A.1, 5.A.2, 5.A.3, 5.A.4, and 5.A.5 in Appendix A. In these figures, binary mixtures in a ratio of 1:10 are used to illustrate the different band shapes of methyl cyanide absorption features in the mixtures. The discussion on the peak position and FWHM changes in the binary mixtures throughout this section is also based on the 1:10 mixtures, since the 1:5 and 1:20 binary mixtures present similar characteristics. The complete peak position and FWHM characterization for all the ice mixtures at all ratios and temperatures are available in the Tables from Appendix B. The integrated absorbance of the CH_3CN features (i.e., the band areas) in all ice mixtures at all temperatures is listed in Appendix C. These values are used for deriving the strength of the methyl cyanide bands in the mixtures at temperatures above 15 K. This procedure is described in details in Appendix C.

5.3.1 The 4000 - 2500 cm^{-1} region (2.5 - 4.0 μm)

In the 4000 - 2500 cm^{-1} region, solid amorphous CH_3CN presents two normal modes, assigned to the C-H antisymmetric stretching, around 3001.7 cm^{-1} (3.331 μm), and the C-H symmetric stretching, at 2940.9 cm^{-1} (3.400 μm). A couple of weaker features associated to overtones are also observed in this region (Beć et al., 2019) but will not be discussed here. At temperatures below 100 K, the peak position of the two CH_3CN normal modes does not change appreciably. Just above 100 K, there is an abrupt sharpening of both features, characteristic of a phase transition. These bands appear in the same region of the C-H features as other interstellar ice molecules. As can be seen in Figure 5.2, the C-H antisymmetric feature of methyl cyanide, at 3001.7 cm^{-1},

overlaps with the strong methane feature at 3010 cm^{-1} (3.322 μm). The feature of the C-H symmetric stretching does not overlap with any of the ice components used in this work, which makes it an interesting band for further study. However, this peak overlaps with the C-H vibrational modes from other COMs, which compromises its potential in tracing methyl cyanide in interstellar ices, as discussed in Section 5.4.

Figure 5.A.1 shows the IR profile of the CH_3 symmetric stretching feature in ice mixtures. The FWHM versus peak position panel shows that for most ice mixtures this feature peaks between 2941 - 2946 cm^{-1}. Peak positions out of this range are found for CH_3CN:NH_3, in which this band shifts to low wavenumbers (2931.8 cm^{-1}) and shows a FWHM of 17.9 cm^{-1} (the value for the pure ice is 10.9 cm^{-1}) and the CH_3CN:CO_2, in which this band shifts to high wavenumbers (around 2954.4 cm^{-1}). These differences in peak position and width can be evidenced in the bottom left panel of Figure 5.A.1, which displays the FWHM and peak position for this peak in the different ice mixtures and the range of temperatures studied here.

5.3.2 The CN stretching feature - 2252 cm^{-1}

The CN stretching vibration gives rise to an absorption band around 2252.2 cm^{-1}, which is the strongest methyl cyanide feature in the mid-IR. By warming the pure ice to 95 -100 K, a pronounced narrowing and an increasing in the intensity of this band are observed. At temperatures above 120 K, this feature peaks around 2251 cm^{-1} and has a FWHM of 1.3 cm^{-1}.

Figure 5.3 shows the profile of the CN stretching band in the different ice matrices. In CH_3CN:CH_4 and CH_3CN:NH_3 ices, this feature peaks between 2257 and 2250 cm^{-1} and has a profile similar to the pure methyl cyanide. In mixtures containing H_2O, CO_2, or CO, this feature shows some different characteristics.

In all the H_2O-containing ices, the CN stretching peaks at high wavenumbers, between 2263 - 2265 cm^{-1}, and it has a broader profile when compared to the other ice mixtures (FWHM $\sim$ 13 - 15 cm^{-1}). The different profile of this band in H_2O-rich ices can be seen in the panel displaying the FWHM versus peak position plot (left bottom of Figure 5.3), where the points representing the water-rich ices with temperatures below 120 K appear grouped in the left top region of the graph. Above 125 K, the CN feature sharpens and shifts to 2251 cm^{-1} for all the ice mixtures, as can be seen in the right corner of the panel. In the CH_3CN:CO_2 ice, the CN stretching band peaks at 2256.8 cm^{-1} and has a broader profile than the band seen in the pure ice. Figure 5.3 shows that the CN feature peaks near the $^{13}CO_2$ feature, around 2282

cm^{-1}. The $^{13}CO_2$ feature is seen in the panels showing CO_2-containing mixtures but is still clearly separated from the CN stretching transition. In CH_3CN:CO ice, the CN stretching band peaks at 2253.9 cm^{-1} and shows a small shoulder at high wavenumbers, which is not seen in other mixtures.

Interestingly, the peak position and FWHM of the CN stretching peak in the ice mixtures above 125 K are close to the values measured for the pure methyl cyanide at the same temperature. This is noticeable from the FWHM versus peak position panel in figure 5.3, in which the points representing the mixtures at high temperatures are grouped in the right corner of the plot. The similarities in the absorption profile of CH_3CN-containing mixtures with pure CH_3CN at high temperatures are also observed for other bands and indicate that segregation of CH_3CN may take place in the ice mixtures.

5.3.3 The 2000 - 500 cm^{-1} region (5 - 20 μm)

Pure amorphous methyl cyanide ice at 15 K has three strong absorption features in the region between 2000 - 1300 cm^{-1}, a strong feature at 1448.3 cm^{-1} assigned to a combination of the CH_3 rock and CCN bending modes (Dello Russo and Khanna, 1996), the CH_3 antisymmetric deformation at 1410 cm^{-1} and the CH_3 symmetric deformation band, at 1374.5 cm^{-1}. In pure CH_3CN at temperatures above 100 K, these bands split into multiple components. Figures 5.A.2, 5.A.3 and 5.A.4 show the thermal evolution of these features in pure and mixed ices. The peak positions of the multiple features at high temperatures are displayed in Tables 5.B.3, 5.B.4, and 5.B.5.

In all the ice mixtures at 15 K, the peak position of the three features shows little changes, shifting less than 5 cm^{-1} with relation to the pure ice. As a general trend, the FWHM of these bands at low temperatures is narrower for the binary mixtures with CO, CO_2, and CH_4. Above 100 K (and 120 K for H_2O-containing ices) these peaks sharpen and split, showing a profile similar to the pure crystalline ice in all the mixtures. At these high temperatures, the feature assigned to a combination of modes, near 1448 cm^{-1}, shifts to around 1453 - 1455 cm^{-1} for all the ice mixtures. The CH_3 antisymmetric deformation band, near 1410 cm^{-1} in pure CH_3CN, splits into three components that peak around 1409, 1416, and 1419 cm^{-1}, similar to the features observed in pure methyl cyanide ice above 100 K. The band assigned to the CH_3 symmetric deformation band, near 1374.5 cm^{-1}, also splits into two components, around 1371.5 and 1378 cm^{-1}.

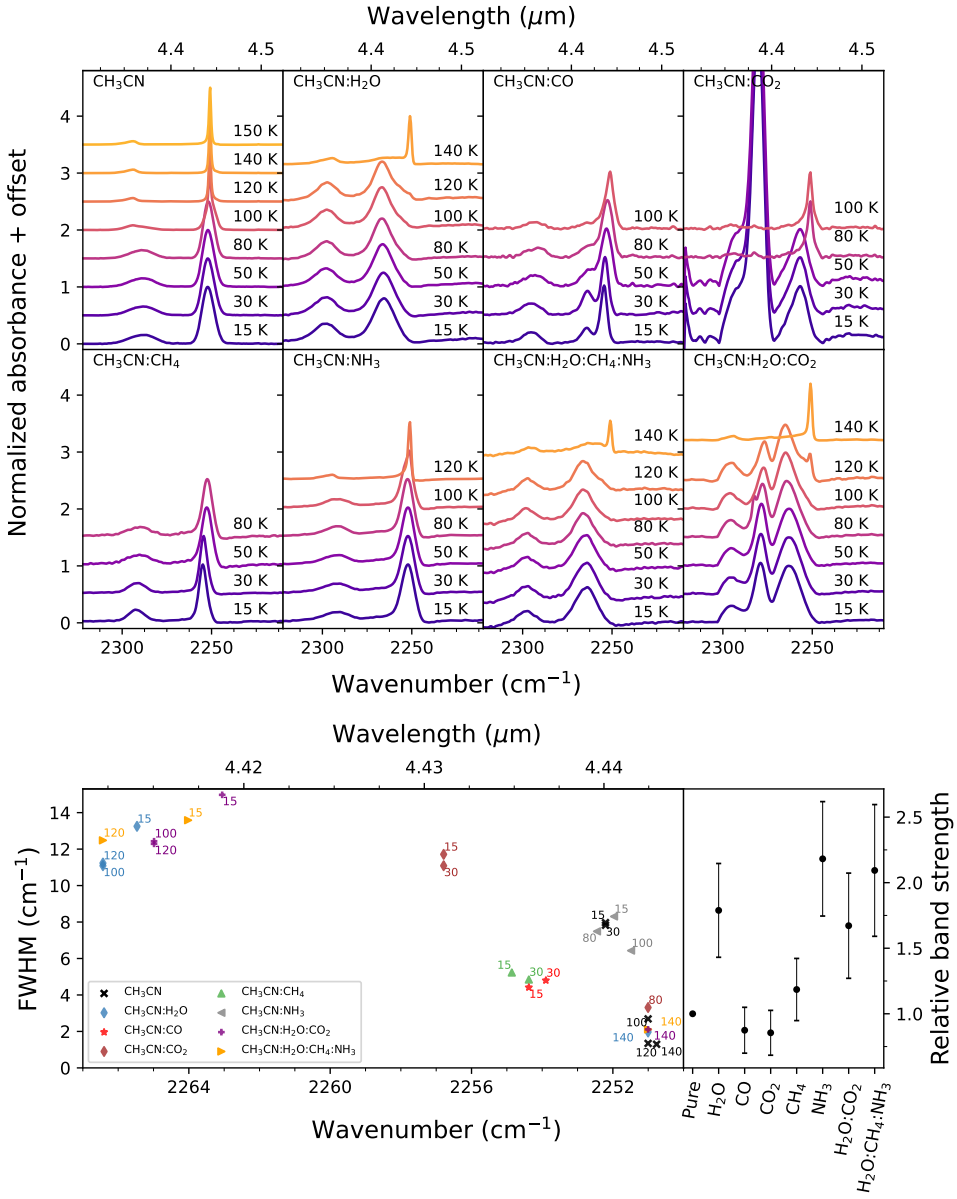

Figure 5.3: Upper panel: Absorption profile of the CN stretching mode of methyl cyanide, around 2252.2 cm^{-1} (4.440 μm), in pure and mixed ices. The ice spectra at different temperatures are indicated by different colors and labels. Bottom left: Peak position and FWHM of the CN stretching mode of CH_3CN in different ice mixtures at selected temperatures. Bottom right: relative band strengths of the CN stretching band in different ice mixtures at 15 K.

Below 1300 cm^{-1}, the pure CH_3CN ice has two strong peaks, at 1041.6 cm^{-1} (CH_3 rock) and 919.6 cm^{-1} (C-C stretching). The CH_3 rock feature overlaps with the low wavenumber ring of the NH_3 umbrella mode, but it can still be seen as a shoulder, even in diluted mixtures. Figure 5.A.5 shows the profile of this band in different ice mixtures. The matrix components are subtracted from mixtures containing H_2O and NH_3 for better visualization of the CH_3 rock feature. The peak position of this ice feature does not change substantially in the ice mixtures, peaking between 1042 - 1037 cm^{-1} in the ice mixtures at 15 K. The width of the CH_3 rock feature is larger in pure methyl cyanide than in the ice mixtures, as can be seen in the peak position versus FWHM plot in Figure 5.A.5 and the values in Table 5.B.6. At temperatures above 120 K, the CH_3 rock feature splits into three narrower features in the ice mixtures, that peak around 1048, 1040, and 1036 cm^{-1}.

The C-C stretching appears as a weak feature in diluted mixtures. This peak has some further disadvantages for being used as a methyl cyanide tracer: it appears at very close wavelengths to the OH bending mode of formic acid, a species that has been tentatively detected toward some Young Stellar Objects YSOs; Schutte et al., 1996, 1999; Bisschop et al., 2007. In an astronomical ice spectrum, this peak may be visible when methyl cyanide is present at relatively high column densities. At low methyl cyanide column densities, this peak will likely be overshadowed by the red wing of the H_2O libration mode (centered around 800 cm^{-1}) and the silicate feature around 10 μm. Because of these reasons, this band is not further characterized in this work.

5.4 Astronomical implications

The spectroscopic data recorded in this work is an essential tool for identifying methyl cyanide features in observations of ices toward dense clouds and protoplanetary disks. Future JWST observations made at unprecedented sensitivity and spectral resolution (e.g., R $\sim$ 3000 around 5 - 10 μm with the Mid InfraRed Instrument Medium Resolution Spectrometer - MIRI MRS, Labiano et al., 2021) will look for weak features of frozen COMs that are inaccessible from past ice surveys (McClure et al., 2021). Robust detection of new ice species will only be possible by the identification of multiple features using laboratory spectra as reference. Below, the potential of the methyl cyanide bands as tracers of this molecule in astronomical ice data is discussed.

Range between 2.5 and 3.4 μm: The C-H stretching features of methyl cyanide, around 3.333 μm (3000 cm^{-1}) and 3.400 μm (2940.9 cm^{-1}), overlap with the low wavenumber (high wavelength) wing of the O-H stretching band of solid H_2O, around 3 μm. In combination with CH_3CN bands observed in other parts of the IR spectrum,

the methyl cyanide features in this region can provide evidence for its presence in ice observations. However, assignments in this region should be done with care, due to the C−H stretching vibration bands of hydrocarbons and other COMs in this region (see, for example, Sandford et al. 1991; Boudin et al. 1998; Boogert et al. 2004; Rachid et al. 2021).

Range between 4.3 and 4.5 μm: The CN stretching feature, around 4.440 μm (2252.2 cm^{-1}), is methyl cyanide's strongest mid-IR band, and the one that offers the most potential for identifying this species in interstellar ice observations. This band does not overlap with features from abundant ice molecules or features from smaller CN-containing species. For example, the CN stretching transitions from HCN, CN^- and OCN^-, peak around 4.76 μm, 4.78 μm, and 4.61 μm, respectively (Moore and Hudson, 2003; Gerakines et al., 2004; Van Broekhuizen et al., 2004). However, we highlight that the presence of strong features near 4.4 μm (e.g., from $^{13}CO_2$ around 4.38 μm and OCN^- between 4.59 - 4.61 μm) may overshadow the CN stretching feature if CH_3CN is present at a low column density.

Range between 6.0−10 μm: Methyl cyanide has four bands in the region between 6.7 - 10 μm: at 6.905 μm (1448.3 cm^{-1}; assigned to a combination of vibrational modes), at 7.092 μm (1410 cm^{-1}; CH_3 antisymmetric deformation), and at 7.275 μm (1374.5 cm^{-1}; CH_3 symmetric deformation). The three features between 6.7−7.5 μm are strong, but they overlap with the CH_3 deformation mode from other COMs (e.g., Boogert et al., 2008), and potential organic refractory residue (Gibb and Whittet, 2002; Boogert et al., 2015; Rocha et al., 2021). The CH_3 rock mode of methyl cyanide, around 9.600 μm (1041.6 cm^{-1}), can be a potential tracer of CH_3CN. Although methanol also shows a vibrational mode near 9.60 μm, the methyl cyanide's CH_3 rock mode is a relatively strong band and peaks at lower wavelengths.

Range above 10 μm: Above 10 μm, methyl cyanide has one band around 10.87 μm (919.6 cm^{-1}) assigned to the C−C stretching vibration. This feature has some disadvantages for being used as a methyl cyanide tracer: it is not readily observed when low quantities of methyl cyanide ($\sim 10^{15}$ molecules cm^{-2}) are mixed with H_2O. Since this feature peaks in a spectral region dominated by strong absorption of H_2O and silicates, this band has limited potential as methyl cyanide tracer.

In this paper, we have searched for signatures of frozen CH_3CN toward four protostars. The first source is W33A, a well-known high-mass protostar (Gibb et al., 2000; Gibb et al., 2004) that was observed with ISO, and thus has broad spectral coverage. A direct comparison of the laboratory spectra and the ISO spectrum shows that there is no convincing signal that would act as a basis for a (preliminary) identification

of CH_3CN. However, it is possible to derive an upper limit for the methyl cyanide column density using the data collected in this work. Figure 5.4 shows the spectrum of W33A around the 4.4 μm region plotted with laboratory spectra of pure CH_3CN, CH_3CN:H_2O (1:10), and CH_3CN:CO_2(1:10) ices, all at 15 K. To calculate the maximum content of solid CH_3CN toward W33A, the optical depth of the CN stretching feature (4.44 μm) in the laboratory spectra is visually scaled to the observational signal in this region. Using the integrated optical depth of the scaled laboratory feature and the CN stretching strength for pure and mixed ices at 15 K derived in this work, we obtain an upper limit for the CH_3CN column density of 2.4×10^{17} molecules cm^{-2}, that corresponds to 1.9% relative to the solid H_2O toward this object ($N_{H_2O} \sim 12.57 \times 10^{18}$; Boogert et al. 2008). By scaling the spectrum of the CH_3CN:H_2O(1:10) and the CH_3CN:CO_2(1:10) to the observations, the CH_3CN upper limit is around 1×10^{17} molecules cm^{-2}, which corresponds to 0.8% relative to H_2O ice.

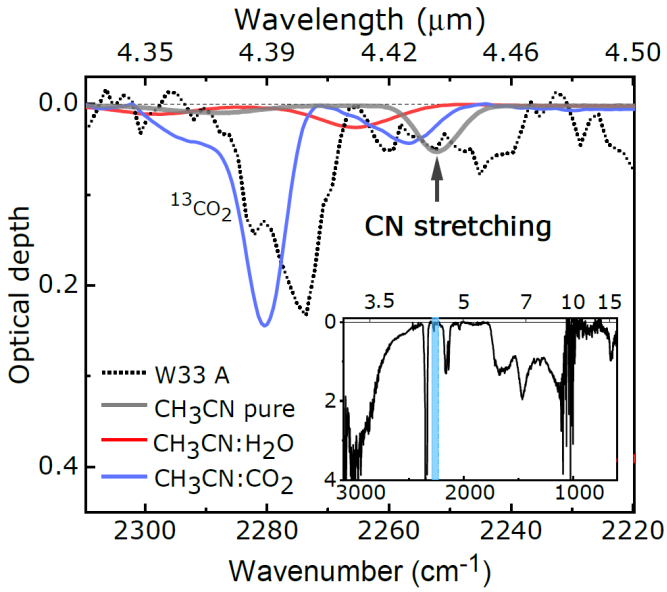

Figure 5.4: ISO spectrum of W33A with subtraction of a local linear continuum between 4.48 - 4.35 μm (dotted line). The laboratory spectra of CH_3CN (gray), CH_3CN:H_2O (red) and CH_3CN:CO_2 (blue) at 15 K are also shown. The CN stretching of methyl cyanide ice in the laboratory spectrum, used for deriving upper limits for this species toward W33A, is indicated with an arrow. The inset in the bottom right shows the complete spectrum of ices toward W33A. The region analyzed for deriving CH_3CN upper limits is indicated by the shadowed area.

In the top panel of Figure 5.5, we show a comparison between the laboratory spectra of CH_3CN ice with the spectra of three low-mass protostars, namely, EC92, IRAS03325, and L1455 IRS3, acquired with the *Spitzer* telescope (Boogert et al., 2008; Bottinelli et al., 2010). The spectral coverage of these observations is between 5.3 and 38 μm, and therefore the region in which the CN stretching absorbs, around 4.44 μm, cannot be analyzed. As previously discussed, the three features between 6.7−7.5 μm (top left) cannot be used to constrain the CH_3CN abundances in the protostar spectra due to overlap with other ice features. For this reason, we use the CH_3 rock band of methyl cyanide, around 9.6 μm (top right), to estimate the upper limits for this molecule in the low-mass protostars observations. We stress that NH_3 and CH_3OH also absorb around this region (Bottinelli et al., 2010). However, the CH_3 rock band of methyl cyanide peaks at shorter wavelengths than the methanol band and it is, in this case, the best feature to estimate upper limits. The bottom panels of Figure 5.5 show the comparison of the laboratory data presented here and the astronomical observations. The absorption profile of the CH_3 rock of the pure methyl cyanide ice at 15 K is plotted superimposed to the spectra of the three YSOs. In each panel, the laboratory data are scaled to the observations to estimate the upper limits for methyl cyanide column density. The low resolution of the observations (R $\sim$ 100) and partial overlap with the methanol absorption feature prohibits distinguishing the different CH_3CN band profiles characterized in this work. For this reason, only the spectrum of pure methyl cyanide at 15 K is employed. The estimated upper-limits for methyl cyanide column density in these objects are 5.2×10^{16}, 1.9×10^{17}, and 8.5×10^{17} molecules cm^{-2} for EC92, IRAS03235+3004, and L1455 IRS3, respectively. Relative to H_2O ice, these upper limits correspond to abundances of 3.1, 1.3, and 4.1% for EC92, IRAS03235+3004, and L1455 IRS3, respectively (considering the H_2O column densities from Boogert et al. 2008).

Figure 5.6 graphically displays the upper limit abundances of frozen methyl cyanide relative to solid-phase methanol derived for W33A, EC92, IRAS0325, and L1455 IRS3. The methanol ice column densities are taken from Boogert et al. (2008). The abundances range from 13% to 34.7% and are higher than the CH_3CN/CH_3OH ratios observed in the gas-phase toward the hot molecular core Sgr B2(N2), the Class 0 protostellar binary IRAS 16293B, and the coma of the Comet 67P/C-G (see Table 2 in Jørgensen et al., 2020). Despite the large uncertainties in the abundance calculation in the solid phase, these numbers suggest that the methyl cyanide content relative to methanol in interstellar ices can be larger than in the gas phase. An explanation would possibly pass through the thermal and nonthermal mechanisms releasing

these molecules to the gas phase, their fragmentation upon desorption, and their full gas-phase reaction network. However, more sensitive ice observations are needed to confirm this trend.

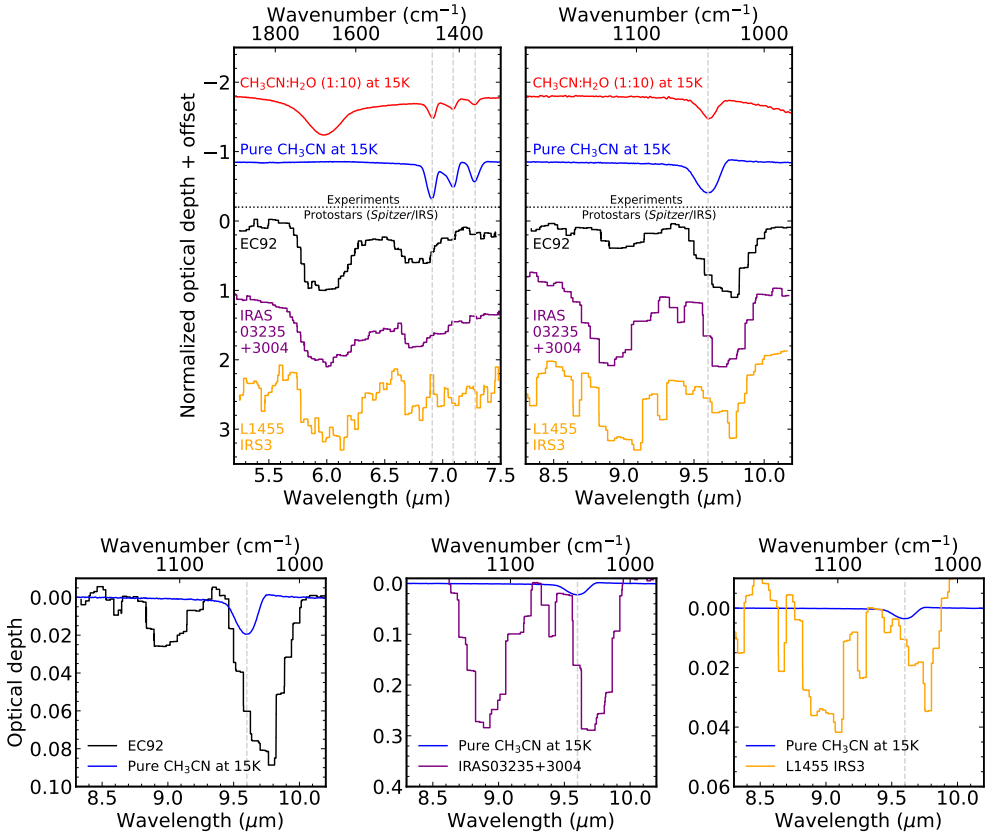

Figure 5.5: Comparison between the normalized *Spitzer*/IRS spectrum of three YSOs (EC92, IRAS03235+3004, and L1455 IRS3) and laboratory spectra of CH_3CN ice. Top panels: the CH_3CN and CH_3CN:H_2O ice spectra at 15 K are plotted with the YSO spectra (the continuum, and contributions from H_2O, and silicate features are subtracted). The 6.90, 7.09, 7.27, 9.60 μm features of CH_3CN are marked with a vertical dashed line. Bottom panels: *Spitzer*/IRS spectrum of EC92, IRAS03235+3004, and L1455 IRS3(from left to right) in the 8.5 - 10 μm region. In addition, the laboratory spectrum of pure CH_3CN ice at 15 K (blue) is shown. In the bottom panels, the spectrum of CH_3CN is scaled to the observations using the 9.60 μm band of methyl cyanide.

Future observations combining the NIRspec (Near-InfraRed Spectrograph; Bagnasco et al., 2007) and MIRI (Mid-InfraRed Instrument; Wells et al., 2015) instruments on-board of JWST will cover the spectral regions where CH_3CN can be observed, in-

cluding the band at 4.440 μm. A multiwavelength detection of methyl cyanide will help to understand the abundance of nitrogen-containing COMs in ices, which is currently less constrained than the O-containing COMs budget (Nazari et al., 2021). The interpretation of future observations using laboratory spectra of CH_3CN in different ice matrices and temperatures will enable not only the identification of this species but also hint at the environment in which methyl cyanide is formed. The CH_3CN nondetection will also open questions regarding the origin of its high gas-phase abundance in hot cores and protostars.

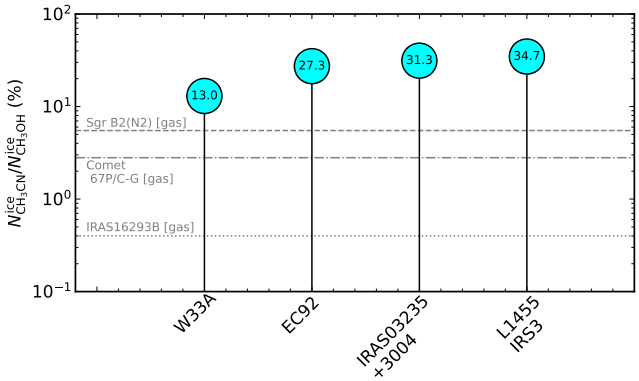

Figure 5.6: Upper limit abundances in the solid phase of CH_3CN with respect to CH_3OH estimated for ices toward W33A, EC92, IRAS03235+3004, and L1455 IRS3. The horizontal dashed lines show the gas-phase values for the hot molecular core Sgr B2(N2), the Comet 67P/C-G coma, and the binary protostar IRAS 16293B (from Jørgensen et al. 2020).

5.5 Conclusions

This work reports a series of mid-infrared spectra measurements of methyl cyanide ice in its pure form and mixed with relevant interstellar ice molecules. The peak position and full width at half maximum of six methyl cyanide absorption bands are characterized in different ice mixtures and for temperatures ranging from 15 K up to 150 K. The refractive index and infrared band strengths of pure methyl cyanide, and relative band strengths for CH_3CN modes in ice mixtures, all measured at 15 K, are presented. The main conclusions of this work are the following:

1. For upcoming JWST observations, the best chance to identify frozen CH_3CN is through its CN stretching mode, which peaks at 2252.2 cm^{-1} (4.440 μm) in the pure ice. This band together with the 1041.6 cm^{-1} (9.600 μm; CH_3 rock)

feature offers the most suitable combination of mid-IR transitions for identifying methyl cyanide in astronomical ice data. Due to the overlap with other interstellar ice components, the methyl cyanide bands at 2940.9 cm^{-1} (3.400 μm; CH_3 symmetric stretching), 1448.3 cm^{-1} (6.905 μm; CH_3CN combination of modes), 1410 cm^{-1} (7.092 μm; CH_3 antisymmetric deformation), 1374.5 cm^{-1} (7.275 μm ; CH_3 symmetric deformation), and (10.8 μm; C-C stretching) are less suited. However, the presence of bands in these regions should be checked as an additional tool to identify frozen CH_3CN.

2. Most of the analyzed infrared bands of CH_3CN in the ice mixtures shift by less than 5 cm^{-1} with respect to the position in the pure ice. The most striking variations are observed for the CN stretching mode (2252 cm^{-1}) in H_2O-containing ices, in which the absorption peak appears around 2265 cm^{-1}. The changes in the FWHM when methyl cyanide is mixed with other molecules are more pronounced, and these are described throughout the work. Above 120 K, the peak position and FWHM of methyl cyanide bands in the mixtures are similar to the pure ice at the same temperature. This indicates that segregation processes may take place in the ice mixtures above 120 K.

3. The comparison between the recorded CH_3CN ice spectra with ISO observations of W33A in the 4 - 5 μm region yields an upper limit for its column density of 2.4 $\times$ 10^{17} molecules cm^{-2}. Compared to H_2O and CH_3OH ice, this value corresponds to relative abundances of $\leq$ 1.9 and 13.0 percent, respectively.

4. The analysis of Spitzer/IRS spectra of ices toward the protostars EC92, IRAS 03235, and L1455 IRS3 in the 1800 - 1000 cm^{-1} (5.5 - 10 μm) region do not allow for the identification of CH_3CN features. Using the 1041.6 cm^{-1} band of CH_3CN, an upper limit for the column density of this species is estimated as 5.2 $\times$ 10^{16}, 1.9 $\times$ 10^{17} , and 3.8 $\times$ 10^{16} molecules cm^{-2} for EC92, IRAS 03235, and L1455 IRS3, respectively. With respect to solid H_2O, these values translate to relative abundances of 3.1, 1.3, and 4.1 percent, and with respect to methanol, to 27.3, 31.3, and 34.7 percent.

The upcoming JWST observations of interstellar ices will reveal new features of solid-state molecules. Within several observing programs, including the JWST early release program Ice Age, several objects at the early stages of stellar evolution are targeted to search for COMs. The work presented here provides essential laboratory data to support the identification and quantification of CH_3CN in the observations.

The identification of frozen methyl cyanide in the astronomical ice data will help to understand the inventory and distribution of nitrogen-bearing molecules in star-forming regions.

References

Abdulgalil, A. G. M., Marchione, D., Thrower, J., et al., 2013, Philosophical Transactions of the Royal Society A: Mathematical, Physical and Engineering Sciences, 371, 20110586

Aladro, R., Martín, S., Martín-Pintado, J., et al., 2011, A&A, 535, A84

Araya, E., Hofner, P., Kurtz, S., et al., 2005, ApJS, 157, 279

Bagnasco, G., Kolm, M., Ferruit, P., et al. (Sept. 2007). "Overview of the near-infrared spectrograph (NIRSpec) instrument on-board the James Webb Space Telescope (JWST)". *Cryogenic Optical Systems and Instruments XII*. Ed. by J. B. Heaney and L. G. Burriesci. Vol. 6692. Society of Photo-Optical Instrumentation Engineers (SPIE) Conference Series, 66920M, 66920M. DOI: 10.1117/12.735602.

Beć, K. B., Karczmit, D., Kwaśniewicz, M., et al., 2019, The J. Phys. Chem. A, 123, 4431

Beltrán, M. D., Molina, R. L., Aznar, M. Á. S., et al., 2015, Sensors, 15, 25123

Bergner, J. B., Guzmán, V. G., Öberg, K. I., et al., 2018, ApJ, 857, 69

Bhuin, R. G., Methikkalam, R. R. J., Sivaraman, B., et al., 2015, The J. Phys. Chem. C, 119, 11524

Bisschop, S. E., Fuchs, G. W., Boogert, A. C. A., et al., 2007, A&A, 470, 749

Bisschop, S., Jørgensen, J., van Dishoeck, E., et al., 2007, A&A, 465, 913

Bockelée-Morvan, D, Lis, D., Wink, J., et al., 2000, A&A, 353, 1101

Boogert, A. C. A., Blake, G. A., and Öberg, K., 2004, ApJ, 615, 344

Boogert, A. C. A, Gerakines, P. A., and Whittet, D. C., 2015, ARA&A, 53, 541

Boogert, A. C. A., Huard, T. L., Cook, A. M., et al., 2011, ApJ, 729, 92

Boogert, A. C. A., Pontoppidan, K. M., Knez, C., et al., 2008, ApJ, 678, 985

Bottinelli, S., Boogert, A. A., Bouwman, J., et al., 2010, ApJ, 718, 1100

Boudin, N., Schutte, W. A., and Greenberg, J. M., 1998, A&A, 331, 749

Bouilloud, M, Fray, N, Bénilan, Y, et al., 2015, MNRAS, 451, 2145

Bulak, M, Paardekooper, D., Fedoseev, G, et al., 2021, A&A, 647, A82

Chuang, K. J., Fedoseev, G., Qasim, D., et al., 2020, A&A, 635, A199

Chuang, K. J., Fedoseev, G., Scirè, C., et al., 2021, A&A, 650, A85

Cuppen, H., Penteado, E., Isokoski, K, et al., 2011, MNRAS, 417, 2809

Dello Russo, N and Khanna, R., 1996, Icarus, 123, 366

d'Hendecourt, L. and Allamandola, L., 1986, A&AS, 64, 453

Dutrey, A, Despois, D, Bockelée-Morvan, D, et al., 1996, International Astronomical Union Circular, 6364, 1

Ehrenfreund, P., Boogert, A. C. A., Gerakines, P. A., et al., 1997, A&A, 328, 649

Ehrenfreund, P, Dartois, E, Demyk, K, et al., 1998, A&A, 339, L17

Ehrenfreund, P, Kerkhof, O, Schutte, W., et al., 1999, A&A, 350, 240

Elsila, J. E., Dworkin, J. P., Bernstein, M. P., et al., 2007, ApJ, 660, 911

Garrod, R. T., Weaver, S. L. W., and Herbst, E., 2008, ApJ, 682, 283

van Gelder, M., Tabone, B., van Dishoeck, E., et al., 2020, A&A, 639, A87

Gerakines, P., Moore, M., and Hudson, R., 2004, Icarus, 170, 202

Gerakines, P. A. and Hudson, R. L., 2015, ApJL, 805, L20

Gerakines, P. A., Yarnall, Y. Y., and Hudson, R. L., 2022, MNRAS, 509, 3515

Gibb, E. L. and Whittet, D. C. B., 2002, ApJL, 566, L113

Gibb, E. L., Whittet, D. C. B., Boogert, A. C. A., et al., 2004, ApJS, 151, 35

Gibb, E., Whittet, D., Schutte, W. a., et al., 2000, ApJ, 536, 347

Goesmann, F., Rosenbauer, H., Bredehöft, J. H., et al., 2015, Science, 349, 2.689

Guzmán, V. V., Pety, J., Gratier, P., et al., 2014, Faraday Discussions, 168, 103

He, J., Góbi, S., Ragupathy, G., et al., 2022, ApJL, 931, L1

Henkel, C, Jacq, T, Mauersberger, R, et al., 1987, A&A, 188, L1
Herbst, E. and van Dishoeck, E. F., 2009, ARA&A, 47, 427
Hudson, R. L., 2020, Icarus, 338, 113548
Hudson, R. L. and Gerakines, P. A., 2018, ApJ, 867, 138
Hudson, R. L., Moore, M. H., Dworkin, J. P., et al., 2008, Astrobiology, 8, 771
Hudson, R. and Moore, M., 2004, Icarus, 172, 466
Huntress Jr, W. and Mitchell, G., 1979, ApJ, 231, 456
Ioppolo, S., Fedoseev, G., Chuang, K. J., et al., 2021, Nat. Astronomy, 5, 197
Jiménez-Escobar, A., Chen, Y. J., Ciaravella, A., et al., 2016, ApJ, 820, 25
Jørgensen, J. K., Belloche, A., and Garrod, R. T., 2020, ARA&A, 58, 727
Jørgensen, J., Wiel, M. Van der, Coutens, A, et al., 2016, A&A, 595, A117
Labiano, A., Argyriou, I., Álvarez-Márquez, J., et al., 2021, A&A, 656, A57
Lee, J.-E., Lee, S., Baek, G., et al., 2019, Nat. Astronomy, 3, 314
Liszt, H., Gerin, M., Beasley, A., et al., 2018, ApJ, 856, 151
Loomis, R. A., Cleeves, L. I., Öberg, K. I., et al., 2018, ApJ, 859, 131
Loren, R. and Mundy, L., 1984, ApJ, 286, 232
Luna, R., Molpeceres, G., Ortigoso, J., et al., 2018, A&A, 617, A116
Mackay, D., 1999, MNRAS, 304, 61
Marten, A, Hidayat, T, Biraud, Y, et al., 2002, Icarus, 158, 532
Maté, B., Molpeceres, G., Timón, V., et al., 2017, MNRAS, 470, 4222
Mauersberger, R, Henkel, C, Walmsley, C., et al., 1991, A&A, 247, 307
McClure, M., Bergin, E. A., Boogert, A. C., et al. (Mar. 2021). *It's COMplicated: Disentangling the formation pathways of complex organic molecules from molecular clouds to comets.* JWST Proposal. Cycle 1.
McGuire, B. A., 2022, ApJS, 259, 30
Methikkalam, R. R. J., Bhuin, R. G., Ghosh, J., et al., 2017, The J. Phys. Chem. C, 121, 2822
Milligan, D. E. and Jacox, M. E., 1962, Journal of Molecular Spectroscopy, 8, 126
Moore, M. H., Ferrante, R. F., Moore, W. J., et al., 2010, ApJS, 191, 96
Moore, M. and Hudson, R., 2003, Icarus, 161, 486
Müller, B., Giuliano, B. M., Goto, M., et al., 2021, A&A, 652, A126
Nazari, P, van Gelder, M., van Dishoeck, E., et al., 2021, A&A, 650, A150
Öberg, K. I., Boogert, A. C. A., Pontoppidan, K. M., et al., 2011, ApJ, 740, 109
Öberg, K. I., Guzmán, V. V., Furuya, K., et al., 2015, Nat., 520, 198
Palumbo, M. E., Baratta, G. A., Fedoseev, G., et al., 2019, Proceedings of the International Astronomical Union, 15, 77
Palumbo, M. and Baratta, G., 2000, A&A, 361, 298
Pontoppidan, K. M., Boogert, A. C., Fraser, H. J., et al., 2008, ApJ, 678, 1005
Rachid, M. G., Brunken, N., de Boe, D., et al., 2021, A&A, 653, A116
Rachid, M. G., Terwisscha van Scheltinga, J., Koletzki, D., et al., 2020, A&A, 639, A4
Remijan, A. J., Wyrowski, F., Friedel, D. N., et al., 2005, ApJ, 626, 233
Requena-Torres, M., Martín-Pintado, J., Martín, S, et al., 2008, ApJ, 672, 352
Rocha, W. R. M., Perotti, G., Kristensen, L. E., et al., 2021, A&A, 654, A158
Rocha, W. R. M., Rachid, M. G., Olsthoorn, B., et al., 2022, A&A, 668, A63
Romanescu, C., Marschall, J., Kim, D., et al., 2010, Icarus, 205, 695
Sandford, S., Allamandola, L., Tielens, A., et al., 1991, ApJ, 371, 607
Schutte, W., Boogert, A., Tielens, A., et al., 1999, A&A, 343, 966
Schutte, W., Tielens, A., Whittet, D., et al., 1996, A&A, 315, L333
Scibelli, S. and Shirley, Y., 2020, ApJ, 891, 73
Scirè, C, Urso, R., Fulvio, D, et al., 2019, Spectrochimica Acta Part A: Molecular and Biomolecular Spectroscopy, 219, 288
Sewiło, M., Charnley, S. B., Schilke, P., et al., 2019, ACS Earth and Space Chemistry, 3, 2088
Skinner, C. J., Tielens, A. G. G. M., Barlow, M. J., et al., 1992, ApJL, 399, L79
Smith, R. S., Tylinski, M, Kimmel, G. A., et al., 2021, J. Chem. Phys., 154, 144703
Terwisscha van Scheltinga, J, Ligterink, N., Boogert, A., et al., 2018, A&A, 611, A35

Terwisscha van Scheltinga, J., Marcandalli, G., McClure, M. K., et al., 2021, A&A, 651, A95
Urso, R. G., Scirè, C., Baratta, G. A., et al., 2017, PCCP, 19, 21759
Van Broekhuizen, F., Keane, J., and Schutte, W., 2004, A&A, 415, 425
Volosatova, A. D., Lukianova, M. A., Zasimov, P. V., et al., 2021, PCCP (Incorporating Faraday Transactions), 23, 18449
Wells, M., Pel, J. W., Glasse, A., et al., 2015, Publications of the Astronomical Society of the Pacific, 127, 646
Willacy, K, Williams, D., and Minh, Y., 1993, MNRAS, 263, L40
Zanchet, A., Rodríguez-Lazcano, Y., Gálvez, Ó., et al., 2013, ApJ, 777, 26

Appendix A

Infrared profile of CH_3CN absorption bands in pure and mixed ices

This section presents the infrared spectra of methyl cyanide-containing ices in pure and mixed forms. Each figure displays the profile of one band in different ice mixtures (shown in the different panels) and at different temperatures. The peak position and FWHM for selected temperatures are shown in the bottom left panels of each figure. The relative band strengths of the analyzed absorption band in the different ices at 15 K are graphically presented in the bottom right panels.

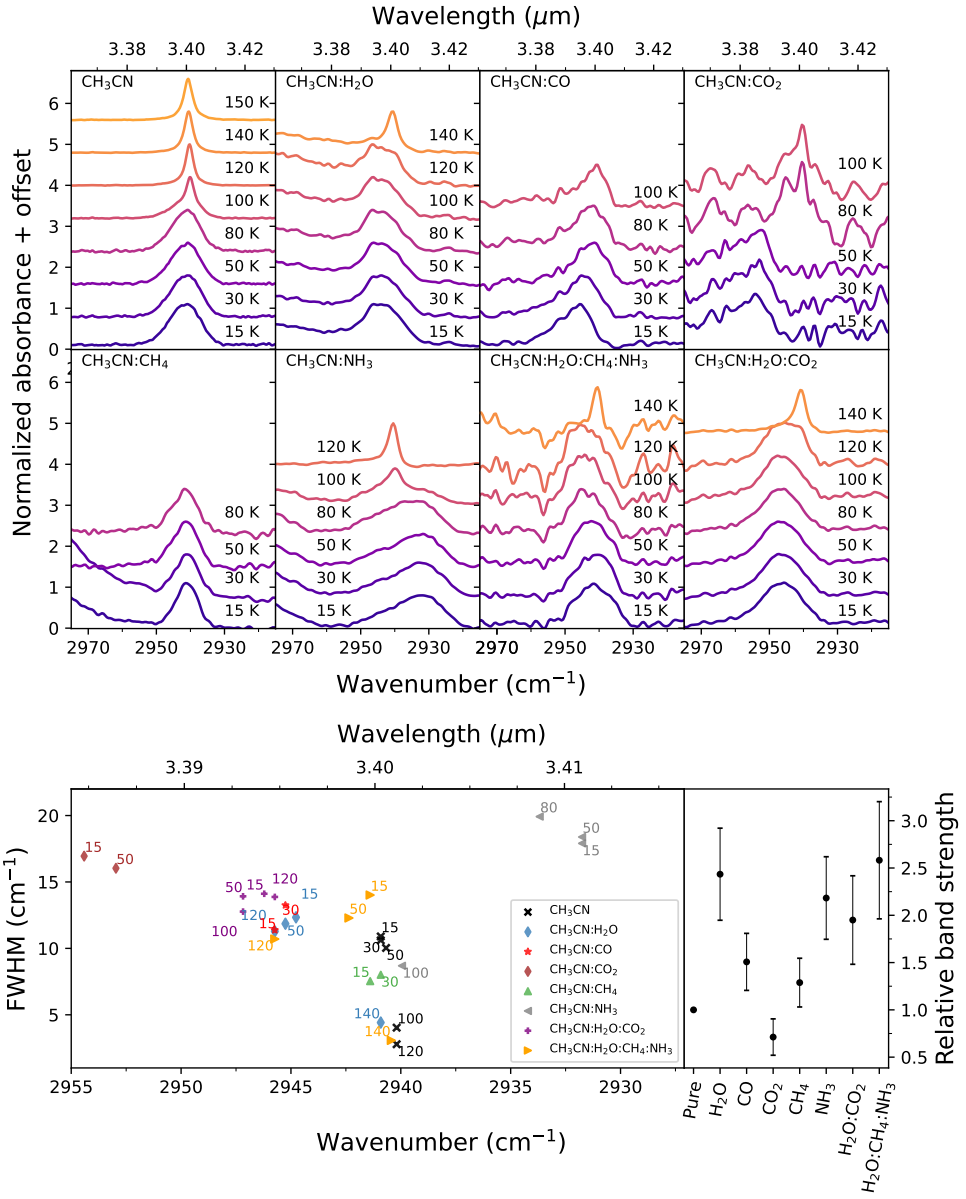

Figure 5.A.1: Upper panel: Absorption profile of the C-H symmetric stretch mode of methyl cyanide, around 2940.9 cm^{-1} (3.400 μm), in pure and mixed ices. The ice spectra at different temperatures are indicated by different colors and labels. Bottom left: Peak position and FWHM of the C-H symmetric stretching mode of CH_3CN in different ice mixtures at selected temperatures. Bottom right: relative band strengths of the C-H symmetric stretch band in different ice mixtures at 15 K.

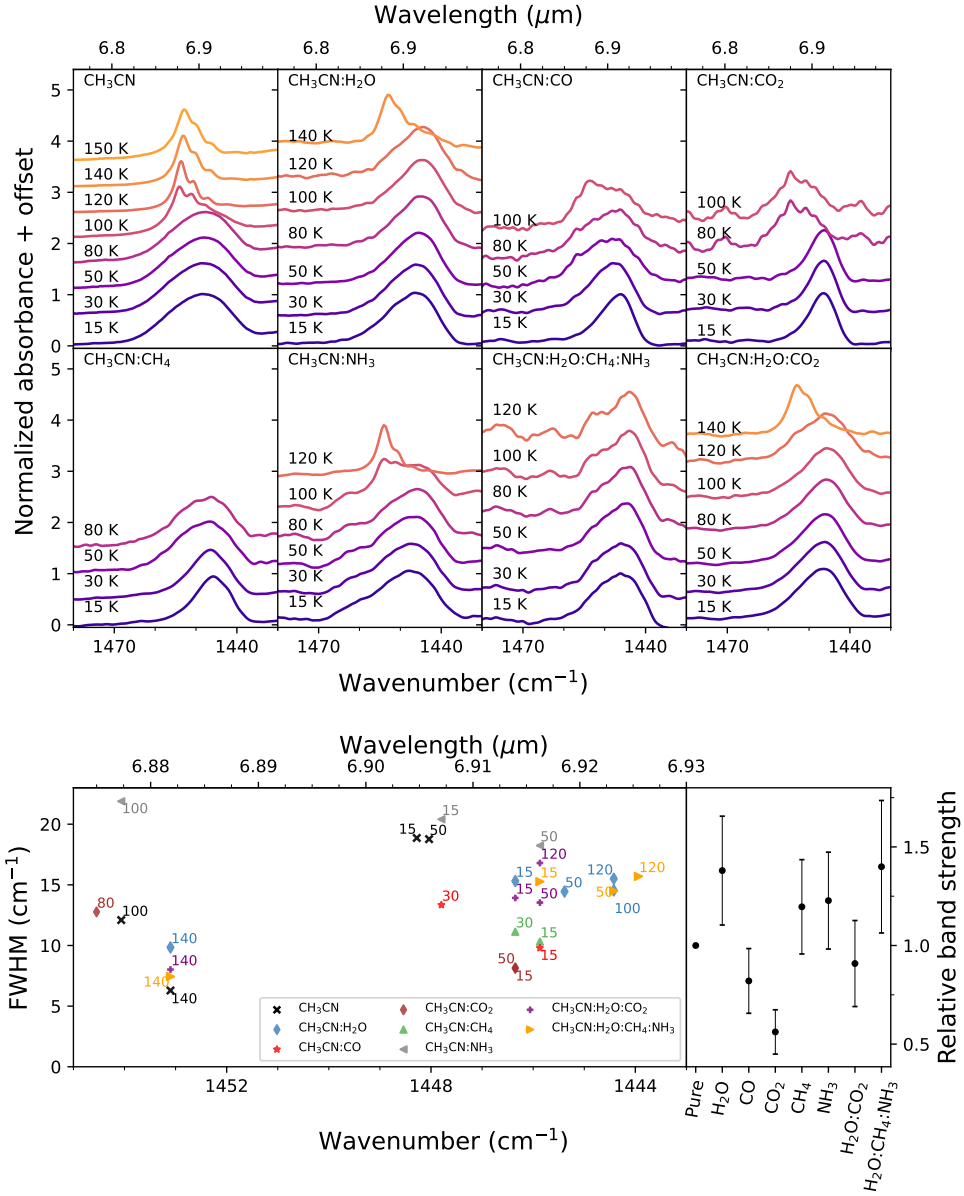

Figure 5.A.2: Upper panel: Absorption profile of the combination mode of methyl cyanide, around 1448.3 cm^{-1} (6.905 μm), in pure and mixed ices. The ice spectra at different temperatures are indicated by different colors and labels. Bottom left: Peak position and FWHM of the combination mode of CH_3CN in different ice mixtures at selected temperatures. Bottom right: relative band strengths of the combination band in different ice mixtures at 15 K.

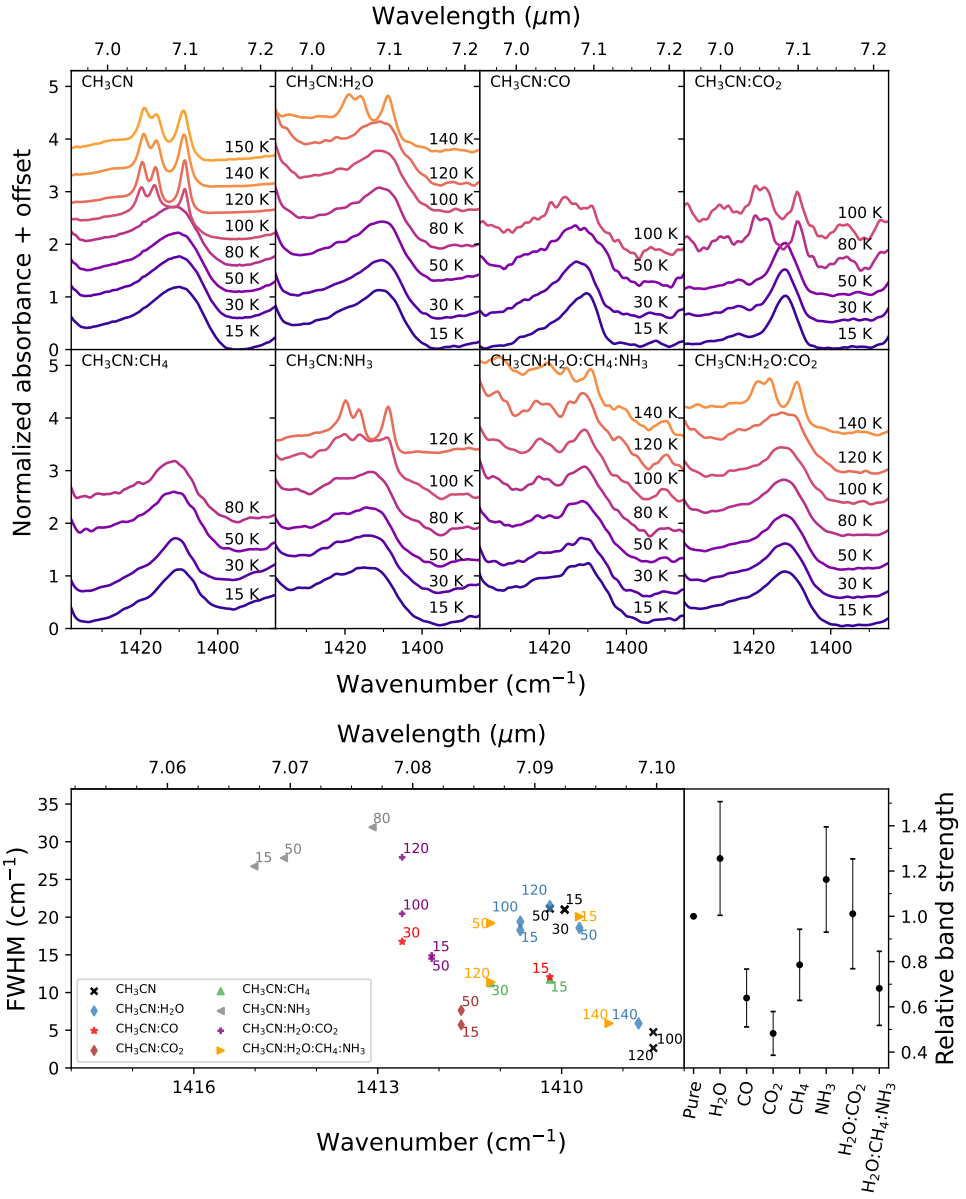

Figure 5.A.3: Upper panel: Absorption profile of the CH_3 antisymmetric deformation mode of methyl cyanide, around 1410 cm^{-1} (7.092 μm), in pure and mixed ices. The ice spectra at different temperatures are indicated by different colors and labels. Bottom left: Peak position and FWHM of the CH_3 antisymmetric deformation mode of CH_3CN in different ice mixtures at selected temperatures. Bottom right: relative band strengths of the CH_3 antisymmetric deformation band in different ice mixtures at 15 K.

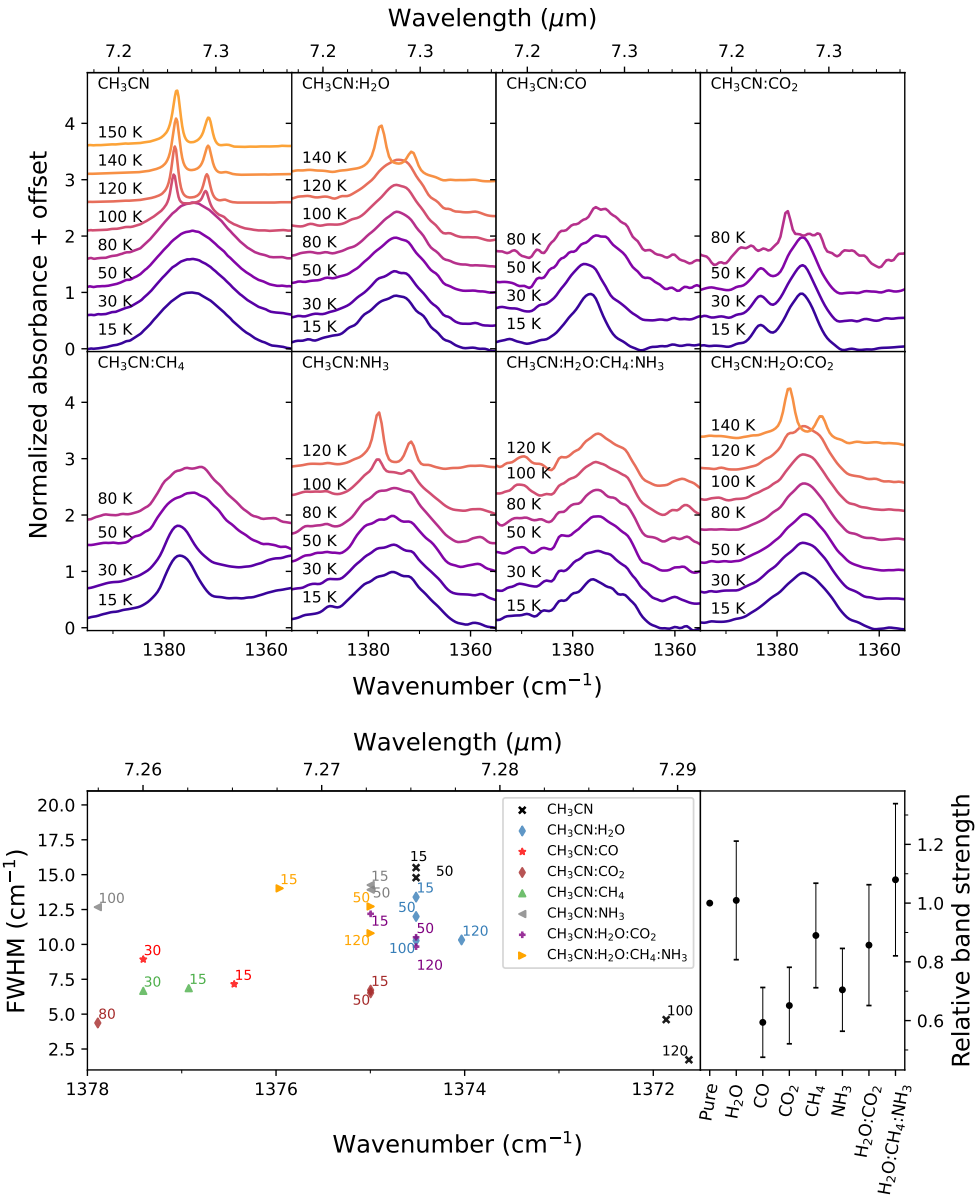

Figure 5.A.4: Upper panel: Absorption profile of the CH_3 symmetric deformation mode of methyl cyanide, around 1374.5 cm^{-1} (7.275 μm), in pure and mixed ices. The ice spectra at different temperatures are indicated by different colors and labels. Bottom left: Peak position and FWHM of the CH_3 symmetric deformation mode of CH_3CN in different ice mixtures at selected temperatures. Bottom right: relative band strengths of the CH_3 symmetric deformation band in different ice mixtures at 15 K.

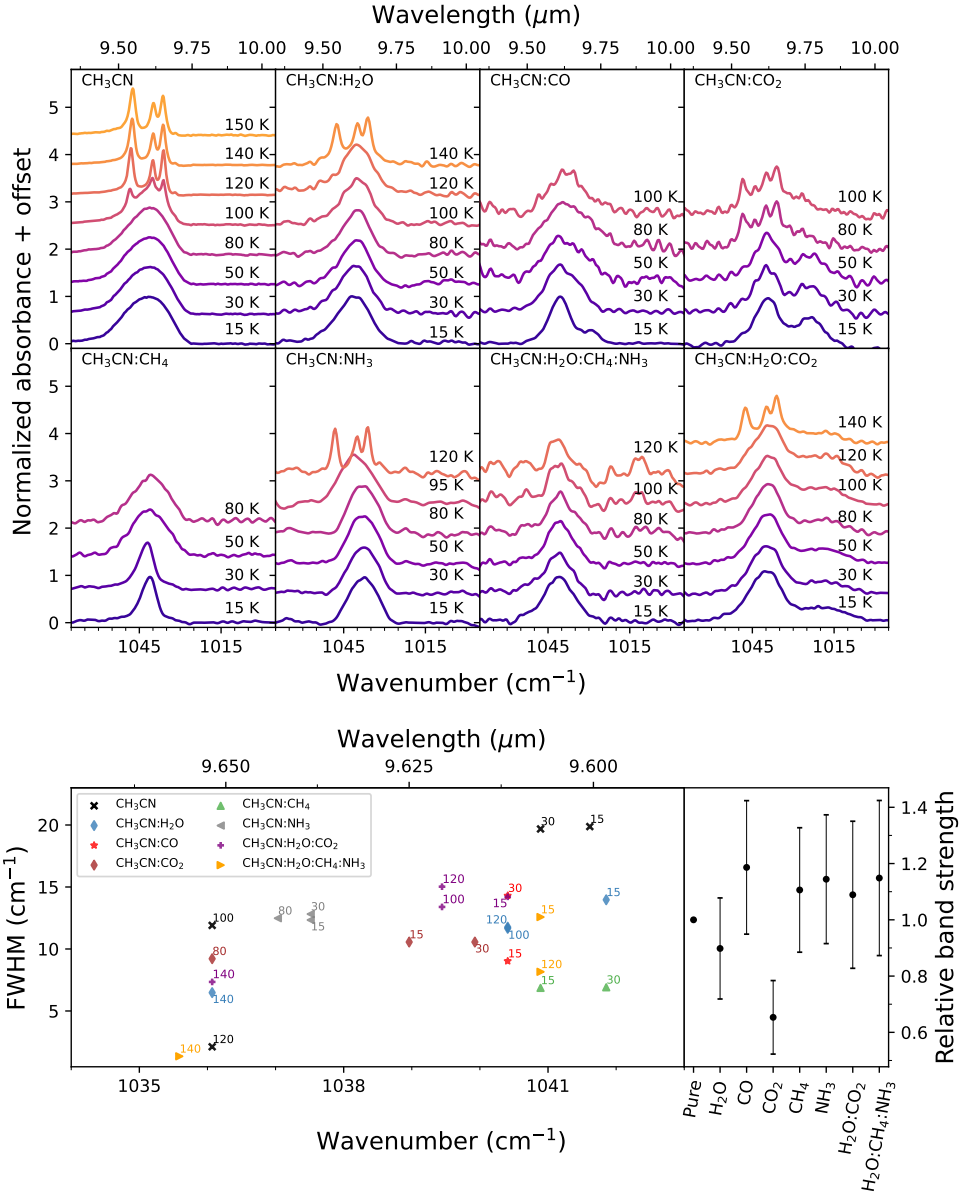

Figure 5.A.5: Upper panel: Absorption profile of the CH_3 rock mode of methyl cyanide, around 1041.6 cm^{-1} (9.600μm), in pure and mixed ices. The ice spectra at different temperatures are indicated by different colors and labels. Bottom left: Peak position and FWHM of the CH_3 rock mode of CH_3CN in different ice mixtures at selected temperatures. Bottom right: relative band strengths of the CH_3 rock band in different ice mixtures at 15 K.

Appendix B

Peak position and FWHM of CH_3CN bands in pure and mixed ices

In this section, the peak position and FWHM of the methyl cyanide features are presented. Each table lists the peak position and FWHM values for one band in the pure ice and mixed with H_2O, CO, CO_2, CH_4, NH_3, H_2O:CO_2 and H_2O:CH_4:NH_3. When the analyzed absorption band splits into multiple components at higher temperatures, the peak position of all the components and the FWHM of the strongest component are given. The uncertainty in the peak position is 1 cm^{-1} and the uncertainty in the FWHM amounts to 1.5 cm^{-1}. The values marked with an asterisk (*) denote peaks for which the FHWM is a combination of more than one peak.

Table 5.B.1: Peak position and FWHM of methyl cyanide CH_3 symmetric stretching mode (2940.9 cm^{-1}/3.400 μm) in pure and mixed ices at temperatures ranging from 15 - 150 K.

T	Matrix	1:5				1:10				1:20			
		Peak (cm^{-1})	FWHM (cm^{-1})	Peak (μm)	FWHM (μm)	Peak (cm^{-1})	FWHM (cm^{-1})	Peak (μm)	FWHM (μm)	Peak (cm^{-1})	FWHM (cm^{-1})	Peak (μm)	FWHM (μm)
15	Pure ice	2940.9	10.9	3.400	0.013	-	-	-	-	-	-	-	-
	H_2O	2942.8	12.5	3.398	0.014	2944.8	12.2	3.396	0.014	2944.8	11.8	3.396	0.014
	CO	2944.3	7.4	3.396	0.009	2945.7	11.7	3.395	0.013	-	-	-	-
	CO_2	2952.0	16.6	3.388	0.019	2954.4	17.9	3.385	0.020	-	-	-	-
	CH_4	2940.4	8.7	3.401	0.010	2941.4	7.5	3.400	0.009	2941.4	8.6	3.400	0.010
	NH_3	2934.2	18.0	3.408	0.021	2931.8	18.0	3.411	0.021	2934.2	15.2	3.408	0.018
	H_2O:CO_2	-	-	-	-	2945.7	13.9	3.395	0.016	-	-	-	-
	4 comp	-	-	-	-	-	-	-	-	2941.4	14.1	3.340	0.016
30	Pure ice	2940.9	10.6	3.400	0.012	-	-	-	-	-	-	-	-
	H_2O	2942.4	12.5	3.399	0.014	2943.8	11.8	3.397	0.014	2944.8	12.1	3.396	0.014
	CO	2943.8	7.9	3.397	0.009	2945.3	13.3	3.395	0.015	-	-	-	-
	CO_2	2951.0	13.9	3.389	0.016	2953.4	17.3	3.386	0.020	-	-	-	-
	CH_4	2940.4	8.3	3.401	0.010	2940.9	7.8	3.400	0.009	2940.4	11.2	3.401	0.013
	NH_3	2933.7	16.8	3.409	0.020	2932.7	17.2	3.410	0.020	2934.6	15.3	3.408	0.018
	H_2O:CO_2	-	-	-	-	2947.2	13.9	3.393	0.016	-	-	-	-
	4 comp	-	-	-	-	-	-	-	-	2940.4	13.2	3.401	0.015
50	Pure ice	2940.7	10.0	3.401	0.012	-	-	-	-	-	-	-	-
	H_2O	2942.8	12.4	3.398	0.014	2945.3	11.8	3.395	0.014	2944.3	12.6	3.396	0.015
	CO_2	2950.6	13.9	3.389	0.016	2953.0	16.1	3.386	0.018	-	-	-	-
	CH_4	2941.4	9.5	3.400	0.011	2941.4	8.3	3.400	0.009	2939.9	11.2	3.401	0.013
	NH_3	2933.2	17.3	3.409	0.020	2931.8	18.5	3.411	0.022	2936.1	15.2	3.406	0.018
	H_2O:CO_2	-	-	-	-	2947.7	13.9	3.392	0.016	-	-	-	-
	4 comp	-	-	-	-	-	-	-	-	2942.4	12.6	3.399	0.014
80	Pure ice	2940.9	9.6	3.400	0.011 -	-	-	-	-	-	-	-	-
	H_2O	2942.8	12.0	3.398	0.014	2945.7	11.2	3.395	0.013	2945.3	10.9	3.395	0.013
	CO_2	2950.1	15.2	3.390	0.017	2942.4	11.1	3.399	0.013	-	-	-	-
	NH_3	2934.6	16.9	3.408	0.020	2933.7	20.1	3.409	0.023	2936.6	14.2	3.405	0.016
	H_2O:CO_2	-	-	-	-	2945.7	13.3	3.395	0.015	-	-	-	-
	4 comp	-	-	-	-	-	-	-	-	2945.3	11.3	3.395	0.013
100	Pure ice	2940.2	4.0	3.401	0.005	-	-	-	-	-	-	-	-
	H_2O	2942.8	11.8	3.398	0.014	2945.7	11.2	3.395	0.013	2945.3	10.4	3.395	0.012
	CO_2	2940.9	9.6	3.400	0.011	-	-	-	-	-	-	-	-
	NH_3	2939.9	9.4	3.401	0.011	2939.9	8.8	3.401	0.010	2938.0	11.9	3.404	0.014
	H_2O:CO_2	-	-	-	-	2947.7	12.8	3.392	0.015	-	-	-	-
	4 comp	-	-	-	-	-	-	-	-	2944.3	10.6	3.396	0.012
120	Pure ice	2940.2	2.8	3.401	0.003	-	-	-	-	-	-	-	-
	H_2O	2941.9	11.1	3.399	0.013	2945.7	11.2	3.395	0.013	2945.3	9.4	3.395	0.011
	NH_3	2940.4	3.4	3.401	0.004	2940.4	3.3	3.401	0.004	2938.0	11.9	3.404	0.014
	H_2O:CO_2	-	-	-	-	2945.7	14.0	3.395	0.016	-	-	-	-
	4 comp	-	-	-	-	-	-	-	-	2945.7	11.0	3.395	0.013
140	Pure ice	2940.4	3.0	3.401	0.003	-	-	-	-	-	-	-	-
	H_2O	2940.9	4.6	3.400	0.005	2940.9	4.4	3.400	0.005	2940.9	4.9	3.400	0.006
	NH_3	-	-	-	-	-	-	-	-	-	-	-	-
	H_2O:CO_2	-	-	-	-	2940.9	3.9	3.400	0.005	-	-	-	-
	4 comp	-	-	-	-	-	-	-	-	-	-	-	-
150	Pure ice	2940.7	3.1	3.401	0.004	-	-	-	-	-	-	-	-

Table 5.B.2: Peak position and FWHM of methyl cyanide CN stretching mode (2252.2 cm^{-1}/ 4.440 μm) in pure and mixed ices at temperatures ranging from 15 - 150 K.

T	Matrix	1:5				1:10				1:20			
		Peak (cm^{-1})	FWHM (cm^{-1})	Peak (μm)	FWHM (μm)	Peak (cm^{-1})	FWHM (cm^{-1})	Peak (μm)	FWHM (μm)	Peak (cm^{-1})	FWHM (cm^{-1})	Peak (μm)	FWHM (μm)
15	Pure ice	2252.2	8.0	4.440	0.016	-	-	-	-	-	-	-	-
	H_2O	2265.0	13.2	4.415	0.026	2265.5	13.2	4.414	0.026	2266.4	14.4	4.412	0.028
	CO	2254.4	4.6	4.436	0.009	2253.9	4.8	4.437	0.009	-	-	-	-
	CO_2	2255.8	9.4	4.433	0.018	2256.8	11.7	4.431	0.023	-	-	-	-
	CH_4	2254.4	5.4	4.436	0.011	2254.9	5.2	4.435	0.010	2255.8	4.8	4.433	0.009
	NH_3	2252.4	8.3	4.440	0.016	2252.0	8.3	4.441	0.016	2252.4	8.8	4.440	0.017
	H_2O:CO_2	-	-	-	-	2263.1	15.0	4.419	0.029	-	-	-	-
	4 comp	-	-	-	-	-	-	-	-	2264.0	13.6	4.417	0.026
30	Pure ice	2252.2	7.8	4.440	0.015	-	-	-	-	-	-	-	-
	H_2O	2265.0	13.0	4.415	0.025	2265.9	13.1	4.413	0.025	2265.9	14.5	4.413	0.028
	CO	2253.9	4.6	4.437	0.009	2253.9	4.8	4.437	0.009	-	-	-	-
	CO_2	2255.8	9.2	4.433	0.018	2256.8	11.1	4.431	0.022	-	-	-	-
	CH_4	2254.4	5.2	4.436	0.010	2254.4	4.8	4.436	0.009	2254.9	4.8	4.435	0.009
	NH_3	2252.4	8.3	4.440	0.016	2252.0	8.2	4.441	0.016	2252.0	8.7	4.441	0.017
	H_2O:CO_2	-	-	-	-	2263.1	14.9	4.419	0.029	-	-	-	-
	4 comp	-	-	-	-	-	-	-	-	2264.0	13.8	4.417	0.027
50	Pure ice	2252.0	7.5	4.441	0.015	-	-	-	-	-	-	-	-
	H_2O	2265.5	12.4	4.414	0.024	2266.4	12.4	4.412	0.024	2265.9	13.7	4.413	0.027
	CO_2	2255.8	8.7	4.433	0.017	2256.8	11.3	4.431	0.022	-	-	-	-
	CH_4	2252.9	6.8	4.439	0.013	2252.4	6.8	4.440	0.013	2252.9	7.1	4.439	0.014
	NH_3	2252.4	8.0	4.440	0.016	2252.0	8.0	4.441	0.016	2252.0	8.4	4.441	0.017
	H_2O:CO_2	-	-	-	-	2263.1	14.5	4.419	0.028	-	-	-	-
	4 comp	-	-	-	-	-	-	-	-	2264.0	13.2	4.417	0.026
80	Pure ice	2252.0	7.1	4.441	0.014	-	-	-	-	-	-	-	-
	H_2O	2265.9	11.5	4.413	0.022	2266.4	11.7	4.412	0.023	2266.9	12.3	4.411	0.024
	CO_2	2255.3	8.0	4.434	0.016	2251.0	3.3	4.442	0.006	-	-	-	-
	NH_3	2252.4	7.5	4.440	0.015	2252.4	7.5	4.440	0.015	2252.4	7.9	4.440	0.016
	H_2O:CO_2	-	-	-	-	2263.1	14.5	4.419	0.028	-	-	-	-
	4 comp	-	-	-	-	-	-	-	-	2266.4	12.5	4.412	0.024
100	Pure ice	2251.0	2.7	4.4425	0.0053	-	-	-	-	-	-	-	-
	H_2O	2265.5	11.1	4.414	0.022	2266.4	11.1	4.412	0.022	2267.4	12.0	4.410	0.023
	CO_2	2251.0	5.7	4.442	0.011	2251.0	3.2	4.442	0.006	-	-	-	-
	NH_3	2251.5	6.3	4.441	0.012	2251.0	2.1	4.442	0.004	-	-	-	-
	H_2O:CO_2	-	-	-	-	2265.0	12.4	4.415	0.024	-	-	-	-
	4 comp	-	-	-	-	-	-	-	-	2266.4	12.2	4.412	0.024
120	Pure ice	2251.0	1.3	4.442	0.003	-	-	-	-	-	-	-	-
	H_2O	2265.5	11.1	4.414	0.022	2266.4	11.2	4.412	0.022	2266.4	11.0	4.412	0.021
	NH_3	-		-		-	-	-	-	2252.4	8.4	4.440	0.017
	H_2O:CO_2	-	-	-	-	2265.0	12.3	4.415	0.024	-	-	-	-
	4 comp	-	-	-	-	-	-	-	-	2266.4	12.5	4.412	0.024
140	Pure ice	2250.8	1.3	4.443	0.003	-	-	-	-	-	-	-	-
	H_2O	2251.0	2.0	4.442	0.004	2251.0	2.0	4.442	0.004	2251.0	2.0	4.442	0.004
	NH_3	2251.0	2.1	4.442	0.004	-	-	-	-	-	-	-	
	H_2O:CO_2	-	-	-	-	2251.0	2.1	4.442	0.004	-	-	-	-
	4 comp	-	-	-	-	-	-	-	-	2251.0	2.1	4.442	0.004

Table 5.B.3: Peak position and FWHM of methyl cyanide combination mode (1448.3 cm^{-1}/ 6.905 μm) in pure and mixed ices at temperatures ranging from 15 - 150 K.

T	Matrix	1:5				1:10				1:20			
		Peak (cm^{-1})	FWHM (cm^{-1})	Peak (μm)	FWHM (μm)	Peak (cm^{-1})	FWHM (cm^{-1})	Peak (μm)	FWHM (μm)	Peak (cm^{-1})	FWHM (cm^{-1})	Peak (μm)	FWHM (μm)
15	Pure ice	1448.3	18.9	6.9045	0.090	-	-	-	-	-	-	-	-
	H_2O	1446.4	15.9	6.914	0.076	-	-	-	-	1446.4	15.0	6.914	0.072
	CO	1447.3	10.7	6.909	0.051	1445.9	9.8	6.916	0.047	-	-	-	-
	CO_2	1446.8	9.8	6.911	0.047	1446.4	8.1	6.914	0.038	-	-	-	-
	CH_4	1446.4	11.5	6.914	0.055	1445.9	10.3	6.916	0.049	1445.4	9.6	6.919	0.046
	NH_3	1446.4	19.8	6.914	0.095	1447.8	20.4	6.907	0.097	1446.8	17.9	6.912	0.086
	H_2O:CO_2	-	-	-	-	1446.4	13.9	6.914	0.066	-	-	-	-
	4 comp	-	-	-	-	-	-	-	-	1445.9	15.3	6.916	0.073
30	Pure ice	1448.5	18.8	6.904	0.090	-	-	-	-	-	-	-	-
	H_2O	1446.4	15.6	6.914	0.075	-	-	-	-	1444.4	14.6	6.923	0.070
	CO	1448.3	12.3	6.905	0.059	1447.8	13.3	6.907	0.063	-	-	-	-
	CO_2	1446.8	9.9	6.912	0.047	1446.4	8.1	6.914	0.039	-	-	-	-
	CH_4	1446.8	12.2	6.912	0.058	1446.4	11.1	6.914	0.053	1445.9	11.0	6.916	0.053
	NH_3	1446.8	19.7	6.912	0.0942	1447.3	19.7	6.909	0.094	1445.9	18.4	6.916	0.088
	H_2O:CO_2	-	-	-	-	1446.4	13.7	6.914	0.066	-	-	-	-
	4 comp	-	-	-	-	-	-	-	-	1445.9	14.8	6.916	0.071
50	Pure ice	1448.0	18.8	6.906	0.089	-	-	-	-	-	-	-	-
	H_2O	1445.4	15.2	6.9186	0.072	-	-	-	-	1444.4	14.3	6.923	0.069
	CO_2	1446.4	10.3	6.914	0.049	1446.4	8.2	6.914	0.039	-	-	-	-
	CH_4	1447.8	16.8	6.907	0.0780	1446.8	14.9	6.911	0.071	1445.9	16.8	6.916	0.080
	NH_3	1446.8	19.0	6.912	0.0908	1445.9	18.2	6.916	0.087	1445.4	18.1	6.919	0.087
	H_2O:CO_2	-	-	-	-	1445.9	13.5	6.9163	0.0648	-	-	-	-
	4 comp	-	-	-	-	-	-	-	-	1444.4	14.5	6.923	0.069
80	Pure ice	1447.6	18.5	6.908	0.088	-	-	-	-	-	-	-	-
	H_2O	1444.9	14.9	6.921	0.071	-	-	-	-	1443.9	13.5	6.925	0.065
	CO_2	1446.4	11.9	6.914	0.057	1454.5	12.8	6.875	0.060	-	-	-	-
	NH_3	1446.8	18.3	6.912	0.0874	1445.9	17.9	6.916	0.085	1445.4	17.4	6.919	0.083
	H_2O:CO_2	-	-	-	-	1445.9	13.7	6.916	0.066	-	-	-	-
	4 comp	-	-	-	-	-	-	-	-	1443.5	14.8	6.928	0.071
100	Pure ice	1454.1	12.1	6.877	0.057	-	-	-	-	-	-	-	-
	H_2O	1444.9	15.0	6.921	0.072	-	-	-	-	1443.9	13.5	6.925	0.065
	CO_2	1454.1	15.8	6.877	0.075	-	-	-	-	-	-	-	-
	NH_3	1446.8	21.0	6.912	0.100	1454.1	21.9	6.877	0.103	1445.9	20.6	6.916	0.099
	H_2O:CO_2	-	-	-	-	1445.9	14.6	6.916	0.070	-	-	-	-
	4 comp	-	-	-	-	-	-	-	-	1443.9	15.3	6.925	0.073
120	Pure ice	1453.6	5.7	6.880	0.027	-	-	-	-	-	-	-	-
	H_2O	1445.4	16.6	6.919	0.079	-	-	-	-	1443.9	13.8	6.925	0.066
	NH_3	1454.1	6.0	6.8773	0.028	1454.1	5.5	6.877	0.026	1445.9	20.6	6.916	0.099
	H_2O:CO_2	-	-	-	-	1445.9	16.8	6.916	0.080	-	-	-	-
	4 comp	-	-	-	-		-	-	-	1443.9	15.7	6.925	0.075
140	Pure ice	1453.1	6.3	6.882	0.030	-	-	-	-	-	-	-	-
	H_2O	1453.1	7.8	6.882	0.037	-	-	-	-	1452.6	11.4	6.884	0.054
	H_2O:CO_2	-	-	-	-	1453.1	8.0	6.882	0.038	-	-	-	-
	4 comp	-	-	-	-	-	-	-	-	1453.1	7.4	6.882	0.035

5.5. Appendix B

Table 5.B.4: Peak position and FWHM of methyl cyanide CH_3 antisymmetric deformation mode (1410 cm^{-1}/ 7.092 μm) in pure and mixed ices at temperatures ranging from 15 - 150 K.

T	Matrix	1:5				1:10				1:20			
	-	Peak	FWHM	Peak	FWHM	Peak	FWHM	Peak	FWHM	Peak	FWHM	Peak	FWHM
	-	(cm^{-1})	(cm^{-1})	(μm)	(μm)	(cm^{-1})	(cm^{-1})	(μm)	(μm)	(cm^{-1})	(cm^{-1})	(μm)	(μm)
15	Pure ice	1410.0	21.0	7.092	0.106	-	-	-	-	-	-	-	-
	H_2O	1411.6	19.0	7.084	0.095	1411.2	18.3	7.086	0.092	1411.2	18.9	7.086	0.095
	CO	1411.6	12.1	7.084	0.061	1410.2	12.0	7.091	0.060	-	-	-	-
	CO_2	1411.6	9.2	7.084	0.046	1411.6	7.5	7.084	0.038	-	-	-	-
	CH_4	1411.2	12.6	7.086	0.063	1410.2	11.7	7.091	0.059	1408.3	14.5	7.101	0.073
	NH_3	1414.0	26.3	7.072	0.131	1415.0	26.7	7.067	0.133	1412.6	21.1	7.079	0.106
	H_2O:CO_2	-	-	-	-	1412.1	15.1	7.082	0.076	-	-	-	-
	4 comp	-	-	-	-	-	-	-	-	1409.7	20.1	7.093	0.101
30	Pure ice	1410.0	21.0	7.092	0.105	-	-	-	-	-	-	-	-
	H_2O	1410.7	18.4	7.089	0.093	1410.2	18.0	7.091	0.090	1411.2	18.3	7.086	0.092
	CO	1411.2	19.2	7.086	0.096	1412.6	16.8	7.079	0.0084	-	-	-	-
	CO_2	1411.6	9.4	7.084	0.047	1411.6	7.7	7.084	0.039	-	-	-	-
	CH_4	1411.6	12.8	7.084	0.064	1411.2	11.2	7.086	0.056	-	-	-	-
	NH_3	1412.1	25.7	7.082	0.129	1413.6	26.7	7.074	0.134	1412.6	20.0	7.079	0.100
	H_2O:CO_2	-	-	-	-	1411.6	15.1	7.084	0.076	-	-	-	-
	4 comp	-	-	-	-	-	-	-	-	1411.6	19.6	7.084	0.098
50	Pure ice	1410.2	21.1	7.091	0.106	-	-	-	-	-	-	-	-
	H_2O	1411.2	18.3	7.086	0.092	1410.2	18.5	7.091	0.093	1411.2	18.2	7.086	0.092
	CO	1413.1	24.3	7.077	0.122	1414.0	24.2	7.077	0.121	-	-	-	-
	CH_4	1411.2	19.0	7.086	0.095	1411.2	17.6	7.086	0.088	-	-	-	-
	NH_3	1414.0	26.1	7.072	0.130	1414.5	27.8	7.069	0.139	1412.6	19.2	7.079	0.096
	H_2O:CO_2	-	-	-	-	1412.1	14.9	7.082	0.075	-	-	-	-
	4 comp	-	-	-	-	-	-	-	-	1411.2	19.2	7.086	0.096
80	Pure ice	1410.9	22.0	7.088	0.111	-	-	-	-	-	-	-	-
	H_2O	1411.2	19.2	7.086	0.096	1411.2	18.5	7.086	0.093	1411.2	18.1	7.086	0.091
	CO_2	1412.6	10.7	7.079	0.054	1408.7	-	7.100	-	-	-	-	-
	-		-		-	1419.3	-	7.045	-	-	-	-	-
	NH_3	1413.1	26.5	7.077	0.133	1413.1	22.5	7.077	0.113	1413.1	18.1	7.077	0.091
	H_2O:CO_2	-	-	-	-	1412.1	18.5	7.082	0.093	-	-	-	-
	4 comp	-	-	-	-	-	-	-	-	1410.7	18.9	7.089	0.095
100	Pure ice	1408.5	4.8	7.100	0.024	-	-	-	-	-	-	-	-
		1416.6	-	7.060		-	-	-	-	-	-	-	-
		1419.8	-	7.043		-	-	-	-	-	-	-	-
	H_2O	1411.6	19.6	7.084	0.098	1410.7	19.2	7.089	0.096	1411.2	18.3	7.086	0.092
	CO_2	1416.0	19.8	7.062	0.099	-	-	-	-	-	-	-	-
	NH_3	-	-	-	-	1416.5	-	7.060	-	1412.6	21.2	7.079	0.106
	H_2O:CO_2	-	-	-	-	1412.6	21.2	7.079	0.106	-	-	-	-
	4 comp	-	-	-	-	-	-	-	-	1410.7	18.8	7.090	0.094
120	Pure ice	1408.5	2.6	7.100	0.013	-	-	-	-	-	-	-	-
	-	1416.2	-	7.061		-	-	-	-	-	-	-	-
	-	1419.6	-	7.044		-	-	-	-	-	-	-	-
	H_2O	1409.2	23.1	7.096	0.116	1410.7	21.1	7.089	0.106	1411.2	20.1	7.086	0.101
	NH_3	1408.7	3.1	7.098	0.036	1408.7	3.1681	7.099	0.016	1412.6	21.2	7.079	0.106
		1416.4*	7.6	7.060*	0.038	1416.5*	-	7.060	-	-	-	-	-
		1419.8*	-	7.043*	-	1419.8*	8.016	7.043	0.040	-	-	-	-
	H_2O:CO_2	-	-	-	-	1412.6	22.7	7.079	0.114	-	-	-	-
	4 comp	-	-	-	-	-	-	-	-	1411.2	18.4	7.086	0.092
140	Pure ice	1408.7	3.36	7.098	0.017	-	-	-	-	-	-	-	-
		1416.0*		7.062*	-		-	-	-	-	-	-	-
		1419.1*	7.1	7.047*	0.035		-	-	-	-	-	-	-
	H_2O	1408.7	7.1	7.098*	0.022	1408.7	4.9	7.098	0.025	1408.7	4.6	7.098	0.023
		1416.0*	8.9	7.060*	0.044	1416.0	-	7.062		-	-	-	-
		1418.9*	-	7.043	1418.9		-	-		1418.4	9.6	7.050	0.048
	H_2O:CO_2	-	-	-	-	1408.7	4.704	7.098	0.024	-	-	-	-
			-	-	-	1416.0*	8.93	7.062	0.044		-	-	-
			-	-	-	1418.8*		-	7.048		-	-	-
	4 comp	-	-	-	-	-	-	-	-	1409.2	5.9	7.0961	0.0297
150	Pure	1409.0	4.0	7.097	0.0201	-	-	-	-	-	-	-	
		1419.1	7.6	7.046	0.038		-	-	-	-	-	-	-

Table 5.B.5: Peak position and FWHM of methyl cyanide CH_3 symmetric deformation mode (1374.5 cm^{-1}/ 7.275 μm) in pure and mixed ices at temperatures ranging from 15 - 150 K.

T	Matrix	1:5				1:10				1:20			
		Peak (cm^{-1})	FWHM (cm^{-1})	Peak (μm)	FWHM (μm)	Peak (cm^{-1})	FWHM (cm^{-1})	Peak (μm)	FWHM (μm)	Peak (cm^{-1})	FWHM (cm^{-1})	Peak (μm)	FWHM (μm)
15	Pure	1374.5	15.5	7.275	0.0821	-	-	-	-	-	-	-	-
	H_2O	1374.5	13.5	7.275	0.072	1374.5	13.4	7.275	0.071	1374.5	13.9	7.275	0.074
	CO	1377.4	7.9	7.260	0.041	1376.4	7.4	7.265	0.039	-	-	-	-
	CO_2	1375.5	7.7	7.270	0.041	1375.0	6.7	7.273	0.036	-	-	-	-
	CH_4	1377.4	7.4	7.260	0.039	1376.9	6.9	7.263	0.036	1375.5	7.9	7.270	0.042
	NH_3	1375.0	14.9	7.273	0.079	1375.0	15.5	7.273	0.082	1374.5	16.2	7.275	0.086
	H_2O:CO_2	-	-	-	-	1374.5	12.3	7.275	0.065	-	-	-	-
	4 comp	-	-	-	-	-	-	-	-	1376.0	14.0	7.268	0.0740
30	Pure	1374.3	15.3	7.277	0.081	-	-	-	-	-	-	-	-
	H_2O	1375.0	13.1	7.273	0.069	1375.0	13.0	7.273	0.069	1373.1	14.5	7.283	0.077
	CO	1377.9	8.8	7.257	0.047	1377.9	9.8	7.257	0.052	-	-	-	-
	CO_2	1375.5	7.5	7.270	0.040	1375.0	6.6	7.273	0.035	-	-	-	-
	CH_4	1377.4	7.5	7.260	0.040	1377.4	6.7	7.260	0.035	1376.9	7.6	7.263	0.040
	NH_3	1375.5	14.7	7.270	0.078	1375.0	15.4	7.273	0.081	1373.1	16.0	7.283	0.085
	H_2O:CO_2	-	-	-	-	1375.0	11.9	7.273	0.063	-	-	-	-
	4 comp	-	-	-	-	-	-	-	-	1375.0	14.6	7.273	0.077
50	Pure	1374.5	14.8	7.275	0.078	-	-	-	-	-	-	-	-
	H_2O	1374.5	12.1	7.275	0.064	1374.5	12.0	7.275	0.063	1372.6	14.0	7.286	0.074
	CO_2	1375.5	7.5	7.270	0.040	1375.0	6.5	7.273	0.035	-	-	-	-
	CH_4	1375.0	13.2	7.273	0.070	1374.0	13.3	7.278	0.071	1373.1	14.7	7.283	0.078
	NH_3	1375.5	14.3	7.270	0.075	1375.0	15.3	7.273	0.081	-	-	-	-
	H_2O:CO_2	-	-	-	-	1374.5	10.8	7.275	0.057	-	-	-	-
	4 comp	-	-	-	-	-	-	-	-	1375.0	12.7	7.273	0.067
80	Pure	1374.5	14.2	7.275	0.075	-	-	-	-	-	-	-	-
	H_2O	1373.6	11.1	7.280	0.059	1374.5	11.1	7.275	0.058	1373.1	12.9	7.283	0.068
	CO_2	1375.5	7.8	7.270	0.041	1377.9	7.9	7.257	0.042	-	-	-	-
	NH_3	1375.0	12.9	7.273	0.068	1375.0	14.0	7.273	0.074	1373.6	14.8	7.280	0.078
	H_2O:CO_2	-	-	-	-	1374.5	10.0	7.275	0.053	-	-	-	-
	4 comp	-	-	-	-	-	-	-	-	1375.0	12.6	7.273	0.066
100	Pure	-	-	-	-	-	-	-	-	-	-	-	-
	H_2O	1374.0	10.3	7.278	0.054	1374.5	10.3	7.275	0.054	1373.6	12.5	7.280	0.066
	CO_2	1377.9	10.7	7.257	0.056	-	-	-	-	-	-	-	-
	NH_3	1377.9	10.3	7.257	0.054	1377.9	11.9	7.257	0.062	1374.0	13.1	7.278	0.070
	H_2O:CO_2	-	-	-	-	1375.0	9.6	7.273	0.051	-	-	-	-
	4 comp	-	-	-	-	-	-	-	-	1375.5	12.5	7.270	0.066
120	Pure	-	-	-	-	-	-	-	-	-	-	-	-
	H_2O	1374.0	10.1	7.278	0.054	1374.0	10.3	7.278	0.055	1373.6	11.1	7.280	0.059
	NH_3	1371.6	2.4	7.291	0.013	1377.9	2.4	7.257	0.013	1374.0	13.1	7.278	0.070
	-	1377.9	2.4	7.257	0.013	-	-	-	-	-	-	-	-
	H_2O:CO_2	-	-	-	-	1374.5	10.0	7.275	0.053	-	-	-	-
	4 comp	-	-	-	-	-	-	-	-	1375.0	10.8	7.27	0.057
140	Pure	-	-	-	-	-	-	-	-	-	-	-	-
	H_2O	1371.6	3.1	7.291	0.016	1377.4	2.8	7.260	0.015	-	-	-	-
		1377.4	2.6	7.260	0.014	-	-	-	-	-	-	-	-
	H_2O:CO_2	-	-	-	-	1371.6	2.9	7.291	0.014	-	-	-	-
		-	-	-	-	1377.4	2.6	7.260	0.015	-	-	-	-
	4 comp	-	-	-	-	-	-	-	-	1377.4	3.0	7.260	0.016

5.5. Appendix B

Table 5.B.6: Peak position and FWHM of methyl cyanide CH_3 rock (1041.6 cm^{-1}/ 9.600 μm) in pure and mixed ices at temperatures ranging from 15 - 150 K.

T	Matrix	1:5				1:10				1:20			
		Peak (cm^{-1})	FWHM (cm^{-1})	Peak (μm)	FWHM (μm)	Peak (cm^{-1})	FWHM (cm^{-1})	Peak (μm)	FWHM (μm)	Peak (cm^{-1})	FWHM (cm^{-1})	Peak (μm)	FWHM (μm)
15	Pure ice	1041.6	19.9	9.600	0.183	-	-	-	-	-	-	-	-
	H_2O	1040.9	14.6	9.607	0.1351	1041.4	14.0	9.603	0.129	1041.4	13.7	9.603	0.126
	CO	1040.9	8.6	9.607	0.079	1040.4	9.0	9.612	0.083	-	-	-	-
	CO_2	1039.9	11.1	9.616	0.103	1039.0	10.6	9.625	0.098	-	-	-	-
	CH_4	1041.9	7.7	9.598	0.071	1040.9	6.9	9.607	0.063	1040.4	6.3	9.612	0.058
	NH_3	1037.5	13.4	9.638	0.124	1037.5	12.3	9.638	0.115	1037.0	11.4	9.643	0.106
	H_2O:CO_2	-	-	-	-	1039.9	14.4	9.612	0.133	-	-	-	-
	4 comp	-	-	-	-	-	-	-	-	1040.9	12.6	9.607	0.116
30	Pure ice	1040.9	19.7	9.607	0.182		-		-	-	-	-	-
	H_2O	1040.9	13.8	9.607	0.127	1041.4	12.8	9.603	0.118	1040.4	13.7	9.612	0.127
	CO	1041.4	9.7	9.603	0.089	1040.4	14.3	9.612	0.132	-	-	-	-
	CO_2	1039.9	11.0	9.616	0.102	1039.9	10.6	9.616	0.098	-	-	-	-
	CH_4	1042.3	7.8	9.594	0.072	1041.9	6.9	9.598	0.064	1041.9	6.1	9.598	0.057
	NH_3	1037.5	13.5	9.638	0.126	1037.5	12.8	9.638	0.119	1037.0	11.0	9.643	0.102
	H_2O:CO_2	-	-	-	-	1039.4	14.0	9.616	0.129	-	-	-	-
	4 comp	-	-	-	-	-	-	-	-	1040.9	11.3	9.607	0.104
50	Pure ice	1041.4	18.7	9.603	0.173		-		-	-	-	-	-
	H_2O	1040.4	13.5	9.612	0.125	1040.4	12.1	9.612	0.112	1039.9	14.0	9.616	0.130
	CO_2	1039.9	10.8	9.616	0.100	1039.9	10.3	9.616	0.095	-	-	-	-
	CH_4	1041.9	15.7	9.598	0.145	1040.9	15.8	9.607	0.146	1041.9	14.8	9.598	0.136
	NH_3	1037.5	12.8	9.638	0.119	1037.0	12.8	9.643	0.119	-	-	-	-
	H_2O:CO_2	-	-	-		1039.4	13.6	9.629	0.126	-	-	-	-
	4 comp	-	-	-	-	-	-	-	-	1040.4	10.7	9.612	0.099
80	Pure ice	1041.1	17.5	9.605	0.162	-			-	-	-	-	
	H_2O	1040.4	12.4	9.612	0.115	1039.9	11.3	9.616	0.104	1039.0	14.1	9.625	0.130
	CO_2	1039.9	11.6	9.616	0.107	1036.1	9.2	9.652	0.086	-	-	-	-
	NH_3	1037.5	12.6	9.638	0.117	1037.0	12.5	9.643	0.117	-	-	-	-
	H_2O:CO_2	-	-	-	-	1039.0	12.8	9.621	0.119	-	-	-	-
	4 comp	-	-	-	-	-	-	-	-	1040.4	10.4	9.612	0.096
100	Pure ice	1036.1*	-	9.652	0.102	-		-	-	-	-		
		1040.2*	15.07	9.613	0.139	-	-		-	-	-	-	
		1048.4*	-	9.539	0.037	-	-		-	-	-	-	
	H_2O	1039.4	12.2	9.621	0.113	1040.4	11.7	9.612	0.108	1038.5	13.9	9.629	0.129
	CO_2	1040.4	14.8	9.612	0.137	-	-	-	-	-	-	-	-
	NH_3	1039.9	13.1	9.616	0.121	-	-	-	-	-	-	-	-
	H_2O:CO_2	-	-	-	-	1039.0	13.1	9.621	0.121	-	-	-	-
	4 comp	-	-	-	-	-	-	-		1039.9	9.9	9.616	0.091
120	Pure ice	1036.1	2.11	9.652	0.020	-	-	-	-	-	-	-	-
		1039.9	2.45	9.616	0.022	-	-	-	-	-	-	-	-
		1048.1	2.35	9.541	0.021	-	-	-	-	-	-	-	-
	H_2O	1039.9	12.3	9.616	0.114	1040.4	11.8	9.612	0.109	1035.6	12.9	9.656	0.120
	NH_3	1036.1*	7.3	9.652*	0.0684	-	-	-	-	-	-	-	-
		1040.0*	-	9.616*	-	-	-	-	-	-	-	-	-
		1048.1	3.02	9.541	0.027	-	-	-	-	-	-	-	-
	H_2O:CO_2	-	-	-	-	1038.5	14.4	9.621	0.134	-	-	-	-
	4 comp	-	-	-	-	-	-	-	-	1040.9	8.2	9.607	0.075
140	Pure ice	1036.3	2.3	9.650	0.022	-	-	-	-	-	-	-	
		1039.9	2.7	9.616	0.025	-	-		-	-		-	-
		1047.6	2.54	9.545	0.023	-	-		-	-	-	-	
	H_2O	1036.1*	6.3	9.652	0.059	1036.1*	7.3	9.652*	0.068	-	-	-	-
		1040.0*	-		-	1039.9*	-	9.616*	-	-	-	-	-
		1047.6	3.2	9.545	0.029	1047.6	3.6	9.545	0.033	-	-	-	-
	H_2O:CO_2	-	-	-	-	1036.1	7.0	9.652	0.065	-	-	-	-
		-	-	-	-	1047.6	3.5	9.545	0.032	-	-	-	-
	4 comp	-	-	-	-	-	-	-	-	-	-	-	-
150	Pure ice	1038.0	6.9	9.634	0.064	-	-	-	-	-	-	-	-
		1039.7	-	9.618	-	-	-	-	-	-	-	-	
		1047.4	2.8	9.547	0.025	-	-	-	-		-	-	-

Appendix C

Integrated absorbance of CH_3CN bands in pure and mixed ices

This section presents the integrated absorbance of methyl cyanide bands (i.e., band areas) in ice mixtures at different temperatures. Each table lists the integrated absorbance of the absorption bands in a specific ice mixture normalized to the integrated absorbance of the CN stretch in that mixture at 15 K. These values are used to calculate the apparent band strength of the methyl cyanide features in ice mixtures at different temperatures, as explained in the following.

The apparent band strength of the CN stretch feature of methyl cyanide in the IR spectrum of an ice mixture ($A'_{CN,mixt}$ (T)) is related to the band strength of another feature, *i*, ($A'_{i,mixt}$ (T)) by:

$$A'_{i,mixt}(T) = \frac{a_{i,mixt}(T)}{a_{CN,mixt}(T)} \times A'_{CN,mixt}(T), \tag{5.8}$$

where $a_{CN,mixt}$ and $a_{i,mixt}$ are the integrated absorbances of the CN stretching and the feature *i*, respectively. This relation can be rewritten in terms of the band strengths of the pure methyl cyanide at 15 K and the relative band strength of the CN stretching in the ice mixture (both derived in this work):

$$A'_{i,mixt}(T) = \frac{a_{i,mixt}(T)}{a_{CN,mixt}(15K)} \times \eta_{CN,mixt} \times A_{CN}(15K), \tag{5.9}$$

where $\eta_{CN,mixt}$ is the relative band strength of the CN stretch in the analyzed ice mixture (Appendix A), A_{CN} (15 K) is the band strength for the pure CN stretch mode at 15 K (Table 4.2), and the term $\frac{a_i(T)}{a_{CN,mixt}(15K)}$ is the integrated absorbance for the band *i*, in the ice mixture, normalized to the integrated absorbance of the CN stretch in the same ice mixture at 15 K (Table 5.C.1).

To illustrate the use of the data in this Section for calculating the apparent band strength in mixtures at temperatures above 15 K, we derived below the apparent band strength of the CH_3 rock feature of methyl cyanide in the CH_3CN:H_2O (1:10) ice at 80 K ($A'_{CH_3,rock}$ (80 K)). Using η = 1.75 (relative band strength value for the CN stretching in the CH_3CN:H_2O (1:10) ice mixture, shown on Figure 5.3), A_{CN} (15 K) = 1.9×10^{-18} cm molecule^{-1} (Table 4.2) and $\frac{a_{CH_3,rock}(80K)}{a_{CN}(15K)} = 0.31$ (Table 5.C.1) on Equation 5.9, we obtain $A'_{CH_3,rock} = 0.31 \times 1.75 \times 1.9 \times 10^{-18}$ cm molecule^{-1}= 1.0

$\times 10^{-18}$ cm molecule^{-1}.

Table 5.C.1: Integrated absorbance of CH_3CN features in different ice mixtures at different temperatures. The values are normalized with respect to the CN stretching integrated absorbance at 15 K in the mixture.

T (K)	CH_3 rock 1041.6 cm^{-1} (9.600 μm)	CH_3 symm. def 1374.5 cm^{-1} (7.275 μm)	CH_3 antisymm. def. 1410 cm^{-1} (7.092 μm)	Comb. 1448.3 cm^{-1} (6.904 μm)	CN str. 2252.2 cm^{-1} (4.4401 μm)	CH_3 symm. str. 2940.9 cm^{-1} (3.400 μm)
Pure CH_3CN						
15	0.80	0.65	1.06	1.44	1.00	0.29
30	0.80	0.64	1.04	1.41	1.00	0.27
50	0.77	0.61	0.98	1.34	1.01	0.26
80	0.73	0.58	0.89	1.23	1.00	0.23
100	-	-	0.94	1.23	1.05	0.30
120	-	-	1.16	1.26	1.01	0.40
140	-	-	1.11	1.18	0.98	0.40
150	-	-	0.76	0.84	0.87	0.33
Ice mixture: CH_3CN:H_2O (1:10)						
15	0.42	0.36	0.70	1.18	1.00	0.38
30	0.41	0.34	0.68	1.14	0.99	0.35
50	0.36	0.33	0.63	1.05	0.93	0.31
80	0.31	0.33	0.58	0.94	0.89	0.23
100	-	0.30	0.51	0.86	0.84	0.20
120	-	0.32	0.48	0.78	0.85	0.18
140	-	-	-	0.69	0.89	0.26
Ice mixture: CH_3CN:CO (1:10)						
15	1.14	0.49	0.73	1.31	1.00	0.54
30	1.19	0.58	0.98	1.44	1.08	0.64
Ice mixture: CH_3CN:CO_2 (1:10)						
15	0.64	0.48	0.58	0.83	1.00	0.23
30	0.70	0.47	0.60	0.86	1.00	0.19
50	0.66	0.49	0.59	0.85	1.01	-
80	-	0.25	0.38	-	0.58	-
100	-	-	-	-	0.57	-
Ice mixture: CH_3CN:CH_4 (1:10)						
15	0.79	0.51	0.66	1.54	1.00	0.30
30	0.84	0.54	0.69	1.45	1.08	0.35
50	0.67	0.48	0.72	1.09	0.86	0.28
Ice mixture: CH_3CN:NH_3 (1:10)						
15	0.50	0.30	0.60	0.95	1.00	0.49
30	0.84	0.53	0.59	1.60	1.83	0.70
50	0.83	0.52	0.59	1.54	1.82	0.68
80	0.82	0.50	0.56	1.41	1.74	0.60
100	-	0.53	0.65	1.34	1.65	0.56
120	-		0.54	1.16	1.17	0.46
Ice mixture: CH_3CN:H_2O:CO_2						
15	0.57	0.32	0.62	0.84	1.00	0.33
30	0.56	0.31	0.62	0.82	0.99	0.31
50	0.56	0.31	0.60	0.79	0.96	0.29
80	0.52	0.30	0.55	0.69	0.88	0.26
100	0.50	0.26	0.48	0.62	0.72	0.22
120	0.48	0.25	0.44	0.55	0.68	0.20
140	-	-	0.40	0.47	0.63	0.22
Ice mixture: CH_3CN:H_2O:CH_4:NH_3						
15	0.46	0.33	0.67	1.02	1.00	0.35
30	0.41	0.32	0.66	0.99	1.00	0.32
50	0.37	0.26	0.60	0.92	0.99	0.28
80	0.39	0.28	0.52	0.82	0.93	0.18
100	0.27	0.29	0.53	0.79	0.93	0.15
120	0.19	0.26	0.46	0.72	0.91	0.11

6

Morphological changes in CO ices probed by interference measurements

Carbon monoxide (CO) is one of the main constituents of interstellar ices. To comprehend the chemistry in CO-rich ices and accurately interpret astronomical observations, it is important to characterize the optical properties and structure of solid CO through laboratory experiments. Previous laboratory investigations primarily concentrated on the infrared properties of CO ice, with little information available on its behavior in the ultraviolet-visible wavelength range. The goal of this study is to examine the transparency character of μm-thick CO ices in the UV-Vis range and to determine which parameters influence this property, such as ice deposition rate, temperature, and ice thickness. Pure CO ices are deposited under high-vacuum conditions onto an aluminum mirror at temperatures between 7.5 - 18 K. The interference pattern of a HeNe laser (632.8 nm) and a Xe-arc lamp (250 - 750 nm) are simultaneously monitored during and after the ice growth. Our measurements show that freshly deposited μm-thick CO ices scatter light in the visible wavelength range. Spontaneous structural transitions taking place after the ice deposition lead to a CO ice that is transparent to visible light. The structural transitions take more time to complete in i) ices deposited at lower temperatures, and ii) thicker ices. Moreover, there is a threshold for the deposition rate below which CO ice is deposited as a transparent structure. Furthermore, in our experimental conditions, CO ices deposited below a rate of 0.6 μm/h are already transparent upon deposition. The origin of this morphological change is currently under debate. A possible explanation may be linked to the local growth of polycrystalline ice units. The elucidation of the physical changes taking place in the ice will ultimately determine the astronomical relevance of the effects observed here. Finally, the findings presented here also imply that laboratory experiments aimed at investigating CO ice samples under simulated astronomical conditions should be mindful of these morphology changes.

M. G. Rachid, et al. (*about to be submitted to A&A*)

6.1 Introduction

Interstellar ice observations show that ices formed in dense and cold regions of a molecular cloud have higher abundances of carbon monoxide (CO). This contrasts with the composition of ices formed in the outer parts of the molecular cloud (or earlier in the cloud evolution), that are richer in H_2O and other less volatile molecules (see Boogert et al. (2015) for a review). As a result, throughout the evolution stages of a molecular cloud, interstellar dust grains would be coated with a H_2O-rich layer of ice underneath a CO-rich layer. The successive hydrogen additions to the CO molecules can lead to the formation of CH_3OH (Watanabe and Kouchi, 2002; Watanabe et al., 2004) embedded in the CO-rich ice (Pontoppidan et al., 2003; Cuppen et al., 2011). Further radical-radical and radical-molecule reactions would also form larger organic molecules, such as acetaldehyde, glycolaldehyde, ethylene glycol, and methoxymethanol (Chuang et al., 2016; Fedoseev et al., 2022; He et al., 2022). In recent years, much effort has been put into characterizing the CO hydrogenation chain to explain the gas-phase detection of a number of larger organic interstellar molecules. All these findings show that the CO-rich ice layer is not simply an inert layer of frozen molecules but instead serves as a significant source of complex organic species in the interstellar medium (ISM).

A recent study by He et al. (2022b) showed that morphological changes in CO ice at temperatures below 5 K induce the mobility of reactive species embedded in the ice structure, driving chemical reactions without the need to overcome diffusion barriers. The authors also showed that the temperature at which the transition from a disordered ice structure (amorphous) to a more ordered structure (polycrystalline) is thickness dependent and can take place at temperatures as low as 3 K in ices with $\sim$ 600 ML of thickness (1 ML $\sim 10^{15}$ molecules cm^{-2}). In another recent study, Kouchi et al., 2021 used transmission electronic microscopy to show that CO deposited on top of solid H_2O forms crystalline material. Through diffusive processes, these crystals grow in size, forming 3D structures of crystalline CO. Due to the short timescale of this process, the authors conclude that carbon monoxide ice in the ISM would not exist in an amorphous form, but rather a form that is more structurally organized. This is in agreement with the study by He et al. (2021) which reported a similar finding. These studies highlighted the existence of structural transitions taking place below the crystallization temperature of CO and provide information on the morphology and structural transitions taking place in CO-rich ices in space.

In an investigation of the optical properties of thick ($\sim$ 16 μm) carbon monoxide

ice, Carrascosa et al. (2021) observed that the "color" of CO ice samples, as measured by the RGB intensity of light reflected from the CO ice surface, correlates with the degree of order in the solid structure. The authors showed that CO ice deposited at temperatures below 8 K exhibits an "opaque" characteristic where the light is scattered in all directions upon shining on the ice. On the other hand, ices deposited at temperatures above 20 K are transparent to visible light. Ice samples deposited at temperatures between 8 - 15 K have an intermediate character (i.e, translucent). The authors associate the temperature-dependent color properties to the degree of disorder in the ice. The temperature dependent color aspect was also shown to correlate to the observed trend in CO photodesorption yield with temperature. Additionally, the different degrees of organization of solid-phase CO are also reflected in changes in other ice properties, as recently verified by densities and infrared band strength measurements of CO ice (Díaz et al., 2022).

All these studies point to the idea that carbon monoxide ice can exist in various morphologies at temperatures below the crystallization point. These different ice structures have different interactions with light and possible implications for chemical and physical processes taking place in CO-rich ice in astronomical environments. Therefore, the investigation of structural changes of CO ice at temperatures between the ones in which the amorphous and crystalline structures are dominant is essential. In this work, we use optical interference to probe morphological changes in pure CO ice at temperatures ranging from 7.5 K - 18 K. By monitoring visible light reflected from the ice surface, we find that ices displaying an opaque character upon deposition eventually become spontaneously transparent while held at the deposition temperature. The timescale for reaching transparency depends on the ice temperature, deposition rate, and thickness. Our results extend upon the observations reported by Carrascosa et al., 2021 concerning the color properties of CO ice. The results presented here also add to the idea that morphological changes in CO happen at temperatures below the crystallization point. This paper is organized as follows. Section 2 presents the experimental setup and methodology. In section 3 the results are presented and discussed, describing the differences in the opaque/transparent character of CO ice deposited under different conditions. Section 4 presents a comparison of previous literature work and discusses the astronomical implications. Section 5 summarizes our main conclusions.

6.2 Methodology

All the measurements are performed on OASIS (Optical Absorption Setup for Ice Spectroscopy), shown schematically in Figure 2.5. Here, a short description of the setup is given and further details can be found in Kofman et al. (2018), Kofman et al. (2019), and He et al. (2022a). The OASIS setup consists of a high vacuum chamber with a base pressure of $\sim 5 \times 10^{-8}$ mbar at room temperature. An UV-enhanced aluminum mirror is placed at the center of the chamber and is used as substrate for growing ices by background deposition. The aluminum mirror is attached to a closed-cycle helium cryostat and can reach temperatures as low as 7.5 K. During and after the deposition, the ice is probed by laser interference measurements in which a HeNe laser (632.8 nm) hits the substrate at angles of incidence between 2° - 4° and is reflected into a photodetector (Thorlabs PDA36A2). Simultaneously, light from a Xe-arc lamp (250 - 750 nm) impinges onto the growing ice at an angle of incidence of 45°, is reflected towards an Andor 303i Shamrock spectrometer with a 10 μm slit, and is subsequently detected by a thermo-electrically cooled CCD (Andor iDus DV420 OE). CO gas is introduced into the high vacuum chamber via a gas manifold that has a base pressure of 10^{-3} mbar. A leak valve controls the gas pressure in the chamber during the ice growth. During the experiments, the gas manifold is filled with a constant pressure of 100 mbar, which is about five orders of magnitude higher than the base pressure of the manifold, in order to minimize impurities.

6.2.1 Interference measurements

The interference phenomenon occurring by shining light on the ice samples is schematically illustrated in the panel I of Figure 2.5. The interference occurs between the light beam that is reflected on the vacuum-ice interface and the beam that is refracted into the ice and reflected on the ice-mirror interface. These two beams have a phase difference that relates to the optical path of the beam passing through, which in turn depends on the ice thickness, incidence angle, and the refractive index of the material (Beltrán et al., 2015). The resulting signal forms a constructive and destructive oscillation pattern during the ice deposition, when the ice thickness is constantly growing. This pattern is illustrated in panel II of Figure 2.5, which shows an example of the laser interference signal recorded by the photodetector during the ice deposition. In the same way, the interference signal from the Xe-arc lamp is recorded by the UV-vis spectrometer, as shown in panel III of Figure 2.5. In the data displayed in panel III,

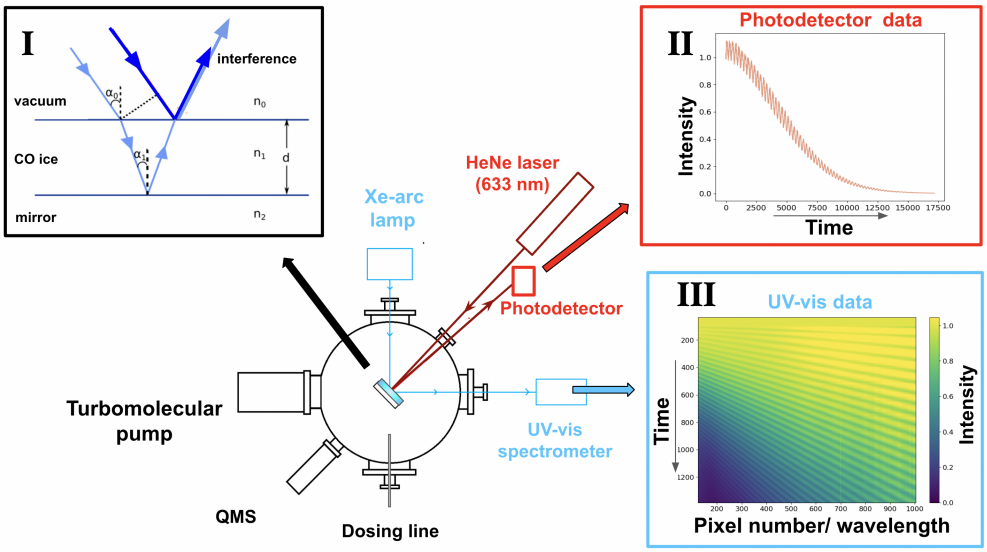

Figure 6.1: Schematic representation of OASIS setup (adapted from He et al. 2022a).

each vertical slice is an interference pattern of light covering a small wavelength range that corresponds to the spectrometer resolution ($\sim$ 0.5 nm).

In a typical measurement, the interference patterns produced by the laser and the Xe-arc lamp light are recorded by the photodetector and the UV-vis spectrometer, respectively, during and after the ice deposition. During these measurements, the ice temperature is kept constant. The changes in the interference signal after the ice deposition are the main focus of the analysis performed here. These changes are systematically characterized for ices deposited at different temperatures, thicknesses, and deposition rates. Experiments in which the ices are deposited at constant temperature and warmed at 0.3 K/min are also performed. In these measurements, the interference signals are monitored during the ice deposition and heating.

6.2.2 Ice thickness

The ice growth rate is estimated following a similar approach in He et al. (2018) based on the impingement rate of molecules onto the substrate per area (τ):

$$\tau = \frac{\mathrm{P}}{\sqrt{2\,\pi\,\mathrm{m\,k\,T}}}, \tag{6.1}$$

where P and T are the gas pressure and temperature inside the chamber, respectively, m is the molecular mass of the species being deposited, and k is the Boltzmann constant. Considering that one monolayer (ML) consists of 10^{15} molecules cm^{-2}, the time to form one monolayer (Δt) is given by :

$$\Delta t = \frac{10^{15}}{\mathrm{S} \times \tau} = \frac{10^{15}\ \sqrt{2\ \pi\ \mathrm{m\ k\ T}}}{\mathrm{S} \times \mathrm{P}}, \tag{6.2}$$

where S is the sticking coefficient and τ is the impinging rate given in Equation 6.1. By monitoring the pressure during the ice growth, considering S =1 (He et al., 2016), and integrating the pressure throughout the ice deposition, the ice column density (N) is:

$$\mathrm{N} = \frac{\int \mathrm{P\ dt}}{\sqrt{2\ \pi\ \mathrm{m\ k\ T}}}. \tag{6.3}$$

Finally, the thickness of a pure ice (d) is estimated by knowing the ice density (ρ) and column density of molecules (N) as:

$$\mathrm{d} = \frac{\mathrm{N} \times \mathrm{M}}{\rho \times \mathrm{N_{Av}}}, \tag{6.4}$$

where M is the molar mass and N_{Av} is Avogadro's number.

In this work, we use $\rho = 0.85$ g/cm^3 for the CO ice (Luna et al., 2022). In a typical experiment, ices are grown for 30 - 35 minutes, during which CO is dosed into the chamber maintaining a constant pressure of P = 5 × 10−5 mbar. Following Equations 6.2 and 6.4, this results in ices of 26000 - 30000 ML, which correspond to thicknesses of 14 - 16 μm. The gas used in all the experiments is carbon monoxide from Linde gas with a purity of 99.997 %.

6.3 Results

Figure 4.10 shows an example of typical data obtained in the measurements: the laser interference signal recorded during and after the ice growth (black), the ice temperature (red) and pressure inside the chamber (blue), and the interference signal of the Xe-arc lamp light at selected wavelengths recorded by the UV-vis spectrometer (curves of varied colors). The interference fringes at the beginning of the measurement are characteristic of the ice growth. The amplitude of the oscillation pattern and the laser signal intensity decrease during the ice deposition. This is caused by scattering

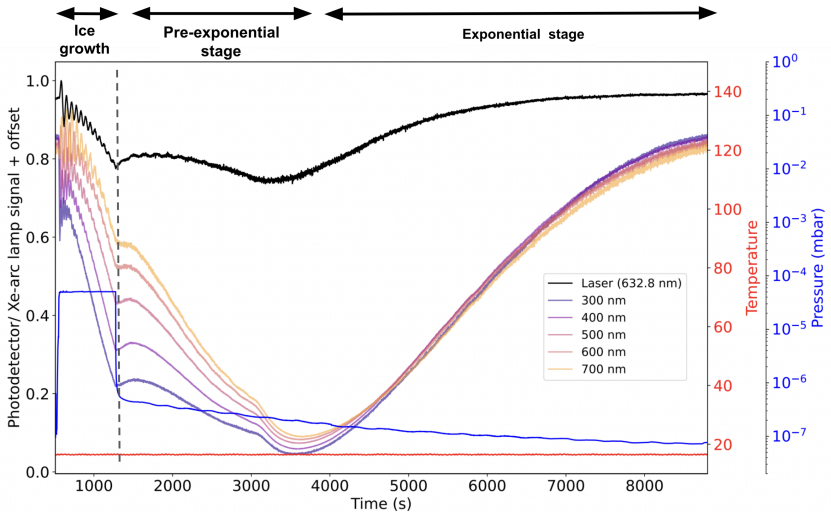

Figure 6.2: Typical measurements performed in this work, shown here for an experiment performed at 16 K. The black curve shows the laser interference pattern as the ice grows, the blue curve shows the pressure in the chamber, and the red curve the temperature. The different interference pattern in colors shows the interference signal of the Xe-arc lamp at selected wavelengths.

due to the irregularities inside the ice, and at the ice-vacuum and ice-mirror interfaces (Filiński, 1972; Romanescu et al., 2010). As pointed out by Romanescu et al. 2010, these scattering losses do not alter the periodicity of the interference fringes, which in our experiment is constant within 2% of the period.

When the deposition is stopped (dashed vertical line), the pressure inside the chamber abruptly drops by more than two orders of magnitude. From this moment, the laser and the Xe-arc lamp interference signals are expected to remain constant over time, as the ice thickness does not change. However, just after deposition has stopped, the interference signals vary, returning to their initial values in a period that depends on the ice temperature and thickness, as will be described in the next sections. Since the temperature during and after the ice growth is substantially below the desorption temperature of CO ($\sim$ 30 K), changes in the UV-vis and laser interference signal are not linked to desorption but to morphological changes in the CO ice, which lead to a structure that is transparent in the visible light range. To verify that the changes in the interference signals were not induced by any energy input from the HeNe laser or the Xe-arc lamp onto the ice or substrate, measurements without these light sources (not shown here) were also performed. In these measurements, the reflected laser signal

was only briefly measured at spaced intervals. It was verified that the measured signal increased to the original value in a period of time comparable to the measurements in which the ice was continuously exposed to the laser. This indicates that the changes in the ice structure are not induced by the incident light.

In Figure 4.10, it is possible to recognize two different moments in the evolution of the laser signal. The first occurs just after the deposition and is characterized by an slight increase and then decrease in the laser signal. The second occurs around 4000 s (for this set of temperature and ice thickness) and is characterized by an exponential increase in the interference signal until it returns to the initial value, indicating that the ice is transparent to the incident light. In this work, we will refer to the first stage of the changes in the signal as the "pre-exponential stage" and the second stage as the "exponential stage".

The timescale for the transition from opaque to transparent ice to take place depends on the deposition temperature, ice growth rate, and ice thickness. The effect of each of these experimental conditions is described in more detail in the upcoming sections. In general, the signal of both the laser and the Xe-arc lamp display the same trend of increase or decrease in time. Because of this, the next sections present only the data for the laser interference signal. Small differences in the interference pattern of these two light sources are mainly associated with the different angles of incidence onto the substrate (the incident angle for the laser beam is around 2° and for the Xe-arc lamp it is around 45°). The understanding of the morphological changes probed here at a molecular level requires dedicated theoretical studies of the CO ice structure at temperatures below the crystallization point, which is not the goal of this work. Nonetheless, we suggest that the morphological changes taking place in the ice are related to the growth of polycrystal domains, as described at the end of the next section.

6.3.1 Temperature dependence

Figure 6.3a shows the laser interference signal recorded during and after deposition of CO ice at selected temperatures above 10 K. All the ices are grown to a thickness of around 30000 ML ($\sim$ 16 μm, determined using Equation 6.4). Since all the ices have roughly the same thickness and are deposited at the same rate, the differences in the time to achieve transparency are due to the difference in deposition temperature. Figure 6.3a shows that ices deposited at higher temperatures become transparent in a shorter amount of time than ices deposited at lower temperatures. For ices deposited

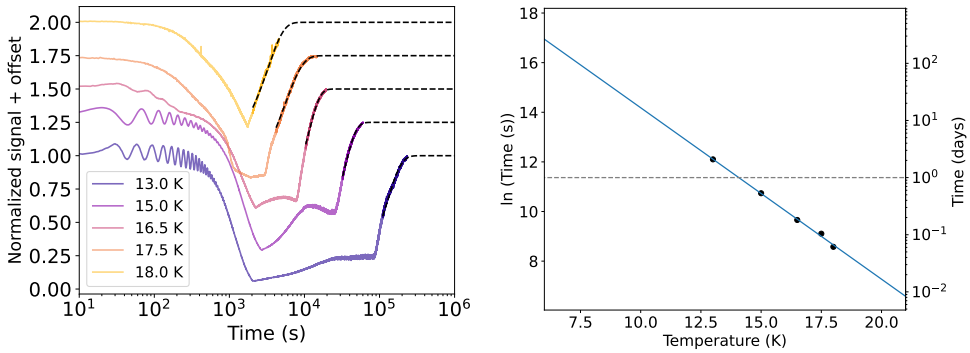

(a) (b)

Figure 6.3: a) Normalized laser interference signal recorded for CO ices with $\sim$ 16 μm of thickness grown at temperatures between 13 - 18 K. The interference signals are normalized and offset for clarity. The dashed black lines are teh fit of the signal to Equation 6.5. b) Time it takes the ice to become transparent at different temperatures. Details of these calculations are in the text.

at temperatures lower than 13 K, the transition to a transparent ice takes more than two days, and the water deposition due to chamber residual gas is no longer negligible. The deposition of large amounts of impurity might also scattering a significant part of the incident light, affecting the time for the ice to become transparent. For this reason, the ices deposited below 13 K are not measured until reaching transparency, as discussed in more detail later. It is also noticeable from Figure 6.3a that the amplitude of the oscillation pattern decreases faster for ices deposited at higher temperatures, and less fringes are seen in the interference signal during the ice growth.

To determine the timescale for the structural changes that lead to transparent CO ices, it is necessary to know the point at which the sample becomes completely transparent. Although monitoring the changes in the interference signal is not challenging, determining the end-point of such transformations is rather complicated. The reasons for this are linked to a lower sensitivity of signal variations at the end of the exponential curve and the effects of the deposition of background gases that causes noise on the signal after long measurements. Here, the time that it takes for the interference signal to return to 90% of its original value is considered as the time to reach transparency. The exponential part of the interference signal is modeled using the JMAK (Johnson–Mehl–Avrami–Kolmogorov) theory, which is widely employed to model phase transitions of solids (Avrami, 1939, 1940, 1941). According to the JMAK theory, during a phase transition, the fraction of the new phase in a solid sample is

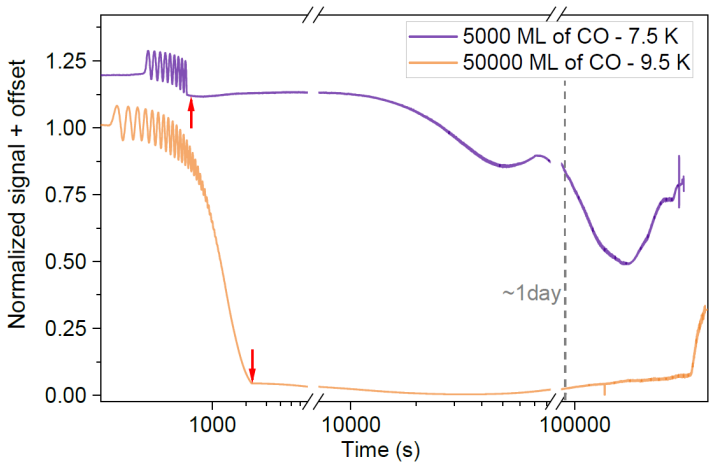

Figure 6.4: Normalized laser interference signal recorded for a 16 μm CO ice at 9.5 K and a 3 μm CO ice at 7.5 K. The signals are offset for clarity. The red arrows indicate the point when ice deposition stopped, and the dashed gray line indicates a time interval of 1 day.

given by:

$$\mathrm{Y} = 1 - \exp(-\mathrm{k(T)}\ \mathrm{t^n}), \tag{6.5}$$

where Y is the normalized fraction of the new phase, t is the elapsed time and $k(T)$ is the temperature-dependent rate constant for the phase transition. Here, we assume that the degree of "crystallinity" is proportional to ice transparency. This assumption might not be precise, as CO ices at temperatures between 5 - 24 K are likely in a polycrystalline-like phase (He et al., 2021; He et al., 2022b) and the phenomenon observed here would not be a phase transition by a strict definition. Nevertheless, Equation 6.5 can fairly model the exponential part of the interference signal and give some hints on the kinetics of the structural changes taking place. With this assumption, the exponential part of the photodetector signal is modeled following Equation 6.5. The fitting of Equation 6.5 to data collected for ices at different temperatures are displayed in Figure 6.3b as dashed lines.

The values of n obtained from the fitting of the JMAK equations are between 1.9 - 2.8. Typical values for these parameters are between 3 and 4, but lower numbers have been reported in studies of the crystallization kinetics of thinner ices (Maté et al., 2012; Harada et al., 2020; He et al., 2021). The n index is related to the formation rate and the volume growth of the new phase during a phase transition. An n value smaller than

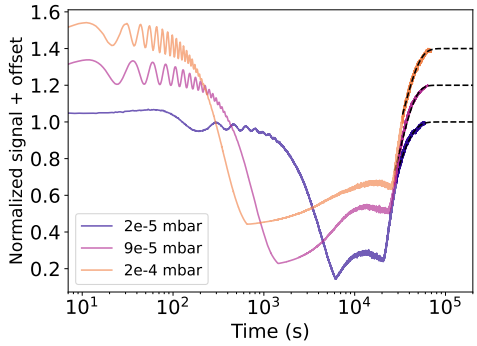

Figure 6.5: CO ice at 15 K deposited at different deposition rates. The CO pressure during deposition is indicated by the different colors.

4 indicates a degree of constraint in the emergence of nucleation sites or the growth of the new phase. Since the ices studied in this work are much thicker than the ones in the previous studies, the growth of a new phase is not expected to be spatially constrained. The relatively low values of n are likely linked to a more complex correlation between the signal in the photodetector and the ongoing structural ice changes. The structural change probed by our interference measurements is probably the polycrystal growth, which is expected to happen in thin CO ices at temperatures below 10 K (He et al., 2021). In this way, our measurements do not probe a transition from one homogeneous phase into another, compromising a deep physical interpretation of the fitted Avrami parameters.

Figure 6.3b shows the time that it takes for the structural transition in the CO ice deposited at different temperatures to complete. Here, this transparency time (t_{transp}) is considered as the time it takes for the laser signal to raise back to 90% of the asymptotic value, as calculated from the fit of Equation 6.5. The transparency time t_{transp} drops exponentially with the ice deposition temperature T, and we use the following equation to describe it:

$$\mathrm{t_{transp}} = \exp(\mathrm{A} + \mathrm{B/T}), \tag{6.6}$$

where A = 21.1 and B = -0.690 are the best fitting parameters. The fit of equation 6.6 to the data is displayed in Figure 6.3b.

Our results show that a 16 μm-thick pure CO ice deposited at temperatures between 13 - 18 K and under the conditions described here can take from a few hours up to a few days to become completely transparent. Extrapolating our results to

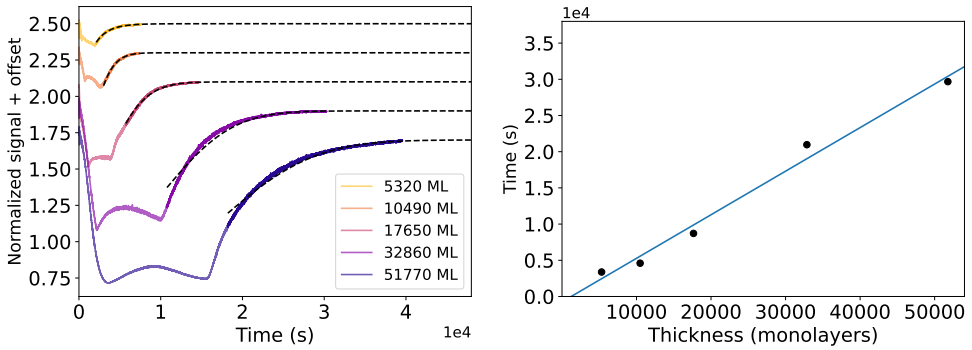

(a) **(b)**

Figure 6.6: a) Normalized laser interference signal recorded for CO ice at 16.5 K and different thicknesses (given here in monolayers). The dashed black lines are the fit of the signal to Equations 6.5. b) Time for the ice at different thicknesses to become transparent. Details of these calculations are in the text.

even lower temperatures implies that a μm-thick CO ice deposited at T $\leq$ 7 K would become completely transparent in about 100 days. As it is shown in the upcoming sections, these time scales also depend on the ice thickness.

Figure 6.4 shows the interference signal recorded during and after deposition of ices grown at temperatures below 10 K: a $\sim$ 16 μm CO ice at 9.5 K and a $\sim$ 3 μm CO ice deposited at 7.5 K. The ice deposited at 7.5 K is made thinner because at this temperature the structural transition that leads to a completely transparent structure may take a few weeks (see Figure 6.3b, which is a not convenient experimental timescale. Although these two samples were not monitored until reaching transparency, it is possible to observe an increase in the interference laser signal value, indicating that the transition that leads to transparent ice had started.

The signal detected from the light reflected by CO ices deposited at temperatures below 10 K is different from the profile for ices below 10 K. For ices at temperatures above 10 K, the photodetector signal increases a few minutes after deposition has stopped. For the ices deposited at temperatures below 10 K, the photodetector signal continues to drop after deposition for a few hours before it starts increasing, as shown in Figure 6.4. This indicates that the CO ice below 10 K initially accommodates into a more scattering structure and later changes to a more translucent/transparent structure.

6.3.2 Ice growth rate dependence

Figure 6.5 shows the interference pattern recorded during and after the growing of CO ice at different deposition rates (here expressed as the pressure in the chamber during the ice growth). All the ices are grown at 15 K until reaching a thickness of about ~ 16 μm. Additional measurements performed dosing CO at pressures of 2×10^{-6} mbar (not shown here) were performed and under these conditions the CO ice is deposited in the transparent form, and no significant changes in the laser signal are observed after hours of deposition. It can be seen from Figure 6.5 that the timescale of the pre-exponential stage is different for the different measurements while the exponential stage shows the same timescale. It is remarkable from Figure 6.5 that the time to reach transparency, as counted from the beginning of the deposition, does not vary significantly with the deposition speed. This may indicate that during the ice deposition the structural transition responsible for the change in the transparent character is already taking place.

6.3.3 Thickness dependence

Figure 6.6a shows the photodetector signal recorded during and after the growth of CO ice of different thicknesses (indicated by the number of monolayers) at 16.5 K and at a fixed deposition rate. It can be seen that CO ice with a thickness below 17000 ML (~ 9 μm) displays a slight drop in the interference signal after deposition compared to thicker ices. This decrease in the signal intensity is, however, less pronounced than the decrease in the signal observed in ices detected at lower temperatures (Figure 6.4). The black dashed curves in Figure 6.6a show the fit of the data to Equation 6.5. From the fitted data, the time for recovering 90% of the signal decrease is derived. The time it takes for CO ice of different thicknesses to become transparent is shown in Figure 6.6b. As can be seen, the time to reach transparency increases monotonically with the ice thickness.

6.3.4 Ice heating

Figure 6.7 shows the laser signal for measurements in which CO ice was deposited at the indicated temperatures and heated at a rate of 0.3 K/min to 19 K. All the ices have a thickness of ~ 16 μm and were deposited at the same rate. The laser interference signal shows that all the samples become transparent in a similar period. This indicates that the morphological changes observed to occur spontaneously in the

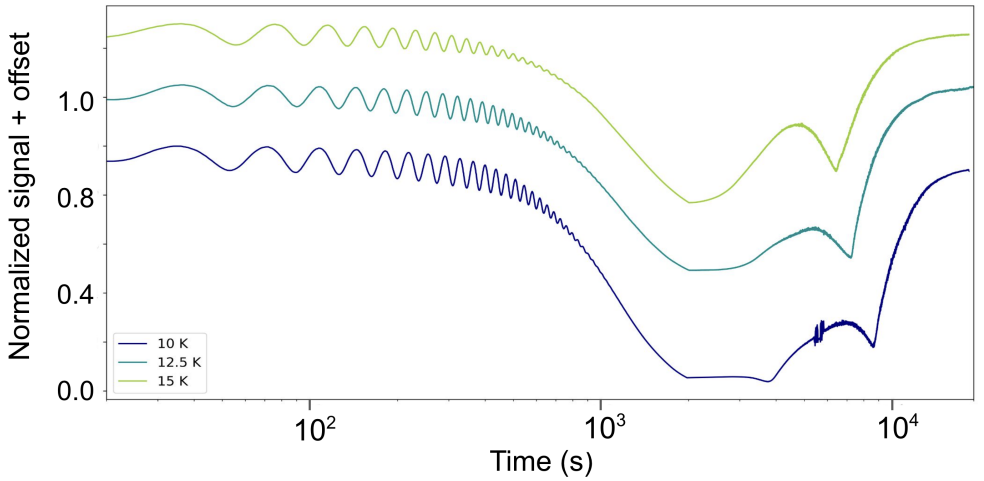

Figure 6.7: Normalized laser interference signal recorded for ices deposited at constant temperature and heated at 0.3 K/min to 19 K.

previously described experiments can also be induced via heating.

6.4 Discussion

This work studies morphological transition in CO ice samples grown at temperature between 7.5 - 18 K. These temperatures are below the crystallization temperature ($\sim$ 24 K). We propose here that the structural transformation monitored by the interference measurements is related to the growth of polycrystalline domains inside the ice structure, as proposed in Figure 6.8. The freshly deposited ice is polycrystalline and strongly scatters visible light. The merging or growing of polycrystalline domains would decrease the light scattering, as these domains' sizes would become significantly larger than the wavelength of light, and the number of boundaries between domains in the light path would decrease.

A relation between polycrystal sizes in freshly deposited ice and deposition temperature could potentially explain the different scattering behavior of ice deposited below and above 10 K. Ices deposited at lower temperatures may have polycrystal domains smaller than the wavelength of visible light. As these domains grow and approach the dimensions of the wavelength of visible light, more radiation is scattered, and the ice becomes more opaque. This would explain the drop in the laser signal in CO ices deposited below 10 K, as shown in Figure 6.4. As the polycrystal sizes reach a size

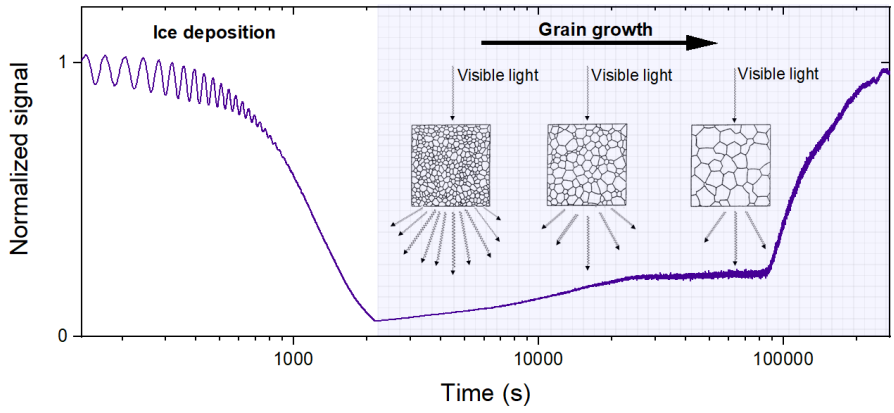

Figure 6.8: Interference signal recorded during and after the ice growth with a schematic cartoon of the suggested structural changes: polycrystal growth at constant temperature.

limit that may be significantly larger than the wavelength of light, further growth would lead to less light scattering.

The time scale for the ice to become transparent in our experiments seems to be in line with the observations of the "ice color" made by Carrascosa et al. (2021). In their work, CO ice deposited at temperatures higher than 15 K is transparent, while CO ice deposited at temperatures below 15 K shows some degree of color, as measured by the RGB intensity of light reflected from the ice sample. The authors showed that the ice deposited at temperatures below 15 K displayed an opaque character. Considering that the time to reach a transparent structure does not change with the deposition rate (Section 3.2), our results show that it would take more than one day for ice deposited at 13 K and below to transform into a transparent structure (see dashed line in Figure 6.3b). Since their ice samples were deposited for a period of 24 hours, this could explain why they observe some "residual color" in their ice, rather than a transparent structure. The only sample that the authors mentioned having monitored for long periods was the ice deposited at 8 K, which was heated to 23 K and monitored for 48 hours. This sample maintained its opaque character and did not become transparent, being the only disagreement between our results and the ones shown by (Carrascosa et al., 2021). The results presented in Section 6.3.4 showed that ices deposited at low temperatures and slowly heated to 19 K become transparent regardless of the deposition temperature. A possible reason for this difference is the

deposition method employed in their work and here. The CO samples in the work by Carrascosa et al. (2021) are deposited by frontal deposition, while the ones studied in this work are grown by background deposition. The compaction of the ice caused by a frontal deposition would lead to a more rigid structure and consequently longer times to reach transparency.

This indicates that the results found by Carrascosa et al., 2021 are a snapshot of the morphological transformations taking place in the ice. The measurements presented here show that CO ice can exist in different morphologies at temperatures between the ones at which it is crystalline and amorphous. It also shows that in the experimental conditions reported here, the ice structure undergoes spontaneous morphological changes after the deposition, which can highly impact the ice's scattering properties. While the time scale of the structural transformation investigated in this work is small compared to astronomical ones, the findings presented here show that laboratory experiments involving μm-thick CO ice samples must consider possible structural changes taking place after ice deposition. Carrascosa et al. (2021) suggested that the photodesorption of CO could be related to the color of the ice samples. Based on the work presented here, we suggest that differences in the CO photodesorption can also be related to the CO polycrystal domain sizes.

In an interstellar context, the scattering of visible light by CO ice layers could potentially provide a protection for the underlying ice material. According to current models of interstellar ice formation, CO-rich ice layers are expected to form in dense regions of molecular clouds, on top of already existing H_2O-rich ice (or polar ice), formed at earlier stages of the cloud evolution (Boogert et al., 2015). In a scenario in which CO highly scatters incident UV and visible light, the CO ice would provide a protection against UV photons for the polar ice underneath. However, due to the different thickness regime, it is likely that CO ices with thickness comparable to the interstellar ones (≤ 0.01 μm) are already in the transparent form.

As suggested by Carrascosa et al. 2021, the scattering behavior of CO ice of different morphologies can have impact on the color and albedo values of Solar System surfaces. To access the relevance of the light scattering by μm-thick CO ice for Solar System surfaces, further study of CO-containing ice mixtures is necessary. The presence of different impurities in the CO ice can influence its "transparency" character and the findings in this work. The systematic characterization of the optical properties of CO-rich ices would reveal in what extend the presence of impurities affect the scattering of visible light by these ices. Ultimately, these studies have the potential to enhance our comprehension of the properties of CO-rich ices and surfaces of larger bodies.

6.5 Conclusion

In this work, we investigated the spontaneous morphological transition in μm-thick CO ices deposited under high vacuum at temperatures from 7.5 - 18 K. The structural transition taking place is likely associated with the growth of polycrystal domains in the ice. The main conclusions of this work are summarized below:

- After deposition, thick CO ices display an opaque character and scatter light in the visible-UV wavelength range. Spontaneous structural transitions after the ice deposition lead to translucent/transparent ice in timescales that are dependent on the deposition temperature and ice thickness. As the CO ice is in a polycrystalline form (deposition temperature higher than 5 K), we propose that the structural transition taking place is polycrystal growth. In this scenario, as the polycrystal domains reach dimensions larger than the wavelength of the incident light, less radiation is scattered.

- After deposition, CO ice at temperatures above $\sim$ 10 K becomes increasingly transparent, while ices deposited at temperatures below $\sim$ 10 K first become opaque and then transparent at a later stage. The time to reach transparency increases for ice deposited at lower temperatures. We propose that these differences are related to the size of the polycrystal formed during deposition. In freshly deposited CO ice below 10 K, the polycrystal sizes are comparable to the wavelength of visible light.

- The time to reach transparency grows linearly with the ice thickness.

- There is a limit for the deposition rate below which the ice is deposited as a transparent structure. For our experimental conditions, this limit is around P $\sim 10^{-6}$ mbar, which corresponds to a deposition of around 0.6 μm/h

- The timescale of the transition of a disordered and opaque CO ice into a polycrystalline structure is negligible when compared to astronomical time scales. In this way, thick, pure CO ice layers in the interstellar medium are expected to be polycrystalline and transparent to UV-visible light.

  The experiments performed in this work show that thick CO ice samples undergo spontaneous structural changes after deposition. Laboratory experiments that aim to study thick CO ice samples in astronomical simulated conditions should be aware of such transitions, as the timescale for these to happen are negligible in space but not in the laboratory.

References

Avrami, M., 1939, J. Chem. Phys., 7, 1103
Avrami, M., 1940, J. Chem. Phys., 8, 212
Avrami, M., 1941, J. Chem. Phys., 9, 177
Beltrán, M., Molina, R., Aznar, M., et al., 2015, Sensors, 15, 25123
Boogert, A. C. A., Gerakines, P. A., and Whittet, D. C. B., 2015, ARA&A, 53, 541
Carrascosa, H, Caro, G. M., González-Díaz, C, et al., 2021, ApJ, 916, 1
Chuang, K. J., Fedoseev, G., Ioppolo, S., et al., 2016, MNRAS, 455, 1702
Cuppen, H. M., Penteado, E. M., Isokoski, K., et al., 2011, MNRAS, 417, 2809
Díaz, C. G., Carrascosa, H., Caro, G., et al., 2022, MNRAS,
Fedoseev, G., Qasim, D., Chuang, K.-J., et al., 2022, ApJ, 924, 110
Filiński, I, 1972, Physica Status Solidi (B), 49, 577
Harada, K., Sugimoto, T., Kato, F., et al., 2020, PCCP, 22, 1963
He, J., Acharyya, K., and Vidali, G., 2016, ApJ, 823, 56
He, J., Diamant, S. J., Wang, S., et al., 2022, ApJ, 925, 179
He, J., Emtiaz, S., Boogert, A., et al., 2018, ApJ, 869, 41
He, J., Góbi, S., Ragupathy, G., et al., 2022, ApJL, 931, L1
He, J., Simons, M., Fedoseev, G., et al., 2022, A&A, 659, A65
He, J., Toriello, F. E., Emtiaz, S. M., et al., 2021, ApJL, 915, L23
Kofman, V, Witlox, M., Bouwman, J, et al., 2018, Review of Scientific Instruments, 89, 053111
Kofman, V., He, J., Kate, I. L. ten, et al., 2019, ApJ, 875, 131
Kouchi, A., Tsuge, M., Hama, T., et al., 2021, MNRAS, 505, 1530
Luna, R., Millán, C., Domingo, M., et al., 2022, ApJ, 935, 134
Maté, B., Rodríguez-Lazcano, Y., and Herrero, V. J., 2012, PCCP, 14, 10595
Pontoppidan, K. M., Fraser, H. J., Dartois, E., et al., 2003, A&A, 408, 981
Romanescu, C., Marschall, J., Kim, D., et al., 2010, Icarus, 205, 695
Watanabe, N. and Kouchi, A., 2002, ApJL, 571, L173
Watanabe, N., Nagaoka, A., Shiraki, T., et al., 2004, ApJ, 616, 638

7

Searching for stable fullerenes in space with computational chemistry

We report a computational study of the stability and infrared (IR) vibrational spectra of neutral and singly ionised fullerene cages containing between 44 and 70 carbon atoms. The stability is characterised in terms of the standard enthalpy of formation per CC bond, the HOMO–LUMO gap, and the energy required to eliminate a C_2 fragment. We compare the simulated IR spectra of these fullerene species to the observed emission spectra of several planetary nebulae (Tc 1, SMP SMC 16, and SMP LMC 56) where strong C_{60} emission has been detected. Although we could not conclusively identify fullerenes other than C_{60} and C_{70}, our results point to the possible presence of smaller (44, 50, and 56-atom) cages in those astronomical objects. Observational confirmation of our prediction should become possible when the James Webb Space Telescope comes online.

A. Candian, M. G. Rachid, H. MacIsaac, V. N. Staroverov, E. Peeters, J. Cami (2019) MNRAS, 485, 1

7.1 Introduction

A significant fraction (∼10%) of elemental carbon in the universe is thought to exist in the form of large organic molecules such as polycyclic aromatic hydrocarbons (PAHs) and fullerenes (Tielens, 2008). These species are of central importance in the physics and chemistry of interstellar environments and star-forming regions of the Milky Way and of other galaxies.

Fullerenes are a fairly recent addition to the inventory of known interstellar species. Since the first detection of infrared (IR) vibrational bands of C_{60} and C_{70} in the emission of the Tc 1 planetary nebula (Cami et al., 2010, PN), similar IR bands have been found in many astronomical objects: various types of evolved stars (García-Hernández et al., 2010; Gielen et al., 2011; Zhang and Kwok, 2011; García-Hernández et al., 2011b,a, 2012; Evans et al., 2012; Bernard-Salas et al., 2012), reflection nebulae and HII regions (Sellgren et al., 2010; García-Hernández et al., 2012; Boersma et al., 2012; Peeters et al., 2012; Castellanos et al., 2014), young stellar objects (Roberts et al., 2012), and recently in the diffuse interstellar medium (Berné et al., 2017). Laboratory measurements and observational analyses have also shown that several diffuse interstellar bands are due to C_{60}^+ (Walker et al., 2015; Campbell et al., 2015, 2016; Walker et al., 2016, 2017; Cordiner et al., 2017; Lallement et al., 2018). It has thus become clear that C_{60} and C_{60}^+ are widespread and abundant in space. Given that their unique spectral features are well characterized and understood, these species can now be used as proxies to study the much larger family of bulky aromatic species in space.

A key question to be resolved in the context of circumstellar and interstellar fullerenes is how they are formed. Most experimental methods on Earth represent bottom-up formation routes starting from a carbonaceous seed gas (see e.g. Jäger et al., 2009); closed network growth through intermediate size cages eventually reaches the most stable fullerene C_{60} (Dunk et al., 2012). Such formation routes require high densities and thus would play out over prohibitively long timescales in astrophysical environments where densities are low (see, e.g., Micelotta et al., 2012). An important clue to the astrophysical formation routes came from the observational analysis of Berné and Tielens (2012) who showed that the abundance of PAHs in NGC 7023 decreases as one approaches the hot central star, while at the same time the abundance of C_{60} increases. This suggests that fullerenes may be formed by ultraviolet photochemistry in a top-down fashion starting from large PAHs with more than 60 carbons. The chemical feasibility of such formation routes was confirmed experimentally (Zhen

et al., 2014). A top-down route may explain the formation of C_{60} in interstellar environments; however, it is not clear whether it can also account for the formation of fullerenes in evolved stars (Cami et al., 2018).

Bottom-up routes grow toward C_{60} through smaller fullerene cages that are intermediate, transient building blocks; the top-down routes on the other hand include smaller fullerene cages as the result of photofragmentation of C_{60}. Interestingly, both bottom-up (e.g. Zimmerman et al., 1991) and top-down (e.g. Rohlfing et al., 1984) routes predict enhanced abundances of so-called "magic-number" fullerenes, smaller cages (with 44, 50 or 56 carbon atoms) that are more stable than other fullerenes. If these intermediate fullerenes are sufficiently stable, they may survive for long enough to be detectable in astrophysical environments.

In this paper, we calculate and analyse several structural stability indicators of various fullerenes which may be relevant for their abundance in space. We also calculate IR vibrational spectra for a representative sample of intermediate fullerenes and compare our results to astronomical observations of several C_{60}-rich PNe.

7.2 Methodology

7.2.1 Definitions

The stability of fullerene-type molecules is determined by several factors. By Euler's polyhedron formula, a fullerene consisting only of pentagons and hexagons (classical fullerenes) must contain exactly 12 pentagons to form a closed cage. The arrangement of the pentagons affects the stability of the cage, the most stable isomer being the one where the pentagons are isolated (Kroto, 1987). The buckminsterfullerene C_{60} and its larger cousin C_{70} are the smallest cages that comply with this rule (Fowler and Manolopoulos, 1995). For cages where isolated pentagons are impossible, the more stable isomers are the ones with the smallest number of adjacent pentagons (Albertazzi et al., 1999). Recently, there has been discussion on whether the isolated pentagon rule remains valid for charged fullerenes and endohedral metallofullerenes (Wang et al., 2015).

Here, we are interested in the relative stability of smaller C_n cages with $n = 44$, 50, 56 as well as cages that arise as intermediates in reversible transformations connecting C_{60} and C_{70}, i.e., $n = 62$, 64, 66, and 68. Guided by the pengaton adjacency rule, we selected for each n the isomers containing the lowest number of adjacent pentagons in both neutral and cationic form. In the case of C_{62} non-classical fullerenes, containing

Table 7.1: Calculated properties of the C_n and C_n^+ fullerene cages studied in this work. All values were obtained at the B3LYP/6-31G* level of theory except for the HOMO–LUMO gap (PBE/6-31G*).

	Neutral C_n						Cation C_n^+			
n	Isomer*	Point group	E_0 (E_h)	$\Delta_f H_0^\circ$ (kcal/mol)	$\Delta\epsilon_{\mathrm{HL}}$ (eV)	$\Delta E_0^{\mathrm{elim}}$ (eV)	Point group	E_0 (E_h)	$\Delta_f H_0^\circ$ (kcal/mol)	$\Delta E_0^{\mathrm{elim}}$ (eV)
44	75	D_2	−1675.934983	823.3	0.76	8.51	C_2	−1675.675080	986.3	8.51
	89	D_2	−1675.933854	824.0	0.84	8.48	D_2	−1675.672880	987.7	8.45
	72	D_{3h}	−1675.922892	830.8	1.23	8.18	C_1	−1675.659056	996.4	8.07
	69	C_1	−1675.905136	842.0	0.57	7.70	C_1	−1675.651777	1001.0	7.87
	87	C_2	−1675.890008	851.4	0.61	7.29	C_2	−1675.640556	1008.0	7.57
	78	C_1	−1675.887802	852.9	0.43	7.23	C_1	−1675.640151	1008.3	7.56
	88	C_1	−1675.887805	852.9	0.43	7.23	C_1	−1675.639885	1008.4	7.55
50	270	D_3	−1904.622648	840.7	1.33	9.57	C_2	−1904.360527	1014.3	9.21
	271	D_{5h}	−1904.614508	845.8	0.41	9.35	C_{5h}	−1904.372567	997.6	9.54
	266	C_s	−1904.610068	848.6	0.92	9.23	C_s	−1904.357248	1007.2	9.12
	263	C_2	−1904.606111	851.1	1.13	9.13	C_2	−1904.344217	1015.4	8.77
	264	C_s	−1904.594589	858.3	0.78	8.81	C_2	−1904.342077	1016.8	8.71
	260	C_2	−1904.587465	862.8	0.54	8.62	C_s	−1904.340925	1017.5	8.68
	262	C_s	−1904.584073	864.9	0.58	8.53	C_s	−1904.334007	1021.8	8.49
56	916	D_2	−2133.263470	887.6	0.68	8.36	C_s	−2133.019324	1040.8	8.31
	864	C_s	−2133.263101	887.8	0.88	8.35	C_s	−2133.017361	1042.0	8.54
	843	C_2	−2133.257250	891.5	0.70	8.19	C_2	−2133.012619	1045.0	8.13
	913	C_{2v}	−2133.252127	894.7	0.50	8.05	C_{2v}	−2133.011996	1045.4	8.11
60		I_h	−2285.799255	850.7	1.67	11.18	D_{5d}	−2285.538791	1014.1	10.47
62	1h†	C_s	−2361.916462	926.8	0.50	5.52	C_s	−2361.681847	1074.0	6.22
	1s‡	C_{2v}	−2361.910879	930.3	0.84	5.36	C_{2v}	−2362.670169	1081.3	5.90
	2378	C_2	−2361.895289	940.1	0.42	4.93	C_1	−2361.655576	1090.5	5.50
	2377	C_1	−2361.894581	940.5	0.34	4.92	C_2	−2361.653374	1091.5	5.44
64	3451	D_2	−2438.155785	926.3	1.23	8.84	D_2	−2437.907149	1082.3	9.17
	3452	C_s	−2438.145459	932.7	1.06	8.56	C_s	−2437.894842	1090.0	8.83
	3457	C_2	−2438.135884	938.8	0.86	8.30	C_2	−2437.885889	1095.6	8.59
66	4466	C_s	−2514.356701	949.8	0.95	7.79	C_{2v}	−2514.113257	1102.6	7.93
	4348	C_{2v}	−2514.350102	954.0	0.30	7.61	C_s	−2514.106888	1106.6	7.76
	4169	C_2	−2514.342759	958.6	0.48	7.41	C_2	−2514.099333	1111.3	7.55
68	6290	C_2	−2590.574909	962.6	1.37	8.26	C_2	−2590.323827	1120.1	8.06
	6328	C_2	−2590.572785	963.9	0.93	8.21	C_2	−2590.324464	1119.7	8.07
	6270	C_1	−2590.557981	973.2	1.05	7.80	C_1	−2590.313048	1126.9	7.76
	6198	C_1	−2590.555998	974.4	0.41	7.75	C_1	−2590.317355	1124.2	7.88
	6148	C_1	−2590.554346	975.5	0.36	7.71	C_1	−2590.321569	1121.6	7.99
	6146	C_2	−2590.554036	975.7	0.07	7.69	C_2	−2590.315973	1125.1	7.84
	6195	C_2	−2590.553849	975.8	0.42	7.70	C_2	−2590.328153	1117.4	8.17
	6094	C_s	−2590.553605	975.9	0.04	7.68	C_s	−2590.319309	1123.0	7.93
70		D_{5h}	−2666.865607	929.8	1.70	10.24	C_{2v}	−2667.046354	1089.6	10.02

*Isomer identification number according to Fowler and Manolopoulos 1995.
†Structure with a heptagon.
‡Structure with a square.

a heptagon and square were also considered, since they are expected to be more stable than the classical cages (Ayuela et al., 1996; Qian et al., 2000; Sánchez et al., 2005).

To quantify the stability of these C_n fullerene molecules, we employ three metrics. The first is $\Delta_f H_0^\circ$, the standard enthalpy of formation of C_n at $T = 0$ K divided by the number of CC bonds. $\Delta_f H_0^\circ$ is defined as the change of enthalpy for the reaction in which 1 mol of C_n is formed from n mol of graphite at 1 bar. Following Alcamí et al. (2007), we compute this quantity using the relation

$$\Delta_f H_0^\circ(C_n) = E_0(C_n) - nE_0(C) + n\Delta_f H_0^\circ(C), \tag{7.1}$$

where $E_0(C_n)$ is the sum of the total electronic and zero-point energies (ZPE) of C_n, $E_0(C)$ is the ground-state electronic energy of a gas-phase C atom, and $\Delta_f H_0^\circ(C) = 171.29$ kcal/mol is the standard enthalpy of formation of gas-phase C atoms at $T = 0$ K. The values of $E_0(C_n)$ and $E_0(C)$ can be calculated with quantum chemistry techniques (see below).

Stability of fullerenes can also be described from a kinetic point of view as a measure of "resistance" to becoming an activated complex that can undergo chemical reactions, such as fragmentation. A useful indicator of kinetic stability is the gap between the highest occupied molecular orbital (HOMO) and lowest unoccupied molecular orbital (LUMO) energy levels,

$$\Delta\epsilon_{\mathrm{HL}} = \epsilon_{\mathrm{LUMO}} - \epsilon_{\mathrm{HOMO}}. \tag{7.2}$$

A large HOMO–LUMO gap correlates with a high kinetic stability (lower chemical reactivity) of C_n molecules (Manolopoulos et al., 1991).

Finally, molecular stability can be interpreted as the enthalpy change associated with a particular fragmentation reaction. For example, it is well established that the dominant fragmentation channel of C_n cages is a sequential elimination of C_2 units. The enthalpy change for this process is

$$\Delta E_0^{\mathrm{elim}} = E_0(C_{n-2}) + E_0(C_2) - E_0(C_n), \tag{7.3}$$

where the E_0 values are the ZPE-corrected total electronic energies of the indicated gas-phase species.

7.2.2 Computational details

Cartesian coordinates of all C_n cages were generated using the `Fullerene` software (version 4.5) (Schwerdtfeger et al., 2013), applying symmetry constraints appropriate

to the corresponding point group. We optimised cage geometries and calculated their vibrational spectra with the `Gaussian 09` program (Frisch et al., 2009) using the B3LYP functional (Stephens et al., 1994), the 6-31G* basis set, and a frequency scale factor $f_{\text{scale}} = 0.978$. We convolved the spectra with a Lorentzian profile function having a full width at half maximum (FWHM) of 10 cm^{-1}, unless noted otherwise. We used `Gabedit` (version 2.5.0; Allouche, 2011) to visualize the cage structures and their vibrational modes. We chose the B3LYP functional because it has been successfully used in the past to obtain the IR spectra of other fullerenes (Adjizian et al., 2016) and conjugated hydrocarbons (Langhoff, 1996) with various basis sets (4-31G, 6-31G, 6-31G*, 6-31G**, 6-311G). The B3LYP/6-31G* combination with the above frequency scaling factor provides the best agreement with experiment (Frum et al., 1991; Kern et al., 2013; Nemes et al., 1994), similar to that of the B3LYP/6-311G method used by Adjizian et al. (2016). We also calculated the C_2 elimination energy of Eq. (7.3) at the B3LYP/6-31G* level. For each cage C_n, we used the most stable isomer of C_{n-2} as the fragmentation product. The B3LYP/6-31G* method predicts the C_2 molecule to have a triplet ground state (Díaz-Tendero et al., 2003), which is the state we used here for computing $E_0(C_2)$ in Eq. (7.3).

Because the B3LYP functional performs poorly for HOMO–LUMO gaps of C_{60} (Kremer et al., 1993), we followed Beu et al. (2005) and calculated orbital energies using the PBE functional (Perdew et al., 1996) with the same 6-31G* basis set, at the PBE/6-31G* geometries.

7.3 Results

7.3.1 Thermochemical stability

We summarise the results of all thermochemical calculations of this work in Table 7.1; Figs. 7.1–7.3 provide a graphical representation of the same results.

Figure 7.1 shows the calculated enthalpy of formation per CC bond (assuming $3n/2$ bonds in C_n) of the neutral C_n cages we considered. The results are in excellent agreement with a previous study (Alcamí et al., 2007). As expected, C_{60} and C_{70} are the most stable structures according to this metric, but we note that several isomers of C_{68} have values close to C_{60}. The general decrease in $\Delta_f H_0^\circ$ (per bond) values observed from C_{40} to C_{70} correlates with the decreasing geometric distortion of the trigonal planar geometry preferred by each sp^2-hybridised carbon. Variations of the $\Delta_f H_0^\circ$ values among isomers are small, especially for larger cages.

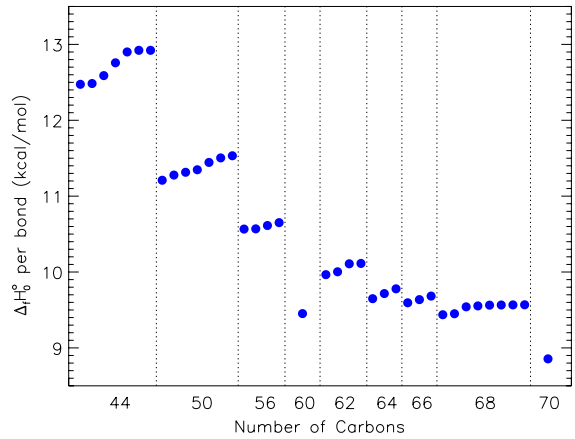

Figure 7.1: Standard enthalpies of formation per CC bond for the isomers of the neutral C_n cages we considered, calculated with the B3LYP/6-31G* method. For each n, the isomers are ordered by their increasing total energy (as in Table 7.1). Dashed vertical lines separate the species with a different number of carbon atoms.

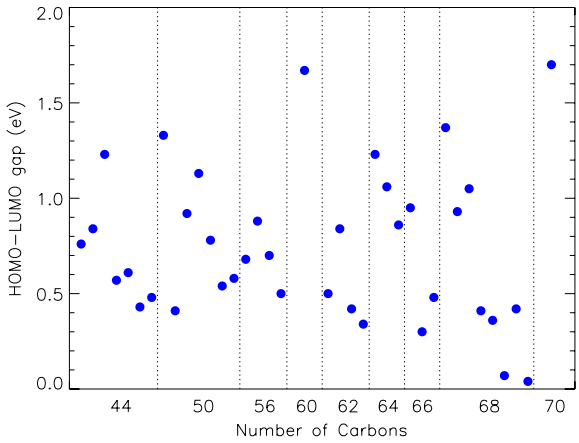

Figure 7.2: The HOMO–LUMO gaps of the isomers of neutral C_n cages we considered, calculated with the PBE/6-31G* method. The isomers are ordered and separated as in Fig. 7.1.

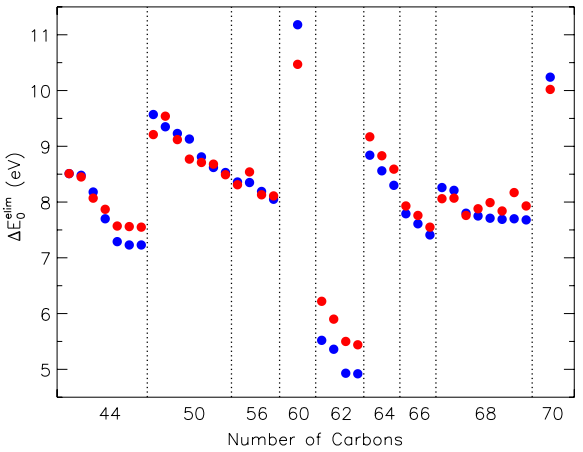

Figure 7.3: C_2 elimination energies of various isomers of C_n (blue circles) and C_n^+ cages (red circles) calculated by the B3LYP/6-31G* method using Eq. (7.3). For each n, the isomers are ordered by their increasing total energy. The order of stability for the C_n^+ cages is the same as for corresponding neutral fullerenes with the exception of $n = 66$ and 68 (see Table 7.1). Dashed vertical lines are drawn to guide the eye.

Figure 7.2 shows the calculated HOMO–LUMO gaps for neutral C_n cages. C_{60} and C_{70} have the largest gaps among the structures examined: 1.67 eV and 1.71 eV, respectively. The smallest gaps are close to zero (0.04 and 0.07 eV for isomers 6094 and 6146 of C_{68}). Note that, among the isomers with a given n, the structures with the largest HOMO–LUMO gaps are not always the most thermodynamically stable ones. Overall, the scatter of the $\Delta\epsilon_{\mathrm{HL}}$ values is considerably greater than that of the standard enthalpies of formation per bond, which suggests that kinetic and thermodynamic stabilities of C_n cages are not strongly correlated.

Figure 7.3 shows the C_2 elimination energies of C_n cages in their neutral and cationic forms. In line with their exceptional stability, neutral C_{60} and C_{70} require the highest energy ($\sim$11 eV) to remove a C_2 unit, followed closely by their cations. These results are in agreement with previous calculations and experimental data (Díaz-Tendero et al., 2003, 2006, and references therein). The next most stable cages according to this metric are C_{50} and C_{64}, while the C_{62} isomers are the least stable. This ordering is preserved for the respective cations. Generally, C_2 elimination energies of the C_n^+ cations are close to the $\Delta E_0^{\mathrm{elim}}$ values of the corresponding neutral C_n structures.

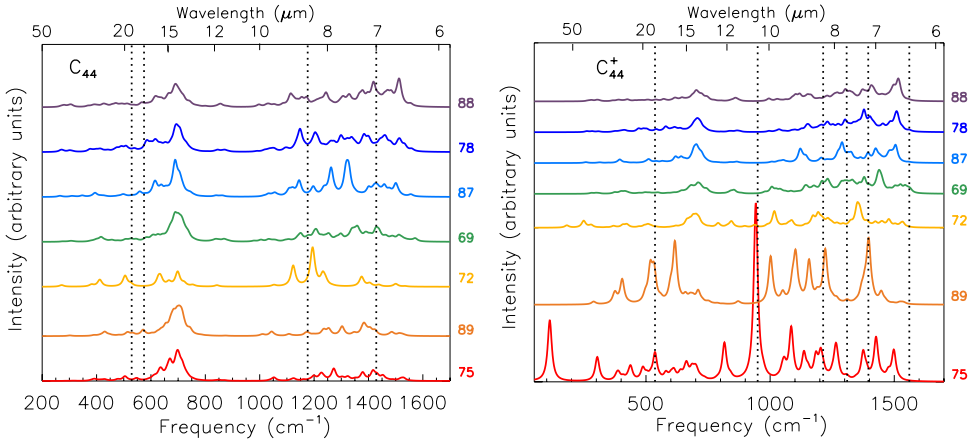

Figure 7.4: Simulated IR absorption spectra of the various isomers of neutral C_{44} (left panel) and of their cationic forms (right panel). The spectra are ordered from top to bottom by increasing standard enthalpy of formation of the neutral (see Table 7.1). The dotted lines show the positions of the IR-active modes of C_{60} at 7.0, 8.5, 17.4, and 18.9 μm (left) and C_{60}^+ at 6.4, 7.1, 7.5, 8.2, 10.4, and 18.9 μm (right).

7.3.2 Infrared spectra

The full collection of the simulated spectra of the fullerenes of Table 7.1 is displayed in Figs. 7.4–7.8. Machine-readable tables with the calculated spectra are available as Supplementary Material. At first glance, IR spectra of all neutral cages display many similarities. Most of the IR-active modes cluster in two spectral regions: 1540–1000 cm^{-1} (6.5–10 μm) for CC stretching modes and 800–550 cm^{-1} (12.5–18.2 μm) for carbon-skeleton breathing modes. This is consistent with the calculated spectra of smaller cages (n = 20, 24, 26, 28, and 30) reported by Adjizian et al. (2016). The extent of the first spectral region is almost constant within our set of spectra while the second is subject to variations. This is a consequence of the fact that the breathing modes are much more unique to each species; therefore, this wavelength range can be considered as a "fingerprint region" for individual species.

In several cases, IR active modes show up around 1000–900 cm^{-1} (10.0–11.1 μm), due to combinations of CC stretching and cage-breathing modes (see, for example, C_{50} and C_{68} in Figs. 7.5 and 7.8). No strong or moderately strong IR-active modes are found below 200 cm^{-1} (50 μm) and above 1600 cm^{-1} (6.25 μm). The detailed appearance of the IR spectrum depends on the specific molecular structure and is influenced by symmetry: the lower the symmetry, the larger the number of low-intensity

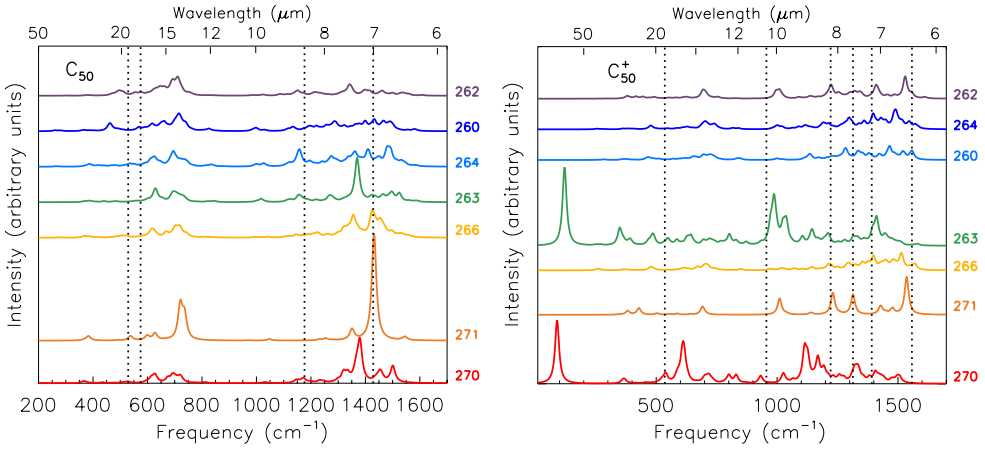

Figure 7.5: Same as in Fig. 7.4 but for C_{50} (left panel) and of their cationic forms (right panel).

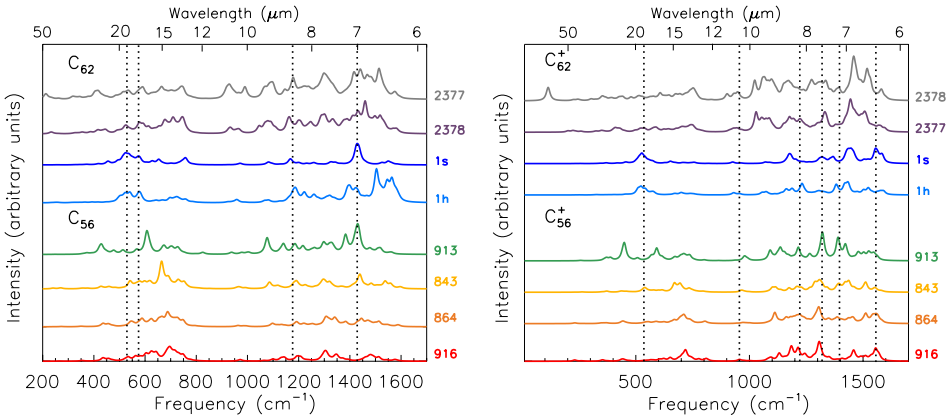

Figure 7.6: Same as in Fig. 7.4 but for C_{56} and C_{62} (left panel) and of their cationic forms (right panel).

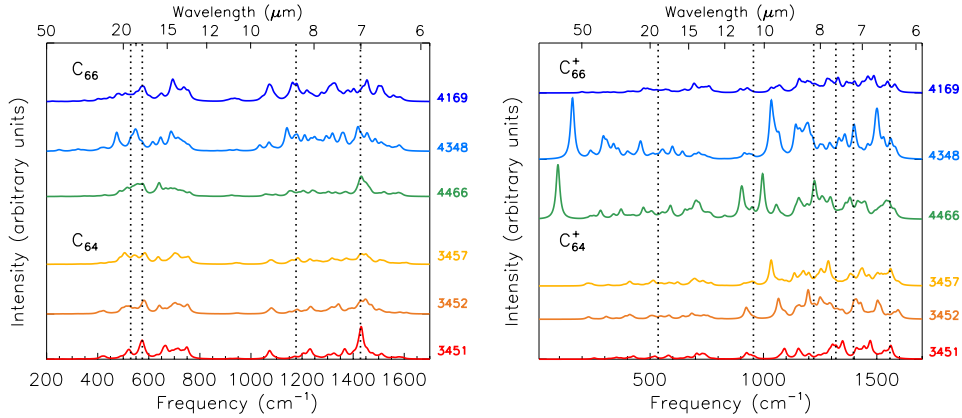

Figure 7.7: Same as in Fig. 7.4 but for C_{64} and C_{66} (left panel) and of their cationic forms (right panel).

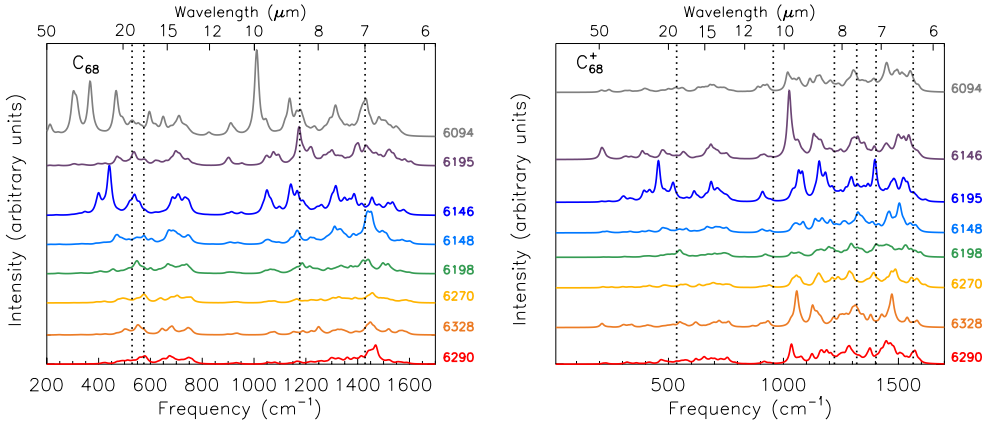

Figure 7.8: Same as in Fig. 7.4 but for C_{68} (left panel) and of their cationic forms (right panel).

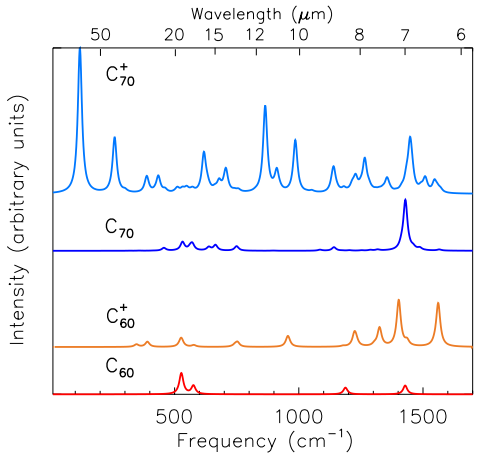

Figure 7.9: IR spectra of C_{60} (neutral in red and cation in orange) and C_{70} (neutral in blue and cation in light blue) calculated with the B3LYP/6-31G* method ($f_{\text{scale}} = 0.978$),

IR modes. This effect is exemplified by C_{50} isomers 271 (D_{5h}) and 260 (C_2) in the left panel of Fig. 7.5 – the 271 isomer has a much higher symmetry than the 260 isomer and consequently exhibits only a few strong bands whereas the 260 isomer shows a large number of weaker bands.

Neutral cages generally have the strongest IR transitions in the 665–714 cm^{-1} region (15.0–14.0 μm). Even when the strongest transition is not in this range, it always contains a group of superposed medium-intensity transitions, creating broad peaks above a what appears as a low-intensity plateau. Some notable exceptions are the highly symmetric C_{50} isomer 270 (D_{5h}) and C_{70} (D_{5h}), all showing their strongest mode around 7 μm (1430 cm^{-1}). Other low-symmetry neutral cages may show strong modes between 1540 and 1000 cm^{-1}, but then the integrated intensity in this region is comparable to that of the breathing mode region.

Few small cages ($n < 60$), but almost all of the larger ones, show strong modes close to the characteristic frequencies of C_{60}: 7.0, 8.5, 17.4, and 18.9 μm. For isomer 271 of C_{50} and for C_{70}, the band at 7.0 μm is the strongest in their spectra.

The spectra of the ionised cages resemble those of their neutral counterparts, but generally show enhanced CC stretching modes (1540–1000 cm^{-1}/6.6–10 μm). Comparing the calculated absolute intensities for neutral and ionised fullerene, one sees that this effect is due to a decrease of the intensity of the skeleton-breathing modes at longer wavelength. Moreover, there is a tendency for the modes to move to shorter wavelength (Adjizian et al., 2016). The effect of ionisation in fullerene thus mirrors

what is seen in other large conjugated system such as PAHs (e.g.,Bauschlicher et al. 2008).

Highly symmetric neutral C_n cages have degenerate but completely filled HOMOs, so they form nondegenerate ground states. After the removal of an electron, the HOMO-level degeneracy comes into play and the ionised cages spontaneously lower their symmetry due to the Jahn–Teller distortion (Jahn and Teller, 1937). C_{60} is particularly notable in that regard (Berné et al., 2013; Kern et al., 2013). The lower symmetry increases the complexity of the cation spectrum, as seen for instance in isomer 271 of C_{50}^+ (Fig. 7.5). In a few cases (including isomer 75 of C_{44}^+, C_{66}^+, and C_{70}^+), the IR spectrum predicted by B3LYP/6-31G* shows anomalously high IR intensities, often for very low energy modes, as well as a complete mismatch with the spectra of their neutral counterparts (see Section 7.3.3 for further discussion of this aspect). Until more experimental data are available, one should thus exercise caution when interpreting calculated vibrational spectra of cationic fullerene cages.

Finally, in our sample we have two non-classical isomers, a C_{62} isomer containing a square, 4-membered ring (1s) and a C_{62} isomer containing a 7-membered ring (1h). For isomer 1s, the spectrum has only a few modes with very low intensities involving the square motif and this does not change much upon ionisation. On the other hand, isomer 1h has medium-strong peaks at 1179, 1222, 1387, and 1391 cm^{-1} (8.52, 8.18, 7.21, and 7.19 μm) originating mostly from the stretching of the 7-membered ring. Also, C_{62}-1h is the only neutral cage in our sample showing strong signals below 1500 cm^{-1}, at 1504 cm^{-1} (6.65 μm), 1546 cm^{-1} (6.47 μm) and 1565 cm^{-1} (6.39 μm) (Fig. 7.6, left panel). While the first mode is due to a CC stretching in two pentagons sharing bonds with the heptagons, the last two originate from the stretching of the CC bond connecting two hexagons opposite of the 7-membered ring (Fig. 7.10). Upon ionisation, the modes involving the heptagon move slightly (10–20 cm^{-1}) to higher frequencies and preserve their intensities. The modes lower than 1500 cm^{-1} (6.67 μm) have decreased intensities by a factor of 2–3.

7.3.3 Challenges of computing the IR spectrum of C_{70}^+

Bauschlicher and Ricca (2010) documented the failure of the B3LYP functional for open-shell cationic PAHs including 5-membered rings. These authors suggested using the BP86 functional to verify the calculated frequencies and intensities. We followed their suggestion and calculated the BP86/6-31G* IR spectrum of C_{70}^+. Fig. 7.11 compares the experimental (Kern et al., 2016) and two calculated spectra of C_{70}^+ for the

correct structure of C_{2v} symmetry. The BP86 spectrum has an intense feature at 1000 cm^{-1} which is not observed in the experimental spectrum. In general, positions of the other modes are in better agreement with experimental values than for the B3LYP spectrum. Kern et al. (2016) reached a similar conclusion even if the symmetry of their structure was lower (C_s and C_i instead of C_{2v}). Popov et al. (2009) calculated the vibrational frequencies of C_{70}^+ with the PBE/TZ2P methods and his results are in better agreement with our BP86/6-31G* frequencies than with the B3LYP/6-31G* results. Interestingly, the strongest B3LYP/6-31G* peak at 121 cm^{-1} corresponds to the splitting of the E_2' mode of C_{70} which arises due to the Jahn–Teller distortion of C_{70}^+. Contributions from other spin multiplicity states can be ruled out, since the quadruplet lies 1.5 eV higher than the doublet. A possible explanation of these anomalous calculated spectra may lie in the breaking down of the Born–Oppenheimer approximation due to the presence of excited states at energies comparable to vibrational energies.

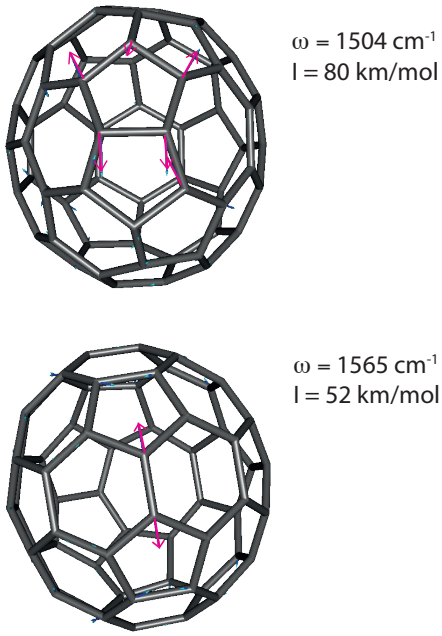

Figure 7.10: Calculated eigenvectors associated with two intense IR active modes in isomer 1h of C_{62}. In the top image the 7-membered ring is on the right hand side of the pentagons involved in the mode; in the bottom image the 7-membered ring can be seen on the back CC bond involved in the mode.

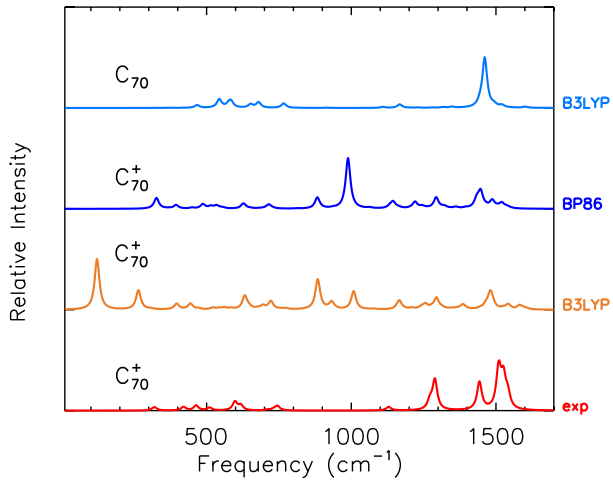

Figure 7.11: Comparison between the experimental IR spectrum of C_{70}^+ (red) obtained by Kern et al. (2016) and theoretical IR spectra calculated with B3LYP/6-31G* (orange) and BP86/6-31G* (blue) for the correct C_{2v} structure. The B3LYP/6-31G* spectrum of neutral C_{70} is also shown for comparison. The spectra are convolved with a Lorentzian function with a FWHM of 10 cm^{-1} and normalised to the strongest feature.

7.3.4 Comparison with astronomical observations

C_n cages with $n = 44$, 50, 56, 62, 64, and 68 are likely contributors to the IR emission of the astrophysical environments known to contain significant amounts of C_{60}. To assess the contribution of those structures, we compared their IR spectra to the observations of the three fullerene-rich PNe studied in Bernard-Salas et al. (2012): the galactic PN Tc 1, and SMP SMC 16 (SMC16 hereafter) and SMP LMC 56 (LMC56 hereafter) – similar objects in the Magellanic Clouds. These observations show C_{60} emission, whereas our theoretical calculations pertain to absorption spectra. The emission process for these species starts by absorption of a UV photon; this is followed by a rapid iso-energetic transition to the electronic ground state, but the process leaves the molecules in a highly excited vibrational state. Fluorescent IR emission then cools the molecule, and this is the emission that we observe. It is possible to carry out a full calculation for this IR fluorescent emission, but for our purposes, we will use an approximation that is simpler and faster to calculate. Indeed, the full fluorescence spectrum can be approximated by multiplying the calculated intensities by a Planck function at a well-chosen temperature; we used $T = 750$ K (see e.g. Bauschlicher et al., 2010). A full numerical fluorescence calculation would primarily differ in pro-

viding different relative intensities between the shortest and the longest wavelengt modes. Given the uncertainties associated with the intrinsic IR intensities and with the details of the emission mechanism, this approximation is thus justified for our purposes. We also convolved the resulting emission peaks with a Gaussian profile with a FWHM of 8 cm^{-1}, corresponding to the width of the observed C_{60} bands (Cami et al., 2010). Since the PNe mentioned above do not show any evidence of C_{60}^{+}, we focus our comparison on the neutral species.

The observed IR spectra of SMC16 and LMC56 have several features in the 770–665 cm^{-1} (13–15 μm) region*, where most of the C_n cages studied in this work show activity. Furthermore, the detailed structure of the peaks in the 6–8 μm range of the observed spectrum is well reproduced by the summed spectra of the small cages (Fig. 7.12). Nevertheless, the correlation between the observed and simulated spectra is too tenuous to prove the presence of any specific C_n cage in these astronomical objects. Such assignment are made especially challenging by the fact that the abundance of non-C_{60} cages is expected to be much lower than that of C_{60}; in addition, the intrinsic intensities of the IR-active modes of other fullerenes are lower than those of C_{60}. Thus, individual species should have very weak emission features at best.

If we cannot detect individual species, could we perhaps detect the spectral fingerprint of an entire cage population? Figure 7.13 shows simulated summed emission spectra of small and large C_n cages, in each case compared to the observational IR spectrum of SMC 16. The smaller cages show features in the 13–15 μm region, and intriguingly, the average spectrum of the smaller cages shows a weak, broad feature that coincides with a feature in both LMC 56 and SMC 16 without overpredicting the flux at any other wavelength (and note that for a lower temperature in our emission model, the emission peaks in the 6–9 μm region would weaken). It is thus conceivable that a population of smaller cages is indeed present in these objects, and the observations are compatible with such a population.

A similar average spectrum of the most stable larger cages (64 to 70 carbon atoms) also yields a small feature in the 13–15 μm region that is weaker and closer to 13 μm. The summed spectra also shows a mode around 7 μm (1728 cm^{-1}), which can be attributed to C_{50} (isomer 271) and C_{70}, and would overlap with the corresponding C_{60} band. Here too, the observations are compatible with a population of larger cages, but they offer no robust detection.

*We note that there is a well-known artifact of the Spitzer IR spectrograph between 13.2 and 14 μm, called the "teardrop", which shows up in observations through the SL1 module; the features discussed here however originate from the LL2 module and hence cannot be attributed to the teardrop artifact.

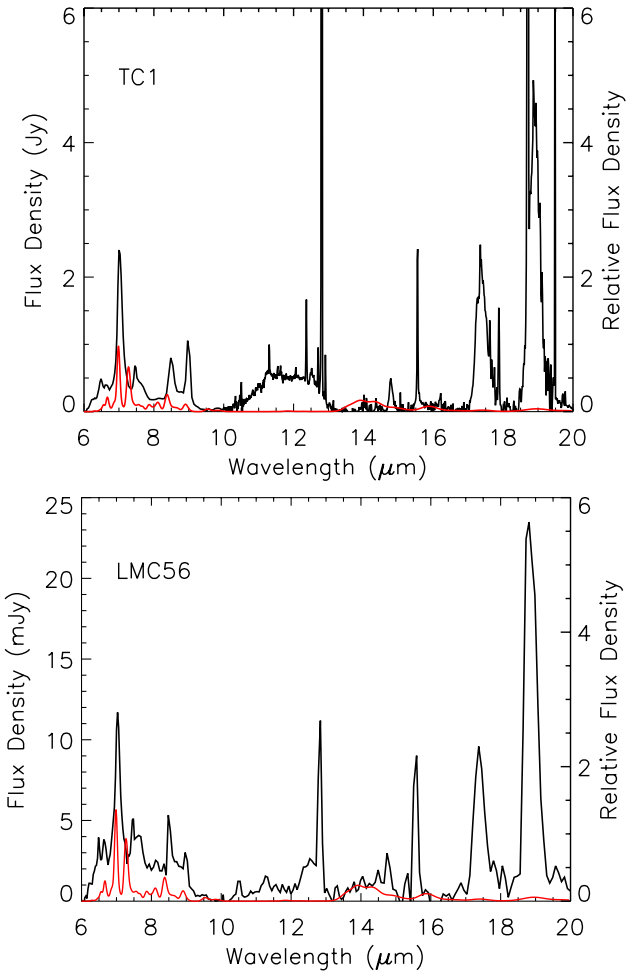

Figure 7.12: Observed Spitzer/IRS mid-IR spectra (black) of Tc 1 and SMC 56 (from Bernard-Salas et al. 2012) compared to the summed emission spectrum (red) of C_{44} (isomers 72, 75, 89), C_{50} (isomers 263, 270, 271), and C_{60}.

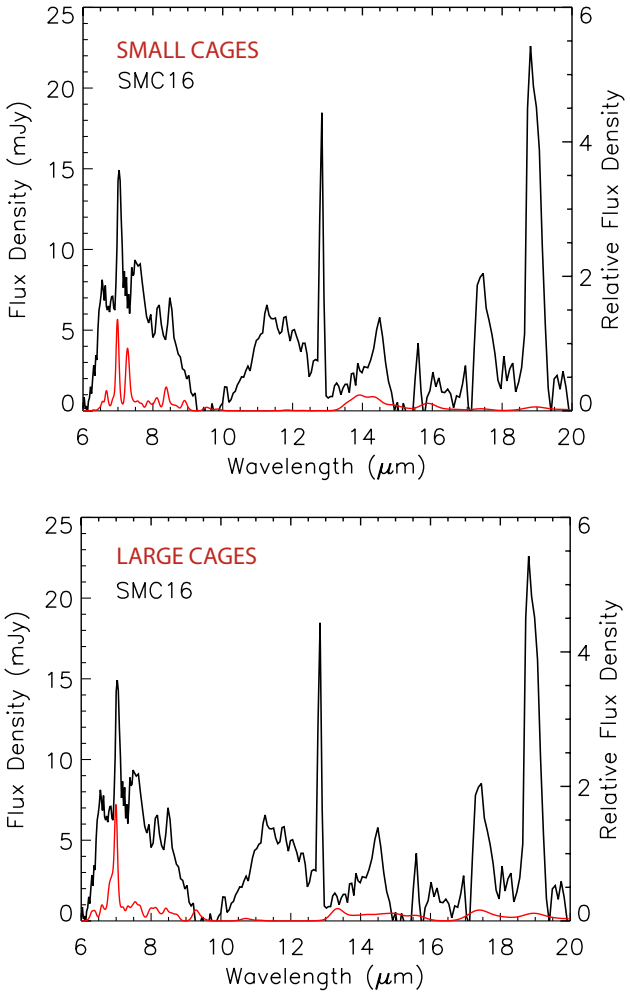

Figure 7.13: Top panel: Observed Spitzer/IRS mid-IR spectrum of SMC 16 (black) from Bernard-Salas et al. (2012) compared to the summed emission spectrum (red) of C_{44} (isomers 72, 75, 89), C_{50} (isomers 263, 270, 271), and C_{60}. Bottom panel: The same observational spectrum of SMC 16 compared to the summed emission spectrum of C_{64} (isomers 3451, 3452), C_{68} (isomers 6290, 6328, 6270), C_{60}, and C_{70}.

Finally, it is worth pointing out that the cages studied here have IR-active modes between 6-9 μm corresponding to a strong plateau that is seen underneath the emission features in all three astronomical objects. A population of smaller and/or larger cages could thus also be partly responsible for this plateau emission. On the other hand, little to no emission is seen in the 10-13 μm region, where another plateau appears in the observations. This emission plateau can thus not be due to fullerenes.

7.4 Conclusions

We have investigated the stability of fullerene cages with 44 to 70 carbon atoms and calculated their IR-active vibrational modes. The IR spectra of different isomers of the same species are similar, and therefore it is difficult to identify a specific isomer based on their IR spectra, except perhaps the highly symmetric species such as C_{50} isomer 271. The spectra of most stable isomers of the cages that are smaller than C_{60} all show features in the 13–15 μm range, where the astronomical spectra of fullerene-rich planetary nebulae also contain characteristic signals. We find that the astronomical observations are compatible with the presence of a population of fullerene cages, but offer no robust evidence for them. Better chances to identify these species will be possible when the James Webb Space Telescope, to be launched in 2021, will provide high-quality spectra of C_{60}-containing objects. The theoretical spectra presented here will be useful in interpreting those data. Finally, we want to emphasize that the presence of low-lying electronic states for the fullerene ions can greatly complicate matters when calculating the vibrational properties of these species with density-functional theory.

References

Adjizian, J.-J., Vlandas, A., Rio, J., et al., 2016, Philos. Trans. Roy. Soc. A, 374, 20150323
Albertazzi, E., Domene, C., Fowler, P. W., et al., 1999, Phys. Chem. Chem. Phys., 1, 2913
Alcamí, M., Sánchez, G., Díaz-Tendero, S., et al., 2007, J. Nanosci. Nanotechnol., 7, 1329
Allouche, A.-R., 2011, J. Comput. Chem., 32, 174
Ayuela, A., Fowler, P. W., Mitchell, D., et al., 1996, J. Phys. Chem., 100, 15634
Bauschlicher, C. W. and Ricca, A., 2010, Mol. Phys., 108, 2647
Bauschlicher Jr., C. W., Boersma, C., Ricca, A., et al., 2010, ApJS, 189, 341
Bauschlicher Jr., C. W., Peeters, E., and Allamandola, L. J., 2008, ApJ, 678, 316
Bernard-Salas, J., Cami, J., Peeters, E., et al., 2012, ApJ, 757, 41
Berné, O., Cox, N. L. J., Mulas, G., et al., 2017, A&A, 605, L1
Berné, O., Mulas, G., and Joblin, C., 2013, A&A, 550, L4
Berné, O. and Tielens, A. G. G. M., 2012, Proc. Nat. Acad. Sci. USA, 109, 401
Beu, T. A., Onoe, J., and Hida, A., 2005, Phys. Rev. B, 72, 155416

7.4. REFERENCES

Boersma, C., Rubin, R. H., and Allamandola, L. J., 2012, ApJ, 753, 168
Cami, J., Bernard-Salas, J., Peeters, E., et al., 2010, Science, 329, 1180
Cami, J., Peeters, E., Bernard-Salas, J., et al., 2018, Galaxies, 6, 101
Campbell, E. K., Holz, M., Gerlich, D., et al., 2015, Nat., 523, 322
Campbell, E. K., Holz, M., Maier, J. P., et al., 2016, ApJ, 822, 17
Castellanos, P., Berné, O., Sheffer, Y., et al., 2014, ApJ, 794, 83
Cordiner, M. A., Cox, N. L. J., Lallement, R., et al., 2017, ApJL, 843, L2
Díaz-Tendero, S., Alcamí, M., and Martín, F., 2003, J. Chem. Phys., 119, 5545
Díaz-Tendero, S., Sánchez, G., et al., 2006, Int. J Mass Spectr., 252, 133
Dunk, P. W., Kaiser, N. K., Hendrickson, C., et al., 2012, Nat. Commun., 3, 855
Evans, A., van Loon, J. T., Woodward, C. E., et al., 2012, MNRAS, 421, L92
Fowler, P. and Manolopoulos, D. (1995). *An Atlas of Fullerenes*. Oxford: Clarendon press.
Frisch, M. J., Trucks, G. W., Schlegel, H. B., et al. (2009). *Gaussian 09, Revision D.01*. Gaussian Inc., Wallingford CT, 2009.
Frum, C. I., Engleman Jr., R., Hedderich, H. G., et al., 1991, Chem. Phys. Lett., 176, 504
García-Hernández, D. A., Iglesias-Groth, S., Acosta-Pulido, J. A., et al., 2011, ApJL, 737, L30
García-Hernández, D. A., Kameswara Rao, N., and Lambert, D. L., 2011, ApJ, 729, 126
García-Hernández, D. A., Manchado, A., García-Lario, P., et al., 2010, ApJL, 724, L39
García-Hernández, D. A., Villaver, E., García-Lario, P., et al., 2012, ApJ, 760, 107
Gielen, C., Cami, J., Bouwman, J., et al., 2011, A&A, 536, A54
Jäger, C., Huisken, F., Mutschke, H., et al., 2009, ApJ, 696, 706
Jahn, H. A. and Teller, E., 1937, Proc. Roy. Soc. A, 161, 220
Kern, B., Böttcher, A., and Strelnikov, D., 2016, J. Phys. Chem. A, 120, 5868
Kern, B., Strelnikov, D., Weis, P., et al., 2013, J. Phys. Chem. A, 117, 8251
Kremer, R. K., Rabenau, T., Maser, W. K., et al., 1993, Appl. Phys. A, 56, 211
Kroto, H. W., 1987, Nat., 329, 529
Lallement, R., Cox, N. L. J., Cami, J., et al., 2018, A&A, 614, A28
Langhoff, S. R., 1996, J. Phys. Chem., 100, 2819
Manolopoulos, D. E., May, J. C., and Down, S. E., 1991, Chem. Phys. Lett., 181, 105
Micelotta, E. R., Jones, A. P., Cami, J., et al., 2012, ApJ, 761, 35
Nemes, L., Ram, R. S., Bernath, P. F., et al., 1994, Chem. Phys. Lett., 218, 295
Peeters, E., Tielens, A. G. G. M., Allamandola, L. J., et al., 2012, ApJ, 747, 44
Perdew, J. P., Burke, K., and Ernzerhof, M., 1996, Phys. Rev. Lett., 77, 3865
Popov, A. A., Burtsev, A. V., Senyavin, V. M., et al., 2009, J. Phys. Chem. A, 113, 263
Qian, W., Bartberger, M. D., Pastor, S. J., et al., 2000, J. Am. Chem. Soc., 122, 8333
Roberts, K. R. G., Smith, K. T., and Sarre, P. J., 2012, MNRAS, 421, 3277
Rohlfing, E. A., Cox, D. M., and Kaldor, A., 1984, J. Chem. Phys., 81, 3322
Sánchez, G., Díaz-Tendero, S., Alcamí, M., et al., 2005, Chem. Phys. Lett., 416, 14
Schwerdtfeger, P., Wirz, L., and Avery, J., 2013, J. Comput. Chem., 34, 1508
Sellgren, K., Werner, M. W., Ingalls, J. G., et al., 2010, ApJL, 722, L54
Stephens, P. J., Devlin, F. J., Chabalowski, C. F., et al., 1994, J. Phys. Chem., 98, 11623
Tielens, A. G. G. M., 2008, ARA&A, 46, 289
Walker, G. A. H., Bohlender, D. A., Maier, J. P., et al., 2015, ApJL, 812, L8
Walker, G. A. H., Campbell, E. K., Maier, J. P., et al., 2016, ApJ, 831, 130
Walker, G. A. H., Campbell, E. K., Maier, J. P., et al., 2017, ApJ, 843, 56
Wang, Y., Díaz-Tendero, S., Alcamí, M., et al., 2015, Nature Chem., 7, 927
Zhang, Y. and Kwok, S., 2011, ApJ, 730, 126
Zhen, J., Castellanos, P., Paardekooper, D. M., et al., 2014, ApJL, 797, L30
Zimmerman, J. A., Eyler, J. R., Bach, S. B., et al., 1991, J. Chem. Phys., 94, 3556

Nederlandse samenvatting

De ruimte tussen sterren, het interstellair medium (ISM) is gevuld met sterk verdunde materie dat bestaat uit atomen, moleculen en vaste stoffen (interstellair stof). Als gevolg van verstoringen in dichtheid en temperatuur, kan deze materie lokaal onder haar eigen zwaartekracht instorten, wat resulteert in de vorming van wolken met een hogere dichtheid, ook wel moleculaire wolken genoemd. In moleculaire wolken ontstaan sterren en planeten. (zie figuur 1). Vanaf het begin van hun vorming tot aan hun "dood" doorlopen sterren verschillende evolutiestadia, gekenmerkt door verschillende temperaturen, dichtheden, verdeling van materiaal rond sterren en interactie met hun omgeving. Deze verschillende omstandigheden beïnvloeden de chemie die plaatsvindt in de verschillende evolutiestadia van sterren. De analyse van de moleculaire samenstelling van objecten in verschillende stadia maakt het mogelijk om niet alleen de chemie en chemische evolutie in buitenaardse omgevingen te begrijpen, maar ook de fysische omstandigheden in deze omgevingen, en de structuur en vorming van objecten gedurende de levenscyclus van sterren.

In de dichte en beschutte gebieden van moleculaire wolken kan de temperatuur dalen tot 10 K ($\sim$ 263°C). Bij zulke lage temperaturen blijven atomen en moleculen uit de gasfase aan het oppervlak van interstellaire stofdeeltjes kleven. Stofdeeltjes worden bedekt door bevroren materiaal. Dit materiaal, bekend als interstellair ijs, speelt een belangrijke rol bij de vorming van zowel kleine als grote moleculen in het ISM. Op deze bevroren oppervlakken bevinden zich moleculen en atomen dicht bij elkaar, wat chemische reacties mogelijk maakt die anders niet zouden plaatsvinden, aangezien botsingen in de gasfase onder ISM-omstandigheden niet vaak voorkomen. Bovendien absorbeert het vaste materiaal energie die vrijkomt bij chemische reacties, fungeert het dus als een derde lichaam en stabiliseert het daarmee de vorming van grotere moleculen. Talrijke laboratorium- en theoretische onderzoeken naar astrochemische processen in de vaste toestand hebben aangetoond dat een breed scala aan moleculen kan worden gevormd onder de omstandigheden in koude moleculaire wolken. Deze moleculen variëren van eenvoudige soorten zoals moleculaire waterstof (H_2), water (H_2O) en koolstofdioxide (CO_2) tot complexe organische moleculen (COM's - door astronomen beschouwd als moleculen met een koolstof-waterstofbinding en minstens

Figure 1: De rand van een stervormingsgebied (NGC 3324) binnen de Carinanevel. Dit is een van de eerste opnames die zijn gemaakt met het NIRCam-instrument aan boord van de James Webb Space Telescope (JWST) en toont de rand van een holte in NGC 3324, waar zware sterren zijn geboren. Het oppervlak van de wolk, weergegeven in rode tinten, wordt weggeduwd door de straling van de nieuw gevormde sterren. De meeste rode en gele kleine puntjes die in het rood gearceerde gebied verschijnen, zijn protosterren (sterren die nog aan het ontstaan zijn) in de wolk. Het binnenste van de moleculaire wolk biedt een beschutte omgeving die de moleculaire bestanddelen beschermt tegen de effecten van de straling die wordt uitgezonden door naburige sterren.

zes atomen), zoals methanol (CH_3OH), grotere alcoholen, suikers en aminozuren, die als essentiële moleculen voor het ontstaan van leven worden beschouwd. Interstellair ijs herbergt dus een reservoir van organische moleculen in de ruimte.

Tijdens de vorming van sterren, klonteren interstellair stof en ijs samen en vormen grotere vaste agglomeraten die uiteindelijk rotsachtige lichamen zoals kometen, manen en planeten vormen. Als de interstellaire ijsmoleculen het instortings- en accretieproces overleven, kunnen ze worden opgenomen in de vaste lichamen van het zich ontwikkelende planetaire systeem. Om deze redenen is het aannemelijk dat een deel van de organische moleculen in planetenstelsels zijn gevormd voor de sterren. De hoeveelheid interstellair ijs dat zich in planetenstelsels bevindt is onbekend. Tijdens het begin van de vorming van een ster kan het interstellaire ijs in de wolk opwarmen, hierdoor sublimeren moleculen uit het vaste ijs. De gesublimeerde moleculen in de gasfase kunnen worden gedetecteerd met behulp van gevoelige submillimeter- en ra-

diotelescopen zoals de Atacama Large Millimeter/Submillimeter Array (ALMA) en de Green Bank Telescope (GBT).

Onze kennis van interstellaire chemie gedurende de levenscyclus van sterren is vooruitgegaan dankzij de detectie en bestudering van moleculen met behulp van verschillende telescopen die diverse astronomische omgevingen hebben geobserveerd. Deze omvatten zowel telescopen op aarde als ruimtetelescopen en bestrijken een groot deel van het elektromagnetische spectrum. Op dit moment worden de eerste waarnemingen van de James Webb Space Telescope (JWST) aan de wereld onthuld. De op 25 december 2021 gelanceerde JWST levert sind de zomer van 2022 waarnemingsgegevens. De JWST maakt astronomische waarnemingen in infrarood (IR) straling mogelijk van ongeveer 0,6 tot 28 μm met een ongekende gevoeligheid en ruimtelijke resolutie, die de gevoeligheid van eerdere IR telescopen overtreft. De JWST is bij uitstek geschikt om interstellair ijs te bestuderen, zowel wat betreft spectraal bereik, spectrale resolutie en scheidend vermogen, waardoor het mogelijk is geworden om de verdeling van interstellair ijs over moleculaire wolken te bestuderen. Om moleculen in de nieuwe JWST-waarnemingen nauwkeurig te identificeren, is het echter essentieel om voorkennis te hebben van de IR-spectra van bevroren moleculen. Het voornaamste doel van **dit proefschrift** is het experimenteel onderzoeken van IR-spectra van moleculen gevonden in de ISM, met een specifieke nadruk op COM's in interstellair en circumstellair ijs.

Hoe "zien" we interstellair ijs?

Moleculen die aanwezig zijn in interstellair ijs kunnen worden geïdentificeerd door hun absorptie van IR-straling. Wanneer moleculen IR-straling van specifieke energieën absorberen, dat wil zeggen op specifieke golflengten, trillen ze. De karakteristieke IR-frequenties waarop een molecuul kan absorberen, zijn afhankelijk van zijn structuur en vormen daarom een kenmerkend patroon dat werkt als een moleculaire vingerafdruk. IR-spectroscopie is een veelgebruikt hulpmiddel in chemische laboratoria om moleculen te identificeren. Om het IR-spectrum van een chemisch monster te meten, bestraalt een IR-stralingsbron het monster en wordt met een detector gekeken welke IR-frequentie worden geabsorbeerd in licht van een IR-stralingsbron dat het monster heeft doorkruist. Hierdoor kan de moleculaire samenstelling van het monster worden bepaald. In een laboratoriumomgeving worden verschillende stralingsbronnen gebruikt om IR-straling te genereren, en in de ruimte dienen sterren achter een moleculaire wolk of een jong stellair object (YSO) als een "interstellaire infraroodlamp". Door de

absorptiekarakteristieken van een astronomisch spectrum te vergelijken met de referentiespectra van moleculen vastgelegd in een laboratorium, kunnen de samenstelling en eigenschappen van interstellair ijs worden bepaald. Samengevat, door de absorptie van IR-straling te onderzoeken, kunnen astronomen moleculen in interstellair ijs waarnemen en identificeren. Dit is een eerste vereiste om te begrijpen welke rol het interstellaire ijs speelt in de kosmochemische evolutie van materie en hoe dit uiteindelijk bijdraagt aan de chemische samenstelling van vaste rotslichamen (bijvoorbeeld kometen en planeten).

Tot op heden zijn slechts een handvol moleculen waargenomen en ondubbelzinnig geïdentificeerd in interstellair ijs, dit zijn H_2O, CO_2, CO, CH_4, NH_3, CH_3OH, OCS, OCN^-, $^{13}CO_2$ en ^{13}CO. Voor verschillende andere soorten, zoals NH_4^+ en grotere organische moleculen, zijn voorlopige identificaties gemeld, maar een definitieve toekenning was niet mogelijk. Dit staat in schril contrast met het veel grotere aantal moleculen dat in de ISM in de gasfase is geïdentificeerd, wat neerkomt op bijna 300 moleculen. Ook opmerkelijk is het feit dat de enige COM die in interstellair ijs werd gedetecteerd, methanol is. Dit is verrassend omdat interstellair ijs wordt beschouwd als de locatie waar grotere organische moleculen (zoals gevonden in de gasfase) ontstaan. Deze moleculen zijn niet gedetecteerd omdat de identificatie van organische moleculen in interstellair ijs een grote uitdaging is. Allereerst komen COM's niet in grote hoeveelheden voor, doorgaans worden hoeveelheden van enkelen procenten ten opzichte van H_2O verwacht. Bij deze hoeveelheden zijn slechts een beperkt aantal absorptie kenmerken van de COM's sterk genoeg om te worden geïdentificeerd. Gezien deze hoeveelheden zijn slechts enkele trillingskenmerken in IR sterk genoeg om te worden gedetecteerd met de gevoeligheid van eerdere telescopen. Dit maakt het mogelijk om een familie van COM's te identificeren, maar zelden een individuele soort toe te wijzen. Bovendien worden de spectrale karakteristieken van moleculen in de vaste toestand beïnvloed door factoren zoals ijstemperatuur, naburige moleculen en de structuur van interstellair ijs. Om de fysische en chemische omstandigheden te bepalen waaronder deze moleculen zich in de ruimte vormen zijn laboratoriumspectra van moleculen onder verschillende fysische omstandigheden (zoals temperatuur) en chemische samenstellingen nodig.

Interstellair ijs in het laboratorium: IRASIS

Interstellair ijs wordt aangetroffen in gebieden van de ISM die worden gekenmerkt door gasdichtheden variërend van ongeveer 10^3 tot 10^6 deeltjes/cm^3 en temperaturen

van ongeveer 10 tot 150 K (-263°C tot -123°C). Deze gasdichtheden en temperaturen zijn aanzienlijk lager dan de gasdichtheid van de aardatmosfeer (ongeveer 10^{19} deeltjes/cm^3) en zijn temperatuur. Voor het creëren van interstellaire ijsanalogen zijn experimentele opstellingen nodig die vacuüm en zeer koude omstandigheden creëren. Het Laboratorium voor Astrofysica van de Sterrenwacht Leiden gebruikt verschillende opstellingen om de omstandigheden in de ISM na te bootsen. In dit proefschrift gebruik ik twee opstellingen, IRASIS (InfraRed Absorption Setup for Ice Spectroscopy, zie figuur 2) en OASIS (Optical Absorption Setup for Ice Spectroscopy). IRASIS wordt gebruikt om hoge resolutie IR-spectra te meten van interstellaire ijsanalogen. IRASIS bestaat uit een ultrahoge[†] vacuümkamer met in het midden een IR-transparant monstersubstraat, dat wordt gebruikt voor het laten groeien van de ijsmonsters. Het substraat is thermisch verbonden met een cryokoeler en kan worden gekoeld tot temperaturen zo laag als 15 K. Gasvormige mengsels die de te onderzoeken moleculen bevatten, kunnen in de vacuümkamer worden gebracht. Wanneer de moleculen het koude substraat raken, blijven ze eraan plakken (adsorberen) en vormen een laag bevroren materiaal, de interstellaire ijsanaloog. Door IR-straling op dit bevroren materiaal te laten schijnen, kan de lichtabsorptie van de verschillende moleculen worden vastgelegd en bestudeerd. Naast de IR-spectra wordt de hoeveelheid geabsorbeerde straling per ijshoeveelheid gekwantificeerd, waardoor de bandsterkte van een moleculaire absorptie band kan worden bepaald. De bandsterkte is een belangrijke parameter voor astronomen, omdat het ook mogelijk is om moleculen in astronomische spectra te kwantificeren. Alle spectroscopische data die in dit proefschrift worden gepresenteerd, zijn openbaar beschikbaar via LIDA, de Leidse ijsdatabase voor astrochemie.

De OASIS-opstelling wordt gebruikt om de interactie van zichtbaar licht en ultraviolet straling met ijsmonsters te onderzoeken. De opstelling bestaat uit een vacuümkamer met in het centrum een reflecterende spiegel die is bevestigd op het koude element van een cryokoeler. IJsmonsters van enkele micrometers dik kunnen op het spiegeloppervlak worden gegroeid en worden verlicht met zichtbaar licht en ultraviolet straling van een Xenon-booglamp (met een bereik van 250-750 nm) en een rode HeNe-laserstraal (632,8 nm). De straling van deze bronnen wordt gedeeltelijk gebroken in het ijsmateriaal en gedeeltelijk gereflecteerd door het ijsoppervlak. Het interferentiepatroon dat wordt gevormd door de straling in het ijsmonster te laten schijnen, wordt tijdens en na de ijsgroei geregistreerd door een fotodetector (voor het laserlicht) en een spectrometer (voor de Xe-booglamp). De analyse van het interferentiepatroon tijdens ijsgroei maakt het mogelijk de brekingsindex van het materiaal in het bereik van 250 - 750 nm

[†]De druk is lager dan 10^{-5} Pa

te bepalen. De analyse van het interferentiepatroon na de ijsgroei maakt het mogelijk om structurele veranderingen van het ijs te volgen. Details van beide experimentele opstellingen zijn te vinden in hoofdstuk 2.

Figure 2: Een foto van IRASIS, de experimentele opstelling gewijd aan het bestuderen van de IR-spectra van interstellaire ijsanalogen

Over dit proefschrift

Hoofdstukken 3, 4 en 5 van dit proefschrift zijn gebaseerd op werk met IRASIS en beschrijven het onderzoek naar de absorptie-eigenschappen van drie belangrijke organische moleculen in de astronomie: aceton (CH_3COCH_3), methylamine (CH_3NH_2), en methylcyanide (CH_3CN). Deze moleculen zijn gedetecteerd in de gasfase in verschillende astronomische omgevingen en er wordt aangenomen dat hun vormingsroutes plaatsvinden in de vaste toestand. Deze studies analyseren de veranderingen in het IR-absorptieprofiel wanneer deze gemengd zijn met typische andere interstellaire ijscomponenten (zoals H_2O, CO_2, CO) en voor temperaturen tussen 15 - 160 K. Bovendien worden de brekingsindex en bandsterktes van deze moleculen gemeten, wat belan-

grijke parameters oplevert om te vergelijken met astronomische waarnemingen. De laboratoriummetingen worden vergeleken met eerdere interstellaire ijswaarnemingen met telescopen zoals Spitzer en ISO. Deze vergelijkingen helpen om de hoeveelheid van deze moleculen in interstellair ijs af te bakenen.

Naast de interacties met IR-straling kunnen de eigenschappen van bevroren materiaal met zichtbaar licht en ultraviolet straling in het laboratorium worden gesimuleerd. Deze eigenschappen zijn erg belangrijk voor de studie van bevroren oppervlakken in het zonnestelsel (dat wil zeggen, ijzige manen), die constant straling van de zon ontvangen. Hoofdstuk 6 rapporteert de studie van de interactie van licht in het golflengtebereik van 250 - 750 nm met μm dik CO_2-ijs met behulp van OASIS. Door het licht te volgen dat door deze dikke ijslagen wordt gereflecteerd, is het mogelijk om de overgang te onderzoeken tussen verschillende ijsstructuren.

Hoofdstuk 7 van dit proefschrift presenteert een theoretische studie die de stabiliteit en trillingsabsorptie van fullerenen onderzoekt. Deze unieke moleculen, die uitsluitend uit koolstofatomen bestaan, vertonen een kooiachtige structuur. In de ISM zijn C_{60}, C_{70} en C_{60}^+ geïdentificeerd in de gasfase in verschillende astronomische omgevingen. Hun aanwezigheid roept intrigerende vragen op over het mogelijke bestaan van andere fullereenkooien in de ruimte. Het meten van het IR-spectrum van deze moleculen door middel van experimenten is moeilijk, dus worden numerieke kwantummechanicamethoden gebruikt om de elektronische structuur en eigenschappen van dergelijke moleculen, inclusief hun trillingsfrequenties, te berekenen. In hoofdstuk 7 wordt dichtheidsfunctionaaltheorie (DFT) gebruikt om de trillingsfrequentie van fullereenkooien bestaande uit 44 tot 70 koolstofatomen te berekenen. De berekende spectra worden vervolgens vergeleken met het astronomische spectrum van planetaire nevels, waardoor de mogelijke aanwezigheid van deze moleculen kan worden onderzocht.

De belangrijkste conclusies van dit proefschrift zijn als volgt:

I) Om interstellaire ijswaarnemingen te begrijpen, is het cruciaal om nauwkeurige laboratoriummetingen van moleculen uit te voeren onder astronomische omstandigheden. Door de waarnemingen te vergelijken met spectra die in het laboratorium onder verschillende omstandigheden zijn verkregen, kunnen we informatie bepalen over de temperatuur en mate van vermenging van de interstellaire ijscomponenten. In de hoofdstukken 3, 4 en 5 van dit proefschrift is spectroscopisch werk verricht om toekomstige zoektochten naar aceton, methylamine en methylcyanide in interstellaire ijswaarnemingen met JWST mogelijk te maken. Uit de spectrale analyse van deze moleculen volgen de volgende conclusies:

- De absorptiebanden bij 5,85, 7,34 en 8,14 μm hebben het grootste potentieel om aceton te identificeren in interstellaire ijswaarnemingen.

- De identificatie van methylamine-absorptiebanden in interstellair ijs is een uitdaging, omdat de belangrijkste absorptiekenmerken zich voordoen in hetzelfde gebied als die van H_2O en NH_3. Met dit voorbehoud hebben de absorptie banden rond van 3,45 en 8,62 μm het meeste potentieel om methylamine te identificeren in ijswaarnemingen. De bovengrens voor methylamine in de richting van YSO's wordt geschat op ongeveer $\leq$ 4% met betrekking tot vast H_2O, met behulp van de 3,45 μm absorptie piek.

- De combinatie van de 4,44 en 9,60 μm kenmerken zijn het beste om methylcyanide in interstellair ijs te identificeren. Met behulp van deze kenmerken wordt de hoeveelheid methylcyanide in de richting van YSO's geschat op enkele tot $\leq$ 4,1% ten opzichte van vast H_2O.

II) IJsstructuurovergangen na de afzetting van μm-dik CO_2-ijs kunnen de verstrooiingseigenschappen veranderen. Een vers afgezet CO_2-ijsmonster verstrooit licht in het golflengtebereik van 250 - 750 nm. Na een bepaalde periode leiden spontane ijstructuurovergangen tot een transparante ijsstructuur. De snelheid waarmee deze overgangen plaatsvinden, wordt beïnvloed door de dikte van het ijsmonster en de temperatuur waarbij het werd afgezet. Bij ijsmonsters van slechts enkele micrometers dik kunnen deze overgangen enkele uren tot dagen duren. Hoewel dit onbeduidend is in vergelijking met astronomische tijdschalen, is het een belangrijke factor waarmee rekening moet worden gehouden bij het bestuderen van CO_2-ijs in een laboratoriumomgeving.

III) Fullerenen bestaande uit 44 tot 70 koolstofatomen hebben IR-pieken tussen 6 – 9 μm die kunnen bijdragen aan het waargenomen emissieprofiel in de richting van fullereenrijke planetaire nevels. Hun trillingsspectra alleen kunnen het emissieplateau van 10 - 13 μm dat in deze objecten wordt waargenomen, niet verklaren.

Sumário em Português

O espaço entre as estrelas, ou meio interestelar (MI), é preenchido com um material rarefeito que consiste de átomos, moléculas e partículas sólidas (poeira interestelar). Em resposta a perturbações nesse meio, esse material pode colapsar gravitacionalmente, resultando na formação de estruturas mais densas, conhecidas como nuvens moleculares. As nuvens moleculares são o local onde estrelas e planetas se formam (ver Figura 3). Ao longo de todo o seu processo evolutivo, que começa com a sua formação e termina com a sua "morte", as estrelas passam por diversos estágios evolutivos. Em cada um desses estágios, fatores como a temperatura do meio e o campo de radiação ao redor da estrela apresentam variações significativas. Como resultado, a composição molecular do material nas proximidades da estrela (ou protoestrela, no caso de estrelas em formação) varia durante todo o ciclo de vida estelar. A investigação da composição molecular de objetos nesses diferentes estágios possibilita a compreensão não somente da evolução química em ambientes extraterrestres, mas também das condições físicas presentes nesses ambientes, e da estrutura e formação de objetos em diferentes etapas do ciclo de vida das estrelas.

Nas regiões densas e protegidas de nuvens moleculares, a temperatura pode chegar a 10 K ($\sim$ 263°C). Nessas temperaturas, átomos e moléculas da fase gasosa aderem à superfície dos grãos de poeira interestelar, revestindo-os com uma camada de material congelado. Este material, conhecido como gelo astrofísico, tem um papel importante na química do MI. Na superfície do gelo astrofísico, átomos e moléculas enctrontram-se próximos uns aos outros, o que facilita reações químicas que não ocorreriam de outra forma, uma vez que colisões na fase gasosa são raras no MI . Além disso, o material sólido (gelo e poeira) absorve a energia que é liberada nas reações químicas, estabilizando a formação de moléculas maiores. Vários estudos experimentais e teóricos que exploraram processos astroquímicos no estado sólido revelaram que uma gama de moléculas pode ser sintetizada sob condições frias análogas às encontradas no interior de nuvens moleculares. Essas moléculas variam desde especies mais simples, como hidrogênio molecular (H_2), água (H_2O) e dióxido de carbono (CO_2), até moléculas orgânicas complexas (COMs, do inglês *Complex Organic Molecules* - consideradas pelos astrônomos como moléculas contendo uma ligação C-H e no mínimo seis átomos),

como metanol (CH_3OH), outros álcoois, açúcares e aminoácidos, que são moléculas consideradas essenciais para a vida como a conhecemos. Assim, o gelo astrofísico é considerado um reservatório de moléculas orgânicas no espaço.

Figure 3: Região de formação estelar (NGC 3324) na nebulosa da Carina. Esta é uma das primeiras imagens obtidas com o instrumento NIRCam do Telescópio Espacial James Webb (JWST) e mostra uma região em NGC 3324 onde estrelas massivas acabaram de se formar. A superfície da nuvem, representada em tons de vermelho, está sendo empurrada pela radiação das estrelas recém-formadas. A maioria dos pontinhos amarelos que aparecem na região sombreada de vermelho são objetos estelares jovens (estrelas ainda não maduras) dentro da nuvem.

Durante o processo de formação estelar, o material solido presente na nuvem coagula, formando aglomerados que podem resultar na formação de corpos rochosos maiores, como cometas, luas e planetas. Se as moléculas de gelo astrofísico sobreviverem ao processo de colapso da nuvem molecular e coagulação dos grãos, elas podem ser incorporadas a esses corpos rochosos do sistema planetário em desenvolvimento. Por essas razões, é provável que parte da matéria orgânica de um sistema planetário tenha sua origem química na fase pré-estelar. Também durante o processo de formação estelar, os grãos de poeira podem ser aquecidos, o que resulta na sublimação do gelo astrofísico. As moléculas formadas no gelo, agora na fase gasosa, podem ser detectadas através de observações astronômicas na faixa de comprimentos de onda submilimétricos e em rádio, usando telescópios como o *Atacama Large*

Millimeter/Submillimeter Array (ALMA) e o *Green Bank Telescope* (GBT).

Os avanços no conhecimento da química interestelar se devem, em grande parte, à detecção de moléculas no MI por meio de diferentes telescópios. Esses telescópios, terrestres e espaciais, cobrem uma ampla gama do espectro eletromagnético. O Telescópio Espacial James Webb (JWST, do inglês *James Webb Space Telescope*) foi lançado em 25 de dezembro de 2021 e fornece dados observacionais desde julho de 2022. O JWST é um telescópio que realiza observações em comprimentos de onda no infravermelho (IV), cobrindo a faixa de 0.6 a 28 μm. Com sensibilidade maior que outros telescópios no IV e alta resolução espacial e espectral, o JWST é capaz de detectar as assinaturas espectrais de moléculas orgânicas complexas em observações de gelos astrofísicos. Identificar essas moléculas em vários ambientes astronômicos fornecerão informações sobre como e onde as moléculas orgânicas são formadas no espaço. No entanto, para identificar com precisão as moléculas nas observações do JWST, é essencial ter conhecimento prévio dos espectro IV das moléculas estudadas. O foco principal **dessa tese** é investigar experimentalmente o espectro IV de moléculas encontradas no MI, com ênfase em moléculas orgânicas complexas que são esperadas estar presentes em gelos astrofísicos.

Como observamos gelos astrofísicos?

Moléculas presentes em gelos astrofísicos são identificadas através de seus padrões de absorção de luz infravermelha. Quando moléculas absorvem radiação IV de energias específicas, ou seja, em comprimentos de onda específicos, elas vibram. As frequências específicas no IV nas quais uma molécula pode absorver dependem de sua estrutura e, portanto, constituem um padrão característico que funciona como uma impressão digital molecular. Isso torna a espectroscopia IV uma ferramenta amplamente usada em laboratórios de química analítica. Para medir o espectro infravermelho de uma amostra, essa deve ser iluminada por uma fonte de luz IV. Detectores de radiação IV, posicionados entre a amostra e a fonte de luz, medem a quantidade de luz absorvida pela amostra em função do comprimento de onda. No laboratório, diferentes fontes de luz são usadas para gerar radiação IV, enquanto no MI, estrelas maduras e estrelas em formação (YSOs, do inglês *Young Stellar Objects*) atuam como "lâmpadas infravermelha no espaço". Ao comparar as características de absorção de um espectro astronômico com o espectros de referência de medidos em laboratório, a composição e as propriedades do gelo astrofísico podem ser determinadas. Isso é essencial para entender o papel o gelo astrofísico na evolução cosmoquímica da matéria e como isso

contribui para a composição química dos sistemas planetários.

Até o momento, menos de dez moléculas foram identificadas inequivocamente em observações de gelo astrofísico, estas são H_2O, CO_2, CO, CH_4, NH_3, CH_3OH, OCS, OCN^-, $^{13}CO_2$ e ^{13}CO. Algumas outras espécies, como NH_4^+ e moléculas orgânicas maiores podem também estar presentes nas observações, mas nenhuma detecção definitiva foi possível. Esse baixo número de detecções contrasta com o número muito maior de moléculas identificadas na fase gasosa no MI, que chega a quase 300. Também notável é o fato de que o única COM detectada em gelos astrofísicos é o metanol. Isso é surpreendente, já que o gelo astrofísico é considerado o local onde essas moléculas orgânicas são formadas. A não detecção dessas especies na fase sólida se deve a alguns desafios relacionados à detecção de COMs em gelos astrofísicos. Em primeiro lugar, não se espera que as abundâncias de COMs sejam altas, figurando no nível de alguns poucos por cento em relação a H_2O ($\leq 5\%$). Levando em conta essas abundâncias, somente alguns poucos modos vibracionais ativos no IV apresentam uma intensidade suficiente para serem detectados com a sensibilidade dos telescópios anteriores. Além disso, diferentes moléculas possuem grupos funcionais semelhantes, o que causa a sobreposição de suas bandas de absorção no IV. Assim, e possível identificar uma família de moléculas, mas raramente uma espécie individual. Além disso, o perfil espectral das moléculas no estado sólido é influenciado por fatores como temperatura do gelo, interação com as moléculas vizinhas e a estrutura do material solido. Portanto, para identificar com precisão e extrair informações sobre as condições físicas e químicas em que essas moléculas se formam no espaço, é essencial ter acesso a uma ampla gama de espectros laboratoriais de moléculas medidas em condições experimentais variadas, como composição e temperatura da amostra e concentração de diferentes moléculas na mistura.

Gelos astrofísicos no laboratório: IRASIS

Os gelos astrofísicos são encontrados em regiões do MI caracterizadas por densidades de gás que variam de aproximadamente 10^3 a 10^6 partículas/cm^3, ordens de magnitude menor que a denisdade na atmosfera terrestre (cerca de 10^{19} partículas/cm^3). Além disso, o gelo astrofísico pode existir em temperaturas que variam de aproximadamente 10 a 150 K (-263°C a -123°C). Assim, produzir análogos de gelo astrofísico em um ambiente de laboratório requer o uso de configurações experimentais capazes de criar vácuo e temperaturas criogênicas. O Laboratório de Astrofísica do Observatório de Leiden (*Laboratory for Astrophysics/Leiden Observatory*) emprega vários

aparatos experimentais para criar essas condições extremas. Nesta tese foram utilizados dois aparatos experimentais: IRASIS (do inglês *InfraRed Absorption Setup for Ice Spectroscopy*, ver Figura 4) e OASIS (do inglês *Optical Absorption Setup for Ice Spectroscopy*). IRASIS é usado para medir espectros IV em alta resolução de amostras de gelo sob condições semelhantes as do MI. Esse aparato experimental consiste em uma câmara de ultra-alto vácuo que abriga um cristal, transparente à radiação IV, que é usado como substrato para o crescimento das amostras de gelo. Esse substrato é termicamente conectado a um criostato e pode ser resfriado a temperaturas tão baixas quanto 15 K. Misturas gasosas contendo as moléculas de interesse podem ser preparadas e introduzidas na câmara de vácuo do IRASIS. Quando as moléculas colidem com o substrato frio, elas aderem (adsorvem) à sua superfície, formando uma camada de material congelado, o chamado análogo do gelo astrofísico. Ao incidir luz IV sobre esta amostra, a absorção de luz das diferentes moléculas pode ser medida e estudada. Além dos espectros IV, a luz que é absorvida por molécula no gelo é quantificada, permitindo determinar a força da banda dos diferentes modos vibracionais da molécula. A força da banda é um parâmetro importante para a astroquímica, pois permite quantificar moléculas em um espectro astronômico. Todos os dados de espectroscopia derivados nos trabalhos aqui compilados estão disponíveis publicamente através do LIDA (do inglês *Leiden Ice Database for Astrochemistry*), o banco de dados de espectros infravermelho compilado pelo Laboratório de Astrofísica do Observatório de Leiden.

O aparato experimental OASIS é usado para investigar a interação da luz visível e ultravioleta com amostras de gelo. O aparato consiste em uma câmara de vácuo que abriga um espelho conectado a um criostato. Amostras de gelo de alguns micrômetros podem ser formadas na superfície do espelho e iluminadas com luz na faixa do ultravioleta e visível usando uma lâmpada de arco de xenônio (na faixa de 250-750 nm) e um feixe de laser HeNe vermelho (632,8 nm). Ao incidir na superfície do gelo, parte da luz dessas fontes e refratadas dentro do gelo e parte é refletida pela superfície. O padrão de interferência resultante da interação dos feixe refletido e refratado é registrado individualmente para o laser e para a luz da lampada de arco de xenônio. No caso da luz do laser, o padrão de interferência é medido usando-se um fotodetector e um para a lâmpada de arco xenônio a medida é feita por um espectrômetro. A análise do padrão de interferência durante o crescimento do gelo permite derivar o índice de refração do material na faixa de 750 - 250 nm. A análise do padrão de interferência após o crescimento do gelo permite monitorar as mudanças estruturais do gelo. Detalhes de ambos aparatos experimentais são apresentados no Capítulo 2.

Figure 4: Foto do aparato experimental IRASIS, dedicado a estudar os espectros IV de análogos de gelo astrofísicos.

Sobre esta tese

Os capítulos 3, 4 e 5 desta tese descrevem a investigação das propriedades de absorção de três moléculas orgânicas importantes no contexto astroquímico: acetona (CH_3COCH_3), metilamina (CH_3NH_2) e cianeto de metila (ou acetonitrila, CH_3CN). Essas moléculas foram detectadas em diferentes ambientes astronômicos na fase gasosa, embora seja esperado que sua formação ocorra em gelos astrofísicos. Os estudos apresentados nessa tese analisam as mudanças no perfil de absorção, na faixa de 2,5 - 20 μm, dessas moléculas quando misturadas com outras moléculas que compõem gelos astrofísicos (por exemplo, H_2O, CO_2 e CO) e para temperaturas entre 15 - 160 K. Além disso, o índice de refração e a força da banda dos modos vibracionais dessas moléculas são medidos. Nesta tese, os espectros de laboratório são comparados a observações de gelo astrofísico, feitas por telescópios como Spitzer e ISO, e ajudam a determinar o limite superior para a abundancia dessas moléculas nas observações.

Além das interações com a luz infravermelha, a interação de amostras de gelo com

luz visível e ultravioleta também podem ser investigadas no laboratório. Essas propriedades são importantes para o estudo de superfícies congeladas no Sistema Solar (por exemplo, superfícies lunares), que constantemente recebem radiação solar. O Capítulo 6 dessa tese reporta o estudo da interação da luz, na faixa de comprimento de onda entre 250 - 750 nm, com gelos de monóxido de carbono (CO) usando o aparato experimental OASIS. Ao monitorar a luz refletida por essas amostras, é possível detectar mudanças estruturais que ocorrem no gelo.

O capítulo 7 desta tese deixa a pesquisa com gelo e apresenta um estudo teórico que explora as características de estabilidade e absorção vibracional de fulerenos. Essas moléculas são compostas apenas por átomos de carbono e exibem uma estrutura semelhante a uma gaiola. C_{60}, C_{70} e C_{60}^{+} foram identificados na fase gasosa em diferentes ambientes astronômicos. Sua presença levanta questões sobre a potencial existência de outras especies de fulereno no MI. Medir o espectro IR dessas moléculas por meio de experimentos não e trivial do ponto de vista experimental. Assim, métodos computacionais de mecânica quântica são usados para calcular a estrutura eletrônica e as propriedades dessas moléculas, o que inclui as frequências vibracionais. No capítulo 7, a Teoria do Funcional da Densidade (DFT, do inglês, *Density Functional Theory*) é usada para calcular a frequência vibracional de fulerenos contendo de 44 a 70 átomos de carbono. Os espectros obtidos são comparados com o espectro astronômico de nebulosas planetárias, possibilitando avaliar a presença dessas moléculas nesses objetos.

As principais conclusões dos trabalhos apresentados nesta tese são resumidas a seguir:

I) Medidas laboratoriais do espectro infravermelho de moléculas em condições análogas as encontradas no MI são essenciais para entender as observações de gelos astrofísicos.

A comparação das observações com espectros obtidos em laboratório em diferentes condições nos permite determinar informações sobre a temperatura e como as moléculas estão misturadas no gelo astrofísico. Nos capítulos 3, 4 e 5 desta tese, o trabalho espectroscópico foi feito para permitir pesquisas futuras de acetona, metilamina e cianeto de metila em observações de gelo astrofísico com JWST. A partir da análise espectral dessas moléculas, pode-se extrair as seguintes conclusões:

- As bandas de absorção em 5,85, 7,34 e 8,14 μm apresentam maior potencial para identificar acetona em observações de gelo astrofísico.

- A identificação de metilamina em gelos astrofísicos sera desafiadora, porque suas principais bandas de absorção ocorrem na mesma região das bandas de absorção

de H_2O e NH_3. Sob esta ressalva, as bandas em 3,45 e 8,62 μm têm o maior potencial para identificar metilamina em observações de gelo. Considerando a banda de absorção em 3,45 μm, o limite superior para a abundância de metilamina em YSOs é estimado em cerca de $\leq 4\%$ em relação a H_2O.

- As bandas de absorção em 4,44 e 9,60 μm apresentam o maior potencial para identificar cianeto de metila em observações de gelo astrofísico. Usando essas bandas, a abundância de cianeto de metila foi estimada em diversas observações de YSOs. Os valores estimados variam de alguns poucos por cento ate no máximo 4,1% em relação ao gelo de H_2O .

II) Transições estruturais no gelo de CO após sua deposição alteram suas propriedades de espalhamento. Foi verificado que, apos a deposição de gelo de CO de alguns micrômetros, transições estruturais espontâneas morfologia levam a amostra de gelo de uma estrutura que espalha a maior parte da luz incidente a uma estrutura transparente transparente. A velocidade com que essas transições ocorrem é influenciada pela espessura da amostra de gelo e pela temperatura em que a amostra foi depositada, e levam de algumas horas até dias para ocorrer. Embora isso seja insignificante quando comparado a escalas de tempo astronômicas, essas transições devem ser levadas em consideração ao estudar gelos de CO em laboratório.

III) Fulerenos contendo 44 até 70 átomos de carbono têm modos IV ativos entre 6 – 9 μm. As bandas presentes nessa região que podem contribuir para o perfil de emissão observado em nebulosas planetárias onde fulerenos já foram detectados. Entretanto, o espectro infravermelho dessas moléculas não podem explicar o perfil de emissão entre 10 - 13 μm observado nos mesmos objetos.

Publications

Refereed publications

1. *An Ice Age JWST inventory of dense molecular cloud ices. Nature Astronomy*
   McClure, M., Rocha, W.R.M., Pontoppidan, K., Crouzet, N., Chu, L., Dartois, E., Lamberts, T., Noble, J., Pendleton, Y., Perotti, G., Qasim, D., **Rachid, M. G.**, Smith, Z. L., Sun, F., Beck, T.L., Boogert, A.C.A, Brown, W.A., Caselli, P., Charnley, S.B., Cuppen, H.M., Dickinson, H., Drozdovskaya, M. N., Egami, E., Erkal, J., Fraser, H., Garrod, R.T., Harsono, D., Ioppolo, S., Jiménez-Serra, I., Jin, M., Jørgensen, J. K., Kristensen, L.E., Lis, D. C., McCoustra, M. R. S., McGuire, B. A., Melnick, G. J., Öberg, K. I., Palumbo, M. E., Shimonishi, T., Sturm, J. A., van Dishoeck, E. F. & Linnartz, H., 2023, Nature Astronomy, https://doi.org/10.1038/s41550-022-01875-w

2. *LIDA - The Leiden Ice Database for Astrochemistry*
   Rocha, W., **Rachid, M. G.**, B. Olsthoorn, E. F. van Dishoeck, M. K. McClure, H. Linnartz, 2022, Astronomy & Astrophysics, 668, A63.

3. *Infrared spectra of complex organic molecules in astronomically relevant ice mixtures - V. Methyl cyanide (acetonitrile)*
   Rachid, M. G., Rocha W., Linnartz, H., 2022, Astronomy & Astrophysics, 665, A89.

4. *Refractive index and extinction coefficient of vapor-deposited water ice in the UV–vis range*
   He, J., Diamant, S. J., Wang, S., Yu, H., Rocha, W. R., **Rachid, M. G.**, & Linnartz, H., 2022, The Astrophysical Journal, 925(2), 179.

5. *Infrared spectra of complex organic molecules in astronomically relevant ice mixtures - IV. Methylamine*
   Rachid, M. G., Brunken, N., De Boe, D., Fedoseev, G., Boogert, A. C. A., Linnartz, H., 2021, Astronomy & Astrophysics, 653, A116.

6. *Infrared spectra of complex organic molecules in astronomically relevant ice mixtures - II. Acetone*
   Rachid, M. G., Terwisscha van Scheltinga, J. , Koletzki, D., & Linnartz, H., 2020, Astronomy & Astrophysics, 639, A4.

7. *Processing of 72-K water-rich ices by keV and MeV oxygen ions: implications for the Saturnian moon Enceladus*
   Rachid, M. G., Pilling, S., Rocha, W. R. M., Agnihotri, A., Rothard, H., & Boduch, P., 2020, Monthly Notices of the Royal Astronomical Society, 494(2), 2396-2409.

8. *Searching for stable fullerenes in space with computational chemistry*
   Candian, A., **Gomes Rachid, M.**, MacIsaac, H., Staroverov, V. N., Peeters, E., & Cami, J., 2019, Monthly Notices of the Royal Astronomical Society, 485(1), 1137-1146.

9. *Destruction of $C_2H_4O_2$ isomers in ice-phase by X-rays: Implication on the abundance of acetic acid and methyl formate in the interstellar medium.*
   Rachid, M. G., Faquine, K., & Pilling, S., 2017, Planetary and Space Science, 149, 83-93.

10. *Systematic theoretical study of non-nuclear electron density maxima in some diatomic molecules*
    Terrabuio, L. A., Teodoro, T. Q., **Rachid, M. G.** & Haiduke, R. L., 2013, The Journal of Physical Chemistry A, 117(40), 10489-10496.

Submitted/About to be submitted

1. *Morphological changes in CO ices probed by interference measurements*
   Rachid, M. G., He, J., Cenic, R, Rocha, W., Slavicinska, K., Henning, T. & Linnartz, H., A&A.

2. *The hunt for formamide in interstellar ices - Laboratory infrared spectra in astronomically relevant ice mixtures and comparisons to ISO, Spitzer, and JWST observations*
   Slavicinska, K., **Rachid, M. G.**, Rocha, W., Chuang, K.-J, van Dishoeck, E.F. & Linnartz, H., A&A

About the author

I was born in Rio Claro, in the countryside of São Paulo state, in Brazil, on August 16th, 1989. My full education has taken place in public schools, and while I have to thank some passionate teachers that helped develop my interest in science, it was my father who truly nurtured my passion for learning. Through our weekly visits to the city library, he sparked in me a deep passion for reading and learning. In an interesting way, my fascination with chemistry and physics was revealed at the age of 11, when I received disciplinary action for running in the school corridors. As part of my "punishment", I was assigned to create a comprehensive homework on the topic of "the atom." It was during this task that I was introduced to the fascinating domain of atoms, orbitals, and molecules. It was like a whole new world had opened up to me! Ever since that moment, I knew that I wanted to know more about those tiny particles and become a scientist when I grew up.

In 2005, I passed an exam to enroll in the highly-regarded school "ETEC Prof. Armando Bayeux da Silva" for my high school studies. Upon completing high school in 2008, I was accepted into the chemistry bachelor's program at the University of São Paulo (USP), in São Carlos. It was during this time that I became captivated by astronomy and was fortunate to have the guidance of Prof. Luiz Vitor de Souza Filho, who graciously accepted me as a guest student in his group. During the final year of my bachelor's program, I conducted a research project on theoretical chemistry, studying the electronic structure of various diatomic molecules under the supervision of Prof. Roberto Luiz Andrade Haiduke. After completing my chemistry degree, in 2012, I opted not to pursue a master's degree immediately. Instead, I decided to broaden my academic horizons by studying physics and astronomy to explore various career paths. To this end, I relocated to São Paulo and enrolled in a physics program, also at the USP. During my time there, I engaged in several research projects until I discover a fascination for astrochemistry. At that time, I had been awarded a prestigious undergraduate scholarship from FAPESP, the research agency of São Paulo

state, to work with Prof. Eduardo Janot Pacheco on a project related to the infrared absorption spectra of nucleobases. During this period, I faced health challenges that resulted in extended hospitalizations, delaying the completion of my studies. With the encouragement and support of those around me and my professors, I concluded my physics degree, and in 2016, after a break to work as a teacher, baker, and traveling in South America, I enrolled in a master's program at the Universidade do Vale do Paraiba, in São Jose dos Campos.

I obtained my master's degree with the support of a FAPESP scholarship and guidance from Prof. Sergio Pilling. My master's research focused on the impact of energetic ions on interstellar ice analogs and their implications for Solar System chemistry. During my scholarship, I had the opportunity to conduct experimental work on ion irradiation at GANIL in Caen-France, working with Prof. Philippe Boduch and Prof. Herman Rothard. Also during my master, I was selected to participate in a LEAPS project in Leiden. Under the supervision of Dr. Alessandra Candian, I conducted a computational study to analyze the IR spectra and stability of fullerenes.

I was admitted to a Ph.D. program at the Laboratory for Astrophysics in the Leiden Observatory in 2018, where I worked under the guidance of Prof. Harold Linnartz and Prof. Ewine van Dishoeck in the field of experimental and observational astrochemistry. My primary responsibility during my Ph.D. was to develop IRASIS (InfraRed Absorption Setup for Ice Spectroscopy), an upgrade to an existing laboratory setup designed for studying the infrared spectra and characteristics of interstellar ice analogs. Alongside Dr. Jiao He, I also worked on the characterization of visible-ultraviolet properties of ice using the OASIS (Optical Absorption Setup for Ice Spectroscopy) setup. In addition to the laboratory work, I have been involved in the upgrade of the Leiden Ice Database for Astrochemistry, a project led by Dr. Will Rocha, and in the analysis of the first interstellar ice observations from the JWST ERS program Ice Age, led by Dr. Melissa McClure. I am presently involved in the observation of COMs in star-forming regions using ALMA observations with Prof. Ewine van Dishoeck. This thesis is the outcome of my laboratory and computational work and has been presented at conferences and symposiums in the Netherlands and abroad. Also during my Ph.D., I was the daily supervisor of many bachelor students working on experimental projects and the teaching assistant of experimental physics.

In April 2023, I joint the research team of Prof. Sander Woutersen at the Van 't Hoff Institute for Molecular Sciences at the University of Amsterdam as a postdoctoral researcher.

Acknowledgements

I feel lucky to have been surrounded by many supportive and inspiring people on my journey. While the list of those who have played a significant role in my life is lengthy, I would like to thank here those who have been particularly present over the last four years. Please accept my apologies if there are any omissions, they are not a result of disregard on my part.

Firstly, I'm grateful to the Leiden Observatory for their efforts in helping me move smoothly to the Netherlands. All their support and events organized for Ph.D. candidates were incredibly helpful in easing my integration into the new cultural and academic environment. Harold - thanks for believing in me and allow for exploring the laboratory and work in a manner that suited me. This ultimately helped me develop independence. Also, your guidance and patience were invaluable in developing my writing skills. Ewine - thanks for supporting and guiding me when I wanted to look also outside the walls of the laboratory and start an observational project. It has been a continuous and rich learning experience for me. Adwin - your help with ice observations and willingness to address my doubts made a real difference. Xander - our discussions during the past years have meant a lot to me. Thanks for guiding me through confusing moments.

Will - unfortunately, I cannot have three paranymphs. I would be enormously happy to also have you by my side during the defense. Our scientific discussions were always a source of excitement for me. Thanks for the friendship and support these last years. Jiao - thanks a lot for being such a patient person and so open to teaching and collaborating. I had great and motivating science discussions with you. Also thanks for teaching me how to use chopsticks! Alessandra - my journey in Leiden started with you. Thanks for your confidence in me and for all that you taught me during LEAPS. Thanja - your enthusiasm and support for my ideas, even when they did not develop to a final point, were essential. Thanks for being available to listen and give advice on so many occasions. Melissa and the whole Ice Age team - thanks for the many interesting discussions. Being able to taste a bit of the flavor of working with JWST data was fantastic!

Lammim - your positive posture in life is an inspiration. At least the pandemic brought me one good thing: it made us closer. Thank you and Ruslan for all the

amazing times together in these last years, the delicious goat biryani, and for being such great friends, even opening your house for me to burn paper until 1 AM to make a piece of art. Danna - not only you were a companion for enjoying good Belgian beers, but you also helped me navigate the lab. On numerous occasions, you generously took the time to help me with how to use equipment and do stuff in the lab. Thanks a lot! Katie - it was a pleasure to work with you and share the office, it has been a lot of fun and I have also learned a lot with you. Take care well of IRASIS and thanks for all the help with photoshop! Sanjana - you were one of my earliest friends here in Leiden, and I'm grateful for all the enjoyable moments we shared. Whether it was in Leiden, Lapland, or canyoning for miles in the heart of Poland. Amanda - it is such a lucky coincidence that you ended up in Leiden! I'm grateful for the opportunity to share more laughs and good times with you!

Gleb and Ko-Ju - thanks for being around and helping with laboratory problems. Nicolas - thanks for all the help with Labview and conversations during long lab working hours. Carlos and Julia, thanks for all the enjoyable time at the observatory and outside. Also thanks to other laboratory members (current and past) for making our group so rich (and fun!) - Michał, Jeroen, Tara, Dominik, Brian, Morgan, Jerry, Pranjal, Niels, Pablo, Helgi, Pavi, Anita, Daniel, and Yu.

Nashanty, Dani, Haochuan, Pien, Casper, and Rastko - being your daily supervisor was a great experience and I also learned many different and valuable things working with each of you. Martijn, Pooneh, and Yuan - thanks a lot for helping me with CASSIS and giving my first steps in ALMA observations! Also thanks to other current and past members of Ewine's group for all the nice conversations, in special to Alice, Benoit, Łukasz, Margot, and Sierk.

Aart - thanks for helping with lab issues and for your sense of humor. I hope you are having a great time in Ireland! Martijn, Peter, Robin, and other members from the mechanical and electronics workshop - all this work could not be done without you, thanks a lot for all the support!

To my observatory colleagues that have made these years funnier: Lydia, the end of our freshmen year was amazing, thanks for the enthusiasm to make it happen! Dario, it is great to have you around, please, don't go to the US again. Martijn, we had great beer chats but your appreciation for Grolsh is a mystery to me. Anna, your sense of humor goes well with Imperial IPA. Also thanks to other dear observatory colleagues - Mantas, Isabel, Andres, Kirsty, Bas, Turgay, Evgeni, Aida, Olivier, Marta, Matus, Fraser, and Hiddo.

Folkert - I have to thank the Leiden Observatory for having allowed me to meet

you, certainly the best thing that happened during my Ph.D. time. For you, my love, thanks for your companionship and support. Also thanks for all your LaTeX help and for being such a great cook!

To my mother Denise, my father Clebio, and my brother Neto. I miss you so much. It is so much. Thanks for being so supportive of my dreams, even when the price to pay is the distance. Daphne, Ger, and the Nobels family, my Dutch family. You make me feel at home. Thanks for all the Sinterklaas, weekends, and other good times together!

To the most fun people that I know, my high school friends Bol, Jown, Marcia, Nielly, and Tati - Wow, it has been 15 years that we don't see each other daily! Despite it, you'll still make me laugh with our online chats! The few times that we could meet in person in these last years kept my heart warm and full of good memories.

Finally, I would like to thank the musicians of my country, Brazil. The amazing sambas, forrós, chorinhos, and many MPBs have the real power of keeping one inspired. During the COVID, many musicians kept producing content and sharing it on social media. For this, I owe you a huge thanks, because, without art, many people (including myself) would have gone crazy!